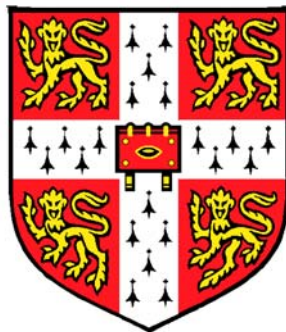


Metallic Magnetic Heterostructures

Chi Wah Leung
St. John's College
Cambridge



A Dissertation Submitted for the Doctor of Philosophy Degree
in the University of Cambridge

December
2002

Abstract

This work studied sputter deposited conventional spin valves (SV) and related structures. In SV layered structures, two ferromagnetic layers are separated by a non-magnetic spacer. Under an external magnetic field, the relative orientation of the magnetization changes in the ferromagnets, exhibiting the giant magnetoresistive effect. The controlled switching of ferromagnets in convention SV is facilitated by the exchange bias (EB) effect, which is achieved by depositing an antiferromagnetic layer next to one of the ferromagnetic layers in a magnetic field.

Two highly related investigations were performed in this work. In the first part the exchange bias effect in the $\text{Ni}_{80}\text{Fe}_{20}/\text{Fe}_{50}\text{Mn}_{50}/\text{Co}$ trilayer structure was studied. Samples were deposited in a low field condition that permitted EB to be established in NiFe/FeMn but not in FeMn/Co bilayer structures. Temperature-dependent magnetic measurements were performed on the trilayer sample, as well as the corresponding NiFe/FeMn and FeMn/Co bilayer samples. Recent literature on similar system showed that an AF spiral could be formed in the trilayer, which was probed by relative EB directions of the NiFe and Co layers. In this work, no exchange bias was found to propagate from the NiFe/FeMn system into the FeMn/Co system, showing that the AF spiral was induced by the specific magnetic treatment and was not the cause of EB effect. Besides, exchange bias field and coercivity of the samples indicated the influence of the EB system in the presence of an adjacent EB system. Explanations of the effect were made with some existing EB models.

In the second part of the work, conventional SV of target structure Nb/NiFe/Cu/Co/FeMn/Nb was studied in a 'built-up samples' strategy. A batch of these built-up samples, which corresponded to the different stages of the deposition of the target top conventional SV structure, were prepared by terminating the sputtering process after a certain number of layers were deposited. These samples were thoroughly characterized by structural, magnetic and electrical measurements. In terms of structural characterization by x-ray techniques, more reliable information concerning the morphology and microstructure of the layers was obtained by probing the built-up samples, instead of relying solely on the information of the full SV structure. For the electric and magnetic measurements, a number of unexpected observations were made in the built-up samples, although the final performance of the full SV structure was of comparable quality to the literature. These results showed the ability of the 'built-up samples' strategy in critical characterization and optimization of magnetic multilayered structures.

Declaration

This dissertation is submitted for the degree of Doctor of Philosophy in the University of Cambridge. Except where specific references are made, this work is entirely the result of my own work and includes nothing that is the outcome of work done in collaboration. No part of this work has been or is being submitted for any other qualifications at this or any other university. This dissertation does not exceed the limit of length.

Some of the works contained in this dissertation are published or presented as listed below.

Publications

- ‘Development of structural, magnetic, and transport properties in NiFe/Co-based top spin valve: Studies by sequential addition of constituent layers’,
C.W. Leung and M.G. Blamire,
J. Appl. Phys. **91**, 8572-8574 (2002).
- ‘Exchange bias in ferromagnet/ antiferromagnet/ ferromagnet trilayers’,
C.W. Leung and M.G. Blamire
App. Phys. Lett., (submitted).
- ‘Control of the switching properties of magnetic thin films and spin valve devices by patterning’,
D. Morecroft, C.W. Leung, N.A. Stelmashenko, J.L. Prieto, D.B. Jardine and M.G. Blamire,
IEEE. Trans. Magn. **37**, 2079-2081 (2001).
- ‘*In-situ* magnetoresistance measurements during patterning of spin valve devices’,
D. Morecroft, J.L. Prieto, C.W. Leung, G. Burnell, M.G. Blamire and D.B. Jardine,
J. Appl. Phys., **91**, 8575-8577 (2002).
- ‘Coercivity cross-over and exchange bias in Co/FeMn/CuNi trilayers’,
M.G. Blamire, M. Ali, C.W. Leung, C.H. Marrows and B.J. Hickey,
Phys. Rev. Lett., (submitted).

Presentations

- Joint Magnetism Workshop 01 (University of Cardiff, Cardiff, 2001)
‘Study of evolution and correlation of structural, transport and magnetic properties in built-up structures of NiFe/Co spin valve’
C.W. Leung, J. D. R. Buchanan, T.P.A. Hase, B.K. Tanner and M.G. Blamire.
- The 46th Annual Conference on Magnetism and Magnetic Materials (Seattle, USA, 2001)
‘Development of structural, magnetic and transport properties in Ni₈₀Fe₂₀/Co- based top spin-valve – studies by sequential addition of constituent layers’
C.W. Leung and M.G. Blamire.
- Joint (G&T)MR and MML Network Workshop (Leeds, 2002)
‘Exchange bias in FM/AF and FM/AF/FM structures: effect of deposition field’
C.W. Leung and M.G. Blamire.

Acknowledgement

This work is possible only with the help and support of lots of people during the course of my study. I would like to thank my supervisor, Dr. Mark Blamire, for his untiring teaching and supervision throughout the project. From time to time his insight into in problems has given clues on many possible directions of progress of the project. I would also like to thank the head of the group, Prof. Jan Evetts, for several occasions of useful discussions.

I also have to thank Dr. A.H.W. Ngan in the Department of Mechanical Engineering in the University of Hong Kong, who was my supervisor of my final year project. Without him, I would not have started my studies in thin films and pursue my research in Cambridge.

Daily laboratory work is enjoyable and yet challenging, and I would like to thank many of my fellow colleagues for their assistance that facilitated the work. Nadia Stelmashenko has brought me through the sample deposition processes at the early stage of my project, and has been helpful in lots of general issues. Jose Prieto and Debbie Morecroft have contributed lots of ideas on magnetic and electrical measurements. Gavin Burnell, the computer expert, has helped so much in the routine computer-related hassles. Dae-Joon Kang, who always come up with plenty of ideas, has inspired me much on the fabrication of magnetic nanostructures and the research work. Chris Bell has been extremely patient in explaining and discussing many physical problems with me. I would also like to express my appreciation towards many of my colleagues in their kind assistance throughout the project, in no particular order: Zoe Barber, Ashish Grag, Karen Yates, Neil Mathur, Bas van Aken, Brian Pang, Moon-Ho Jo, James Chapman, Mary Vickers, Neil Todd, Jerome Wolfman, Pak Kin Wong and Robert Hadfield.

During the course of the project I have spent two weeks in the University of Durham for x-ray analysis of some samples. It is a pleasure to thank Prof. Brian Tanner, Dr. Tom Hase and Mr. James Buchanan for their assistance and discussions. I would also like to extend the acknowledgement to Prof. Bryan Hickey, Dr. Chris Marrows and Dr. Mannan Ali in the University of Leeds for their helpful discussions for the experimental work on exchange bias.

Life in England would have been much more difficult for me without the help of Mr. Paul Lam and his family in London. Their hospitality during my (frequent) weekend visits, their generous treats of typical English cuisine (fish and chips, which they sell in their shop) and traditional

Chinese meals (which I enjoy more), and their care towards my daily life have provided me the warmth that I savour outside my home. Encounters with the family, especially with my cousin Danny and his friends, gave me much exposure (and sometimes shocks) towards the English (particularly youth) culture.

There are three people in particular to whom I would like to express my deepest thanks and love for their endless support. My parents have been extremely understanding and constantly supportive towards my study. Their encouragement and attention has brought me through many of the difficult times in these days. And certainly I will not miss out. These years have been horribly long for both of us, especially we seem to be constantly '8-time zones' away from each other. I am much indebted of her patience, tolerance and support in these days.

I would like to express my gratitude towards the Croucher Foundation in Hong Kong for their financial assistance in the form of a Croucher Foundation Scholarship.

Chi-Wah
(alias Dennis)

To my parents and Frances

List of symbols

$A_{FM/AF}$	Exchange stiffness of FM/AF interface region
A_{FM}	Exchange Stiffness of ferromagnet
α	Angle between ferromagnetic magnetization and anisotropy axes of ferromagnet
$\alpha_{1,2}$	Relative orientation between magnetization of two ferromagnetic layers
β	a. Angle between (staggered) antiferromagnetic magnetization and anisotropy axes of antiferromagnetic b. Angle between incoming ions and the line of centres during collision in sputter deposition c. Integral breath of diffraction peaks
D	a. Vertical grain/crystallite size b. Target-substrate distance in sputter deposition
d_{hkl}	d-spacing between successive atomic planes (hkl)
δ	a. Mean-free-path of electrons b. Domain wall width
ε	Strain
ϕ	Angle between measurement field and <i>in-situ</i> deposition field
H	Applied magnetic field
H_c	Coercivity
H_{ex}	Exchange bias field
H_o	Free-layer offset field in spin valve structures
H_s	Saturating field
h	a. Peak-to-valley distance on rough surfaces b. Roughness exponent
η	Angle between ferromagnet magnetization and current direction
J_{ex}	Exchange constant
$J_{FM/AF}$	Interfacial exchange coupling energy
J_1	Bilinear interlayer exchange coupling strength
J_2	Biquadratic interlayer exchange coupling strength
K_{FM}	Uniaxial anisotropy of ferromagnet
K_{AF}	Uniaxial anisotropy of antiferromagnet
K_s	Surface anisotropy

L	Distance between peaks on rough surfaces
Λ	Period of oscillation of bilinear interlayer exchange coupling energy
λ	Wavelength of x-ray
M_{FM}	Volume saturation magnetization of ferromagnet
M_r	Remanent magnetization of a ferromagnetic sample
M_s	Saturation magnetization of a FM sample
θ	a. Angle between applied magnetic field and anisotropy axis b. <i>Half</i> of the detector angle in x-ray diffractometry
P	Sputtering gas pressure
R	Source-sample (sample-detector) distance in Bragg-Breneto x-ray diffractometer geometry
ρ	Resistivity
S	Spin
σ	a. Root-mean-square (rms) roughness b. Conductivity
T	Temperature
T_B	Blocking temperature of exchange bias structure
T_C	Curie temperature of ferromagnet
T_m	Melting point
T_N	Néel temperature of antiferromagnet
T_s	Substrate temperature during sputter deposition
t	Thickness
t_{crit}	Critical thickness of antiferromagnetic layer in exchange bias structure
ω	Sample angle in x-ray diffractometry
x	Sample surface displacement from the sample rotation axis in x-ray diffractometry
$\xi_{//}$	Lateral (spatial) correlation length
ξ_{\perp}	Vertical correlation length
ψ	Angle between uniaxial and surface anisotropies directions

Table of Contents

Abstract	ii
Declaration	iii
Acknowledgement	v
List of symbols	viii
A note on the units	xv
Chapter 1 – Introduction	1
1.1 Sputter deposition of thin films	1
1.1.1 Principle of sputter deposition	1
1.1.2 Magnetron sputtering	4
1.1.2.1 Disadvantages of conventional sputtering process	4
1.1.2.2 Magnetron sputtering process	4
1.1.3 Microstructures of sputtered thin films	5
1.1.3.1 Film formation and growth	5
1.1.3.2 Structural zone model and microstructure of sputtered films	6
1.1.3.3 Control of film properties	8
1.2 Magnetic properties of sputtered thin films	9
1.2.1 Energetics of magnetic thin films	9
1.2.1.1 Exchange interaction	10
1.2.1.2 Zeeman term	10
1.2.1.3 Anisotropy in thin magnetic films	11
1.2.1.3.1 Shape anisotropy	11
1.2.1.3.2 Induced anisotropy	12
1.2.2 Domains and magnetization processes	13
1.2.2.1 Domains and domain walls	13
1.2.2.2 Magnetization reversal and hysteresis	15
1.2.2.3 Modelling of magnetization process	17
1.3 Sputter deposition of thin films in this project	20
1.3.1 Substrate preparation	20
1.3.2 ‘UFO –1’ dc magnetron sputter deposition system	20
References for Chapter 1	22

Chapter 2 – Characterization of Layered Magnetic Heterostructures	24
2.1 Structural characterization	24
2.1.1 Atomic force microscopy (AFM)	26
2.1.2 X-ray	28
2.1.2.1 Experimental methods	29
2.1.2.2 High angle regime ($2\theta > 15^\circ$)	29
2.1.2.3 Low angle regime ($2\theta < 15^\circ$)	31
2.2 Magnetic characterization	32
2.3 Electrical characterization	33
2.3.1 Electrical resistivity of thin films	33
2.3.2 Van der Pauw resistivity measurement	34
2.3.3 Field-dependent resistance (MR) measurements	35
References for Chapter 2	36
Chapter 3 – Interlayer Exchange Coupling and Giant Magnetoresistive Effect	37
3.1 Interlayer exchange coupling	37
3.1.1 Introduction	37
3.1.1.1 Bilinear coupling	37
3.1.1.2 Biquadratic coupling	38
3.1.1.3 Phenomenological descriptions	39
3.1.2 Theoretical models	41
3.1.2.1 Bilinear coupling	41
3.1.2.1.1 RKKY coupling model	41
3.1.2.1.2 Quantum well model	43
3.1.2.2 Biquadratic coupling	43
3.1.2.2.1 Rough interface models	45
3.1.2.2.2 Loose spin model	46
3.1.2.2.3 Magnetic proximity effect	46
3.2 Giant magnetoresistive (GMR) effect	48
3.2.1 Introduction	48
3.2.2 Theory of GMR effect	49
3.2.2.1 Principle	49
3.2.2.2 GMR models	51
3.2.2.2.1 Semi-classical model	51
3.2.2.2.2 Quantum-mechanical approach	52
3.3 Summary	54
References for Chapter 3	55

Chapter 4 – Exchange Anisotropy	57
4.1 Introduction	57
4.1.1 Occurrence	58
4.1.2 Shifting and widening of hysteresis loops	59
4.1.3 Training effect and memory effect	59
4.2 Exchange bias theory	61
4.2.1 Meiklejohn and Bean (MB) model	61
4.2.2 Random field model	63
4.2.3 AF domain wall (Mauri) model	64
4.2.4 Spin flop model	67
4.2.5 Stiles and McMichael model	68
4.2.6 Models explaining enhanced coercivity in exchange bias structure	69
4.3 Comparison of models and experiments	70
4.3.1 Influence of individual layers	70
4.3.1.1 FM layer	70
4.3.1.2 AF layer	71
4.3.1.3 FM/AF interfaces	73
4.3.2 Effect of T_C and T_N	74
4.3.3 AF spin structure	76
4.4 Summary	77
References for Chapter 4	79
Chapter 5 – Experiments on Exchange Bias Systems	81
5.1 Introduction	81
5.2 Experiment procedures	83
5.2.1 <i>In situ</i> deposition field control	83
5.2.2 Temperature dependent $M(H)$ measurements	84
5.3 Experimental results	84
5.3.1 Single FM layers	84
5.3.2 FM/FeMn bilayers	85
5.3.3 FeMn/FM bilayers	86
5.3.4 NiFe/FeMn/Co trilayer	88
5.4 Discussion	97
5.4.1 AF spiral?	97
5.4.2 H_{c-co} behaviour in bilayers and trilayers	98
5.5 Summary	100
References for Chapter 5	101

Chapter 6 – Spin Valves	102
6.1 Introduction	102
6.1.1 Problems with GMR repeated bilayers	102
6.1.2 Spin valve structures	102
6.1.3 Variations of spin valve structures	104
6.2 Control of magnetoresistive performance in spin valves	105
6.2.1 Layer thickness	106
6.2.2 Roughness and intermixing at interfaces	107
6.2.3 Capping and buffer layers	108
6.3 Coupling effect in spin valve structures	108
6.3.1 Magnetic bridges	108
6.3.2 Interlayer exchange coupling	109
6.3.3 Magnetostatic (‘orange peel’) coupling	111
6.3.4 Domain wall coupling	112
References for Chapter 6	113
Chapter 7 – Evolution of the Structural Properties in NiFe-Co Based Top Spin Valve Structures	115
7.1 Introduction	115
7.2 Experimental	116
7.2.1 Sample fabrication	116
7.2.2 Structural characterization	117
7.2.2.1 X-ray reflectivity (XRR) measurements	117
7.2.2.2 AFM surface imaging	123
7.2.2.3 High-angle XRD	125
7.2.3 Discussion	130
7.3 Summary	131
References for Chapter 7	132
Chapter 8 – Electrical and Magnetic Characterization of NiFe/Co Spin Valve Built-up Samples	133
8.1 Control full SV results	133
8.2 Electrical measurements	134
8.2.1 Van der Pauw resistivity measurements	134
8.2.1.1 Cu layer resistivity investigation	136
8.2.1.2 FeMn layer resistivity investigation	137

8.2.2	Field dependent resistivity ($R(H)$) measurements	138
8.3	Magnetic measurements	141
8.3.1	Nb/NiFe and Nb/NiFe/Cu samples	141
8.3.2	Pseudo SV sample	143
8.3.3	SV samples	143
8.4	Discussions	144
8.4.1	Shifted anisotropy in NiFe films	144
8.4.2	Coupling in pseudo SV samples	147
8.5	Summary	150
	References for Chapter 8	151
 Chapter 9 – Conclusions and Outlook		152
9.1	Conclusions	152
9.1.1	Exchange bias study	152
9.1.2	Spin valve built-up sample investigations	152
9.2	Outlook	153
9.2.1	Spin valves	153
9.2.2	Exchange anisotropy	153
9.2.3	Nanomagnetism	154
	References for Chapter 9	156

A note on the units

Magneticians and thin film scientists are well known in the field of physics for their stubborn use of non-SI units. Unfortunately this work involved the studies of both areas, so a choice has to be made on the sets of units to be employed.

Throughout the thesis the *cgs* magnetic units will be used instead of SI units for their general use in the literature, while the SI pressure units (Pa) is employed instead of the old units (torr and mbar). Another liberty is taken on the occasional appearance of the length unit Angstrom (\AA , which is 0.1 nm) in the text. While all experimental works performed in this project employed the SI length unit (i.e. m), the unit \AA is used widely in the literature concerned with x-ray studies and condensed matter physics.

Chapter 1 Introduction

This chapter is broadly divided into three sections, considering the fundamental subjects on which this thesis is based on.

In the first section a summary will be given on the subject of sputter deposition of thin films. Sputtering is by far the most commonly employed method of depositing metallic films in industry and research. The mechanism of sputtering and the structure of films so yielded will be discussed. The second part of this chapter will be concerned with basic magnetism, with particular emphasis on magnetic thin films. Energetics of ferromagnets and the concept of domains will be presented. Finally, a summary will be given on the preparation of thin film samples in this project. While the general technique will be shown in this part of the thesis, specific techniques or methods employed in particular stages of the project will be discussed in the corresponding chapters.

1.1 Sputter deposition of thin films

Sputter deposition has a high degree of significance in thin film science as well as in industry. The major attraction of this technique comes from its high deposition rate (in the range of Å per second) and yet a large degree of control over film crystallinity and morphological properties. A wide range of materials can be sputter deposited, including high purity metallic films, metallic oxides, nitrides and carbides. The thickness of films so prepared can range from approximately 1 nm to several microns, and the film properties are highly reproducible.

1.1.1 Principle of sputter deposition

The principle of the sputtering process can be seen in Figure 1.1. In its simplest form, the target is placed at the cathode. A working gas, usually an inert gas such as Ar, is put between the electrodes. Occasionally some other gases (such as oxygen or nitrogen) are mixed with the inert gases during sputtering, for the purpose of depositing oxides or nitrides.

When a voltage is applied across the electrodes, electrons are emitted from the cathode. These electrons, being accelerated by the electric field across the electrodes, collide with the working gas molecules, generating ions and yet more electrons (secondary electrons). The ions of the inert gas molecules, being positively charged, are accelerated towards the cathode, setting up a cascade

of collisions and momentum transfer events in the target (Figure 1.2). The system comes to a steady state when the amount of secondary electrons emitted is sufficient to sustain the glow discharge. Collisions of the target by neutrals or accelerated working gas ions knock the atoms out of it, which finally condenses on the substrate on their way to the anode, producing thin films.

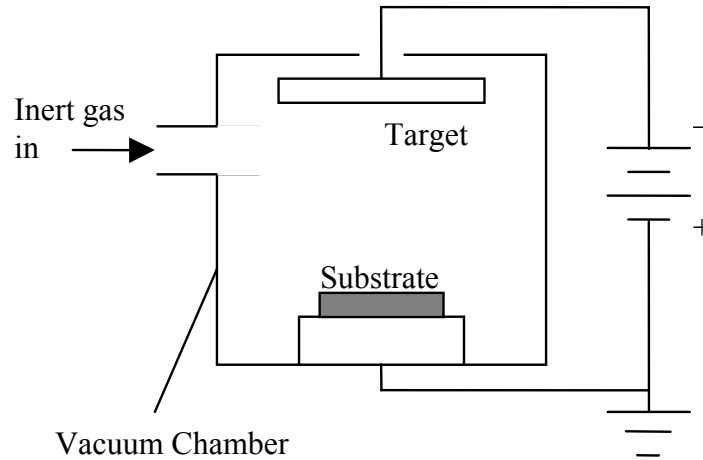


Figure 1.1 Schematic diagram of a dc sputtering system.

The mechanism of sputtering, from the above discussion, is therefore concerned with the momentum transfer between target atoms and incoming gas ions. Considering the collisions being elastic, the energy transfer from an incoming ion with mass m_i to a target atom of mass m_t , by means of the classical mechanics, is given by [1]

$$\frac{E_t}{E_i} = \frac{4m_i m_t}{(m_i + m_t)^2} \cos^2 \beta \quad [1.1]$$

where the subscripts i and t denote the properties of the incoming and target atoms/ions, E refers to the energy of the corresponding species and β is the angle defined by the initial trajectory of the incoming ion and the line joining the centres of the colliding species when they come into contact.

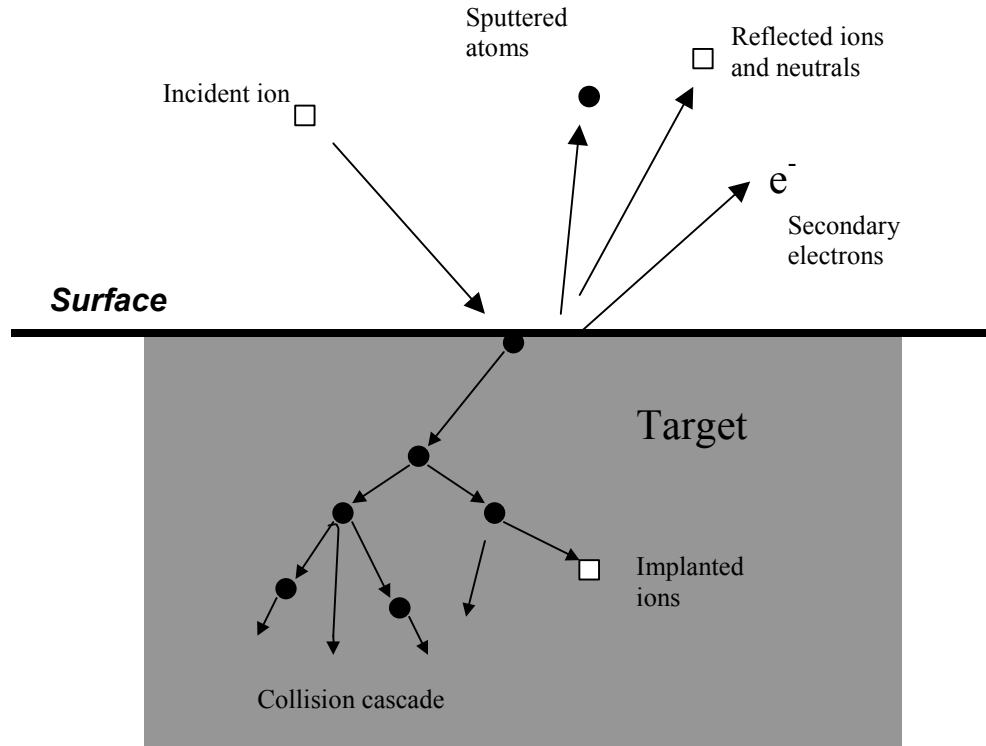


Figure 1.2 Interactions of incident ions with the target surface.

A few points are worth noticing about the sputtering processes. The use of inert gas during sputtering is to prevent any chemical reaction between the colliding gas molecules and the target. In fact, other working gases, such as krypton or xenon, have been used in sputter deposition of thin films. Deposition rate changes from the case in which Ar is used as the working gas due to the different molecular masses, which in turn affect the momentum transfer processes when they collide with the targets. Donnet *et. al.* [2] have sputtered [Co/Cu] giant magnetoresitive (GMR) (Chapter 3) repeated bilayers using argon, krypton and xenon as working gases. Drastic differences in film properties were obtained from the samples so prepared, including differences in maximum GMR ratio, coercivity, grain sizes and interfacial roughness of the films. In practice argon is almost always used due to its relatively low cost.

Sputtering is a very inefficient process in terms of energy conservation, with less than 10% of energy of incident ions being used for removing atoms out of the targets. A great proportion of the energy is lost in the form of internal energy of the targets. Water has to be circulated around the cathodes to cool down the targets during the sputtering process.

1.1.2 Magnetron sputtering

1.1.2.1 Disadvantages of conventional sputtering process

The major problems associated with the conventional sputtering technique mentioned above are the low deposition rates and the poor film microstructures. A high sputtering gas pressure (P) of ~ 10 Pa is typically used, otherwise the plasma formation process cannot be self-sustained and the sputtering process fails. The trade-off for such a high gas pressure is the high degree of thermalization [3] occurring within the plasma, as discussed below.

Seldom in the sputtering process do atoms travel directly from the surface of the target to the substrate. A cascade of collisions usually occurs, removing part of the kinetic energy from the incoming atoms and the reflected neutrals to the plasma. This process is called thermalization. The process is dependent on the working gas and the material being sputtered, as thermalization is again a momentum transfer process which, as expected, depends on the relative masses of the atoms involved. Besides, it depends highly on the PD product of the system (D is the substrate-target distance), as these parameters control the probability and the frequency of occurrence of collisions.

Incoming adatoms lose kinetic energy as a consequence of thermalization. Besides, the cascade of collisions results in a proportion of adatoms arriving onto the substrate in an oblique and random direction. The complex interaction yields a film structure containing lots of voids (for example see [4]), which is associated with the problems such as abnormally high resistivities, low mechanical strength, to name a few. Microstructures of sputtered thin films are discussed more fully later in this chapter.

1.1.2.2 Magnetron sputtering process

A great advance in the field of sputtering came with the introduction of the magnetron sputtering. Electrons in the plasma are accelerated towards the anode due to the presence of an electric field. However, their trajectories can be diverted in the presence of a magnetic field (which can be provided by a piece of permanent magnet sitting behind the target, as shown in Figure 1.3), leading to a certain degree of confinement of electrons around the cathode (target) surface. This effectively increases the chance of ionization of the working gas molecules, permitting a larger deposition rate by working at a lower sputtering gas pressure. Plasma stabilization becomes

possible with a working gas pressure as low as tenths of Pa, which cannot be realized in conventional sputtering set-ups. The regions in which the electron confinement is strongest are usually the most highly sputtered areas, leaving the well-known ‘race track’ pattern on the sputtering targets in these areas.

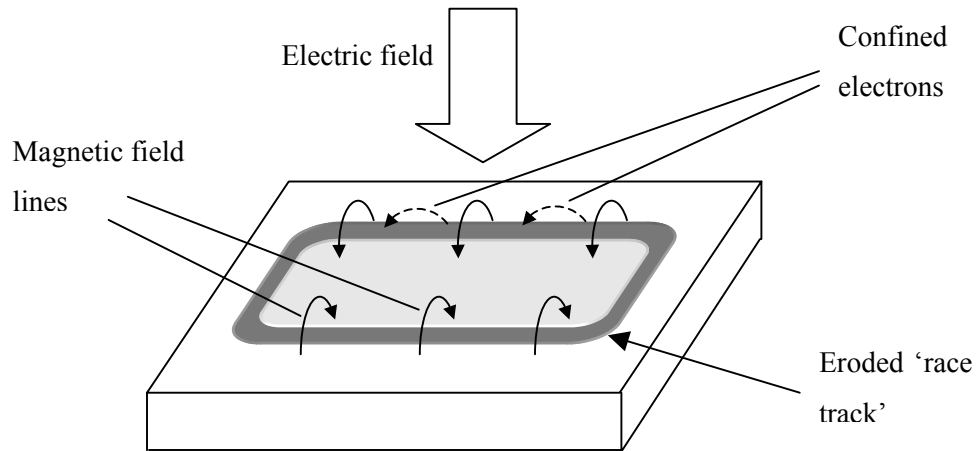


Figure 1.3 Schematic diagram showing the combined effects of magnetic and electric fields on electrons in a planar magnetron sputtering target.

1.1.3 Microstructures of sputtered thin films

1.1.3.1 Film formation and growth

Three stages of film formation processes can be identified in general [5], although there are no clear boundaries for transitions from one stage to another. At the early stage of deposition, target atoms impinge on the substrate surface and become bonded adatoms. These adatoms usually possess high mobility, and can either be desorbed from the substrate surface or (more commonly) condense to form nuclei. The nuclei then grow into islands and grains, through the absorption of other incoming adatoms and/or through the coalescence with other nuclei. Such processes continue until the channels and voids between various grains and islands are filled, forming continuous films. The atoms arrive at their final positions in the film by means of diffusion (surface or bulk diffusions), giving the final structure of the films.

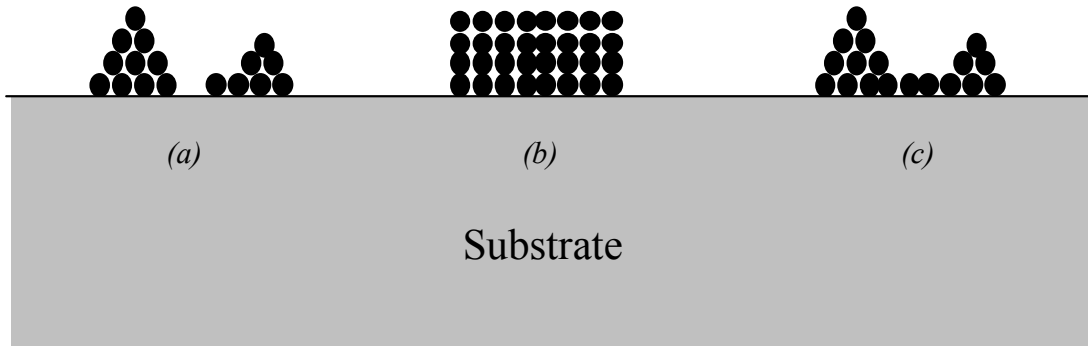


Figure 1.4 Different modes of film growth: (a) island growth mode, (b) layer growth mode, and (c) Stranski-Krastanov growth [6].

The nucleation and growth processes mentioned above can also be classified into three different modes: island (or Volmer-Weber) growth, layer (or Frank-van der Merwe) growth and Stranski-Krastranov (SK) growth (for example see [6]). In the island growth mode (Figure 1.4(a)) the nuclei or grains develop into three-dimensional hillocks before they join together and form continuous films. The other extreme of film growth behaviour is the layer growth mode (Figure 1.4(b)), in which adatoms tend to spread into two-dimensional structures and form planar sheets. In between these two cases is the SK growth, in which the initial tendency of two-dimensional growth is broken and followed by the subsequent development of island structures.

1.1.3.2 Structural zone model and microstructure of sputtered films

The microstructure of sputtered thin films can be qualitatively described by the ‘structural zone model’, developed initially from the observation of thick (300 – 2000 μm) evaporated films and modified by Thornton to discuss the cases on magnetron sputtered thin (20 – 250 μm) films [4]. The model considered the formation of film microstructures as a consequence of geometric shadowing effect and atomic diffusion in the film. Shadowing effect refers to the hindering of the line-of-sight impingement of the arriving adatoms from the sources. Atomic diffusion refers to the migration of incorporated atoms within the films, which could either be along the grain boundaries or in the bulk of the grains. The relative importance of these two kinds of diffusion is highly dependent on the characteristic diffusion activation energies of the atomic species and the substrate temperatures, T_s .

An exploded view of the structural zone model is depicted in Figure 1.5, showing the effect of the aforementioned processes (shadowing and diffusion) on the structure of the films, as functions of normalized substrate temperature (T_s/T_m , T_m being the melting point of the target material) and P . The shadowing process, for example, could be affected by the inert gas pressure due to thermalization (section 1.1.2.1). The diffusion process, on the other hand, is more related to the substrate temperature, as mentioned in the last paragraph. Enhanced diffusion with increasing T_s/T_m in zones 2 and 3 lead to large grains or even epitaxial structures. The effects of these processes superimpose onto each other, giving the final microstructures of the films.

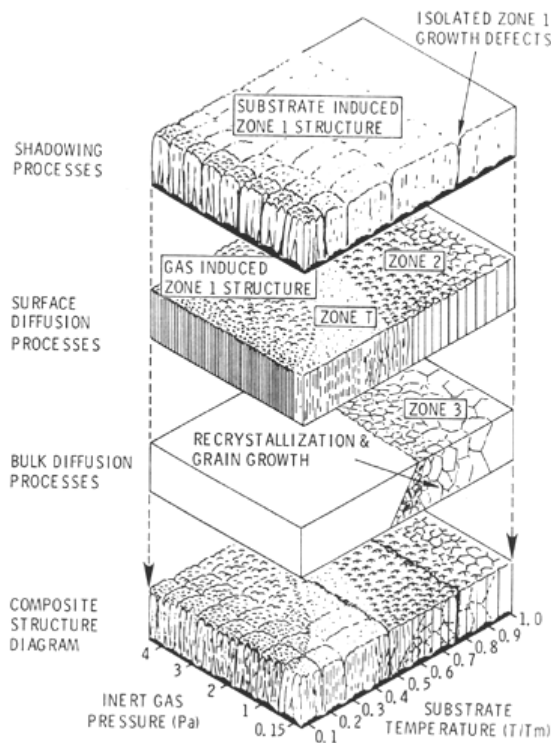


Figure 1.5 Structural zone model of sputtered thin films [4].

In Thornton's scheme the film structures can be divided into zones 1, T, 2 and 3 (zone T, which is absent from the model for evaporated films, is a transition between zones 1 and 2). In zones 1 and T the growth mechanism is dominated by the geometric shadowing, with limited diffusion of adatoms. Crystallites are surrounded by voided boundaries. In the treatment of Thornton, zone T was regarded as the extreme case of zone 1 growth on infinitely smooth substrates. Grains are more densely packed and appear fibrous in zone T crystallites, due to a more homogenous impingement of adatoms compared with growth on rough substrates (zone 1). In zone 2, where surface diffusion become important due to an increase of the normalized temperature T_s/T_m , large and columnar grains separated by relatively dense boundaries are observed. Finally at high

temperature (zone 3) bulk diffusion of adatoms take place extensively, resulting in epitaxial film growth.

1.1.3.3 Control of film properties

The understanding of the film microstructure is important, as it permits control or even engineering of particular aspects of the film's properties. Highly epitaxial sputtered films, for example, can be prepared by depositing films on heated substrates with low deposition rates. The high substrate temperature increases the mobility of adatoms on the substrate surface, and the slow arrival rate of adatoms ensures that they have sufficient time to fall into equilibrium positions. On the contrary, polycrystalline and amorphous films can be formed by depositing at low T_s with high sputtering rates.

Another property of interest in sputtered films is film stress. The general rule-of-thumb can be qualitatively understood as follows. At low values of P , highly energetic neutrals and adatoms arrive at the growing film surface without much thermalization, inducing compressive stress through the 'shot-peening' effect. With increasing gas pressure, however, thermalization effect increases and the adatoms start to arrive from a wider range of angles due to numerous collisions on their path to the substrate. Films so formed become tensile, less packed and have higher density of defects. Figure 1.6 shows these general trends.

It has to be stressed that sputtering is a highly complex process. There is no simple, one-to-one relationship between a certain sputtering parameter and a particular film property. Film stress, for example, can be affected by T_s , P , or even the film thickness. A change in a single parameter, say sputtering gas pressure, can lead to changes in a number of film properties such as the film crystallinity and stress. Care thus has to be exercised when particular parameters are used to alter the film properties.

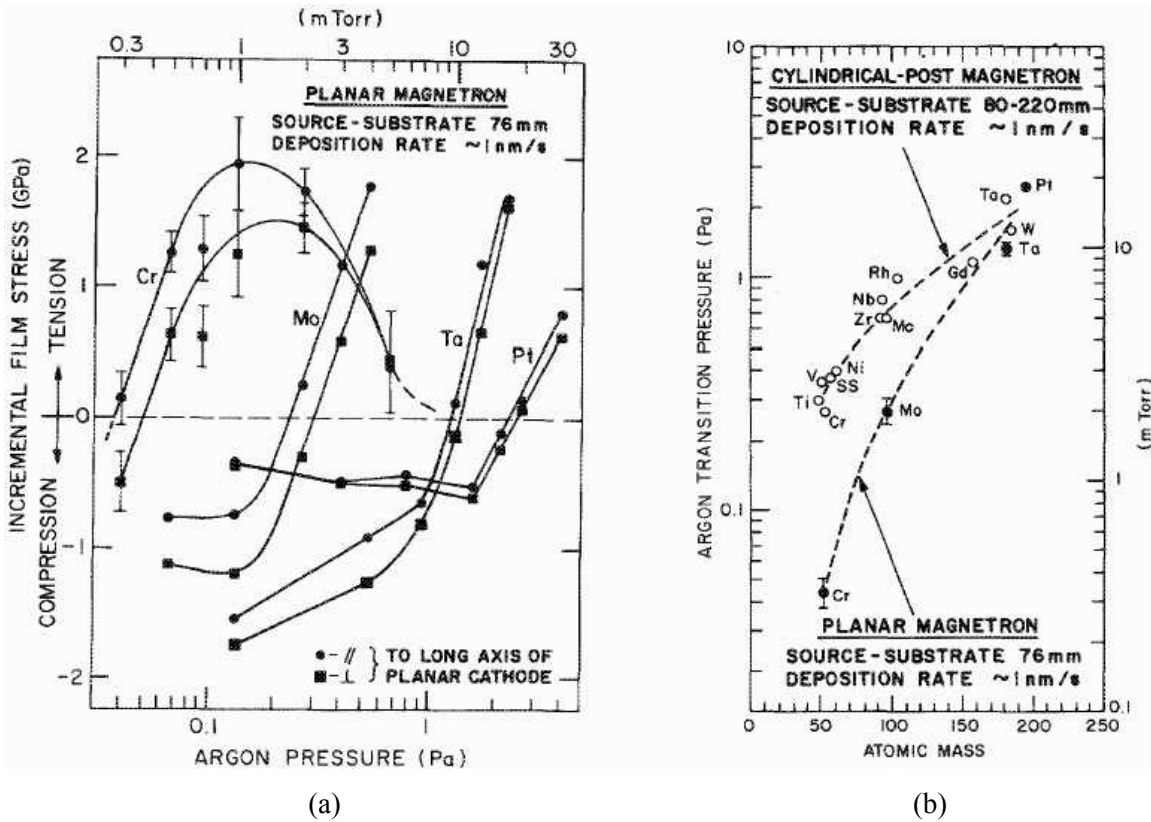


Figure 1.6 (a) Bi-axial internal stress of magnetron sputtered films from planar magnetrons, showing the effect of argon pressure P on the final stress states on the films (50 – 350 nm thick). The compiled ‘transition pressure’ between compressive and tensile stresses are shown in (b) for cylindrical-post magnetron and planar magnetron targets. After [7].

1.2 Magnetic properties of sputtered thin films

In this part of the chapter, a summary on some topics in magnetism will be given, with particular emphasis on thin films. Energetics concerned with magnetic films will first be treated, based on which many of the models and explanations about magnetism are developed. This is followed by a discussion on magnetic domains. Discussions in this chapter are made only on single ferromagnetic films. Interaction between ferromagnetic films (interlayer exchange coupling, magnetostatic coupling and exchange coupling) will be discussed in the later parts of the thesis.

1.2.1 Energetics of magnetic thin films

An understanding of the energies involved in the behaviour of ferromagnets and their interactions (with other ferromagnets or with the environment) is of great importance. It is often useful to

build simple models in explaining the complex behaviour of magnetic structures. One can start the process by listing out the (phenomenological) energy terms, based on some parameters such as applied magnetic field H , volume saturation magnetization of the ferromagnet M_{FM} or anisotropy constants K_{FM} . By minimizing the energy of the system one can obtain its (local) equilibrium states at particular experimental conditions, such as field or angular dependence of magnetizations. This provides a quick means of analysis without referring to the complex formalities of the rigorous theories, and permitting a quick examination on the existing theories.

Energetics of ferromagnetic films is fairly similar to that of the bulk materials. While some energies, such as those concerned with the interaction between magnetization M and H (Zeeman energy) [8] are common in both cases, there are some terms (such as demagnetization energy and interlayer coupling energy) which are rather unique to the case of thin films.

1.2.1.1 Exchange interaction

An important characteristic of ferromagnetic materials is the presence of a *long-range* magnetic order among magnetic spins of the atoms, which can be written in the form [9]

$$E = -\sum_{i \neq j} J_{i,j} \mathbf{S}_i \cdot \mathbf{S}_j \quad [1.2]$$

In the above equation $J_{i,j}$ refers to the exchange constant between two atomic spins \mathbf{S}_i and \mathbf{S}_j . The sign convention of $J_{i,j}$ is such that a positive $J_{i,j}$ implies a parallel alignment of spins is preferred, which is the case of ferromagnets.

1.2.1.2 Zeeman term

In the presence of an external magnetic field H , there is an interaction between the field and the spins in the ferromagnet. The energy of such an interaction in a ferromagnetic sample, or Zeeman energy, per unit area is:

$$E_{Zeeman} = -t_{FM} \mathbf{H} \cdot \mathbf{M}_{FM} \quad [1.3]$$

where t_{FM} is the thickness of the ferromagnetic layer, and M_{FM} is the saturation magnetization of the ferromagnet. Equation [1.3] should, strictly speaking, only be applied to systems that have homogeneous magnetization, which only happens in particular systems (for example ellipsoids or small magnetic particles). In most systems the magnetization is broken up into regions called

domains. While the magnetization is homogenous inside a domain, they are not always aligned in the same orientation and are separated by domain walls, as discussed later in the chapter.

1.2.1.3 Anisotropy in thin magnetic films

Magnetization behaviour of ferromagnets usually shows a directional dependence. In bulk single crystal ferromagnets for example, magnetocrystalline anisotropy along different crystal orientations is present due to the spin-orbit coupling and the crystallographic structure of material [10]. However this contribution is not of particular concern in this work for two reasons:

- In the case of permalloy (NiFe) and face-centred-cubic (fcc)-Co (which are the two ferromagnets used in this work) they are practically zero [11].
- Sputtered magnetic films are usually polycrystalline or even amorphous in nature. Under such condition it is not likely for the films to have any *in-plane* crystallinity, although they tend to have a strong *out-of-plane* texture, usually the closed-packed planes [12]. Therefore the *in-plane* magnetocrystalline anisotropy is averaged out in this case.

In practice, however, anisotropy still exists in magnetic thin films, as discussed below.

1.2.1.3.1 Shape anisotropy

If there is a magnetization component along the film normal direction, dipoles are formed at the film surfaces and a *demagnetizing* field H_d is generated that opposes the magnetization. This effect can be characterized by a demagnetizing factor $N_d = -H_d/M_{FM}$, where M_{FM} is the saturation magnetization of the ferromagnet. A very detailed treatment of this subject has been given by [13]. For a simple treatment [14] we can regard thin films as an oblate (disk-like) ellipsoid (which always has a uniform magnetization within its volume) with a large thickness-to-diameter ratio. By doing this one can obtain a demagnetization factor close to 4π along the short ellipsoid axis (film normal direction), and close to zero along the long axes (film plane direction). The volume energy density associated with this shape anisotropy is given by

$$E_d = -\frac{1}{2} \int_{sample} \mathbf{H}_d \cdot \mathbf{M} dV = \frac{1}{2} \int_{sample} N_d M^2 dV \quad [1.4]$$

From the above argument one can expect that M would tend to lie within the film plane, which would otherwise give rise to a large energy penalty were it magnetized along the film normal direction. This is true in most cases, but one also needs to take into account of other factors in the energy consideration. In some bubble-domain materials [15] for example, the anisotropy field

$(K_{FM}/2M_{FM})$ is so high that they have an out-of-plane easy axis even in thin film form, if the anisotropy axis is along the film normal direction.

1.2.1.3.2 Induced anisotropy

Anisotropies in magnetic thin films can be induced artificially in a number of ways, for example by annealing or depositing the films in a magnetic field [16]. In general such anisotropies are uniaxial in nature, and can be represented in the following phenomenological form:

$$E_u = -K_{FM}t_{FM} \cos^2 \alpha \quad [1.5]$$

with α being the angle between M and K_{FM} , and the subscript u denotes the uniaxial nature of the energy.

On the other hand, anisotropies can also be induced by means of oblique deposition [17-19]. In most common sputtering schemes the plasma incidence to the substrate is normal to the substrate plane. However, in some cases the plasma can be arranged to impinge onto the substrate at an angle from the substrate's normal direction. Films so formed tend to have stronger anisotropy compared with films deposited at normal incidence, possibly due to the tilted microstructures [17].

Another possible source of induced anisotropy is the magnetoelastic effect, which is essentially the reverse of the magnetostrictive effect [20]. By subjecting films to stress, anisotropy axes can move either towards or away from the stress axis, depending on the sign of the magnetostrictive constant λ_s . Materials with positive λ_s tend to switch the anisotropy axis towards the tensile stress direction, while those with negative λ_s tend to switch the axis towards a compressive stress direction. The problem is complicated, however, by the behaviour of λ_s with, for example, applied field, which may be able to change the sign of magnetostriction [21].

While the majority of literature has reported a negligible magnetostrictive effect in NiFe around the permalloy composition (Ni atomic content $\sim 78\%$), λ_s of magnitude 10^{-6} has been found in polycrystalline NiFe films with thickness less than 10 nm [22, 23] (Figure 1.7). The variation could be represented in the phenomenological form

$$\lambda_s = \lambda_s^{bulk} + \frac{\lambda_s^{surf}}{t_{FM}} \quad [1.6]$$

with the superscripts indicating the bulk and surface contributions to λ_s . Equation [1.6] indicates the strong surface contribution on the magnetostrictive effect. For Co the bulk polycrystalline λ_s is negative and is also of the magnitude 10^{-6} [21].

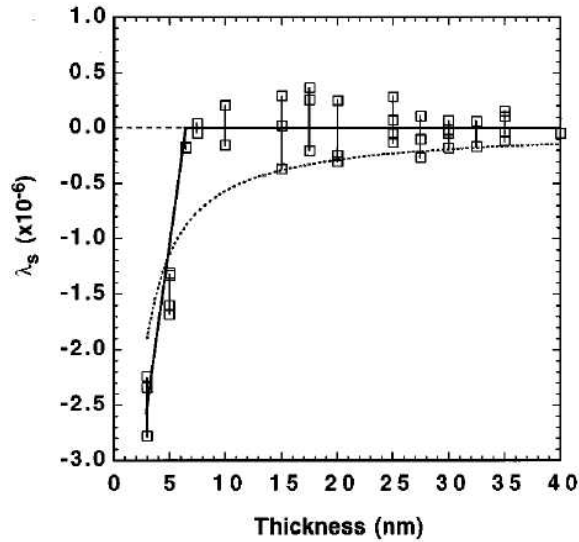


Figure 1.7 Variation of the magnetostrictive constant λ_s with $Ni_{80}Fe_{20}$ thickness [23]. Dashed line is a fit of the equation [1.6].

1.2.2 Domains and magnetization processes

1.2.2.1 Domains and domain walls

Existence of domains in ferromagnetic materials was first postulated by Weiss, but it was Landau and Lifshitz who first explained domain formation as a consequence of energy minimization [24]. If the magnetization were homogenous throughout the sample, there would be a high cost of magnetostatic energies due to the formation of free poles. This could be avoided if the magnetization was divided into regimes known as domains and arranged in a way to minimize the stray field energy (Figure 1.8 (a)-(e)). In the process boundaries are formed between adjacent domains having different magnetization directions. Abrupt transitions, however, are not favourable due to the strong exchange interaction in the ferromagnets. Instead these boundaries spread out into a region of finite thickness known as domain walls, in which the magnetization directions twist and form relatively smooth transitions between two domains.

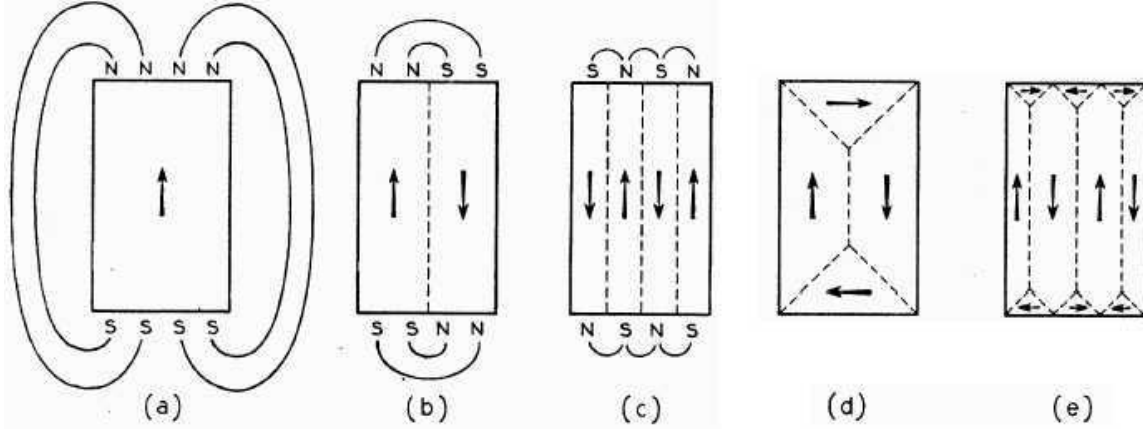


Figure 1.8 Origin of domains, after Kittel [25].

The areal energy density associated with such domain walls can be expressed as a sum of exchange energy plus anisotropy energy [26]. In the particular case of a 180° wall (in which the adjacent domains have antiparallel magnetizations),

$$E = \left(\frac{\pi^2 J_{ex} S^2}{wa} \right) + K_{FM} w \quad [1.7]$$

where w is the width of the domain wall, J_{ex} is the exchange constant between two spins S , and a is the lattice constant of a cubic crystal. The value of w can then be calculated by solving the

equation $\frac{\partial E}{\partial w} = 0$, giving

$$w = \sqrt{\frac{\pi^2 J_{ex} S^2}{K_{FM} a}} \quad [1.8]$$

The domain wall described above is known as the Bloch wall, in which the magnetization transition takes place in a direction perpendicular to that of the neighbouring domain magnetization (Figure 1.9(a)). This may not be favourable in the case of ultrathin films, due to dipole formation at the film surfaces. In such cases Néel walls could be formed, in which the transition occurs within the plane of the adjacent domain magnetization directions (Figure 1.9 (b)).

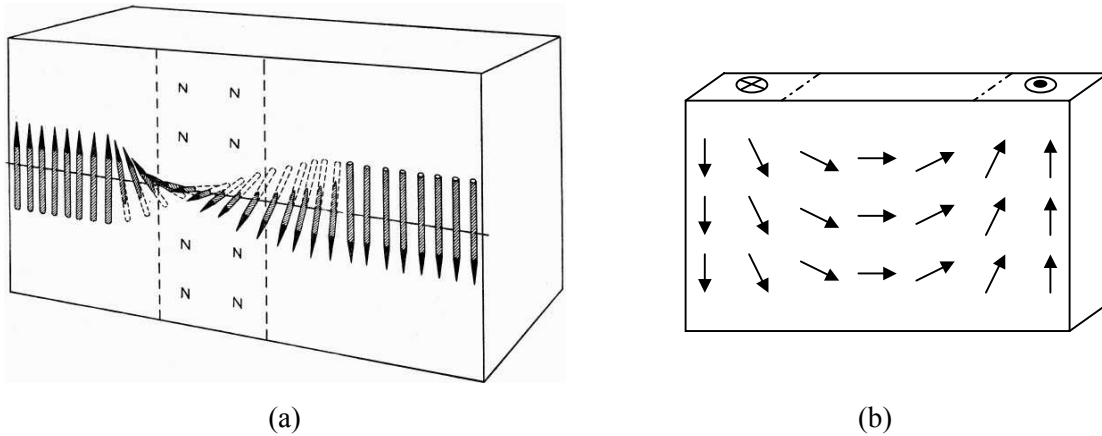


Figure 1.9 Schematic diagrams showing (a) a 180° Bloch wall [25] and (b) a Néel wall [13].

1.2.2.2 Magnetization reversal and hysteresis

The domain theory has permitted the understanding of the reversal of magnetization within ferromagnets under the influence of an external magnetic field. The process can be described qualitatively by domain nucleation, domain wall motion and magnetization rotation [27], with the aid of a hysteresis loop ($M(H)$ loop) (Figure 1.10). Starting from a saturation field (point A in the figure), reversible magnetization rotation occurs as the field decreases (section A-B), returning the magnetization back to its anisotropy axes. As the field continues to decrease (section B-C), new domains are nucleated within the existing ones. The Zeeman energy associated with individual domains favours the ‘growth’ of domains with magnetization vectors along (or with a component along) the field direction, which takes place by domain wall motion. This process continues until the unfavourable domains are eliminated. The final stage of the reversal process (section C-D) involves the rotation of remaining domains from their anisotropy axes towards the field direction, finishing half of the reversal cycle. The above descriptions are highly simplified from the actual situation, and deviations are likely to happen locally due to inhomogeneities.

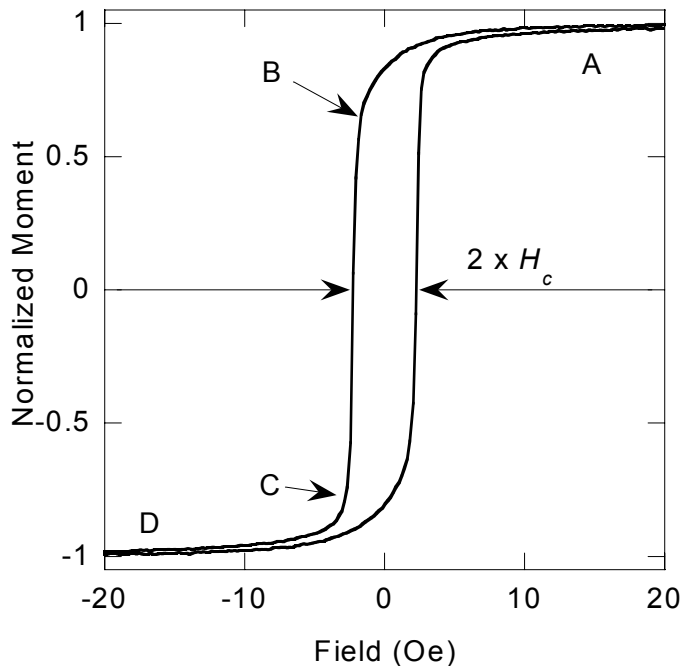


Figure 1.10 A typical magnetic hysteresis loop of a single layer of magnetic film (in this case the film is NiFe). H_c is the coercivity of the film. Labels on different parts of the descending field cycle of the loop refers to the different stages of magnetization reversal, as described in the text.

Typical among the magnetization measurements of different ferromagnetic materials is the phenomenon of hysteresis: The magnetization of the sample does not vanish when the field sweeps towards zero. There is some lapse of field before the magnetization comes to zero.¹ Such a lapse, in the special case in which the sample was previously brought to saturation before the reverse field cycle commences, is called the coercivity of the sample (H_c). The size of coercivity is important in determining the potential applications of particular materials, and is the consequence of a number of intrinsic and extrinsic factors.

- Anisotropy

As discussed in the previous section, it is the tendency of the magnetization to stay along particular axes. Anisotropy could be both intrinsic (magnetocrystalline) or extrinsic (induced and shape) in nature. The strength of the anisotropy is the dominating factor in determining the coercivity of bulk ferromagnets and epitaxial films.

¹ It should be stressed that it is the *global* magnetization *along the applied field direction* that has vanished in the hysteresis loop shown in Figure 1.10. The local magnetization is usually non-zero, due to the presence of domains. Another possibility is that the magnetization is switched away from the field, as in single domain particles.

- Grain size and defects

In polycrystalline and amorphous films, other mechanisms that hinder the magnetization reversal processes can be extra sources of coercivity. These include the grain boundaries and numerous defects in the films. In general, these features act as additional barriers for the motion of domain walls. Magnetization reversal becomes more energy consuming than in perfect lattice structures, giving rise to the enhanced coercivity. On the other hand, it is also known that amorphous films do have extremely low coercivity in general [28]. In this case the defect separations are smaller than the domain wall size, which become inefficient in impeding the magnetization processes. This, together with the virtual absence of magnetocrystalline anisotropy in such films due to their amorphous nature, gives very low H_c values.

1.2.2.3 Modelling of magnetization process

It is certainly desirable to incorporate the effects of the intrinsic and extrinsic material parameters discussed above into a single model to describe the magnetization reversal of ferromagnets. The difficulty is that the reversal process is complicated by the domain walls-defects interactions. Besides, magnetization processes can take the form of domain nucleation, wall motion and magnetization rotation. A realistic theory should incorporate all these processes. The most commonly accepted models of hysteresis have taken simplified pictures on the real situation, with particular emphasis on particular reversal mechanisms [29].

The Stoner-Wohlfarth (SW) model [30] is the most commonly employed model in describing the hysteresis behaviour of magnetic materials, although strictly speaking it deals only with polycrystalline, non-interacting, single domain particles with uniaxial anisotropy. In such a model the reversal mechanism is assumed to be entirely due to magnetization rotation, according to the energy equation

$$E = -HM_{FM} \cos(\theta - \alpha) + K_{FM} \sin^2 \alpha \quad [1.9]$$

where the terms correspond to the Zeeman and (uniaxial) anisotropy energies. The definitions of symbols are shown in Figure 1.11. Magnetization behaviour of the system is determined from the *local* minima of equation [1.9].

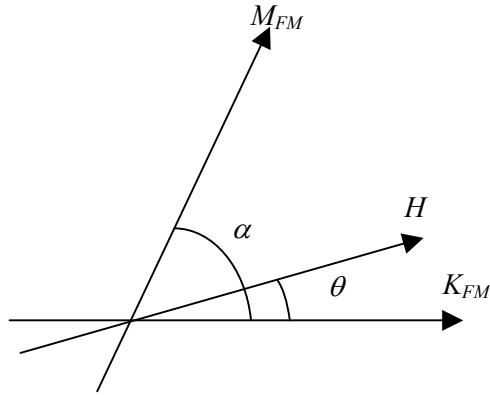


Figure 1.11 Definition of symbols used for the SW model.

Figure 1.12 summarizes the numerical modelling results of angular behaviour of a system obeying the SW model. The simulations were done in a manner similar to that mentioned in [31]:

- The system was first saturated by applying a large positive saturating field H_s . The energy minimum of $E(\alpha)$, which was *around* the positive field direction θ , was found numerically (it might not be exactly the positive field direction but should be close to it).
- The applied field was decreased.
- The energy of the system, under the new applied field H , was calculated in the range $[(\alpha - \delta\alpha), (\alpha + \delta\alpha)]$.
- If the α_{new} value that gave energy minima under H was the same as the previous one α , the iteration stopped and a new iteration started with a lower field; otherwise, $E(\alpha)$ in the range $[(\alpha_{new} - \delta\alpha), (\alpha_{new} + \delta\alpha)]$ was calculated until an energy minima was found.
- The process continued until the descending and ascending field cycles were finished. The magnetic moment along θ gave the $M(H)$ behaviour.

The angular dependence of H_c and remanence are shown in Figure 1.12(b) and (c). The H_c behaviour was complicated in a sense that it cannot be fitted with a simple function. On the other hand, M_r/M_s could be fitted surprisingly well with a $|\cos\theta|$ relation, assuming a uniaxial anisotropy behaviour in the system.

The major advantage (or disadvantage) of the SW model is its simplicity, in which the reversal is treated solely in terms of rotations. While this allowed easy modelling and interpretation of results, the true picture of magnetization processes was neglected. Besides, the origin of hysteresis was confined to the anisotropy energy in this model.

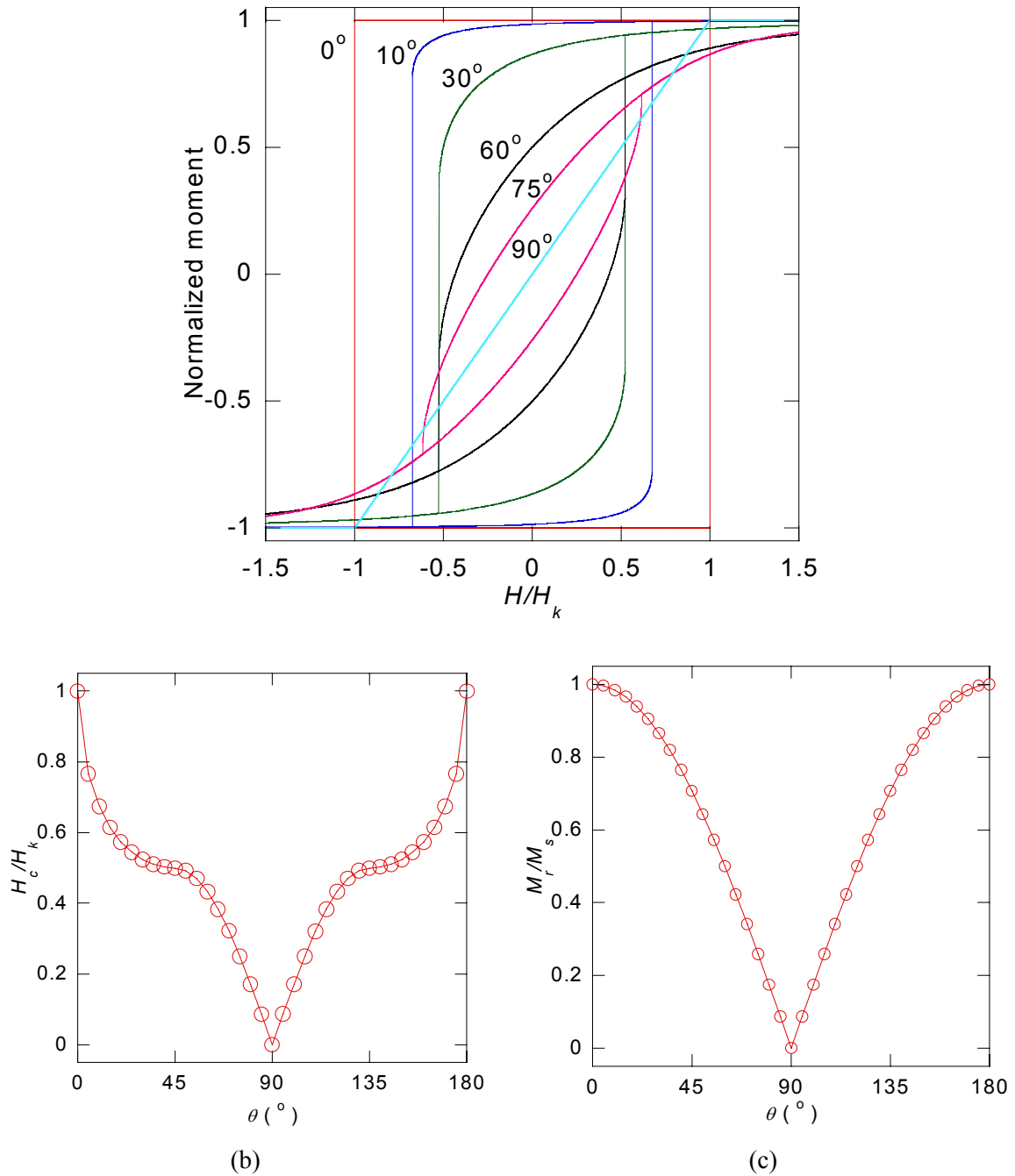


Figure 1.12 Numerical simulations of the SW model. (a) Angular $M(H)$ loops (figures next to the loops indicate the applied field direction θ). (b) Angular dependence of H_c , normalized by the anisotropy field H_k ($= 2K_{FM}/M_{FM}$). Solid line is a guide to the eyes only. (c) Angular dependence of remanence M_r/M_s , where M_r refers to the remanent magnetization. Solid line is a fit with the equation $\frac{M_r}{M_s} = |\cos \theta|$.

Simple models such as equation [1.9] are easier to be solved analytically (such calculations can be found in many textbooks, for example [32]), which can give more physical insight than simply evaluating the model numerically. In more complicated systems, for example when more anisotropy and coupling terms are involved, such equations are hard to be solved without making assumptions. In such cases, one has to resort to numerical modelling for assessing the magnetization behaviour of the systems.

1.3 Sputter deposition of thin films in this project

1.3.1 Substrate preparation

All samples prepared in this project were deposited on Si(100) substrates coated with a thick (~250 nm) layer of oxide. Wafers were diced into (5×10) mm² chips with a diamond saw. Since wax was used to hold the wafers firmly during the dicing process, extra care has been taken in removing the wax and any sawdust that may contaminate the substrates. The following procedures were employed to ensure the cleanliness of the substrates:

- Diced chips were soaked in chloroform or trichloroethylene for at least 2 hours to dissolve the wax attached. Afterwards they were removed from the used solvent, put into a new beaker of solvent and ultrasound bathed for 5 minutes.
- Chips were transferred into a beaker of acetone, and are ultrasound bathed again for further 5 minutes.
- Acetone was sprayed by an airbrush to further clean the surface of the substrates.
- Before the acetone was fully dried, ethanol was splashed onto the substrate, which was then blown dry by a spray of dry air.

1.3.2 'UFO –1' dc magnetron sputter deposition system

Samples investigated in this project were dc magnetron sputter deposited in a custom-built planetary sputtering system (UFO-1) (Figure 1.13), equipped with five 3-inch diameter sputtering guns. Substrates were transferred between the main chamber and the atmosphere via a load-lock, maintaining a high level of vacuum within the chamber (typically below 1×10^{-6} Pa). A liquid nitrogen cold-trap was used to further improve the cleanliness inside the chamber. Usually the base pressure could be further lowered by an order of magnitude after the cold trap was employed. Another potential advantage of using the cold trap was that surface diffusion of

adatoms during film growth could be suppressed. While the actual substrate temperature was not measurable in the system, the temperature of the inner chamber wall was always below $-100\text{ }^{\circ}\text{C}$ during the deposition, as registered by a thermocouple. The advantage of using the cold trap has been demonstrated by Marrows [33], who has shown a drastic improvement in the performance of [Co/Cu] sputter deposited repeated bilayers.

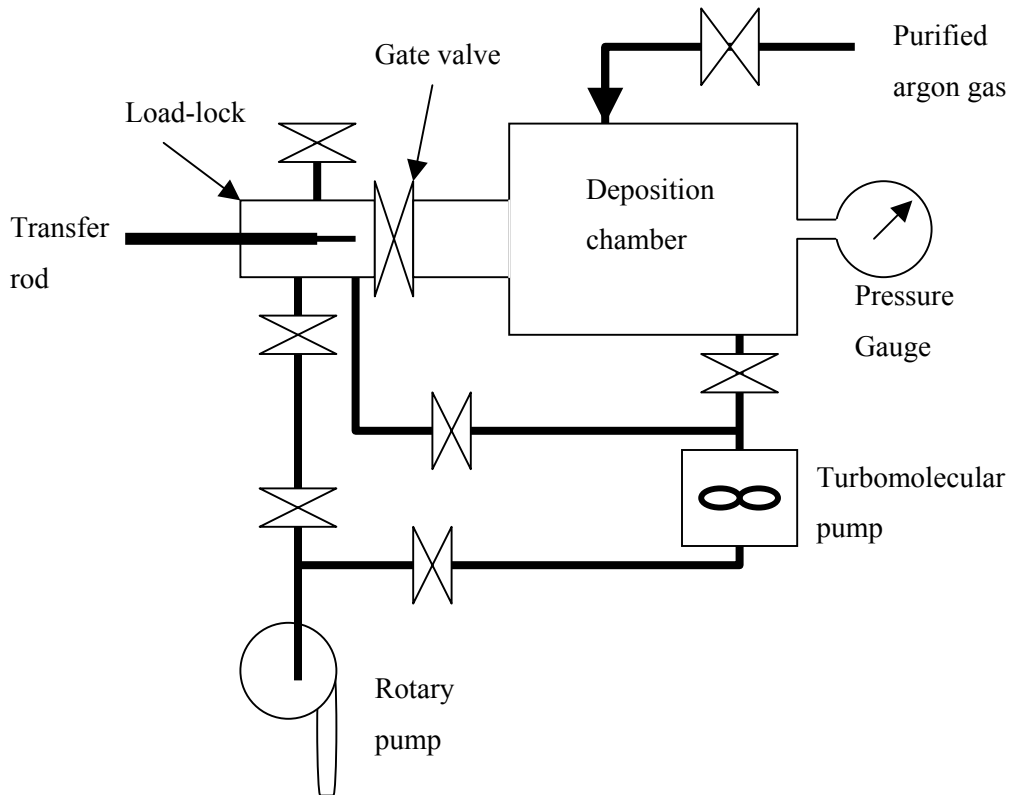


Figure 1.13 Schematic of the 'UFO-1' sputter deposition system used in this project.

Samples were deposited in an argon gas environment of 0.5 Pa in all the samples prepared in this project. Substrate-target distance was maintained at 90 mm . These measures standardize the effect of thermalization on the adatoms. Films of different thickness were deposited by rotating samples with different speeds under the magnetron guns, with constant applied powers for each target material. This minimizes the effect of sputtering rate dependence of film microstructures. Typical sputtering rates was maintained around $0.2 - 0.3\text{ nm s}^{-1}$ for all the targets, which was calibrated by stylus profilometry of thick (200 to 500 nm) calibration samples.

References for Chapter 1

1. M. Ohring, *The materials science of thin films*, pp. 101-109, Academic Press (1992).
2. D.M. Donnet, K. Tsutsumi, P. de Haan and J.C. Lodder, *J. Appl. Phys.* **79**, 6243-6245 (1996).
3. R.E. Somekh, *J. Vac. Sci. Technol. A* **2**, 1285-1291 (1984).
4. J.A. Thornton, *Ann. Rev. Mater. Sci.* **7**, 239-260 (1977).
5. C.V. Thompson, *Annu. Rev. Mater. Sci.* **30**, 159-190 (2000).
6. M. Ohring, *The materials science of thin films*, pp. 219-223, Academic Press (1992).
7. D.W. Hoffman and J.A. Thornton, *J. Vac. Sci. Technol.* **20**, 355-358 (1982).
8. S. Blundell, *Magnetism in condensed matter*, in *Oxford master series in condensed matter physics.*, pp. 9,10, Oxford University Press (2001).
9. S. Blundell, *Magnetism in condensed matter*, in *Oxford master series in condensed matter physics.*, pp. 74-76, Oxford University Press (2001).
10. B.D. Cullity, *Introduction to magnetic materials*, in *Addison-Wesley series in metallurgy and materials*, pp. 214-215, Addison-Wesley Pub. Co (1972).
11. M.T. Johnson, P.J.H. Bloemen, F.J.A. den Broeder and J.J. de Vries, *Rep. Prog. Phys.* **59**, 1409-1458 (1996).
12. R.E. Somekh, W.C. Shih, K. Dyrbye, K.H. Huang and C.S. Baxter, *SPIE Proc. Series* **1140**, 453-463 (1989).
13. A. Hubert and R. Schäfer, *Magnetic domains: the analysis of magnetic microstructures*. Springer (1998).
14. B.D. Cullity, *Introduction to magnetic materials*, in *Addison-Wesley series in metallurgy and materials*, pp. 56-57, Addison-Wesley Pub. Co (1972).
15. B.D. Cullity, *Introduction to magnetic materials*, in *Addison-Wesley series in metallurgy and materials*, pp. 542-547, Addison-Wesley Pub. Co (1972).
16. R.F. Soohoo, *Magnetic thin films*, pp. 93-133, Harper & Row (1965).
17. H. Aitlamine, L. Abelmann and I.B. Puchalska, *J. Appl. Phys.* **71**, 353-361 (1992).
18. R.D. McMichael, C.G. Lee, J.E. Bonevich, P.J. Chen, W. Miller and W.F. Egelhoff, *J. Appl. Phys.* **88**, 5296-5299 (2000).
19. J.H. Wolfe, R.K. Kawakami, W.L. Ling, Z.Q. Qiu, R. Arias and D.L. Mills, *J. Magn. Magn. Mater.* **232**, 36-45 (2001).
20. S. Chikazumi and C.D. Graham, *Physics of ferromagnetism*, in *The international series of monographs on physics: 94*, pp. 182-184, Clarendon Press; Oxford University Press (1997).
21. B.D. Cullity, *Introduction to magnetic materials*, in *Addison-Wesley series in metallurgy and materials*, pp. 264, 277, Addison-Wesley Pub. Co (1972).
22. O. Song, C.A. Ballentine and R.C. Ohandley, *Appl. Phys. Lett.* **64**, 2593-2595 (1994).
23. Y.K. Kim and T.J. Silva, *Appl. Phys. Lett.* **68**, 2885-2886 (1996).
24. L.D. Landau and E.M. Lifshitz, *Phys. Z. Sowjetunion* **8**, 153-169 (1935).
25. C. Kittel, *Rev. Mod. Phys.* **21**, 541-583 (1949).
26. B.D. Cullity, *Introduction to magnetic materials*, in *Addison-Wesley series in metallurgy and materials*, pp. 287-292, Addison-Wesley Pub. Co (1972).
27. B.D. Cullity, *Introduction to magnetic materials*, in *Addison-Wesley series in metallurgy and materials*, pp. 313-317, Addison-Wesley Pub. Co (1972).
28. J. Evetts, *Concise encyclopedia of magnetic & superconducting materials*. 1st ed. Advances in materials science and engineering. Pergamon Press (1992).
29. F. Liorzou, B. Phelps and D.L. Atherton, *IEEE Trans. Magn.* **36**, 418-428 (2000).
30. E.C. Stoner and E.P. Wohlfarth, *Phil. Trans. Roy. Soc. A* **240**, 599-642 (1948).
31. D. Tietjen, D. Elefant and C.M. Schneider, *J. Appl. Phys.* **91**, 5951-5956 (2002).

32. D. Jiles, *Introduction to magnetism and magnetic materials*, pp. 370-375, Chapman & Hall (1997).
33. C.H. Marrows, *Ph. D. Thesis*, University of Leeds (1997).

Chapter 2 Characterization of Layered Magnetic Heterostructures

This chapter presents the experimental techniques employed to characterize various types of magnetic multilayered structures in this project. Structural properties were investigated by atomic force microscopy (AFM) and x-ray techniques (x-ray diffraction and reflectivity). Magnetic behaviour of the samples was assessed by the vibrating sample magnetometer (VSM). Electrical measurements were also performed, either to investigate the field dependence of resistance (magnetoresistive behaviour) or the resistivity of the heterostructures.

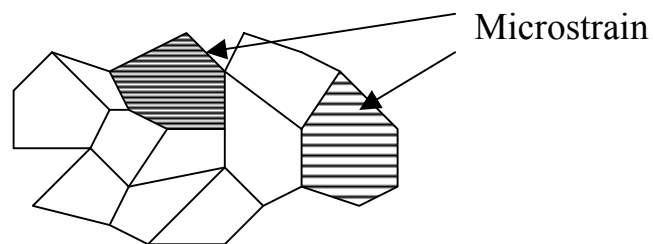
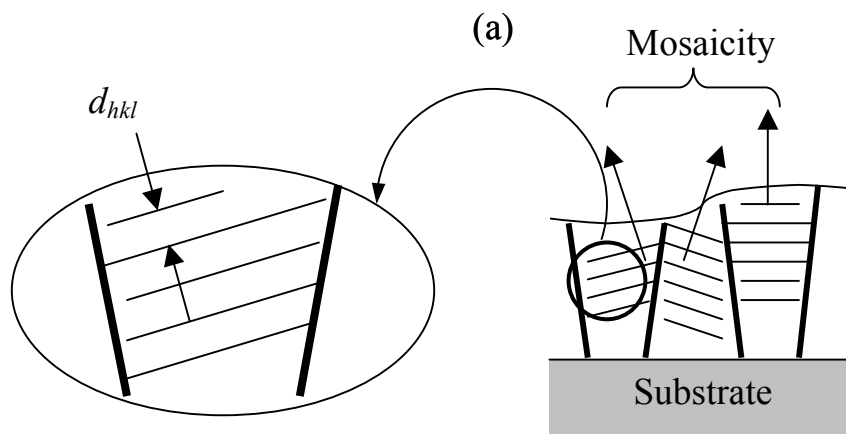
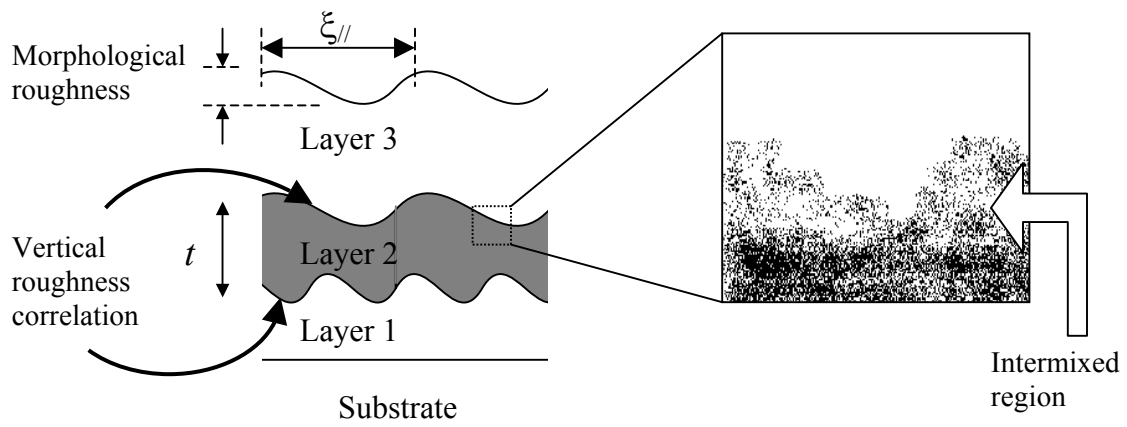
2.1 Structural characterization

Before the techniques for structural characterization are introduced, it is helpful to have an idea what is meant by the term ‘structural properties’ that are of interest in the studies of magnetic multilayers. It can be broadly divided into two categories:

- Morphological structure

This refers to the properties which describe the ‘geometry’ of the layered structures. These include (Figure 2.1(a)):

- The (average) thickness of individual layers t .
- The morphological roughness of the layers, which is the deviation of the actual surface from the mean values. While it can be represented by the peak-to-valley value h , statistically this quantity is expressed in terms of the root-mean-squared (rms) deviation from the mean interface, namely σ .
- The chemical roughness of the interfaces: real interface between two film layers is not usually a sharp boundary between two different chemical species. A concentration gradient can be present in the film growth direction due to, for example, intermixing or chemical reactions.
- Spatial and vertical correlation lengths ($\xi_{//}$ and ξ_{\perp}): these refer to the extent in which the interfacial modulations are copied along and normal to the film planes respectively.



(b)

Figure 2.1 Structural properties of multilayered structures in terms of morphology (a) and microstructures (b).

- Microstructure (Figure 2.1(b))

This category deals with the arrangement of atomic planes within the films. In sputtered systems the following properties are of particular concern:

- Grain sizes: As explained in Chapter 1, sputtered films tend to have columnar structures when deposited at low substrate temperatures and gas pressures. The size of these grains has dramatic impact on the film properties (for example coercivity of magnetic films).
- Crystallinity: Sputtered films, unless amorphous, tend to show a particular out-of-plane orientation (in many cases this refers to the stacking of close packed planes [1]), giving rise to *texture* of films. Even so the actual stacking pattern varies from grain to grain, and it tends to show a distribution around the film normal direction. This gives an idea of the degree of *mosaicity* of films. Epitaxial orientations, on the other hand, are generally absent from films sputtered at low substrate temperatures and are not considered here.
- Strains: At least two types of strains can occur in sputtered films. The first type is present *globally* throughout the film that induces a strained state on the whole film. The second type is present *locally* as a consequence of, for example defects or local impurities, which leads to a localized stress state different from the rest of the film.

Two major techniques were employed to investigate these aspects of structural properties of magnetic heterostructures.

2.1.1 Atomic force microscopy (AFM)

The AFM (Digital Instrument Nanoscope III) was used to investigate the surface topology of the deposited films. Commercially purchased microfabricated cantilevers with Si_3N_4 tips were used to image the film surfaces in the ‘tapping mode’ configuration. In the tapping mode AFM, the cantilever is set oscillating as it is dragged across the surface of the sample. As the tip comes across surface features with varying heights the tip interacts with the surface, inducing a change in the amplitude of oscillation. Such oscillations are detected by a laser spot reflecting at the back of the cantilever, which is probed by a photodiode and converted into surface profile information. Resolution at atomic height scales can be achieved.

The power of the AFM is that it yields the real topology of the film surfaces. Instead of providing only images for qualitative descriptions, AFM data can be quantitatively analysed to obtain useful surface topological data such as surface roughness and spatial correlation length [2]. Such data

are useful, for example in estimations of magnetostatic coupling ('orange peel' coupling) in magnetic multilayers [3].

A brief account on the extraction of the aforementioned parameters using AFM is described as follows [4]. 'Roughness' on its own is not a very precise quantity, as it varies with the lateral dimension being measured. When measurements are made at atomic scale in lateral directions, height variations between any two points are generally small, and the measured 'roughness' is small in this case. The roughness tends to increase with the lateral size of measurement, but it has to converge in physically realistic surfaces. Such kind of lateral scale dependence of roughness has been considered as a consequence of the short-range diffusion-driven smoothing effect, together with a random surface roughening effect by parameter variation (such as deposition rate), which can take effect at all length scales. The result is that growing film surfaces tend to possess a time-invariant short-distance behaviour, together with a long-distance behaviour that is invariant towards lateral scale of measurements. This can be quantified by assuming a self-affine scaling behaviour of the film roughness. Under such a picture, the vertical dimension of measurements on a film surface scales by a factor of k^h when the lateral dimensions is multiplied by k . h is known as the roughness exponent and contains important information regarding the growth mechanism of films. (The case $h = 1$ is known as the self-similar case, which is basically a direct scaling of vertical and horizontal dimensions).

A quantity of importance in the growing surface problems is the height-height correlation function, which is defined as the mean of the square of the height difference between two points on the film surface separated by a distance r :

$$H(r) = \langle [z(r) - z(0)]^2 \rangle \quad [2.1]$$

where the $\langle \rangle$ sign refers to the average of the quantity¹. From the previous discussion the following can be written:

$$H(r) \sim r^{2h}, \quad r \ll \xi_{||} \quad [2.2(a)]$$

$$H(r) \rightarrow 2\sigma^2, \quad r \gg \xi_{||} \quad [2.2(b)]$$

and hence one can write

¹ A more generalized formulation of the height-height correlation function should take into account the potential directional dependence. In such a case a vector approach should be employed. In the discussions here isotropic roughness behaviour is assumed.

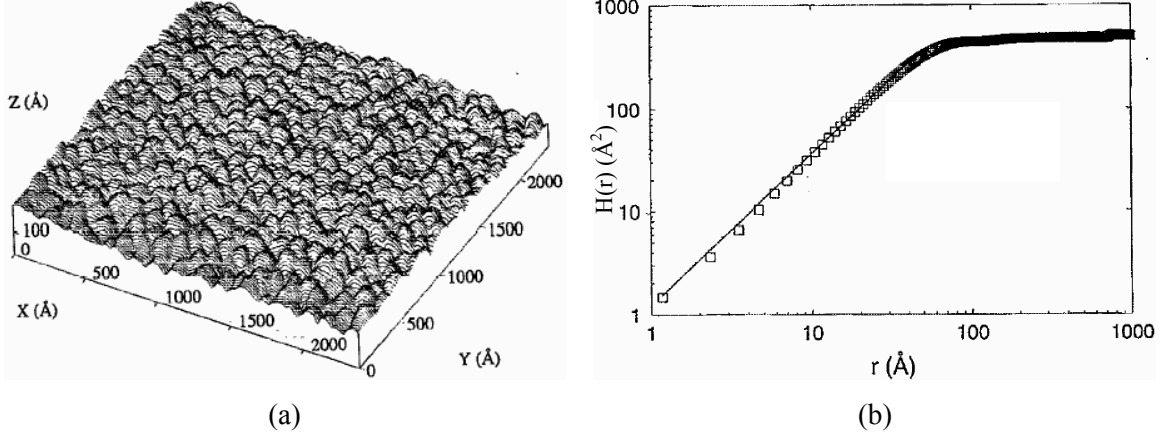


Figure 2.2 STM profile of an evaporated Au-Pd alloy film (a) and the corresponding height correlation function (b). Fitting by means of equations [2.3] and [2.4] gives $\sigma = 1.5$ nm, $\xi_{//} \sim 4$ nm and $h = 0.75$. After [5].

$$H(r) = \langle [z(r) - z(0)]^2 \rangle = 2\sigma^2 f\left(\frac{r}{\xi_{//}}\right) \quad [2.3]$$

$f(x)$ is a scaling function that can satisfy equations [2.2]. In one of the forms it is written as [6]

$$f(x) = 1 - \exp(-|x|^{2h}) \quad [2.4]$$

By calculating the height difference function for various r the values of σ , $\xi_{//}$ and h could be calculated. An example of the surface roughness analysis using such technique is shown in Figure 2.2.

2.1.2 X-ray

As a means of investigating the structural properties of sputtered thin films, x-ray technique has a number of advantages. It is a non-local and non-destructive technique, has a large range of resolution (from tens of nm down to Å). While in most of the laboratory sources the x-ray wavelength is fixed (determined by the material used to construct the anode of the radiation source), the use of synchrotron sources permits a choice of wavelengths which, when tuned close to the absorption edges of particular elements within the samples [7], element-selective analysis can be performed.

2.1.2.1 Experimental methods

X-ray characterization was carried out in the project using a Philips X'Pert diffractometer with Cu K_{α} radiation ($\lambda = 0.1541$ nm) and the Bragg-Bertano geometry. The sample was placed on a piece of glass slide and held flat by plasticine with the aid of a pair of supporting slides on both sides (Figure 2.3). These steps were important as they ensured that the whole assembly, being clamped on the pair of supporting slides, rotated about an axis lying on the surface of the film. Failure to do so would lead to errors in the measured peak values, which is given by

$$\delta(2\theta) = \frac{2x \cos \theta}{R} \quad [2.5]$$

x is the displacement of sample surface from the rotation axis, and R is the distance from the beam source to the axis. A sample displacement of 0.1 mm, for instance, would lead to an error of about 0.07° for 2θ below 60° ($R = 173$ mm from the diffractometer geometry used in this project). Such an error can be detrimental to the quantitative analysis of data at low 2θ values.

Two different regimes of x-ray diffraction can be employed to investigate the structural properties of layered thin films at different length scales.

2.1.2.2 High angle regime ($2\theta > 15^{\circ}$)

X-ray diffraction techniques (coupled θ - 2θ and ω -scans) were used to clarify the microstructure of multilayers. In θ - 2θ scans, sample and detector angles are moving in a fixed ratio of 1:2 with respect to the direction of incoming radiation. In such a configuration, the lattice spacing of the constituent layers can be determined whenever the Bragg condition is met:

$$n\lambda = 2d_{hkl} \sin \theta \quad [2.6]$$

where n is an integer and d_{hkl} refers to the d -spacing between successive (hkl) planes. On the other hand, ω -scans (rocking curves) were used to determine the mosaicity of the films so deposited [8].

In order to extract information from the scans, quantitative analyses were carried out by best-fitting the scans with the PROFIT program developed by Langford *et. al.* [9]. By means of a Pseudo-Voigt function the peaks were deconvoluted into a Gaussian and a Lorentzian part, depending on the ratio of the peak width at half maximum intensity $2w$ (FWHM) to the integral breadth β [10]. The importance of the step is that instrumental broadening can affect Lorentzian

and Gaussian profiles in different ways [10]. For the deconvoluted Gaussian and Lorentzian parts of integral breadths the following relations hold:

$$\text{Gaussian:} \quad (\beta_G^t)^2 = (\beta_G^m)^2 - (\beta_G^i)^2 \quad [2.7 (a)]$$

$$\text{Lorentzian:} \quad \beta_L^t = \beta_L^m - \beta_L^i \quad [2.7 (b)]$$

where the subscripts G and L refer to the Gaussian and Lorentzian parts, and superscripts t , m and i refer to the true profiles, the measured profiles and the contributions from instrumental broadening. β^i 's can be determined by deconvoluting the peak profile of a single crystal substrate.

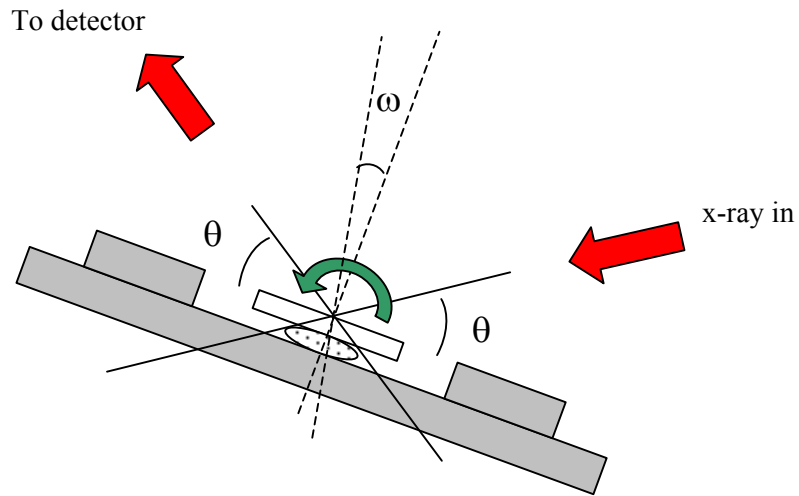


Figure 2.3 X-ray measurements sample set-up and measurement geometry

Out-of-plane grain sizes can be determined by means of the Scherrer equation [11]

$$D = \frac{\lambda}{\beta \cos \theta} \quad [2.8]$$

where D is the vertical grain size. One can also determine the grain size and strains of the crystallites by the Williamson-Hall plot [9]. The breadth of the peaks can be represented by the following equation:

$$B_{2\theta} \cos \theta = \frac{k_1 \lambda}{D} + k_2 \varepsilon \sin \theta \quad [2.9]$$

k_1 and k_2 are constants, and $B_{2\theta}$ is either $2w$ or β of the peaks (if the latter is used, the rms strain can be obtained).

2.1.2.3 Low angle regime ($2\theta < 15^\circ$)

X-ray reflectivity, which exploits the low angle regime ($2\theta < 15^\circ$), was used to investigate the morphological properties of multilayer structures. X-rays travel with different speed in different materials. In general the refractive index of x-ray is slightly below 1, and is determined by the electron density (hence the mass density and the atomic number) of the material [6]. In the high angle regime this is not a problem, since refraction is minimal. In the low angle regime, on the other hand, the effect becomes more important. Potential refraction, absorption and multiple reflection of x-rays have to be taken into account to fully model the effect.

A qualitative idea of various effects on the reflectivity scans can be shown with the aid of Figure 2.4. The following features are noteworthy.

- There is an initial drop of the intensity at the very low 2θ value ($< 1^\circ$), known as the critical angle $2\theta_c$, which is due to the total external reflection of x-ray from the external surface of the film.
- The closely spaced oscillations along the scan, known as the Kiessig fringes, is due to the interference of x-rays from the bottom (film/substrate interface) and the top (film/air interface) surfaces of the films. The closer are the fringes, the thicker is the film. The total film thickness can be roughly calculated, from the 2θ values of consecutive peaks, as [12]

$$\sin^2 \theta_m - \sin^2 \theta_{m-1} = \left(\frac{\lambda}{2t_{film}} \right)^2 \quad [2.10]$$

By plotting $(\sin^2 \theta_{m+1} - \sin^2 \theta_m)$ for successive peaks against n (n can be an integer starting at any arbitrary value) the film thickness can be determined from the slope.

- In the particular case when there is a repeated structure within the sample ([Cu/Co] repeated bilayers as in Figure 2.4), a Bragg peak with the 'lattice parameter' being the repeated layer thickness can be observed. This permits a quick estimate of the repeated bilayer thickness.
- The very general trend of film or interface roughness on the reflectivity scans is to cause a more rapid drop in the reflectivity. The contrast of modulation can also be reduced due to the presence of film roughness.

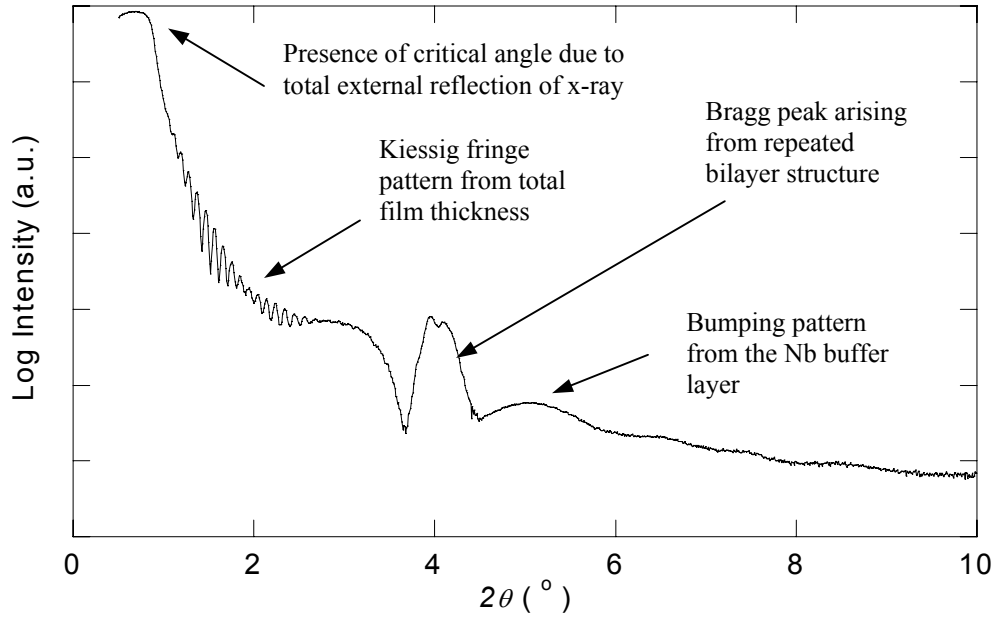


Figure 2.4 Low angle specular reflectivity profile for GMR repeated bilayer sample Nb (4.5 nm)/[Cu (0.9 nm)/Co (1.3 nm)]₃₀.

In general, morphological parameters cannot be obtained easily by just measuring certain parameters in the reflectivity scans, and fitting must be performed to obtain an accurate estimate of the parameters.

2.2 Magnetic characterization

The study of magnetic properties in this project was done by the vibrating sample magnetometer (VSM), which measured the global magnetic response of the sample with regards to an external applied field. Developed by Foner about half a century ago [13, 14], the VSM is a commonly employed technique in the characterization of all kinds of magnetic samples, ranging from thin films to bulk materials, with a sensitivity generally down to the range of μemu . The technique is non-destructive, and no sample preparation is needed in general.

The schematic of a VSM set-up is shown in Figure 2.5. Sample to be examined is placed in the middle of an applied magnetic field, together with a pair of stationary pick-up coils. By vibrating the sample in a uniform field, the sample is set into relative motion with the pick-up coils and signals (in the form of induced e.m.f., according to the Faraday's Law) are generated in the pick-up coils due to the presence of the oscillating magnetic flux from the sample. By calibrating the

VSM with a known strength of magnetization, absolute values of magnetic moments in the samples along the field direction can be obtained.

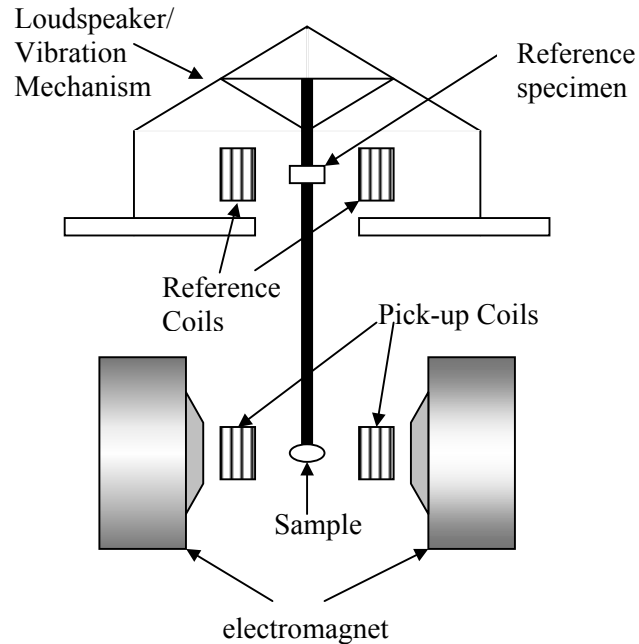


Figure 2.5 Schematic of a vibrating sample magnetometer, after [13].

2.3 Electrical characterization

2.3.1 Electrical resistivity of thin films

Compared with the bulk state, thin films are subjected to the scattering effect of the surface, which can lead to an increase in the resistivity. Also important is the presence of numerous defects in general in sputter deposited thin films. It is common for resistivities of such films to be higher than the literature values obtained from the same bulk materials.

A commonly employed theory of resistivity in thin films was due to Fuchs and Sondheimer [15, 16]. They started with the Boltzmann transport equation [17], which is a steady-state condition statement that the electron distribution function is in dynamic equilibrium, as a consequence of the combined effect of acceleration due to the presence of electric field E and electron scattering effects. By assuming a uniform field E along the x-direction and that the film was infinite in the

x-y plane, they calculated the current density $J(z)$. Integrating over the whole thickness of film the conductivity was obtained as:

$$\frac{\sigma(t)}{\sigma(\infty)} = 1 - \frac{3}{8\kappa} + \frac{3}{2\kappa} \int_1^\infty e^{-\kappa x} \left(\frac{1}{x^3} - \frac{1}{x^5} \right) dx, \quad \kappa = \frac{t}{\delta} \quad [2.11]$$

with δ being the electron mean free path in the homogenous film of thickness t and $\sigma(t)$ $\left(= \frac{1}{\rho(t)} \right)$ is the thickness-dependent conductivity of the film. The derivation of equation [2.11]

has assumed perfectly diffuse scattering at the film surfaces. Similar equation has also been provided in [16] to take into account the specular scattering effect at the surfaces.

2.3.2 Van der Pauw resistivity measurement

The measurements of the room-temperature (RT) resistivity in thin films samples were done by means of the technique suggested by van der Pauw [18]. He showed that the electrical resistivity of uniform thin films of any surface geometry could be deduced through measuring a combination of resistances with leads attached to its edges (Figure 2.6 (a)), according to the following relations

$$\exp\left(-\frac{\pi t_{film}}{\rho} \times \frac{V_{CD}}{I_{AB}}\right) + \exp\left(-\frac{\pi t_{film}}{\rho} \times \frac{V_{DA}}{I_{BC}}\right) = 1 \quad [2.12]$$

where symbols carry their usual meanings, and subscripts of V and I denote the configurations under which the corresponding measurements are made.

In the course of this project, van der Pauw measurements were made by means of ultrasonic wire bonding to the edges of the films. The technique is rather general, with differences between measured *sheet* resistance $\left(\frac{\rho}{t_{film}} \right)$ less than 5% for wires bonded to different sites of the edges.

Alternatively the conventional four-point probe measurements could be employed. Extra care has to be taken on the film geometry in this case, as current paths in the samples has to be consider if the absolute film resistivity has to be measured. A compilation of the correction factors with different film and probe geometry can be found in [19]. All the measurements were made with a low-frequency (40 Hz) a.c. current of peak value 10 mA.

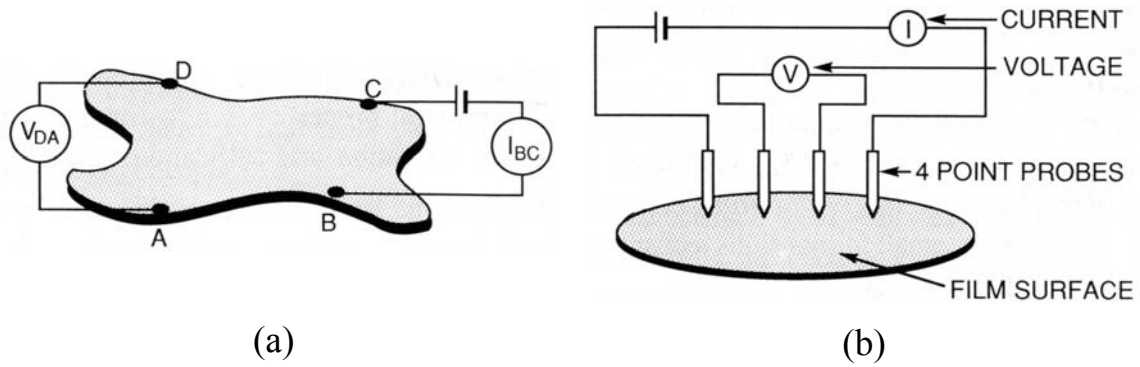


Figure 2.6 Configuration of van der Pauw thin film resistivity measurement (a) and four-point probe resistance measurement (b). After [20].

2.3.3 Field-dependent resistance (MR) measurements

MR measurements were performed by the four-point probe geometry with an applied a.c. current of 10-mA peak-value, in the vicinity of an external field. Both RT and low temperature (liquid nitrogen temperature, which is 77 K) measurements have been made. The MR ratio of the sample was then determined according to the following equation:

$$\frac{R(H) - R(H_s)}{R(H_s)} \times 100\% \quad [2.13]$$

MR measurements are complimentary to the magnetic characterization mentioned in section 2.2. Yet they can provide unique information on the properties of the structures that cannot be easily obtained through magnetic measurements. MR measurements can be useful in probing the *magnetic* properties of artificially fabricated nanostructures, whose magnetic signals are generally weak and difficult to be probed by conventional magnetic means [21-23].

References for Chapter 2

1. R.E. Somekh, W.C. Shih, K. Dyrbye, K.H. Huang and C.S. Baxter, *SPIE Proc. Series* **1140**, 453-463 (1989).
2. J.M. Bennett and L. Mattsson, *Introduction to surface roughness and scattering*. 2nd ed. Optical Society of America (1999).
3. J.C.S. Kools, W. Kula, D. Mauri and T. Lin, *J. Appl. Phys.* **85**, 4466-4468 (1999).
4. H.N. Yang, G.C. Wang and T.M. Lu, *Diffraction from rough surfaces and dynamic growth fronts*, pp. 136-168, World Scientific Pub. (1993).
5. H.N. Yang, A. Chan and G.C. Wang, *J. Appl. Phys.* **74**, 101-106 (1993).
6. T.P.A. Hase, *Ph. D. Thesis*, University of Durham (1998).
7. B.D. Cullity, *Elements of x-ray diffraction*, pp. 13-19, Addison-Wesley Pub. Co. (1978).
8. B.D. Cullity, *Elements of x-ray diffraction*, pp. 277-278, Addison-Wesley Pub. Co. (1978).
9. J.I. Langford and D. Louer, *Powder Diffr.* **1**, 211-221 (1986).
10. T.H. Dekeijser, J.I. Langford, E.J. Mittemeijer and A.B.P. Vogels, *J. Appl. Crystallogr.* **15**, 308-314 (1982).
11. B.D. Cullity, *Elements of x-ray diffraction*, pp. 99-106, Addison-Wesley Pub. Co. (1978).
12. K.Y. Kok, *Ph. D. Thesis*, University of Cambridge (1997).
13. S. Foner, *IEEE Trans. Magn.* **17**, 3358-3363 (1981).
14. S. Foner, *J. Appl. Phys.* **79**, 4740-4745 (1996).
15. K. Fuchs, *Proc. Camb. Phil. Soc.* **34**, 100-108 (1937).
16. E.H. Sondheimer, *Adv. Phys.* **1**, 1 (1952).
17. N.W. Ashcroft and N.D. Mermin, *Solid State Physics*, pp. 319-322, Saunders College (1976).
18. L.J. van der Pauw, *Philips Res. Rep.* **13**, 1-9 (1958).
19. S.M. Sze, *VLSI technology*, in *McGraw-Hill series in electrical engineering. Electronics and electronic circuits.*, p 188, McGraw-Hill (1988).
20. M. Ohring, *The materials science of thin films*, p 454, Academic Press (1992).
21. N. Garcia, M. Munoz and Y.W. Zhao, *Phys. Rev. Lett.* **82**, 2923-2926 (1999).
22. J.A. Katine, A. Palanisami and R.A. Buhrman, *Appl. Phys. Lett.* **74**, 1883-1885 (1999).
23. R.D. Slater, J.A. Caballero, R. Loloee and W.P. Pratt, *J. Appl. Phys.* **90**, 5242-5246 (2001).

Chapter 3 Interlayer Exchange Coupling and Giant Magnetoresistive Effect

This chapter summarizes the important aspects concerned with the phenomena of interlayer exchange coupling and giant magnetoresistive (GMR) effect in ferromagnetic (FM)/non-magnetic (NM) metallic heterostructures. Magnetic heterostructures exhibiting these effects are of physical interest and technical importance, most notably in magnetic data storage applications, sensors and device fabrication [1].

3.1 Interlayer exchange coupling

3.1.1 Introduction

Consider the case in which two thin ferromagnets (FM)¹ are separated by a non-magnetic (NM) spacer layer in the absence of an external magnetic field, as shown in Figure 3.1. Two particular cases are shown in the figure. In (a) the magnetization vectors of the two magnetic layers (FM1 and FM2) show an antiparallel alignment (or ‘antiferromagnetic (AF) coupling’) between them, while Figure 3.1(b) shows the case of parallel alignment (‘ferromagnetic (FM) coupling’). The study of interlayer exchange coupling, as will be shown later, is concerned with the alignment of FM layers that are separated by a spacer.

3.1.1.1 Bilinear coupling

The study of interlayer exchange coupling in FM/NM heterostructures is not a new subject. In 1960s experiments have been performed [2], which showed a long range (between 5 to tens of nm) FM coupling between evaporated ferromagnetic films across a spacer layer. These results were sometimes complicated by poor sample preparation techniques [3]. Bridging between

¹ Throughout the text the abbreviation ‘FM’ would mean both ‘ferromagnets’ and ‘ferromagnetic’. Still, the word ‘ferromagnetic’ carries two meanings in the text. It describes the long-range parallel spin correlation within a single layer, as well as the state in which two (or more) magnetic layers show a parallel alignment of magnetizations. The specific meaning should be explicit from the context, otherwise clear wordings will be used. The same applies to the abbreviation ‘AF’ (meaning ‘antiferromagnet’ or ‘antiferromagnetic’).

ferromagnetic films through pinholes, which were channels of voids, grain boundaries in the spacer or even crossing-over of interfaces (due to high degree of interface roughness) would effectively couple the two films via direct exchange interaction. Only FM-type coupling has been observed in FM/NM heterostructures in these early studies.

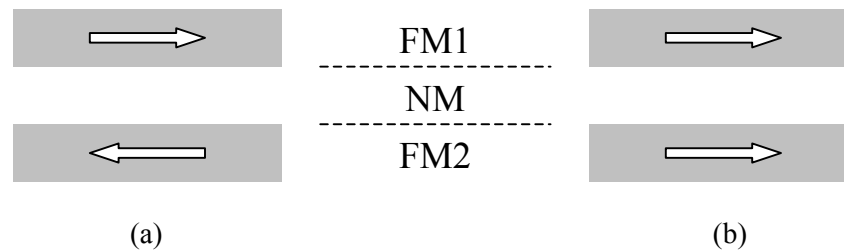


Figure 3.1 Schematic diagrams illustrating the phenomena of (a) antiferromagnetic coupling and (b) ferromagnetic coupling between two ferromagnetic layers separated by a spacer layer. Arrows indicate the magnetization direction of the ferromagnetic layers.

In 1986 Majkrzak *et. al.* first observed AF-type coupling between Gd layers in [Gd/Y] repeated bilayer ‘superlattice’ structure [4]. Later, Grünberg *et. al.* reported AF coupling in MBE-grown Fe/Cr/Fe samples [5]. Grünberg *et. al.* also observed that the magnetization of the layers were perpendicular to the applied field when the field magnitude was small, analogous to the ‘spin-flop’ state in antiferromagnets.

The interest in interlayer exchange coupling was further raised when the AF coupling was later found to be present in sputter deposited samples [6]. More importantly, such coupling was oscillatory with the spacer thickness, and existed generally for two FM separated by a transition metal spacer [7, 8]. In certain systems such as epitaxially grown Fe/Cr [9] or Co/Cu [10], multiple oscillatory periods have been observed.

3.1.1.2 Biquadratic coupling

Apart from the two distinct states of alignment mentioned in Figure 3.1, another interesting situation has been found in some experiments of Fe/Cr/Fe trilayers [11]. At relatively large Cr thickness ($> 2-3$ nm), magnetization measurements have shown a particular phase with the total magnetization equal to one-half of the saturation value of the trilayer structure, when the two Fe layers were of identical thicknesses. Kerr microscopy performed on such samples revealed that

the magnetization of the two Fe layers preferred to align perpendicular to one another, and such kind of coupling is known as the biquadratic coupling [12].

3.1.1.3 Phenomenological descriptions

Phenomenologically, the interlayer exchange coupling energy per unit area ($E_{1,2}$) between two FM layers FM1 and FM2 (magnetization \mathbf{M}_1 and \mathbf{M}_2 , respectively), separated by a spacer of thickness t_{NM} , can be written in the following form:

$$E_{1,2}(t_{NM}) = -J_1(t_{NM})\cos\alpha_{1,2} - J_2(t_{NM})\cos^2\alpha_{1,2} \quad [3.1]$$

where $\alpha_{1,2} = \cos^{-1} \frac{\mathbf{M}_1 \cdot \mathbf{M}_2}{|\mathbf{M}_1||\mathbf{M}_2|}$ refers to the relative magnetization orientations of FM1 and

FM2, J_1 and J_2 are the bilinear and biquadratic coupling constants. At the moment $E_{1,2}$ (and hence J_1 and J_2) is assumed to be dependent only on t_{NM} , and more parameters will be included in the forthcoming discussions. The competition between J_1 , J_2 and anisotropy terms can lead to a very rich phase diagram [13]. In the limit of vanishing anisotropy energy (as discussed in [14]), positive or negative values of J_1 represent FM and AF coupling respectively. For 90°-phase to be observed J_2 has to be negative and larger in magnitude compared with that of J_1 . Higher order terms can be present theoretically but they usually have negligible contributions.

Values of J_1 can be estimated from the magnetization measurements, for example, by VSM (section 2.2.1) or magneto-optical Kerr effect (MOKE) measurements. An example is presented in Figure 3.2(a), which shows the magnetization curves of Fe/Mo/Fe trilayer samples. When the two FM layers are antiferromagnetically aligned, the coupling between the layers can be determined according to the equation

$$cJ_1 = -H_s M_{FM} t_{FM} \quad [3.2]$$

in which c takes the value 1 when there is a first order re-orientation (with an abrupt jump to saturation), or 2 when the orientation is of second-order (smooth $M(H)$ dependence before saturation) [14]. In the case that repeated bilayers are used, J_1 is further halved to take into account that two surfaces of each FM layer are being coupled (sample surface effect is neglected).

As is evident from Figure 3.2(a), equation [3.2] is only applicable to AF coupled multilayers. Determination of the coupling strength in the case of FM alignment is not straightforward. A solution was provided by Parkin and Mauri [15], who determined the FM coupling in the

[NiCo/Ru] system by pinning one of the FM layers in the FM/NM/FM structure by means of strong interlayer coupling through a thin spacer (Co/Cu in the case of [15]). The NiCo layer lying next to the Co/Cu bilayers was so strongly AF coupled that the other NiCo layer could be switched easily without causing the reversal of the pinned layer, permitting the coupling in NiCo/Ru/NiCo to be measured (Figure 3.2(b)).

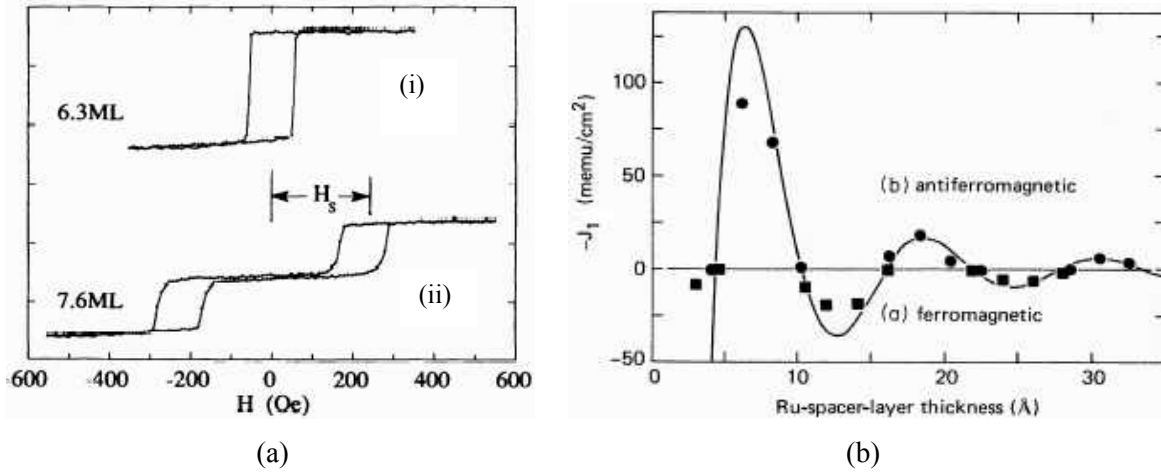


Figure 3.2 (a) Determination of antiferromagnetic coupling in Fe (14 ML)/Mo/Fe(100) (14 ML) trilayers, by means of MOKE magnetometer [16]. The two Fe layers are FM coupled at $t_{Mo} = 6.3$ ML (i), but AF coupled when $t_{Mo} = 7.6$ ML (ii). To determine the FM coupling strength, some means have to be provided to fix one of the FM layers (refer to text for explanation). An example of J_1 determination in $Ni_{80}Co_{20}/Ru/Ni_{80}Co_{20}$ is shown in (b) [15].

The case of biquadratic coupling is more complicated. In-plane magnetic anisotropy becomes an influencing parameter on the final behaviour of the heterostructures. In case that the anisotropy energy is negligible, canting of magnetization in zero field occurs as a consequence of the competition between J_1 and J_2 . More general cases of incorporating anisotropies into the energy equation require numerical solutions for obtaining the exact behaviour. A more comprehensive discussion can be found in [14].

3.1.2 Theoretical models

3.1.2.1 Bilinear coupling

Two general approaches have been employed to tackle the bilinear interlayer exchange coupling effect. The first one is an extension from the phenomenological theory (the Ruderman-Kittel-Kasuya-Yoshida, or RKKY, theory) originally developed to explain the oscillatory spin polarization behaviour of dilute magnetic clusters in a non-magnetic host, which has a striking resemblance with the oscillatory behaviour of J_l in the [FM/NM] multilayer heterostructures. The second approach is based on the consideration of the quantum confinement effect arising from the periodic modulations of the superlattice structures.

3.1.2.1.1 RKKY coupling model

The very original model of the RKKY theory [17] was developed by Ruderman and Kittel to describe the coupling between two nuclear spins in the nearest neighbour atoms via the conduction electrons. It was modified by Kasuya and Yoshida, extending its applicability to the case of interaction between localized magnetic moments via the conduction electrons of a non-magnetic host. The conduction electrons of the host help to mediate the coupling between the two embedded localized moments, which are not necessarily next neighbours. The coupling strength, according to the RKKY theory and in the limit of free electron host, is oscillatory with decaying amplitude, the strength of which is inversely proportional to the cube of the distance between the moments.

As soon as the AF coupling was discovered in rare-earth/Y superlattices, theoretical modelling was performed by Yafet to extend the RKKY model from localized ‘point’ moments to continuous FM layers [18]. The calculated coupling, in the limit of $t_{NM} \rightarrow \infty$, has the form:

$$J_1 \propto \frac{\sin(2k_F t_{NM})}{t_{NM}^2} \quad [3.3]$$

where k_F is the Fermi wavevector. A quick check on the validity can be made by fitting the data in Figure 3.2(b) with the function of the form $J_1 \propto \frac{\sin(\psi + 2\pi t_{NM} / \Lambda)}{t_{NM}^p}$ (Λ being the period of oscillation), yielding $p = 1.8$ and $\Lambda = 1.15$ nm. While the rate of decay of the coupling strength was in accord with the prediction, the period was far too large compared with the estimation

(~ 0.25 nm) by equation [3.3]. A simple explanation on the discrepancy can be made by considering the discrete nature of atomic planes in multilayers [19]. Sampling of the coupling strength through the spacer can only take place at integral values of atomic planes in the growth direction. The period of oscillation, after taking into account of such an *aliasing effect*, is given

$$\text{by } \Lambda = \left| \frac{k_F}{\pi} - \frac{n}{d} \right|^{-1}, \text{ } d \text{ being the lattice parameter along the growth direction and } n \text{ is an integer.}$$

While the RKKY model captured the spirit of the oscillatory behaviour of J_l with t_{NM} , it suffered from a number of drawbacks. The model, strictly speaking, should not be applicable to $3d$ transition metal ferromagnets due to their itinerant nature: electrons responsible for magnetism in these metals also take part in conduction. Besides, the above model is based on the free electron assumption, which have spherical Fermi surface. The true Fermi surface topology (which is never spherical even in the case of noble metals like Cu or Au) plays a decisive part of the oscillation period(s). By taking the true picture into account, Bruno and Chappet [20] managed to predict the presence of the multiple periods of oscillations in some systems, which have been observed experimentally (Table 3.1).

Spacer	Theory	System	Experiment
Cu(111)	$\Lambda = 4.5$ AL	Co/Cu/Co(111)	$\Lambda \approx 5$ AL
		Co/Cu/Co(111)	$\Lambda \approx 6$ AL
		Co/Cu/Co(111)	$\Lambda \approx 4.5$ AL
		Fe/Cu/Fe(111)	$\Lambda \approx 6$ AL
Cu(001)	$\Lambda_1 = 2.6$ AL $\Lambda_2 = 5.9$ AL	Co/Cu/Co(001)	$\Lambda \approx 6$ AL
		Co/Cu/Co(001)	$\Lambda_1 \approx 2.6$ AL $\Lambda_2 \approx 8$ AL
		Co/Cu/Co(001)	$\Lambda_1 \approx 2.7$ AL $\Lambda_2 \approx 6.1$ AL
		Co/Cu/Co(001)	$\Lambda_1 \approx 2.7$ AL $\Lambda_2 \approx 5.6$ AL
		Fe/Cu/Fe(001)	$\Lambda \approx 7.5$ AL
Ag(001)	$\Lambda_1 = 2.4$ AL $\Lambda_2 = 5.6$ AL	Fe/Ag/Fe(001)	$\Lambda_1 \approx 2.4$ AL $\Lambda_2 \approx 5.6$ AL
		Fe/Au/Fe(001)	$\Lambda_1 \approx 2$ AL $\Lambda_2 \approx 7-8$ AL

Table 3.1 Comparison of the J_1 oscillation periods in different spacer systems, as predicted from the RKKY model and measured from experiments [20].

3.1.2.1.2 Quantum well model

A different approach in tackling the problem of bilinear interlayer exchange coupling was proposed by Edwards *et. al.* [21], who attributed the coupling effect as a consequence of spin-dependent confinement of electrons in the quantum well provided by the spacer layers. Electron wavefunctions can be transmitted or reflected at FM/NM interfaces, depending on the degree of matching of electron bands at the Fermi level. Consider the simplest case of one-dimensional wave propagation, with perfect matching of the majority spin band of the FM and the NM layers and a large exchange splitting of the FM. The consequences of the above assumption is a total confinement of the minority spin band within the NM spacer, leading to the oscillatory coupling strength due to the interference of the electron wavefunctions. $J_I(t_{NM})$ was then computed by comparing the energy difference between the parallel and antiparallel alignment of the FM layers.

Computed results of the quantum well model indicated some similar features compared with the RKKY model, most notably the periodicity of oscillations and the rate of decay of J_I (in the form of $\frac{1}{t_{NM}^2}$). In fact the RKKY model is related to the quantum well model, as described by Bruno [22]. He provided a unified picture of the two approaches, treating the interlayer exchange coupling as the interference of wavefunctions travelling in different directions, by considering the possible reflections and transmissions at the boundaries (interfaces). He showed that while the RKKY model was the extreme case of weak reflection at the boundaries, the full-confinement quantum well model was actually the strong reflection limit of such a model. Detailed reviews of the bilinear interlayer coupling effect can be found in [23-25].

3.1.2.2 Biquadratic coupling

While the intrinsic natures of the spacer have been successfully employed in explaining the bilinear interlayer exchange coupling, this was not the case of biquadratic coupling. Calculations of the biquadratic terms based on intrinsic exchange energy usually yielded J_2 values much smaller than experimental results, or they could only be observed at the J_I oscillation nodes. These facts have led to attempts of explaining biquadratic coupling by extrinsic effects [26].

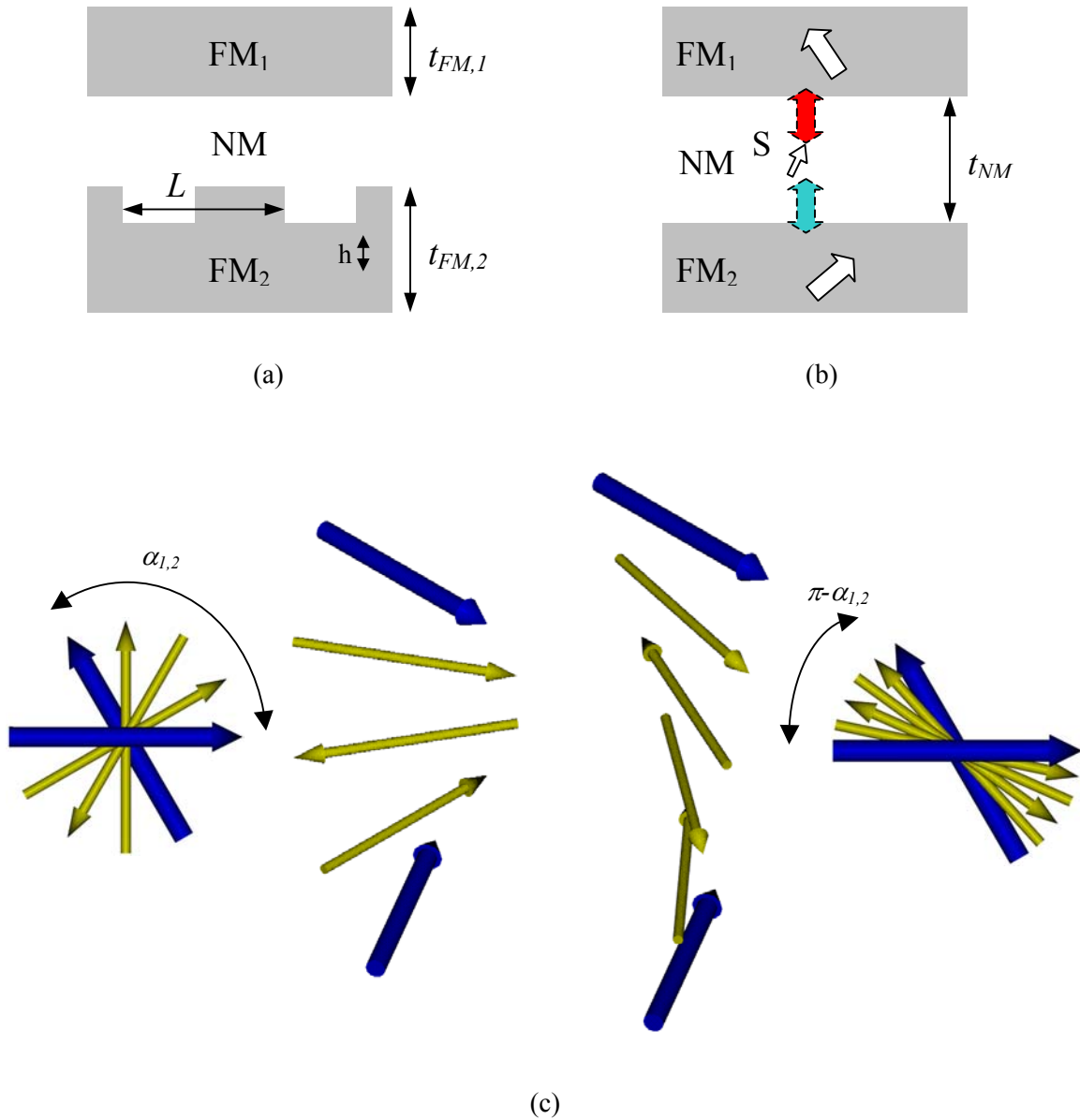


Figure 3.3 Three of the commonly invoked models for biquadratic interlayer exchange coupling based on extrinsic mechanisms: (a) roughness induced fluctuation model, (b) loose spin model and (c) proximity magnetism model [26]. Blue arrows in (c) refer to the FM magnetization, and yellow arrows represent the AF sublattice magnetization. The diagrams at the sides of (c) are the top-views of the corresponding 3-dimensional spin structures in the middle (shown in isometric views).

3.1.2.2.1 Rough interface models

The first attempt to model biquadratic coupling, as proposed by Slonczewski [27], took account of the spacer thickness fluctuations. In some systems like Fe/Cr, J_1 has been shown to change signs with the addition of a ML at the spacer [9]. Consider the hypothetical surface in Figure 3.3(a). If L is long enough, it is possible for domains to be formed on the terraces, separated by domain walls at the step edges [28]. However, when L is short, it is energetically unfavourable to form a large number of domain walls. The energy of the system is minimized when the two FM layers adopt an orthogonal coupling condition. According to Slonczewski's calculation the effective coupling is given by

$$J_2 = \frac{L(\Delta J_1)^2}{\pi^3} \sum_{i=1,2} \frac{\cot(2\pi t_{FM,i}/L)}{A_i} \quad [3.4]$$

where A_i is the exchange stiffness of the corresponding FM layer (A_{FM}), L is the width of the terraces and ΔJ_1 refers to the variation of coupling across the steps.

It is assumed in equation [3.4] that $L \gg t_{NM}$, which is true in the most systems with observable interlayer coupling effect: t_{NM} in such systems prepared by sputtering or MBE are usually in the range of nanometres, which is about an order of magnitude smaller than L . The effect of t_{NM} is reflected through ΔJ_1 . According to equation [3.4] J_2 increases with the terrace width, which is valid as long as J_2 is smaller than ΔJ_1 , beyond which domain formation within terraces is energetically preferred, as stated in the previous paragraph.

Demokritov *et. al.* have provided another model of biquadratic coupling based on the roughness effect of the interfaces [29]. Instead of relying on the J_1 variation with t_{NM} , this model investigated the effect of stray field induced by the roughness. In their calculations, Demokritov *et. al.* assumed identical FM layers (same material and $t_{FM,1} = t_{FM,2} = t_{FM}$), and that only one of the interfaces were rough (Figure 3.3(a)). The coupling strength was found to be

$$J_2 = \frac{M_{FM}^4 \hbar^2 L}{A_{FM} \pi} \sum_{m=1}^{\infty} \frac{(-1)^{m-1}}{(2m-1)^3} \exp\left[-\frac{4\pi t_{NM}}{L}(2m-1)\right] \left\{ 1 - \exp\left[-\frac{8\pi t_{FM}}{L}(2m-1)\right] \right\} \quad [3.5]$$

Similar to equation [3.4], equation [3.5] shows an increasing J_2 strength with the terrace widths.

3.1.2.2.2 Loose spin model

The ‘thickness fluctuation’ mechanism has only a moderate temperature dependence, since J_I and A_{FM} varies weakly with temperature (from zero temperature to RT) for 3d FM [30]. However it has been found, for example in Fe/Al system [31], that the temperature dependence of biquadratic coupling is much stronger than expected from thickness fluctuation mechanism.

Slonczewski then proposed another theoretical model [32] to tackle the problem. He considered the case in which magnetic impurities were present in the spacer or at its interfaces, as shown by a small arrow of spin S in the NM layer in Figure 3.3(b). The situation is the same as that described by the RKKY-type indirect exchange interaction discussed in the previous section. In the current situation, however, one of the FM layers is replaced by the embedded magnetic impurities in the spacer. Such impurities interact with the two FM layers on both sides of the NM and mediate the interaction of the two FM layers.

At high temperature, S is not strongly interacting with the exchange field due to thermal excitation. This brings a weak effect on the exchange coupling between the two FM layers and so a relatively small magnitude of J_2 . As temperature decreases the effective interaction between the FM layers and S increases rapidly due to suppressed thermal activation. This brings in the strong non-collinear coupling term.

3.1.2.2.3 Magnetic proximity effect

As it was seen previously, the first discoveries of the biquadratic coupling were found in systems with Cr spacers, which is an antiferromagnet. In the simplest form an AF layer can be considered to consist of two sublattices (hence not simple NM) pointing in opposite directions (hence not FM). AF spins at the interface are also coupled to the FM, as shown in Figure 3.3(c).

Consider the case in which there is a deviation of collinear alignment of the FM magnetizations M_1 and M_2 . It is known that the J_{ex} roughly scale with their transition temperatures (T_C and T_N for FM and AF respectively) [33]. T_C s in FM are usually above 600 K for 3d ferromagnets, which is much higher than the T_N of most of the AF elements (Cr = 310 K [34], for example). It is therefore justified to consider that the FM layers have uniform magnetization (in the transverse

direction), and that the AF layers deviates from their collinear alignment, with the free energy given by

$$\sum_{i \neq j} J_{i,j} S_i S_j (1 - \cos \beta_{i,j}) \quad [3.6]$$

$J_{i,j}$ being the exchange between two layers of spins in the AF (which can take positive or negative values when coupled to even or odd number neighbours, respectively), and $\beta_{i,j}$ being the angular separation between the two AF layers. The most important contributions of the free energy arise from the next-neighbour interaction.

If the AF layer is thick enough, $\beta_{i,j}$ between neighbouring AF sublattice magnetizations are roughly constant and equals to $\frac{[\alpha_{1,2}]}{n}$ or $\frac{[\pi - \alpha_{1,2}]}{n}$, depending on the number of AF monolayers (Figure 3.3(c)) (the square bracket notation ensures that $\alpha_{1,2}$ and $(\pi - \alpha_{1,2})$ must be smaller than π , as winding up the spins more than this is unfavourable compared with the situation of winding up in the opposite chirality). It can then be seen that equation [3.6] is approximately quadratic in $\beta_{i,j}$ (and so in $[\alpha_{1,2}]$ or $[\pi - \alpha_{1,2}]$). Based on these Slonczewski [32] proposed the phenomenological formula for $E_{1,2}$

$$E_{1,2} = C_+ [\alpha_{1,2}]^2 + C_- [\pi - \alpha_{1,2}]^2 \quad [3.7]$$

where C_+ and C_- are constants. In case the constant terms in equation [3.7] are of comparable magnitude the system would prefer perpendicular alignment based on this energy term.

Equation [3.7] can be shown to approach saturation asymptotically rather than being achieved at a finite field. This prediction has been observed experimentally in Fe/Mn/Fe system [35], showing the validity of the model. Recently a more generalized formulation of the proximity magnetism model has been developed by Xi and White [36], which took into consideration of the spin structure in the AF layer in the calculations. While the Xi and White model possibly gave a more accurate description of the problem (if the model was correct) than that by Slonczewski, the basic idea is the same.

3.2 Giant magnetoresistive (GMR) effect

3.2.1 Introduction

Shortly after the discovery of the AF coupling effect, Baibich *et. al.* [37] discovered in AF-coupled [Fe/Cr] repeated bilayers a drastic change in the resistance with an application of magnetic field at 4.2 K. The MR ratio, according to equation [2.10], was about 80%, with $H_s \sim 20$ kOe. Before this discovery it was known that the resistance of conductors can change under the application of an external magnetic field [38]. The effects, however, were generally small, especially at low magnetic fields (below 10 kOe). For example, the anisotropic magnetoresistive (AMR) effect [39] has been known to exist in ferromagnets when there is a relative orientation η between the current and magnetization direction (Figure 3.4 (a)):

$$R(\eta) = R_0 + \Delta R_{AMR} \cos^2 \eta \quad [3.8]$$

The MR for the AMR effect is about 4 % in bulk NiFe alloys at RT, and is usually smaller in thin films [39]. Therefore the effect discovered by Baibich *et. al.* was a much more dramatic effect, and was therefore coined as the ‘giant magnetoresistance’.

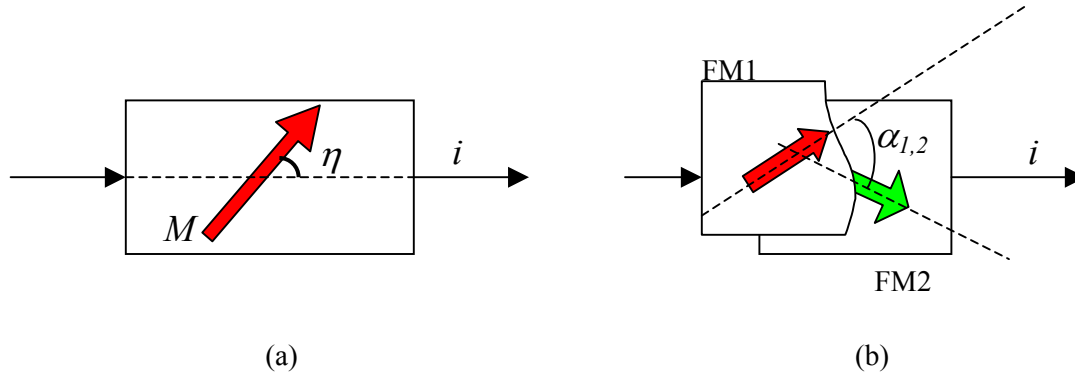


Figure 3.4 Plain view of the AMR effect (a) and the GMR effect (b). Current is flowing in the plane of the film in both cases.

The discovery of the GMR effect soon after the experimental realization of AF interlayer exchange coupling was not coincidental. A direct comparison of t_{NM} dependence of the interlayer exchange coupling (represented by the saturation field) and the GMR effect (represented by the MR ratio) in sputter deposited Fe/Cr repeated bilayers can be seen in Figure 3.5. One can immediately observe the identical periods and phases of the oscillating GMR and J_I coupling behaviour. This clearly shows the close relations between the two effects.

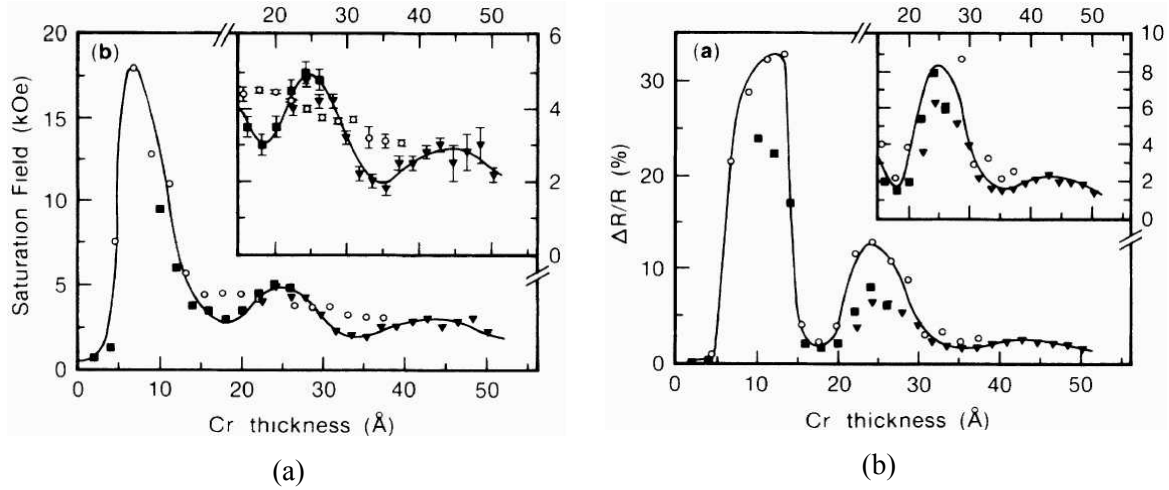


Figure 3.5 Saturation Field (a) and magnetoresistance (b) of sputter deposited Si (111)/Cr (10 nm)/[Fe (2 nm)/Cr (t_{Cr} nm)]_N/Cr (5 nm) ($N = 20$ (○) or 30 (●, ▼)) measured at 4.2 K [6].

The resistance in GMR multilayers is closely related to the magnetization states of the structure. In the case of a trilayer structure (Figure 3.4 (b)) the resistance can be written in the following form comparable to equation [3.8] [40]:

$$R(\alpha_{1,2}) = R_o + \frac{\Delta R_{GMR}}{2} (1 - \cos \alpha_{1,2}) \quad [3.9]$$

Such formulation is also useful conceptually in understanding the resistance change in repeated bilayers and spin valves (Chapters 6-8).

One should also notice that there are two different geometries of extracting the GMR response of multilayered sample. In the current-in-plane (CIP) geometry electric field is applied along the plane of the film, while in the current perpendicular to plane (CPP) geometry the electric field direction is along the film normal. The electronic transport configuration is very different in the two situations, and in the following only the CIP geometry will be covered. Further discussions on the CPP GMR can be seen in [41].

3.2.2 Theory of GMR effect

3.2.2.1 Principle

The main idea behind all the models developed for the GMR effect is the difference of resistivities between the spin up and spin down electron channels, first proposed by Mott [42].

Consider a hypothetical band structure of a $3d$ ferromagnet (Ni, Fe or Co) (Figure 3.6 (a)). Ferromagnetism can be thought to arise from the asymmetry or splitting of the $3d$ electron bands in these elements, which lead to the presence of net spins and thus a magnetic moment.

Another consequence of the band splitting which is relevant to the GMR effect is the unequal density of states at the Fermi energy level E_F . As known from the Fermi's Golden Rule [43], the degree of scattering of a particular spin of electrons is dependent on the density of states of the corresponding spin at E_F . The two spin channels are subjected to different degrees of scattering, leading to a difference in resistivities. The resistivity of the material, neglecting spin-flipping events, is the parallel sum of the two spin channels.

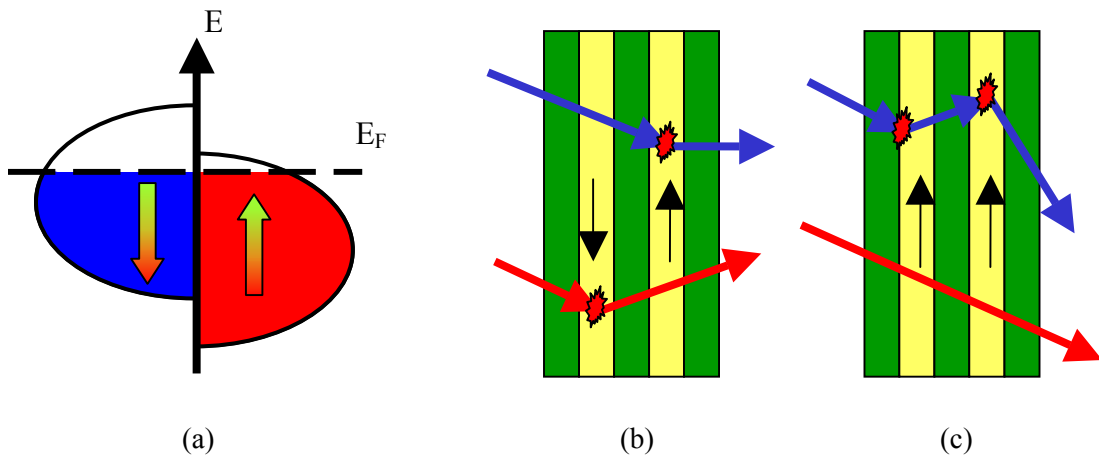


Figure 3.6 (a) Hypothetical representation of d -electron bands of a $3d$ ferromagnet. Note the different density of states at the Fermi energy level E_F . Also shown are the paths for up (red arrows) and down (blue arrows) spin electrons as they travel through the GMR heterostructures, with the ferromagnetic layers in AF (b) and FM (c) alignment.

Consider the case in which the magnetization vectors are aligned antiparallel in the FM layers (Figure 3.6 (b)). Majority spin electrons in one FM layer would become minority spin electrons in the nearest FM layers, as they travel through the spacer. There is not a particular spin channel in this case that has a lower resistivity (in fact the two channels should have the same resistivities by symmetry argument). On the other hand, in the case of parallel magnetization alignment, there is a particular spin channel that has a lower resistivity. Since the resistivity of the whole structure is the parallel sum of the two spin channels, the resultant resistivity is lowered, hence explaining the GMR effect.

3.2.2.2 GMR models

3.2.2.2.1 Semi-classical model

Shortly after the discovery of the GMR effect, Camley and Barnas [44] proposed a semi-classical approach to tackle the problem, in the spirit of which Fuchs and Sondheimer developed the theory of resistivity of thin films [45, 46] (section 2.3.1). In order to calculate the resistivity of a magnetic multilayered structure, phenomenological spin-dependent conditions were included, including the probabilities of diffuse electron scattering in the bulk, as well as transmission and specular reflection at the interfaces.

The model has been employed in the early GMR investigations, most notably on the effect of bulk and interface spin-dependence on the GMR effect. For example, Willekens *et. al.* [47] investigated the effect of interfacial intermixing by depositing sub-atomic layers of Cu and Co at the interface of [Co/Cu] repeated GMR multilayers. They compared the results with a model [48] modified from that by Camley and Barnas, which considered intermixing effect as an additional layer between the otherwise abrupt FM/NM interfaces. Their calculations suggested that intermixing produced spin-independent scattering at the Co/Cu interfaces, which led to the drop of the MR ratio with an increasing degree of intermixing. Besides, the model has successfully modelled the thickness dependence of t_{NM} and t_{FM} [49].

The major shortcoming of the model was that it was phenomenological, with a lot of parameters to be adjusted (transmission, reflection and scattering probabilities for two spins of electrons). Often assumptions have to be made to simplify the calculations [44, 50]. Besides, the free-electron approach (as used by Fuchs and Sondheimer in deriving the thin film resistivity) may encounter problems in modelling the GMR structures that contains $3d$ transition metal FMs. Hybridization of sp and d -band electrons are known in these FMs. In other words, electrons that are responsible for the magnetism can also take part in the conduction process. This has been clearly shown by Tsymbal and Pettifor [51].

A very clear demonstration of the failure of the semiclassical model has been provided by Bailey *et. al.* [50, 52], who measured *in situ* the conductance change of the NiO/Co/Cu/Co structure with the gradual addition of layers. As shown in Figure 3.7(a), there is a highly asymmetric behaviour

in the conductance between the Co/Cu and Cu/Co interfaces. While the structure showed an increase in the slope of conductivity with the deposition of Cu, there is an abrupt drop of conductance with the addition of Co on Cu. With semiclassical models they could not even qualitatively model the different behaviour between the two interfaces (Figure 3.7(b)).

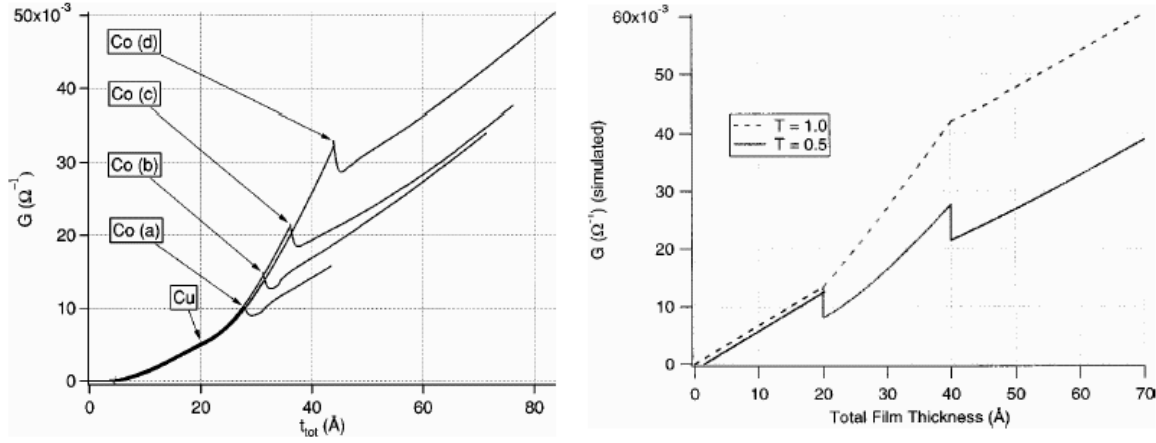


Figure 3.7 Conductance variation of NiO/Co (20 Å)/Cu (t_{Cu} Å)/Co (40 Å), measured in-situ during the ion-beam deposition process (a) and modelling results (b). Legends in (b) refer to the probability of interface scattering employed in the modelling. None of the models could even fit qualitatively the asymmetric behaviour of Co/Cu and Cu/Co interfaces shown in (a). After [50, 52].

3.2.2.2.2 Quantum-mechanical approach

More rigorous treatment on the problem can be proceeded by means of a quantum-mechanical approach, which was first investigated by Levy, Zhang and Fert [53]. They included the effect of scattering, both bulk and interface, by introducing spin-dependent scattering potential functions in the calculation of the conductivity of heterostructures. The employment of the quantum-mechanical approach avoided the problem concerned with the thickness of the layers. As the thickness of the layers decrease, quantum effect has to be taken into account for the transport behaviour, rendering the semi-classical approach not applicable. However, the model by Levy *et al.* strongly overestimated the GMR effect. The problem of the approach was that they have not taken the spin-dependent electronic structure into account, which seemed to be an important factor in examining the GMR effect as introduced below.

In most of the early experiments, attention has been paid to the whether bulk or interface scattering effects were making contributions to the GMR effects. A number of recent results,

however, could not be addressed by such approaches. Marrows and Hickey, for example, doped the FM layers in the Co (2.5 nm)/Cu (3 nm)/Co (2.5 nm)/FeMn (8 nm) with sub-atomic layers of transition metals, with varying distance away from the Co/Cu interfaces [54]. The interesting result was that the GMR could be enhanced as the doping layer (Cu for example) moved *away* from the Co/Cu interfaces. One would expect that any NM impurities could increase the spin-independent scattering and thus a drop in the GMR effect, which was not the case observed. If the GMR effect in Co/Cu/Co were due to spin-dependent scattering in the bulk, moving the dopants in the Co layer should not affect the GMR ratio. Again this was not the case.

In another example, Stanley *et. al.* inserted progressively thicker Co layers at the FM/Cu interfaces (FM = NiFe, Ni, Fe, Gd and Dy in this case) to replace gradually the FM in the FM (3 nm)/Cu (2.4 nm)/FM (3 nm)/FeMn (7.5 nm) [55] structure. They found that the GMR values saturated exponentially with increasing Co thickness, in accord with the results by Parkin [8]. However, the rate in which the MR returned to the value of Co/Cu/Co/FeMn structure varied significantly in different cases. They fitted the data with the exponential form $A + B [1 - \exp(-x/t)]$ (A , B being constants, x is the thickness of Co replacing the FM layers, t is a characteristic length showing the speed in which the saturation is attained). The t value was found to range from ~ 0.2 to 0.3 nm in Ni and NiFe to about 2 nm in Dy. The result is not expected if only spin-dependent scattering models, either in the bulk or at the interfaces, were considered, since similar amplitudes of t should be expected.

Recent GMR models seem to provide some more insight on the origin of the GMR effect. It has been stressed that realistic GMR models should take into account the real electron band structure of the layers. Such an approach was adopted by Tsymbal and Pettifor [51, 56], who considered the GMR effect to arise from the *spin-dependent* electronic structures of the constituent layers. They suggested that diffuse scattering occurred due to the *spin-independent* disorders in the heterostructures, which commonly exist in thin films as bulk defects, interfacial roughness or intermixed boundaries. Such disorders were included as random scatters in the scattering potentials in their calculations. By using realistic band structure calculations they obtained GMR values [Co/Cu] and [Fe/Cr] repeated bilayer structures close to literature values [57]. Besides the model was able to address a number of problems mentioned above, more notably on the asymmetric conductivity of Cu/Co and Co/Cu interfaces shown in Figure 3.7. Comparisons between experimental results and calculations performed by Bailey *et. al.* [52] is shown in Figure 3.8.

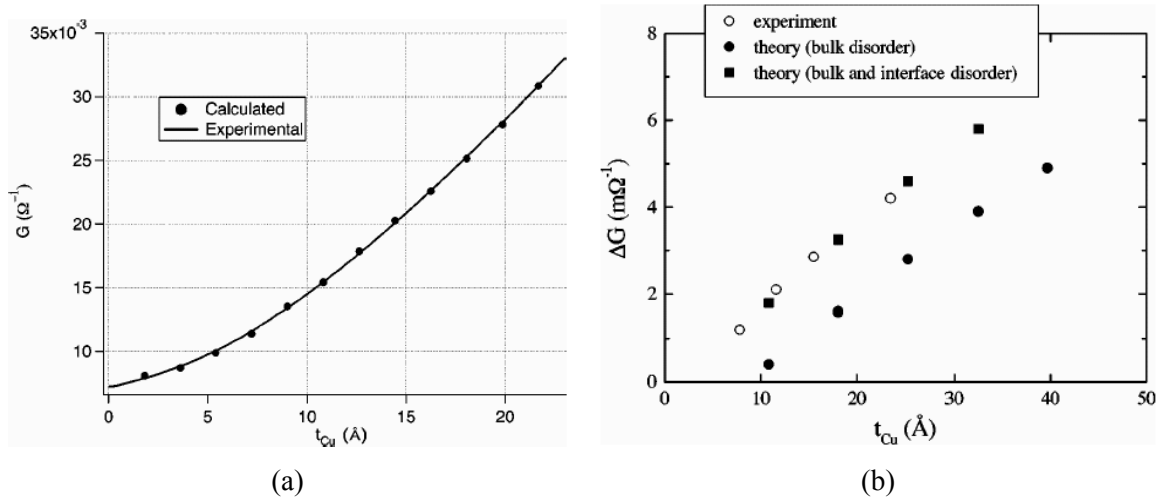


Figure 3.8 t_{Cu} dependence of the measured conductivity in NiO/Co/Cu (a) and conductivity drop in NiO/Co/Cu/Co due to the addition of Co on Cu (b) (refer to caption of Figure 3.7 for the structures). Theoretical fits (solid line in (a) and solid symbols in (b)) were based on [51]. After [52].

3.3 Summary

In this chapter the interlayer exchange coupling and giant magnetoresistive effects were introduced. Based on these phenomena practical magnetic multilayer structures have been constructed. In particular, the spin valve structures is of particular relevance to these effects and are studied in Chapters 6-8 of this thesis.

References for Chapter 3

1. U. Hartmann, *Magnetic multilayers and giant magnetoresistance: fundamentals and industrial applications*. Springer series in surface sciences ; 37. Springer (2000).
2. J.C. Bruyère, G. Clerc, O. Massenet, D. Paccard, R. Montmory, L. Néel, J. Valin and A. Yelon, *IEEE Trans. Magn.* **1**, 174-180 (1965).
3. O. Massenet, F. Biragnet, H. Juretschke, R. Montmory and A. Yelon, *IEEE Trans. Magn.* **2**, 553-556 (1966).
4. C.F. Majkrzak, J.W. Cable, J. Kwo, M. Hong, D.B. McWhan, Y. Yafet, J.V. Waszczak and C. Vettier, *Phys. Rev. Lett.* **56**, 2700-2703 (1986).
5. P. Grünberg, R. Schreiber, Y. Pang, M.B. Brodsky and H. Sowers, *Phys. Rev. Lett.* **57**, 2442-2445 (1986).
6. S.S.P. Parkin, N. More and K.P. Roche, *Phys. Rev. Lett.* **64**, 2304-2307 (1990).
7. S.S.P. Parkin, R. Bhadra and K.P. Roche, *Phys. Rev. Lett.* **66**, 2152-2155 (1991).
8. S.S.P. Parkin, *Phys. Rev. Lett.* **71**, 1641-1644 (1993).
9. J. Unguris, R.J. Celotta and D.T. Pierce, *Phys. Rev. Lett.* **67**, 140-143 (1991).
10. M.T. Johnson, S.T. Purcell, N.W.E. McGee, R. Coehoorn, J. Destegge and W. Hoving, *Phys. Rev. Lett.* **68**, 2688-2691 (1992).
11. P. Grünberg, S. Demokritov, A. Fuss, M. Vohl and J.A. Wolf, *J. Appl. Phys.* **69**, 4789-4791 (1991).
12. M. Rührig, R. Schafer, A. Hubert, R. Mosler, J.A. Wolf, S. Demokritov and P. Grunberg, *Phys. Status Solidi A* **125**, 635-656 (1991).
13. M. Maccio, M.G. Pini, P. Politi and A. Rettori, *Phys. Rev. B* **49**, 3283-3293 (1994).
14. S.O. Demokritov, *J. Phys. D: Appl. Phys.* **31**, 925-941 (1998).
15. S.S.P. Parkin and D. Mauri, *Phys. Rev. B* **44**, 7131-7134 (1991).
16. Z.Q. Qiu, J. Pearson, A. Berger and S.D. Bader, *Phys. Rev. Lett.* **68**, 1398-1401 (1992).
17. J.K. Kübler, *Theory of itinerant electron magnetism*, pp. 256-266, Clarendon Press; Oxford University Press (2000).
18. Y. Yafet, *Phys. Rev. B* **36**, 3948-3949 (1987).
19. R. Coehoorn, *Phys. Rev. B* **44**, 9331-9337 (1991).
20. P. Bruno and C. Chappert, *Phys. Rev. B* **46**, 261-270 (1992).
21. D.M. Edwards, J. Mathon, R.B. Muniz and M.S. Phan, *Phys. Rev. Lett.* **67**, 493-496 (1991).
22. P. Bruno, *J. Magn. Magn. Mater.* **121**, 248-252 (1993).
23. P. Bruno, *J. Phys.: Condes. Matter* **11**, 9403-9419 (1999).
24. J.K. Kübler, *Theory of itinerant electron magnetism*, pp. 254-279, Clarendon Press; Oxford University Press (2000).
25. *Ultrathin magnetic structures*, edited by A. Bland and B. Heinrich. Vol. II, Chapter 2, Springer (1994).
26. J.C. Slonczewski, *J. Magn. Magn. Mater.* **150**, 13-24 (1995).
27. J.C. Slonczewski, *Phys. Rev. Lett.* **67**, 3172-3175 (1991).
28. C.H. Marrows, *Ph. D. Thesis*, University of Leeds (1997).
29. S. Demokritov, E. Tsymbal, P. Grunberg, W. Zinn and I.K. Schuller, *Phys. Rev. B* **49**, 720-723 (1994).
30. J. Lindner, C. Rüdte, E. Kosubek, P. Pouloupoulos, K. Baberschke, P. Blomquist, R. Wappling and D.L. Mills, *Phys. Rev. Lett.* **88**, article no. 167206 (2002).
31. C.J. Gutierrez, J.J. Krebs, M.E. Filipkowski and G.A. Prinz, *J. Magn. Magn. Mater.* **116**, L305-L310 (1992).
32. J.C. Slonczewski, *J. Appl. Phys.* **73**, 5957-5962 (1993).

33. B.D. Cullity, *Introduction to magnetic materials*, in *Addison-Wesley series in metallurgy and materials*, pp. 131-136, Addison-Wesley Pub. Co (1972).
34. D. Jiles, *Introduction to magnetism and magnetic materials*, p 236, Chapman & Hall (1997).
35. M.E. Filipkowski, J.J. Krebs, G.A. Prinz and C.J. Gutierrez, *Phys. Rev. Lett.* **75**, 1847-1850 (1995).
36. H.W. Xi and R.M. White, *Phys. Rev. B* **62**, 3933-3940 (2000).
37. M.N. Baibich, J.M. Broto, A. Fert, F.N. Vandau, F. Petroff, P. Eitenne, G. Creuzet, A. Friederich and J. Chazelas, *Phys. Rev. Lett.* **61**, 2472-2475 (1988).
38. J. Singleton, *Band theory and electronic properties of solids*, in *Oxford master series in condensed matter physics*, Chapter 10. Oxford University Press (2001).
39. T.R. McGurie and R.I. Potter, *IEEE Trans. Magn.* **11**, 1018-1038 (1975).
40. J.C.S. Kools, R. Coehoorn, W. Folkerts, M.C. DeNooijer and G.H.J. Somers, *Philips J. Res.* **51**, 125-148 (1998).
41. E.Y. Tsymbal and D.G. Pettifor, *Perspectives of giant magnetoresistance*, in *Solid State Physics*. Vol. 56, pp. 113-237, Academic Press Inc. (2001).
42. N.F. Mott, *Adv. Phys.* **13**, 325-422 (1964).
43. P.L. Rossiter, *The electrical resistivity of metals and alloys*, in *Cambridge solid state science series.*, p 3, Cambridge University Press (1987).
44. R.E. Camley and J. Barnas, *Phys. Rev. Lett.* **63**, 664-667 (1989).
45. K. Fuchs, *Proc. Camb. Phil. Soc.* **34**, 100-108 (1937).
46. E.H. Sondheimer, *Adv. Phys.* **1**, 1 (1952).
47. M.M.H. Willekens, T.G.S.M. Rijks, H.J.M. Swagten and W.J.M. deJonge, *J. Appl. Phys.* **78**, 7202-7209 (1995).
48. B.L. Johnson and R.E. Camley, *Phys. Rev. B* **44**, 9997-10002 (1991).
49. B. Dieny, *J. Magn. Magn. Mater.* **136**, 335-359 (1994).
50. W.E. Bailey, S.X. Wang and E.Y. Tsymbal, *J. Appl. Phys.* **87**, 5185-5187 (2000).
51. E.Y. Tsymbal and D.G. Pettifor, *Phys. Rev. B* **54**, 15314-15329 (1996).
52. W.E. Bailey, S.X. Wang and E.Y. Tsymbal, *Phys. Rev. B* **61**, 1330-1335 (2000).
53. P.M. Levy, S.F. Zhang and A. Fert, *Phys. Rev. Lett.* **65**, 1643-1646 (1990).
54. C.H. Marrows and B.J. Hickey, *Phys. Rev. B* **63**, art. no.-220405 (2001).
55. F.E. Stanley, C.H. Marrows and B.J. Hickey, *J. Appl. Phys.* **87**, 4864-4866 (2000).
56. E.Y. Tsymbal and D.G. Pettifor, *J. Magn. Magn. Mater.* **202**, 163-173 (1999).
57. E.Y. Tsymbal and D.G. Pettifor, *J. Phys.: Condes. Matter* **8**, L569-L575 (1996).

Chapter 4 Exchange Anisotropy

4.1 Introduction

In 1956, Meiklejohn and Bean [1] discovered some fascinating behaviour in oxide-coated Co particles with sizes ranging from 10 to 100 nm in diameter. When these particles were field cooled in a 1 kOe external field from room temperature to 77 K, they observed a clear shifting of the hysteresis loop (~ 490 Oe) from the zero field axis, in a direction opposite to that of the cooling field (Figure 4.1). Besides, the coercivity of the hysteresis loop increased from ~ 850 Oe to ~ 1200 Oe. As the effect was postulated to arise from the interaction between the spins of Co atoms in the metallic Co cores and that of the Co ions in the antiferromagnetic oxide coatings, the effect was coined as the ‘exchange anisotropy’ or the ‘exchange bias (EB) effect’.

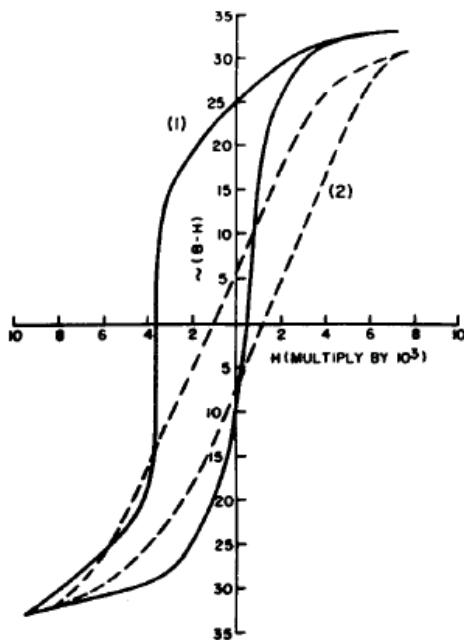


Figure 4.1. Hysteresis loops of oxidized Co particles at 77 K, cooled in zero field (dashed line) and with a 10-kOe field cooling (solid line) [1].

In the nearly three decades after the discovery of the effect, there has been little progress in terms of the basic understanding of the actual microscopic mechanism underneath the exchange bias effect. The major obstacle was the difficulty in establishing the actual spin structure of the antiferromagnetic layers, as well as the interfacial spin structure of both the FM and AF layers.

This situation has drastically changed since the late 1980s. With the discovery of the GMR effect (Chapter 3) and development of spin valve structures (Chapter 6), there has been a revived

interest in understanding the basic mechanism of the exchange bias effect, as well as improving the performance of the EB structures for device applications. Besides, the advancement in the computation power has enabled numerical modelling of the spin configuration in the EB systems, accelerating the theoretical understanding of the phenomenon. Finally, the improvement of the experimental techniques, such as neutron diffraction and synchrotron radiation, has enabled in-depth studies of the spin structures of both the FM and AF layers as well as the interfaces. These will be discussed in the forthcoming sections in this chapter.

4.1.1 Occurrence

The EB effect occurs quite generally in ferromagnet/antiferromagnet systems. In fact, such effect has also been observed in ferromagnetic/ferrimagnetic and ferromagnetic/spin glass systems. An extensive literature review has been provided by [2]. The following discussions will be mainly on FM/AF layered systems, although references will also be made on particulate structures.

Thickness is an important parameter in the EB layered structures. For an observable EB effect, the ferromagnet is typically below micron size. Therefore such effect can be observed in oxidized FM nanoparticles (as in [1]) or in layered heterostructures. On the other hand, there does not seem to be a particular upper limit in the dimension of the AF material for EB to be observed. In fact biasing has been frequently observed in FM films deposited on single crystals of AF materials [3]. However, there is a critical thickness t_{crit} for the AF below which the EB effect ceases to exist.

Magnetic treatment is required for the EB effect to occur. Two methods are commonly employed. One can cool the system from above the Néel temperature (T_N) when the FM is in a saturated state (for example, by applying a saturating magnetic field). When the sample is cooled, exchange anisotropy is established across the interface, achieving the EB effect. One can also deposit the structure in a magnetic field to establish the EB effect. It should be mentioned that the first method is, strictly speaking, applicable only when T_C is greater than T_N , which is usually the case for $3d$ ferromagnets (Co, Ni, Fe) and their binary or ternary alloys. The case of $T_C < T_N$ is relatively rare but physically interesting [4, 5], and is the discussion of section 4.3.2.

4.1.2 Shifting and widening of hysteresis loops

As mentioned before, one of most outstanding phenomena of the EB effect is the shifting of the hysteresis loop from the zero field position. Figure 4.2 shows the typical result obtained from a sample prepared in this project. In most of the EB systems, the loops are shifted opposite to the cooling field/*in situ* deposition field direction, which is generally known as the negative exchange bias effect. However, *positive* EB effect, i.e. H_{ex} has the same sign as the cooling field, can occur in some of the systems such as Fe/FeF₂ or Fe/MnF₂, which is thought to arise from the antiferromagnetic coupling between AF and FM layers [6].

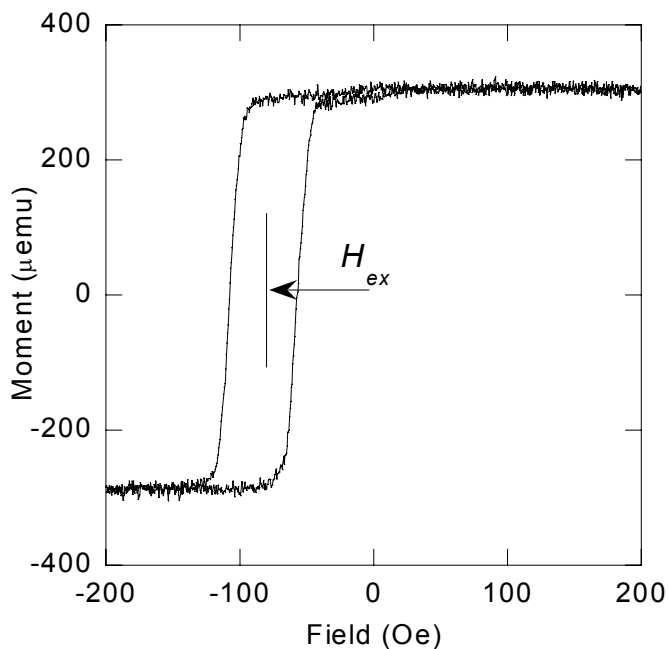


Figure 4.2. Hysteresis loop of a plane film $Ni_{75}Fe_{20}Mo_5$ (10 nm)/ $Fe_{50}Mn_{50}$ (20 nm), deposited with a +200 Oe *in-situ* magnetic field, measured at room temperature. H_{ex} (-82 Oe in this case) denotes the exchange bias field. Note also the H_c (25 Oe) compared with a single layer of 250-nm thick NiFeMo (0.7 Oe).

Another equally noticeable but less heavily investigated effect is the dramatic increase of the coercivity of the hysteresis loops of the bilayer structure. The example in Figure 4.2 is a typical illustration of this effect.

4.1.3 Training effect and memory effect

The behaviour of the EB systems is highly dependent on the magnetic history of the samples. This point can be illustrated by the training effect [7] and the memory effect [8]. A typical example of the training effect can be seen in Figure 4.3. The magnitudes of H_{ex} and H_c in a particular measurement are highly dependent on the number of magnetic measurements previously performed on the sample, and their magnitudes fall asymptotically with the number of

measurements made. Usually H_{ex} and H_c become practically constant after about 10 field sweeping cycles at room temperature. Besides, the effect is more prominent in polycrystalline systems than in single crystal AF systems [2].

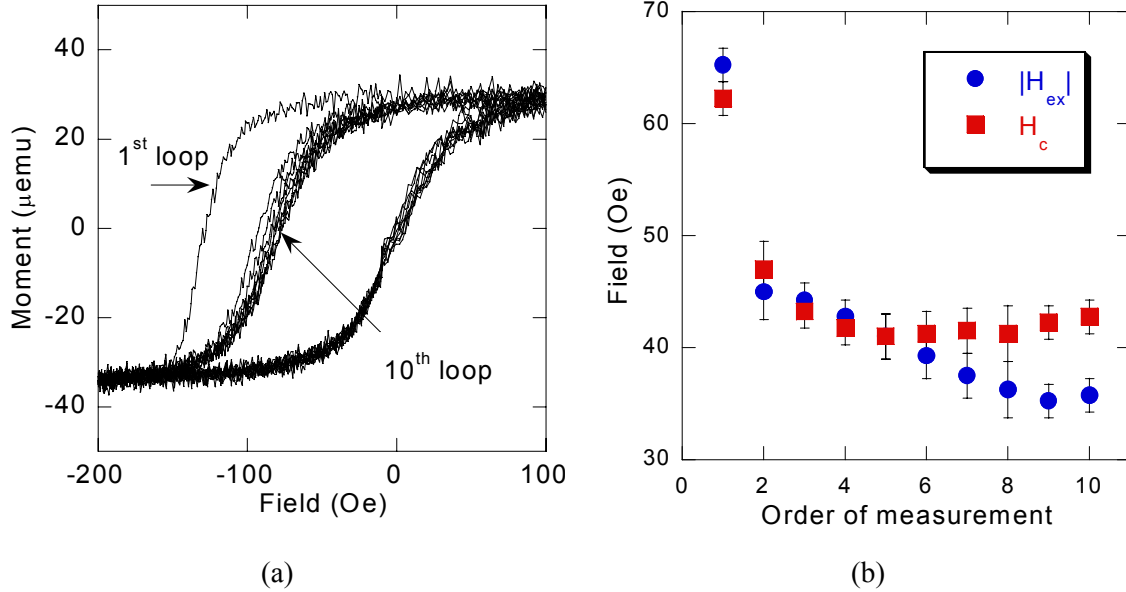


Figure 4.3 (a) A typical set of ten hysteresis loops, showing the training effect of the Co/FeMn system deposited in the project. The widths of the loops are diminishing in size (the 1st and the 10th loops are labelled in the figure) as repeated field sweepings are performed. Note that the descending field cycles shrink much faster than the ascending cycle, which is typical among metallic AF systems like FeMn or IrMn [7]. Values of H_{ex} (in absolute values) and H_c are extracted and plotted in (b).

It is suggested that spin re-organization at the FM/AF interfaces could have contributed to the training effect [2, 7]. As the AF layers are deposited or field cooled from above T_N , the spins at the interface are metastable. Sweeping the field between positive and negative H_s helps the interfacial spins to locate the equilibrium positions, leading to a reduced proportion of metastable spin structure and a drop of the switching field.

The memory effect can be understood as follows. The exchange coupling effect is highly dependent on the magnetic state of the FM layer and the temperature from which the cooling process starts. Field cooling with magnetization other than the saturated state would yield hysteresis loops drastically different from a single loop shifting behaviour [8, 9]. Besides, H_{ex} can be altered or even reversed, if the field cooling process is disturbed in between the initial and final

(measurement) temperatures, although the memory effect does not seem to have any effect on the H_c of EB systems [8]. The above discussions underline the importance of any magnetic disturbance on the behaviour of EB systems, especially when temperature variation is involved.

4.2 Exchange bias theory

A large number of theories have emerged to tackle the EB effect since it was discovered (for example see Berkowitz and Takano [10], Stamps [11] and Kiwi [12]). The last fifteen years, however, has witnessed the most rapid advancement in the field. In the following, a summary of the theoretical models developed so far will be presented.

4.2.1 Meiklejohn and Bean (MB) model

The earliest model of EB effect was proposed by Meiklejohn and Bean [1] (MB model) in explaining their results on oxide-coated nanoparticles. A number of assumptions have been made in this model:

1. The AF interface is perfectly smooth, totally uncompensated, and coupled ferromagnetically with the FM spins.
2. The AF anisotropy axis is collinear with that of the FM layer.
3. AF magnetization is assumed to be rigid along its anisotropy direction.
4. The magnetizations of FM and AF are homogenous, i.e. they do not possess spatial variation within the corresponding layers.

The energy of the system under an applied magnetic field H is then written as:

$$E = -HM_{FM}t_{FM} \cos(\theta - \alpha) - J_{FM/AF} \cos \alpha - K_{FM}t_{FM} \cos^2 \alpha \quad [4.1]$$

where the energy terms represent the Zeeman energy, the coupling energy between FM and AF at the interface, and the anisotropy energy of the FM spins. For $\theta = 0^\circ$, this can be written in the form analogous to the Stoner-Wohlfarth model (section 1.2) with an effective field H' given by

$$H' = H + H_{ex}, \quad H_{ex} = \frac{J_{FM/AF}}{M_{FM}t_{FM}} \quad [4.2]$$

which means that the whole magnetization curve shifts towards the negative field direction by the amount H_{ex} , explaining the occurrence of the negative EB effect. If the condition $K_{AF}t_{AF} \gg J_{F/AF}$ was not satisfied, the AF spins will follow the motion of the FM layer. An enhanced coercivity instead of a loop shift will be observed.

A quick examination of the model can be performed by direct substitution of suitable values of parameters into equation [4.2]. Taking $J_{FM/AF} \approx 25 \text{ erg/cm}^2$ for Fe-based alloys [13], $M_{FM} = 860 \text{ emu/cm}^3$ for permalloy ($\text{Ni}_{78}\text{Fe}_{22}$) [14] one would obtain $H_{ex} \approx 3 \times 10^4 \text{ Oe}$ for a 10 nm thick NiFe film on antiferromagnetic FeMn, which is about 2 orders of magnitude larger than the usual values ($\sim 100 \text{ Oe}$) obtained in NiFe/FeMn bilayer systems [13]. This demonstration shows the inadequacy of this simple model.

A number of assumptions made in the MB model are wrong or doubtful in real situations. The most obvious example is concerned with the flatness of interfaces. Real interfaces are never perfectly smooth. The presence of geometrical (roughness) and chemical (intermixing) fluctuations at the interfaces of thin film heterostructures are well recorded, as discussed in Chapter 1. The implication is that it is impossible to obtain a *perfectly smooth* interface. This is somehow related to the dubious assumptions of totally uncompensated FM/AF interfacial spin structures and homogenous magnetizations. Since roughness is always present, one runs into a dilemma that either the totally uncompensated interface assumption is incorrect, or the system cannot have a homogenous magnetization (Figure 4.4). Besides, if the assumption of uncompensated surfaces were true, this assumption would indirectly suggest that EB should be absent in systems with compensated interfacial AF spins, which is not the case [13]. Modifications are therefore necessary for the construction of more realistic models.

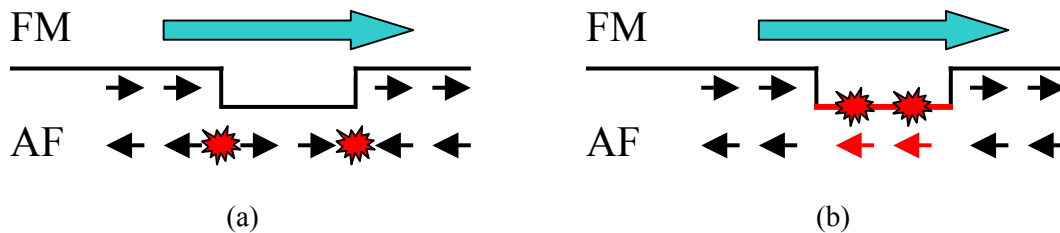


Figure 4.4 Problems associated with the 'flat interface' assumption of the MB model. The presence of roughness causes violation of either the coherent AF magnetization assumption (a) or the assumption of totally uncompensated interfacial AF spins (b), leading to the formation of AF 'domain walls' (as in (a)) or interfacial magnetic frustration (b).

Despite all these failures, the MB model has provided a very intuitive picture on the exchange bias effect, namely the effect arises from the coupling between FM and AF at the interface.

Models built later can by and large be regarded as the refined versions of the MB model, which are usually constructed with modified assumptions as listed above.

4.2.2 Random field model

Nearly 30 years after the MB model was proposed, Malozemoff [15-17] proposed that the EB effect can arise from the randomness of exchange interaction at the FM/AF interface (or the ‘random field’ as coined by Malozemoff). As mentioned previously, real interfaces are never totally flat as assumed by the MB model (Figure 4.4). Any surface inhomogeneities would generate magnetic frustrations, either at the AF or FM layer (AF frustration is depicted in Figure 4.4). To this end, Malozemoff argued that the AF would break up into domains. The random field is thus a consequence of the statistical averaging of the net magnetization within these AF domains due to surface irregularities.

Some events have to take place for the (anisotropic) random field to be present. In exchange biased bilayer structures, the asymmetry is brought about by the magnetic treatments mentioned before. The external field defines the FM magnetization as well as the AF spins. Once the process is finished the AF spin structure, at least away from the interface, has to be stabilized, otherwise the AF spin structure can be dragged along by the FM during the magnetization reversal, and no EB effect can be observed.

Within each AF domain, due to surface imperfections, different species of the possible staggered magnetizations in the AF arise at the interface. The size of the random field is dependent on the AF domain size and the amount of surface inhomogeneities. A statistical average of the net spins within the AF domains leads to the reduction of the interfacial coupling energy. The presence of H_{ex} is a consequence of such an averaged coupling energy. Analysis by Malozemoff suggested

that H_{ex} scaled with $\frac{\sqrt{A_{AF}K_{AF}}}{M_{FM}t_{FM}}$ (with a scaling factor of the order of unity), The correction to the

‘order of 2’ error can be shown by a simple calculation from the formula. Using NiFe/FeMn bilayer structure as an example ($K_{AF} \approx 1 \times 10^5$ erg/cm³, $A_{AF} \approx 3 \times 10^{-7}$ erg/cm [18]), one can obtain H_{ex} around 200 Oe and is much closer to the experimental values [13, 19].

Another interesting feature of the random field model is the dependence of the H_{ex} on t_{AF} [17], as shown in Figure 4.5. Three sections can be recognized from the figure. Between the two critical

thicknesses, there is a constant value of H_{ex} . When t_{AF} drops below t_{crit2} , there is an inverse relation between t_{AF} and H_{ex} , until a certain thickness when the coercive force of the AF is not strong enough to preserve the AF domain structure. This leads to a zero interfacial energy difference and hence the absence of H_{ex} . The prediction did match some (but not all) of the experimental observations, including the presence of t_{crit} (Figure 4.7(b)), the drop of H_{ex} between t_{crit} and t_{crit2} , and the approximately constant H_{ex} values for high t_{AF} values in most of the systems [20, 21].

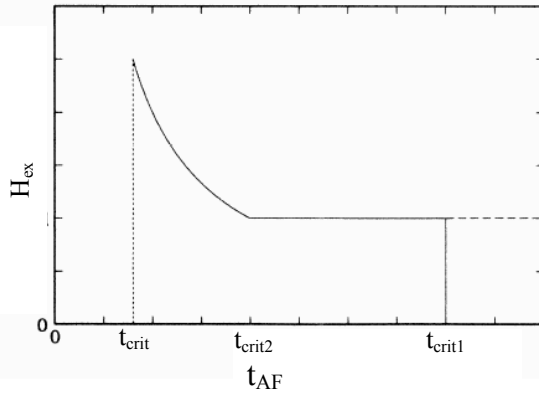


Figure 4.5 t_{AF} dependence of H_{ex} according to the random field model. After [17].

The random field model suffers from the problem that the exchange bias effect is highly dependent on the interface structure, which is so far a parameter that is difficult to be quantified. Given the similar H_{ex} values obtained in compensated and uncompensated AF surfaces [13], It is doubtful how the *similar amount* of uncompensated interfacial spins (as they have similar H_{ex}) could exist both in totally compensated and uncompensated surfaces, if the bulk spin structures were assumed at the interfaces. It is only until recently that some direct experimental evidence is provided to support the presence of random field (e.g. thermal remanent magnetization, spin imaging), which will be discussed later.

4.2.3 AF domain wall (Mauri) model

At the same time, Mauri *et. al.* [18] proposed a competing model which can correct the ‘order of two’ problem in the MB model. They suggested that the spins in the AF layer, instead of being rigidly coupled together, were capable of twisting. This occurred when the EB system tries to minimize the interfacial coupling energy, and this creates a magnetization spiral (analogous to a Bloch wall of a ferromagnet) in the AF layer (Figure 4.6). By taking account of the AF domain

wall formation, the energy equation was written as follows (H directed along positive y direction):

$$E = -HM_{FM}t_{FM} \cos \alpha + 2\sqrt{A_{AF}K_{AF}}(1 - \cos \beta_{int}) + \frac{A_{FM/AF}}{d_{FM/AF}}[1 - \cos(\beta_{int} - \alpha)] + K_{FM}t_{FM} \cos^2 \alpha \quad [4.3]$$

in which the second term ($2\sqrt{A_{AF}K_{AF}}(1 - \cos \beta_{int})$) is the AF wall energy, assuming the AF anisotropy axis lies along the y -direction. The third term represents the interfacial coupling energy, in which the exchange stiffness is represented by $A_{FM/AF}$.

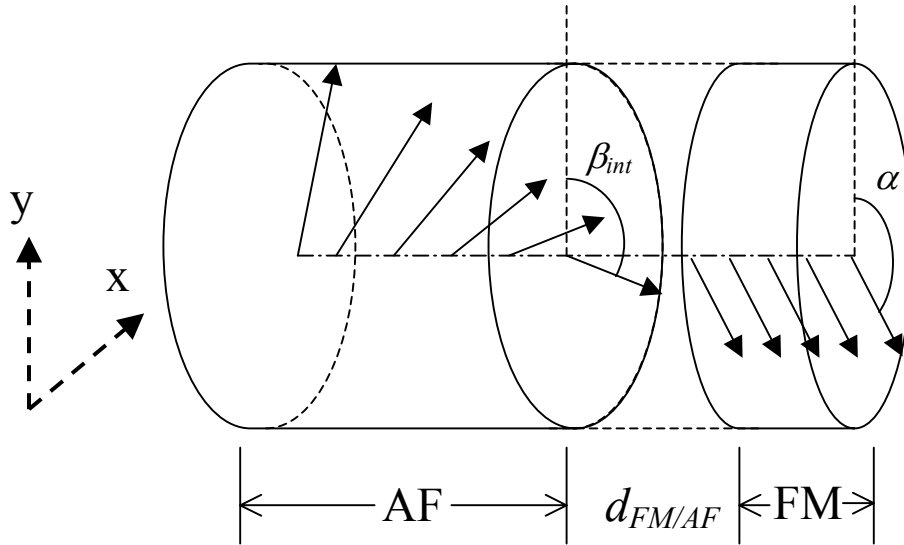


Figure 4.6 Parameters of the AF domain wall (Mauri) model [18]. Note that only one of the AF sublattices is shown for clarity.

Mauri *et. al.* calculated the $M(H)$ loops numerically by finding the ordered pair (α, β_{int}) at various H which minimized equation [4.3]. At $A_{FM/AF} = 0$, the familiar $M(H)$ loops as described by the Stoner-Wohlfarth model was obtained. As $A_{FM/AF}$ varied Mauri *et. al.* found a number of interesting features from the hysteresis loops:

1. With increasing values of $C_1 \left(\frac{A_{FM/AF}}{d_{FM/AF} \sqrt{A_{AF}K_{AF}}} \right)$, they observed an increasing value of H_{ex} ,

which was bounded by $\frac{2\sqrt{A_{AF}K_{AF}}}{M_s t_{FM}}$;

2. Their $M(H)$ loop simulations have shown asymmetric reversal behaviour between decreasing and increasing field paths with C_I less than or close to 1; for higher values the asymmetric behaviour vanishes.

Finding 2 has illustrated the possibility of reversal asymmetry in EB systems, which arises when the AF spins decouple from the FM spins at the interface. With the system biased towards positive field direction ($H_{ex} < 0$), a decreasing field cycle from positive H along y-axis (easy axis) would invoke magnetization reversal of the FM layer. Depending on the strength of C_2

($\frac{K_{FM}t_{FM}}{2\sqrt{A_{AF}K_{AF}}}$), the AF layer may choose to remain aligned along the uniaxial direction (for

$C_2 \ll 1$), switches abruptly to some intermediate values ($C_2 \sim 1$), or switches completely with the FM magnetization ($C_2 \gg 1$). In the ascending field cycle the AF layer returns to the positive y-direction with different paths, according to their magnetic status at the end of the descending field cycle (Figure 2 of [18]). Such results were consistent with the observation that the ascending and descending field cycles can have dissimilar behaviour in some EB systems [19, 22, 23].

A number of doubts were cast over this model [12]. It retained the assumption of totally uncompensated and smooth interfaces as in the MB model, the problems of which have already been discussed in 4.2.1. Besides, the large range of K_{AF} in different materials implies that the Mauri model may not be general enough to explain the exchange bias effect in the whole range of materials (Table 4.1). Nevertheless, the model has successfully described the EB effect in some systems, in particular the systems using AF-coupled GMR-type repeated bilayers as antiferromagnet [24]. Besides, the model was modified to deal with the coupling effect between two FM layers separated by an AF layer [25, 26] (section 3.1).

Table 4.1 Exchange stiffness A_{AF} , magnetocrystalline anisotropy K_{AF} and Néel Temperature T_N of some common antiferromagnetic materials. It should be noted that these values correspond to that of bulk single crystals (except K_{AF} of FeMn, which was estimated from polycrystalline thin film sample [27]).

AF	A_{AF} (erg/cm)	K_{AF} (erg/cm ³)	T_N (K) [2]
Fe ₅₀ Mn ₅₀	3×10^{-7}	1.3×10^5 [18]	490
NiO	1×10^{-6}	2.7×10^2 [28]	520
FeF ₂	7×10^{-8}	4×10^7 [28]	79

4.2.4 Spin flop model

In 1997, Koon performed micromagnetic simulation, in an attempt to settle the queries concerned with the EB systems with *compensated* FM/AF interfaces [29]. In his calculations, magnetization of the FM layer was assumed homogenous, and both the AF and FM magnetizations were free only within the plane of the film. Calculations were performed by fixing the spins at the outer FM and AF surfaces (i.e. the film surfaces away from the FM/AF interface) along the uniaxial direction, which was a variable in the study. With different interfacial spin configuration, spin relaxation was performed to evaluate the energy of the system under the situation of having varying uniaxial direction in the FM and AF layers. In the case in which the FM and the AF interfacial spins coupled homogeneously across the interface, Koon showed that an energy minimum occurred when the FM and AF layers had collinear uniaxial axis. However, in case of a *frustrated* interface, a minimum was found when the two axes were *perpendicular* to one another. The more important point was that the ‘frustrated interface’ energy minimum was found to be smaller than that of homogenous coupling across the interface, given the same values of exchange and layer thicknesses. Besides, Koon also claimed that a domain wall was still ‘observable’ within the AF layer, a result in echo with the Mauri model. The model by Koon also suggested the potential problem of the random field model, as the model has shown that a flat and compensated interface alone could generate the EB effect.

The calculation, however, was based on the assumption that the spin motion of the layers took place only within the film planes. This assumption was usually true for the FM layers due to the strong demagnetizing effect in the out-of-plane direction. Such effect, however, should be minimal in an AF layer due to the vanishing net magnetization. This fact was noted by Schulthess and Bulter [30]. They performed numerical calculation along the same line as Koon, except that they included a magnetostatic term to take account of the energy associated with the out-of-plane AF spins. Their calculations showed that, for a flat and compensated AF interface, the model proposed by Koon could only yield an enhanced coercivity in the FM/AF bilayers instead of any H_{ex} . To move a step further, they suggested that the presence of additional mechanisms was required to generate H_{ex} , and they called into the use of the Malozemoff’s random field model. Instead of being contradictory models, Schulthess and Bulter suggested that the random field model and the Koon’s model could be combined together to generate the exchange anisotropy. By introducing ‘defects’ at the interface in their calculations, they showed the presence of H_{ex} and an enhancement of H_c in the compensated EB systems.

It is seen that the spin flop model differs from the previous models in a number of senses. Firstly, it attempted to deal with a compensated AF interface instead of a totally uncompensated AF interface spin structures, as it was in many previous models. In order to explain the exchange bias effect, defects were introduced by Schulthess and Butler, in the spirit of the random field model. Besides, based on calculations their model has shown that the anisotropy axes of the FM and AF should adopt a perpendicular configuration. In other models collinear alignment of FM and AF anisotropies were assumed.

4.2.5 Stiles and McMichael model

Recently Stiles and McMichael proposed a very comprehensive model on the exchange bias effect [28, 31, 32]. They pointed out that in order to explain some experimental results (for example non-vanishing rotational hysteresis even at high magnetic fields [1]) concerning EB effect, magnetic reversal within the AF layer has to be included. Based on this they built a model for *polycrystalline* EB systems. Under such a model the AF grains at the FM/AF interfaces have a net magnetization depending on the grain sizes, similar to the idea of the random field model. During the reversal of the FM layer, spins in the AF layers are dragged along by the FM, forming an AF domain wall within the grain. This is similar to the Mauri model, except that in the Stiles and Michael model this happens in each individual AF grain and that they are not interacting with one another.

As the FM layer is reversed, two possible events can happen in the AF grains. In some of the grains the AF can survive the reversal of the FM layer, provided that they are large enough to accommodate the AF wall within the grain, and that the spins at the FM/AF interface are twisted less than the ‘critical angle’ of the AF grain, which is related to the direction of the anisotropy axis of the AF layer. Otherwise the magnetization of the AF grain switches, losing the previous memory of the biasing states. Therefore only the former type of grains is responsible for the shifting of the hysteresis loops, since otherwise all the biasing information can be lost during the AF reversal process and no H_{ex} would be observed.

On the other hand, both types of the AF grains can contribute to the enhancement of H_c in the EB system. The grains that perform reversible switching contribute to the H_c increase by hindering the reversal of the FM layer, while AF grains that switch irreversibly increase the energy cost for switching the system and increases the H_c . At low temperature the former mechanism dominates,

since the possibility of AF irreversible losses is reduced as a result of the suppressed thermal activation. At higher temperature AF reversal becomes more important, and it is expected to be the strongest around T_N . Often in the EB systems the H_c exhibit a peak around the blocking temperature [33, 34]. Such phenomenon can be explained easily by the above arguments in the Stiles and McMichael model.

4.2.6 Models explaining enhanced coercivity in exchange bias structure

As mentioned in section 4.1.2, the $M(H)$ loop of an exchange biased system is usually accompanied by an enhanced H_c compared with that of a single FM layer. However, theories are less well developed concerning this effect. In the majority of the early models (MB model and Mauri model, for example), coherent rotation of the FM layer was invoked as the only switching mechanism of the bilayer structure. While this approach permitted the use of analytical solution [1] or simple numerical calculation [18] for the exchange bias effect, it definitely failed to model the reversal mechanism in actual systems. A number of studies on the reversal of exchange bias systems have shown its complexity. Magnetization reversal observation on FM/AF bilayers or repeated bilayers by transmission electron microscopy [35], neutron reflectometry [23], and studies on wedged FM layers [36] have shown signs of domain nucleation and propagation. Coherent magnetization models simply fail to explain all these effects.

One of the earliest models of enhanced H_c in exchange bias systems that is widely used today was due to Fulcomer and Charap [33]. They considered the case in which a FM layer was covered with non-interacting AF particles with a distribution of sizes, and both the FM and AF layers had anisotropy axes lying in the film plane. As a consequence of thermal fluctuation, these AF particles could be activated, with a probability of switching depending on their sizes and temperature. The idea is analogous to the superparamagnetism in ferromagnetic particles [37]. In the system of Fulcomer and Charap, large particles remained stable with the applied field cycles. Smaller particles, on the other hand, may have surface moments following the FM's magnetization and hence contribute to the hysteretic losses of the systems, hence leading to a H_c enhancement. The model has been extended to explain the temperature [38] and switching field rate dependence of exchange bias effects [39].

Again, the Fulcomer and Charap model was based on a single FM domain assumption, which could not explain the complex reversal behaviour in exchange bias system. Micromagnetic

simulations are now usually performed to address this issue by solving the micromagnetic Landau-Lifshitz equation [40]. This requires careful definition of the suitable interface and/or AF spin structures [32, 41, 42].

4.3 Comparison of models and experiments

The rush of research in exchange bias effect in the last two decades has led to a rich collection of experimental data in the literature. An effort is made here to compare the models introduced in the previous section with the experimental results.

4.3.1 Influence of individual layers

4.3.1.1 FM layer

- Thickness

One of the major areas of study in EB bilayer systems is the thickness of the layers, which are some of the parameters that permit rapid examination of the existing theories. The two variables associated with FM layers are the thickness t_{FM} and the value of saturation magnetization M_{FM} .

The basic theories of exchange bias [1, 15, 18] suggest that there is an inverse relationship between H_{ex} and t_{FM} . This has been verified by many of the experiments (an example is shown in Figure 4.7(a)). The major argument behind such effect is that the interfacial pinning effect is somehow ‘diluted’ when the ferromagnetic layer thickness has been increased.

- Saturation magnetization

Unlike the film thickness, it is relatively hard to adjust M_{FM} to compare the effect of saturation magnetization of the FM layer to H_{ex} simply by changing the FM materials, given that exchange bias effect is intricately linked to the combination of materials as well as the interface structures. From the simplest model (section 4.2.1) it is predicted that H_{ex} is inversely proportional to M_{FM} .

The only attempts of explicitly tackling this problem so far were by Parker *et. al* [43] and Zhou and Chien [44]. Parker *et. al.* deposited five different FM materials of a wide range of M_{FM} (from 512 emu/cm³ for Ni to 1745 emu/cm³ for Fe) on CoO. They found that the interfacial coupling energy ($J_{FM/AF} = H_{ex}M_{FM}t_{FM}$) was not constant but dropped with M_{FM} . The authors suggested that

this could be due to *direct* exchange between FM layer and Co ions at the interface (instead of superexchange via O^{2-} ions), or due to the different interfacial oxidation behaviour of FM layers.

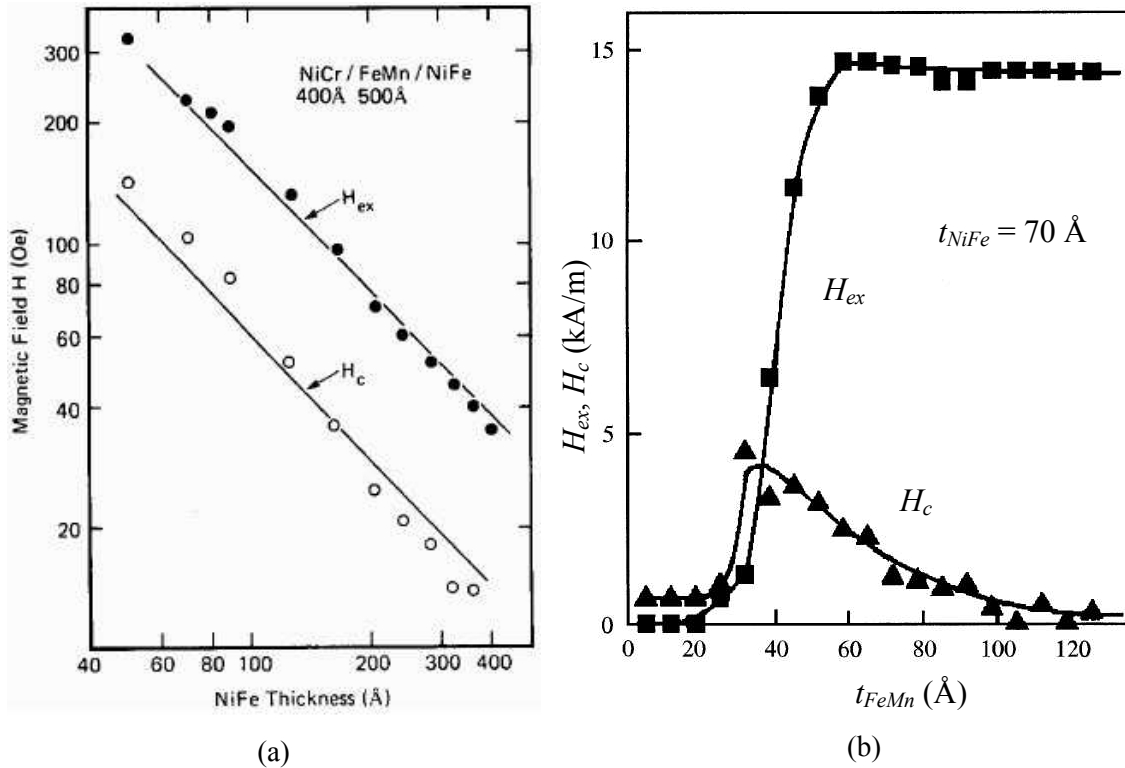


Figure 4.7 H_{ex} and H_c dependence of sputter deposited NiFe/FeMn system on t_{NiFe} (a) [27] and t_{FeMn} (b) [13] at RT. In (a) the solid lines show the $1/t_{NiFe}$ relation. The NiCr buffer is for stabilizing the antiferromagnetic FeMn. Note the units of magnetic field in (b) (kA/m, where $1kA/m \approx 80$ Oe).

On the other hand, Zhou and Chien obtained a variation of the M_{FM} value with a factor of two difference by depositing Co_xNi_{1-x} ($0.06 < x < 0.64$) onto 15 nm of FeMn. Their results showed a $(M_{FM})^{1/2}$ variation of $J_{FM/AF}$, in contrary with the common belief that $J_{FM/AF}$ is a constant. The authors attributed the effect to the local field strength from the FM layer that affected the AF spin structure. An attempt was made to fit such a $(M_{FM})^{1/2}$ dependence of $J_{FM/AF}$ into the results of Parker *et. al.*, but it failed to yield any convincing results.

4.3.1.2 AF layer

Figure 4.7(b) shows the effect of t_{AF} on H_{ex} and H_c in the (111) epitaxial NiFe/FeMn system, measured at RT [13]. The H_{ex} vs. t_{AF} behaviour can be divided into three regimes. At very low

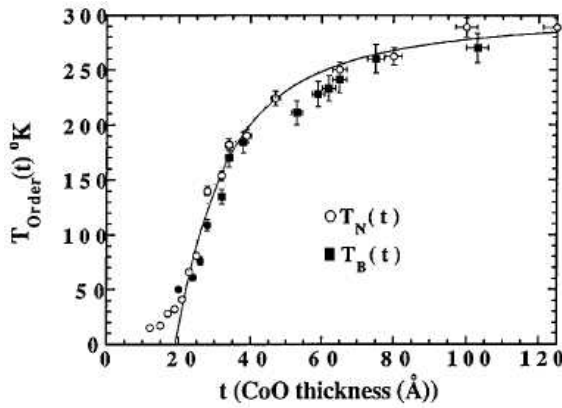
FeMn thickness ($t_{FeMn} < 20 \text{ \AA}$) no H_{ex} was observed. Starting from 20 \AA onwards, however, the H_{ex} values rose rapidly until about 60 \AA , beyond which H_{ex} show a plateau like behaviour or a slow drop, depending on the NiFe layer thickness [13]. The H_c variation can also be divided into three regimes. In the first regime ($0 < t_{FeMn} < 20 \text{ \AA}$), the coercive field is similar to that of a plain NiFe film. In the second regime H_c value rises until about the FeMn thickness of which the H_{ex} is half of the maximum it can be achieved, beyond which the H_c value drops slowly. It should be stressed that the behaviour mentioned above is quite general among exchange bias systems [6], and the example illustrated in the figure is typical, though the values of t_{crit} differs from one AF material to another.

The critical thickness, however, is a temperature dependent property [21, 45, 46]. It turns out that for every t_{AF} there is a characteristic temperature, called the blocking temperature (T_B), above which H_{ex} vanishes. At low t_{AF} the blocking temperature rises with the AF thickness, and at high t_{AF} values the blocking temperature is virtually identical to T_N [46]. It should be noted that the absence of H_{ex} does not imply the absence of exchange interaction between the FM and the AF layers. A plot of H_{ex} and H_c vs. T reveals a very interesting feature: H_c peaks as H_{ex} vanishes at T_B [33]. Such phenomenon usually happens at low values of t_{AF} . As t_{AF} increases the peak flattens out. An intuitive description of this effect is that the spins in the AF is ‘dragged’ by the FM layer, leading to the increase in H_c . The lower the volume anisotropy of AF layer (which is proportional to t_{AF}), the more easy the AF spins can be influenced by the FM layers and the more prominent the H_c peaking effect.

The blocking temperature itself is an interesting topic. It has been suggested [47] that the finite size effect of the AF layer is responsible for the blocking temperature of the exchange bias effect. The finite thickness of the AF layer reduces its effective Néel temperature. In fact, the relation between T_B and T_N are so close to each other [48] that they were thought to be identical by some literature (Figure 4.8). However, it has been pointed out by van der Zaag *et. al.* [49] that T_N of the AF layer, *in close proximity with the FM layer*, can in fact be increased, showing that the drop in T_N is not the cause of thickness dependence of T_B (Figure 4.9). No conclusion can be drawn on this topic so far, and further examinations await to resolve the issue.

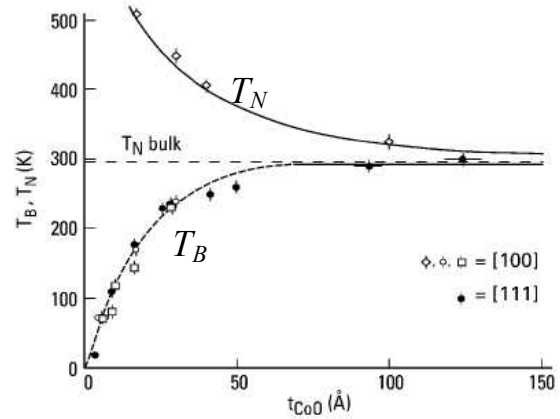
4.3.1.3 FM/AF interfaces

Antiferromagnetic crystals have a long-range spin arrangements in such a way that they cancel out each other in the bulk form. In the case of fcc FeMn for example (which is used in this project for the study of exchange bias as well as spin valve deposition (Chapter 6)), first principle calculations [50] and experiments [51-53] showed that the spins of individual atoms align in the so-called ‘3Q’ state, in which the spins are all pointing along the [111] directions, cancelling each other as a whole (Figure 4.10). Across the surface of some planes (such as (111)) there is a net cancellation of spins, resulting in a compensated surface. The (110) planes, on the other hand, have a totally uncompensated interface. However, it has been clearly shown [13] that exchange bias could occur in both of compensated and uncompensated FeMn systems when FeMn/NiFe bilayers were deposited. It could be that the interfacial roughness can introduce uncompensated spins on the (111) surfaces that had led to the EB effect, or that the AF layer interfacial spin structure is actually highly modified from the bulk state.



(a)

Figure 4.8 Blocking temperature (T_B) and Néel temperature (T_N) dependence on CoO thickness [48]. T_B was obtained from magnetic susceptibility measurements of $(\text{CoO} (t \text{ \AA})/\text{SiO}_2 (50 \text{ \AA}))_{100}$ repeated bilayers, while T_N was measured from NiFe (300 \AA)/CoO ($t \text{ \AA}$)/Cu (300 \AA) samples.



(b)

Figure 4.9 T_N and T_B dependence of $\text{Fe}_3\text{O}_4/\text{CoO}$ system [49]. \diamond indicates T_N (measured by neutron diffraction) and the other symbols represent T_B (obtained from SQUID measurements). Divergence of T_N and T_B is evident at low CoO thicknesses.

4.3.2 Effect of T_C and T_N

So far most of the exchange bias experiments reported in literature have concentrated on systems with $T_C \gg T_N$. The trend is understandable, given that most of the technically important FM materials (mainly $3d$ transition metals Ni, Fe, Co, together with their alloys and compounds) have T_C (above 600 K) typically above T_N of all the AF materials (Table 4.1). It is, however, of great physical interest in knowing what would occur in the case $T_C < T_N$. Since EB theories developed so far discussed only cases in which $T_C \gg T_N$, they may not be applicable in the regime of $T_C < T_N$. Some major modifications of existing models may be needed to adapt to the situation. Besides, a thorough study of such system may provide some further insight in the possible microscopic mechanism of the exchange bias phenomena.

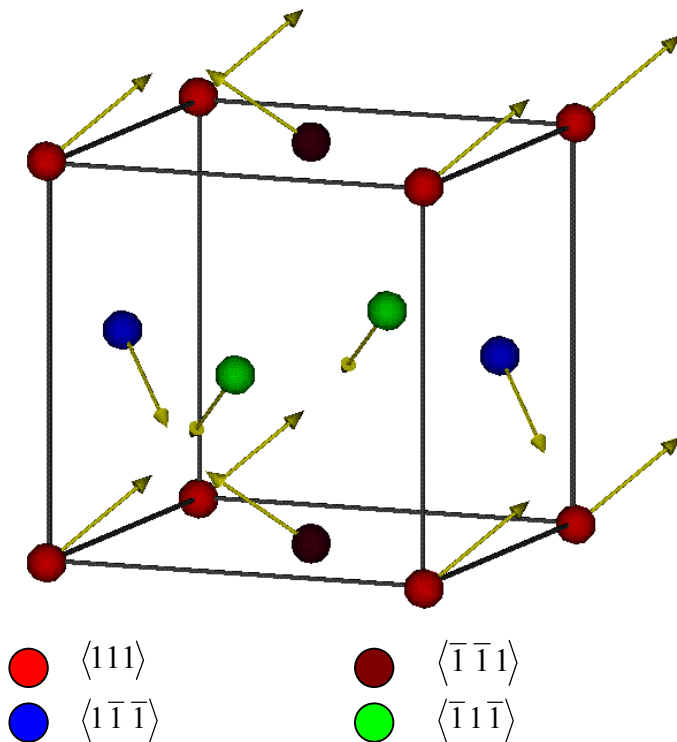


Figure 4.10 '3Q' nonlinear spin configuration in fcc FeMn [50]. Spins at different lattice points are pointing at directions as indicated in the legend.

Some of the pioneering works in this aspect have been done by Chien and co-workers. They used amorphous alloys of Ni, Fe and B to tune the T_C close to [5] or far below [4] the T_N of CoO (291 K). By field cooling the samples, they found in both cases exchange bias occurred once the temperature dropped below T_N , regardless of the magnetic state of the FM layer. The behaviour can be directly visualized from the shifted magnetization curve of the paramagnet, with the absence of H_c (Figure 4.11). The authors suggested that such phenomenon could be understood as that the (uncompensated) AF spins gave rise to an effective magnetic field, which shifted the

paramagnet from the zero bias direction. The study in this field is far less comprehensive as that of $T_C \gg T_N$ systems, and is yet another area of research interest.

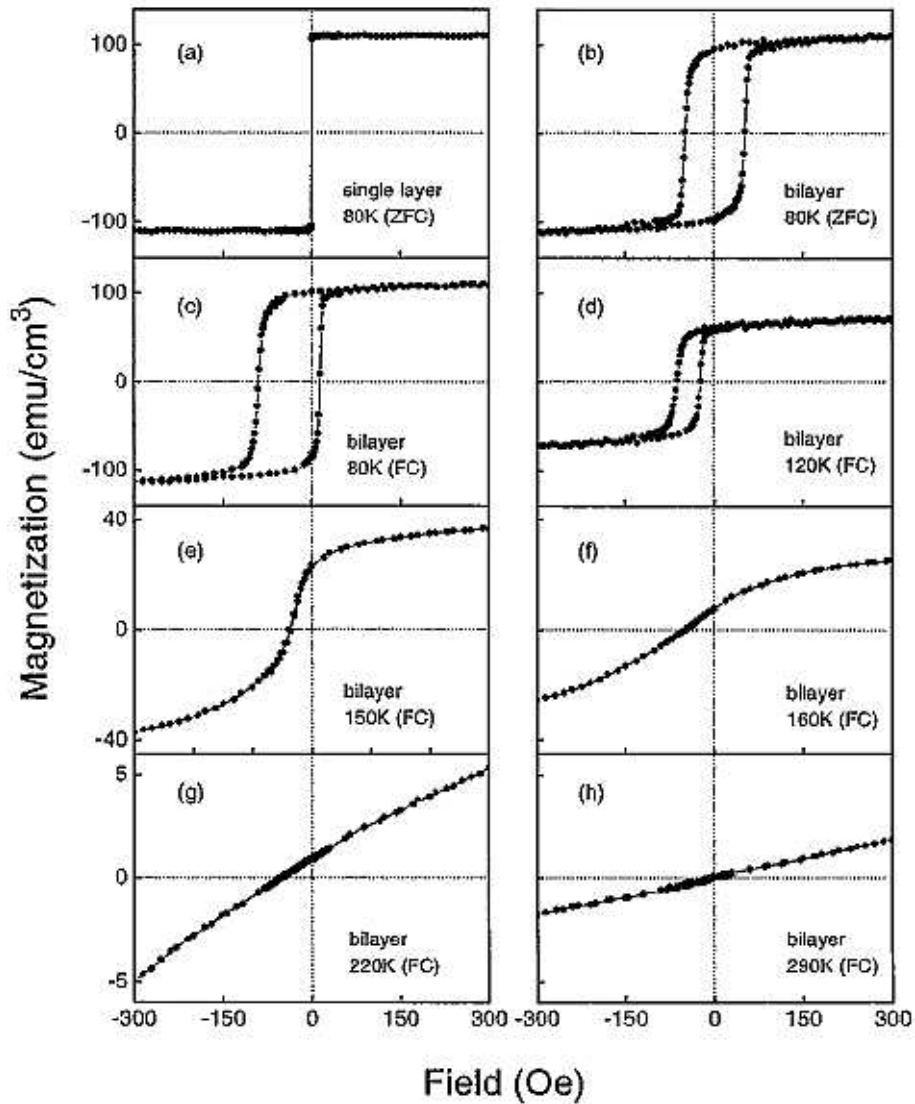


Figure 4.11 Hysteresis loops of α - $\text{Fe}_4\text{Ni}_{76}\text{B}_{20}/\text{FeMn}$ bilayer system [4]. Except (a) (a single layer of the FeNiB alloy) and (b) (a bilayer sample zero field cooled (ZFC) from RT to 80 K), all samples were 10 kOe field cooled (FC) to temperatures shown in the corresponding figures. Note the scales of y-axes.

4.3.3 AF spin structure

- AF spin axis direction

As we have seen from the theoretical considerations above, there are two major beliefs on the direction of the AF spin axis direction. The earlier models (the original MB model, random field model and the Mauri model) presumed collinear spin axes between FM and AF layers, whereas the spin flop model suggested perpendicular alignment was preferred in such systems. Both models have found experimental supporting evidences. For example, perpendicular coupling has been observed in $\text{Fe}_3\text{O}_4/\text{CoO}$ [54] and Fe/FeF_2 systems [55], while collinear spins have been observed in Co/FeMn [56] and Co/NiO and Fe/NiO systems [57]. No particular trend or tendency can be seen to determine which systems would show parallel or perpendicular alignment.

- Compensated/ Uncompensated interfaces?

It is generally agreed that there is somehow an uncompensated interface existing at the FM/AF interface. The most striking demonstration can be seen in the work by Takano *et. al.* [58] They performed thermo-remnant magnetization (TRM) measurement on CoO/MgO repeated bilayers (which involved the measurement of the remanent magnetization of the sample, after field cooling from above the measurement temperature). Their experiment revealed two effects. The shape of the TRM vs. temperature was the same for various t_{CoO} values, revealing the interfacial nature of the measured magnetic moment. The measured moment, compared with the magnetic moment of Co^{2+} ions in CoO , scales to $\sim 1\%$ that of an uncompensated monolayer. This result matched perfectly with the ‘order of two’ problem encountered by the totally uncompensated AF interface spin analysis.

The origin of the uncompensated AF interface spins, however, is not completely understood. The most typical arguments over this is that the uncompensated spins results from the interfacial roughness [58] or defects [30]. These arguments are not particularly convincing, given that similar exchange bias results can be obtained from compensated and uncompensated surfaces. [13]. This would imply that similar quantity of uncompensated spins have to be yielded from these surfaces due to the interfacial imperfection.

To this end the field cooling (or *in situ* field deposition) procedure may have to be invoked to address the issue. In fact Zhu *et. al.* [59] have found that when the CoFe/NiO system was field cooled from above T_B , a repopulation of Ni spins at the interface occurred. These spins tended to

align along the field cooling direction, supporting the uncompensated spin model. This change, according to the authors, was accomplished by the repopulation of NiO domains, in particular those with magnetic axes close to the cooling field direction.

The above discussion is based on the assumption that there is an abrupt transition from FM to AF layer across the interface. As seen in Chapter 2, this is not true in reality. Interfacial mixing can be significant in samples prepared by sputtering for example. In that case, uncompensated spin arises due to chemical modulation. By means of polarization dependent x-ray spectroscopy and microscopy Ohldag *et. al.* [57] detected uncompensated spin at the NiO/Co interface. Certainly interfacial roughness and intermixed interface can co-exist to give rise to the exchange bias effect.

4.4 Summary

Table 4.2 summarizes the EB theories introduced in this chapter. The study of the EB effect is a fast growing area. The existing theories are not general enough to cover all the aspects of the exchange bias effect in any systems. New experiments have to be performed to investigate this phenomenon in greater details.

	Meiklejohn-Bean (MB) model (4.2.1)	Random Field model (4.2.2)	Mauri model (4.2.3)	Spin-flop model (4.2.4)	Stiles and McMichael model (4.2.5)
M_{AF} distribution	Homogenous, totally uncompensated interface	Spatial (interfacial) variation, partially uncompensated interface	Isotropic in plane; totally uncompensated interface	Frustrated interface, compensated interface,	Spatial (interfacial) variation, partially uncompensated interface
M_{AF} spin structures	In-plane, globally rigid structure	AF domain wall formation; rigid structure within domains	Bloch AF wall formation	Heisenberg spin (3D variation)	Bloch AF wall; Uniaxial AF spins with 3D anisotropy axes
K_{FM} and K_{AF} relations	$K_{FM} // K_{AF}$	$K_{FM} // K_{AF}$	$K_{FM} // K_{AF}$	$K_{FM} \perp K_{AF}$	Not specified
H_{ex}	$\frac{J_{FN/AF}}{M_{FM} t_{FM}}; 2$ orders of magnitude too large	$\frac{2z\sqrt{A_{AF}K_{AF}}}{\pi^2 M_{FM} t_{FM}}$; reasonable estimates	No simple relations, but <i>bounded</i> by $\frac{2\sqrt{A_{AF}K_{AF}}}{M_{FM} t_{FM}}$; reasonable estimates	No simple relations, results from micromagnetic simulations.	No simple relations, results from micromagnetic simulations.
Comments	Simple model but incorrect estimation of the strength	Realistic interfacial spin structure, but depends on AF microstructure	Unrealistic interface spin, domain wall formation depends on system	Depends on interface defect density; applicability depends on system	Only apply in polycrystalline samples

Table 4.2 Major exchange bias theories. Adopted from [12].

References for Chapter 4

1. W.H. Meiklejohn and C.P. Bean, *Phys. Rev.* **105**, 904-913 (1957).
2. J. Nogués and I.K. Schuller, *J. Magn. Magn. Mater.* **192**, 203-232 (1999).
3. H. Matsuyama, C. Haginoya and K. Koike, *Phys. Rev. Lett.* **85**, 646-649 (2000).
4. J.W. Cai, K. Liu and C.L. Chien, *Phys. Rev. B* **60**, 72-75 (1999).
5. X.W. Wu and C.L. Chien, *Phys. Rev. Lett.* **81**, 2795-2798 (1998).
6. J. Nogués, D. Lederman, T.J. Moran and I.K. Schuller, *Phys. Rev. Lett.* **76**, 4624-4627 (1996).
7. H. Fujiwara, K.L. Zhang, T. Kai and T. Zhao, *J. Magn. Magn. Mater.* **235**, 319-328 (2001).
8. N.J. Gokemeijer, J.W. Cai and C.L. Chien, *Phys. Rev. B* **60**, 3033-3036 (1999).
9. P. Miltényi, M. Gierlings, M. Bammig, U. May, G. Guntherodt, J. Nogués, M. Gruyters, C. Leighton and I.K. Schuller, *Appl. Phys. Lett.* **75**, 2304-2306 (1999).
10. A.E. Berkowitz and K. Takano, *J. Magn. Magn. Mater.* **200**, 552-570 (1999).
11. R.L. Stamps, *J. Phys. D: Appl. Phys.* **33**, R247-R268 (2000).
12. M. Kiwi, *J. Magn. Magn. Mater.* **234**, 584-595 (2001).
13. R. Jungblut, R. Coehoorn, M.T. Johnson, J.A. Destegge and A. Reinders, *J. Appl. Phys.* **75**, 6659-6664 (1994).
14. D. Jiles, *Introduction to magnetism and magnetic materials*, p 94, Chapman & Hall (1997).
15. A.P. Malozemoff, *Phys. Rev. B* **35**, 3679-3682 (1987).
16. A.P. Malozemoff, *J. Appl. Phys.* **63**, 3874-3879 (1988).
17. A.P. Malozemoff, *Phys. Rev. B* **37**, 7673-7679 (1988).
18. D. Mauri, H.C. Siegmann, P.S. Bagus and E. Kay, *J. Appl. Phys.* **62**, 3047-3049 (1987).
19. C. Tsang, N. Heiman and K. Lee, *J. Appl. Phys.* **52**, 2471-2473 (1981).
20. M. Takahashi, M. Tsunoda and K. Uneyama, *J. Magn. Magn. Mater.* **209**, 65-70 (2000).
21. J. van Driel, F.R. de Boer, K.M.H. Lenssen and R. Coehoorn, *J. Appl. Phys.* **88**, 975-982 (2000).
22. C. Leighton, M. Song, J. Nogués, M.C. Cyrille and I.K. Schuller, *J. Appl. Phys.* **88**, 344-347 (2000).
23. M.R. Fitzsimmons, P. Yashar, C. Leighton, I.K. Schuller, J. Nogués, C.F. Majkrzak and J.A. Dura, *Phys. Rev. Lett.* **84**, 3986-3989 (2000).
24. P. Steadman, M. Ali, A.T. Hindmarch, C.H. Marrows, B.J. Hickey, S. Langridge, R.M. Dalgliesh and S. Foster, *Phys. Rev. Lett.* **89**, art. no.-077201 (2002).
25. J.C. Slonczewski, *J. Magn. Magn. Mater.* **150**, 13-24 (1995).
26. H.W. Xi and R.M. White, *Phys. Rev. B* **62**, 3933-3940 (2000).
27. D. Mauri, E. Kay, D. Scholl and J.K. Howard, *J. Appl. Phys.* **62**, 2929-2932 (1987).
28. M.D. Stiles and R.D. McMichael, *Phys. Rev. B* **59**, 3722-3733 (1999).
29. N.C. Koon, *Phys. Rev. Lett.* **78**, 4865-4868 (1997).
30. T.C. Schulthess and W.H. Butler, *Phys. Rev. Lett.* **81**, 4516-4519 (1998).
31. M.D. Stiles and R.D. McMichael, *Phys. Rev. B* **60**, 12950-12956 (1999).
32. M.D. Stiles and R.D. McMichael, *Phys. Rev. B* **63**, 4405-+ (2001).
33. E. Fulcomer and S.H. Charap, *J. Appl. Phys.* **43**, 4190-4199 (1972).
34. C. Leighton, M.R. Fitzsimmons, A. Hoffmann, J. Dura, C.F. Majkrzak, M.S. Lund and I.K. Schuller, *Phys. Rev. B* **65**, art. no.-064403 (2002).
35. J.P. King, J.N. Chapman, M.F. Gillies and J.C.S. Kools, *J. Phys. D: Appl. Phys.* **34**, 528-538 (2001).
36. V.I. Nikitenko, V.S. Gornakov, A.J. Shapiro, R.D. Shull, K. Liu, S.M. Zhou and C.L. Chien, *Phys. Rev. Lett.* **84**, 765-768 (2000).

37. B.D. Cullity, *Introduction to magnetic materials*, in *Addison-Wesley series in metallurgy and materials*, pp. 410-418, Addison-Wesley Pub. Co (1972).
38. K. Nishioka, C.H. Hou, H. Fujiwara and R.D. Metzger, *J. Appl. Phys.* **80**, 4528-4533 (1996).
39. J. Camarero, Y. Pennec, M. Bonfim, J. Vogel, S. Pizzini, A. Fontaine, M. Cartier, F. Fettar and B. Dieny, *J. Appl. Phys.* **89**, 6585-6587 (2001).
40. L.D. Landau and E.M. Lifshitz, *Phys. Z. Sowjetunion* **8**, 153-169 (1935).
41. Z.J. Li and S.F. Zhang, *Appl. Phys. Lett.* **77**, 423-425 (2000).
42. Z.J. Li and S.F. Zhang, *Phys. Rev. B* **61**, R14897-R14900 (2000).
43. F.T. Parker, K. Takano and A.E. Berkowitz, *Phys. Rev. B* **61**, R866-R869 (2000).
44. S.M. Zhou and C.L. Chien, *Phys. Rev. B* **63**, 4406-+ (2001).
45. O. Allegranza and M.M. Chen, *J. Appl. Phys.* **73**, 6218-6222 (1993).
46. A.J. Devasahayam and M.H. Kryder, *IEEE Trans. Magn.* **35**, 649-654 (1999).
47. T. Ambrose and C.L. Chien, *Phys. Rev. Lett.* **76**, 1743-1746 (1996).
48. T. Ambrose and C.L. Chien, *J. Appl. Phys.* **83**, 6822-6824 (1998).
49. P.J. van der Zaag, Y. Ijiri, J.A. Borchers, L.F. Feiner, R.M. Wolf, J.M. Gaines, R.W. Erwin and M.A. Verheijen, *Phys. Rev. Lett.* **84**, 6102-6105 (2000).
50. T.C. Schulthess, W.H. Butler, G.M. Stocks, S. Maat and G.J. Mankey, *J. Appl. Phys.* **85**, 4842-4844 (1999).
51. H. Umeybayashi and Y. Ishikawa, *J. Phys. Soc. Jpn.* **21**, 1281-1294 (1966).
52. S.J. Kennedy and T.J. Hicks, *J. Phys. F: Met. Phys.* **17**, 1599-1604 (1987).
53. J.S. Kouvel and J.S. Kasper, *J. Phys. Chem. Solids* **24**, 529-536 (1963).
54. Y. Ijiri, J.A. Borchers, R.W. Erwin, S.H. Lee, P.J. van der Zaag and R.M. Wolf, *Phys. Rev. Lett.* **80**, 608-611 (1998).
55. T.J. Moran, J. Nogues, D. Lederman and I.K. Schuller, *Appl. Phys. Lett.* **72**, 617-619 (1998).
56. W.J. Antel, F. Perjeru and G.R. Harp, *Phys. Rev. Lett.* **83**, 1439-1442 (1999).
57. H. Ohldag, T.J. Regan, J. Stohr, A. Scholl, F. Nolting, J. Luning, C. Stamm, S. Anders and R.L. White, *Phys. Rev. Lett.* **87**, 7201-+ (2001).
58. K. Takano, R.H. Kodama, A.E. Berkowitz, W. Cao and G. Thomas, *Phys. Rev. Lett.* **79**, 1130-1133 (1997).
59. W. Zhu, L. Seve, R. Sears, B. Sinkovic and S.S.P. Parkin, *Phys. Rev. Lett.* **86**, 5389-5392 (2001).

Chapter 5 Experiments on Exchange Bias Systems

This chapter summarizes the experimental results obtained from the investigation of EB systems. In particular, the NiFe/FeMn/Co trilayer system is studied. Samples were deposited under special field conditions that permitted the study of potential coupling effects between FM layers across the FeMn layer. It is hoped that the study could provide some insight on the mechanism of the EB effect.

5.1 Introduction

It can be seen from the last chapter that a lot of the EB studies are made on bilayer (FM/AF or AF/FM) systems. While most of such studies concentrated on the effect of coupling at FM/AF interfaces, many of the models (such as the Mauri or random field models) did suggest the importance of the *bulk* of the AF in connection with the observed results. Both of the models mentioned above, for example, suggested that domain walls in the AF have to be invoked to account for the reduced H_{ex} compared with the ideal MB model (section 4.2), although different mechanisms of wall formation were involved in the two models.

There are also experimental efforts to investigate the effect of the bulk AF properties in relation to the EB effect. A noted example was due to the studies of Co/CoO by Miltényi *et. al.* [1]. They doped the bulk of CoO with non-magnetic impurities (either with Mg or oxygen deficiencies), and have observed an increase of H_{ex} up to a factor 3 compared with the undoped samples. They attributed the effect to the formation of domains within the AF by such impurities, since the dopants act as additional sources of imbalance for the sublattice magnetization. According to Miltényi *et. al.*, such domains can affect the spin structure at the *interface*, leading to a rise in the H_{ex} .

Another route of investigating the bulk effect of the AF is by depositing FM/AF/FM trilayers. Interesting effects could be possible in the EB structure in the vicinity of another FM layer across the AF spacer. Some studies have been made on such trilayers [2-6]. In many of the reports, biquadratic coupling have been found between the FM layers, and in all these cases the authors have attributed the effect to the roughness of the interfaces.

Yang and Chien [6], on the other hand, had some more exciting findings in the structure NiFe/FeMn (t_{FeMn})/Co. By cooling the samples in a field in between the H_c of NiFe and Co from above the T_{N-FeMn} to RT, they found that the EB direction of the NiFe layer was not necessarily along the field-cooling axis. As shown in Figure 5.1, the angular difference of the EB directions between the FM layers ($\alpha_{1,2}$) was found to be a linear function of t_{FeMn} , starting from 90° for $t_{FeMn} \sim 5$ nm (which is about t_{cr}) to 180° from $t_{FeMn} = 10$ nm onwards. The striking resemblance of the result with the Mauri model was apparent.

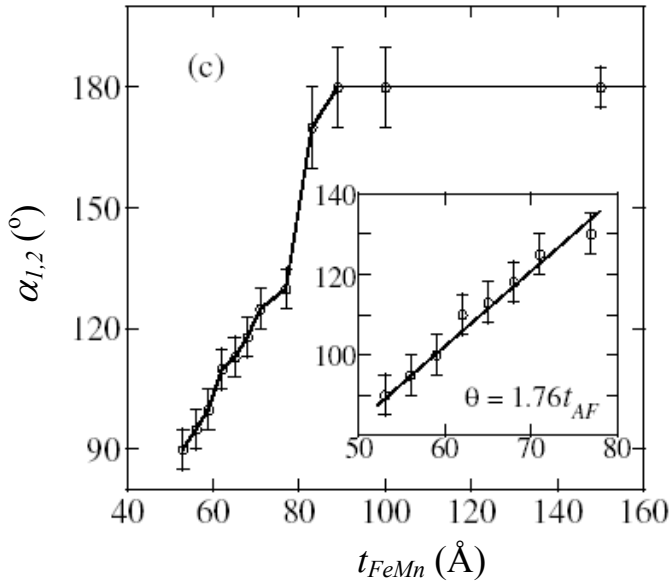


Figure 5.1 t_{AF} dependence of the relative EB directions between NiFe and Co layers in NiFe (200 Å)/FeMn (t_{AF})/Co (100 Å) structure ($\alpha_{1,2}$), after cooling from 400 K to RT in a field between H_{c-Co} and H_{c-NiFe} . After [6].

The major query of the results by Yang and Chien was whether the wall was induced due to the field treatment or if it was formed naturally within the AF layer. If the spirals were formed as the mechanism of EB in the FM/AF systems, the relative orientation of the NiFe and Co layers would imply that the NiFe layer was actually acting as a probe for the AF domain structure. This is an amazing fact, given that the AF could then be studied easily in common laboratory set-up instead of resorting to complicated techniques such as neutron or synchrotron sources.

In light of these, experiments were designed to test the same NiFe/FeMn/Co trilayer structure under a different magnetic treatment process. The samples were deposited in a magnetic field that was enough to saturate the NiFe but not the Co layers. While the NiFe layers were biased, the effect on the Co layer was not known. Besides, the coupling effect between the NiFe and the Co layer was not certain. The objectives of these experiments were to provide a special field deposition environment in order to investigate the potential biasing of the Co layer through an

established biasing system on the other side of FeMn layers, and to gain some further insight on the mechanism of EB effect.

5.2 Experiment procedures

A standard structure of Nb (5 nm)/NiFe (4 nm)/FeMn (t_{FeMn} nm)/Co (2 nm)/Nb (5 nm) was used for the investigation. Nb layers served as the buffer and capping layers. For comparison some basic structures such as single FM layers of NiFe and Co, FM/FeMn and FeMn/FM bilayers were deposited, using Cu to replace some of the layers whenever necessary. Specific experimental procedures applied in this part of the project are listed below.

5.2.1 *In situ* deposition field control

Central in the design of the experiment was the deposition of the structures in a suitable field condition, such that only the NiFe layer was saturated. This was circumvented by controlling the magnetic stray field from the chamber (Figure 5.2). As measured by a Hall effect probe, the field within the chamber was found to be dominating along the sample rod direction (~ 15 Oe), and such field was enough to saturate both NiFe and Co during the deposition process. On the other hand, with the permalloy washer and ring sitting on the sample holder, the field strength in the middle of the assembly was found to be ~ 5 Oe along the sample rod direction. The effect of using such field shielding assembly is assessed in the results section.

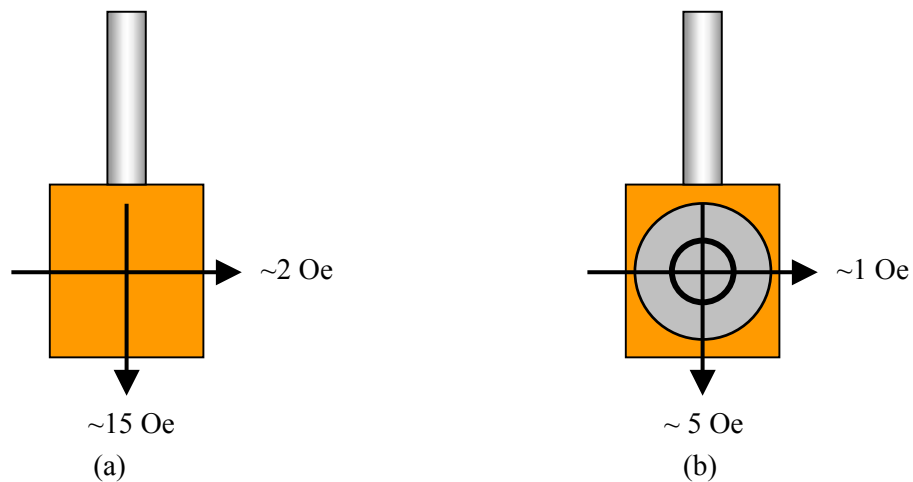


Figure 5.2 Magnetic stray field strength as measured by a Hall effect probe (a) without field shielding; and (b) with shielding by means of a permalloy ring and washer assembly.

5.2.2 Temperature dependent $M(H)$ measurements

As discussed in the previous chapter, the EB effect is highly dependent on the magnetic history of the sample. In the case of temperature dependent $M(H)$ measurements the memory effect is of particular concern. Given that some of the layers were deposited in a field-shielded condition, it is important that the samples have to be magnetically undisturbed before any measurements.

Samples taken out from the chamber were zero-field cooled (ZFC) directly to the lowest measurement temperature (~ 20 K) in the VSM without any magnetic disturbances. Hysteresis loops were then taken, usually after 10 cycles between ± 2 kOe field (~ 15 sec per cycle) before a loop was taken. The procedure was necessary to eliminate the possible training effects. The problem associated with the memory effect, on the other hand, was minimized by only measuring loops with increasing temperatures.

Field-cooling (FC) of the samples was also performed by heating up to 460 K in a He-rich environment before a 1 kOe field was turned on. The sample was then cooled down to ~ 20 K, from which measurements started, using the same procedures as employed in the ZFC measurements (measuring with ascending temperatures, training loops prior to measurements).

5.3 *Experimental results*

5.3.1 Single FM layers

Figure 5.3 shows the results of H_c vs. T for single FM layer samples, measured along their easy axis. H_{c-NiFe} was about 1 Oe at RT, and remained very small even at low temperature (~ 4 Oe at 35 K). H_{c-Co} of both samples, on the other hand, were higher than 5 Oe at RT (9 Oe in sample without Cu buffer, and 28 Oe in Cu-buffered samples, respectively). In such a case it can be expected that the NiFe layers are saturated during the deposition but not the Co layer, even if the samples were cooled to -100 °C (173 K). The use of thick Cu buffer (which acted as the dummy to replace the NiFe and FeMn layers) increased the H_c value at the temperature range accessible within this work ($\sim 20 - 460$ K). Nevertheless, all the data could be fitted excellently by a model by Gaunt [7]. Under this model, H_c was postulated to arise from domain wall pinning by inhomogeneities within the FM. The trapped walls bow out from the pinning sites until the field is strong enough to release them. Thermal activation assists the escape of domain walls and hence

leads to a drop in H_c . The model suggested that $H_c^{3/7}$ varied linearly with $T^{2/3}$. The difference of H_{c-Co} between two Co samples can be attributed to their differences in the density of pinning sites.

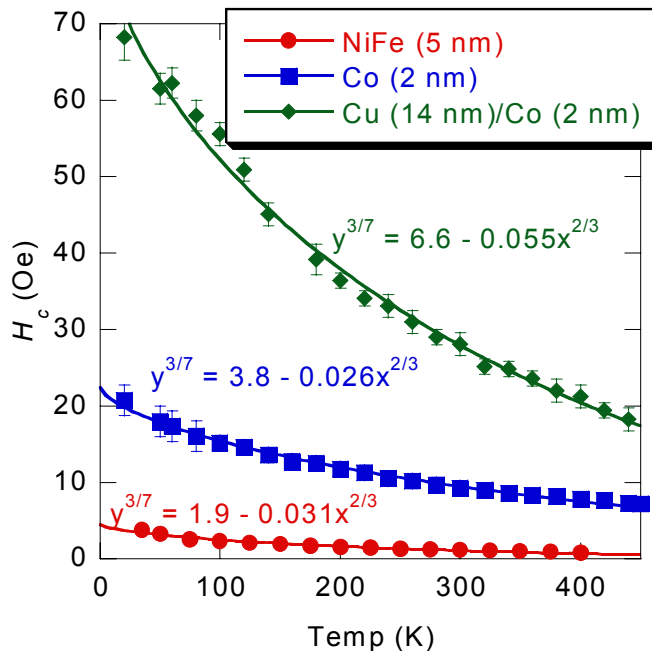


Figure 5.3 Temperature dependence of H_c of NiFe (5 nm) and 2 nm-thick Co layers, deposited directly on Nb (5 nm) or buffered by thick (14 nm) Cu. The Cu layer replaces the otherwise NiFe/FeMn layers. Solid lines are fits based on the model by Gaunt [7].

5.3.2 FM/FeMn bilayers

The effect of field shielding can be observed directly from the magnetic behaviour of the FM/FeMn bilayers so deposited. For the NiFe/FeMn bilayer structure (Figure 5.4(a)), a biasing behaviour was observed along the sample rod direction, when field shielding was provided by the permalloy washer and ring assembly. This indicated that the NiFe layer was saturated along this direction before the FeMn layer was deposited on top of it. In the following discussions in this chapter the angle between the *in situ* stray field (sample rod) direction and the VSM measurement field direction is assigned as θ .

On the other hand, interesting behaviour can be seen in the Co/FeMn bilayers deposited in different field conditions (Figure 5.4(b)). When deposited without field shielding, the Co layer was saturated, thus the bilayer gave a single biased hysteresis loop. In case the bilayer was deposited with field shielding, two hysteresis loops could be seen, with very similar biasing fields but in opposite directions of H . The *in situ* field, which was insufficient to saturate the Co layer, still induced a uniaxial anisotropy in the Co film (section 1.2). A uniaxial domain structure was

formed in this case. Such domain structure was ‘frozen’ upon the deposition of the FeMn layer, giving rise to two hysteresis loops in opposite directions. Both the H_{ex} (~ 350 Oe) and H_c (45-50 Oe) of the two loops were close to one another, indicating that similar biasing conditions (at least locally) were present in these two samples.

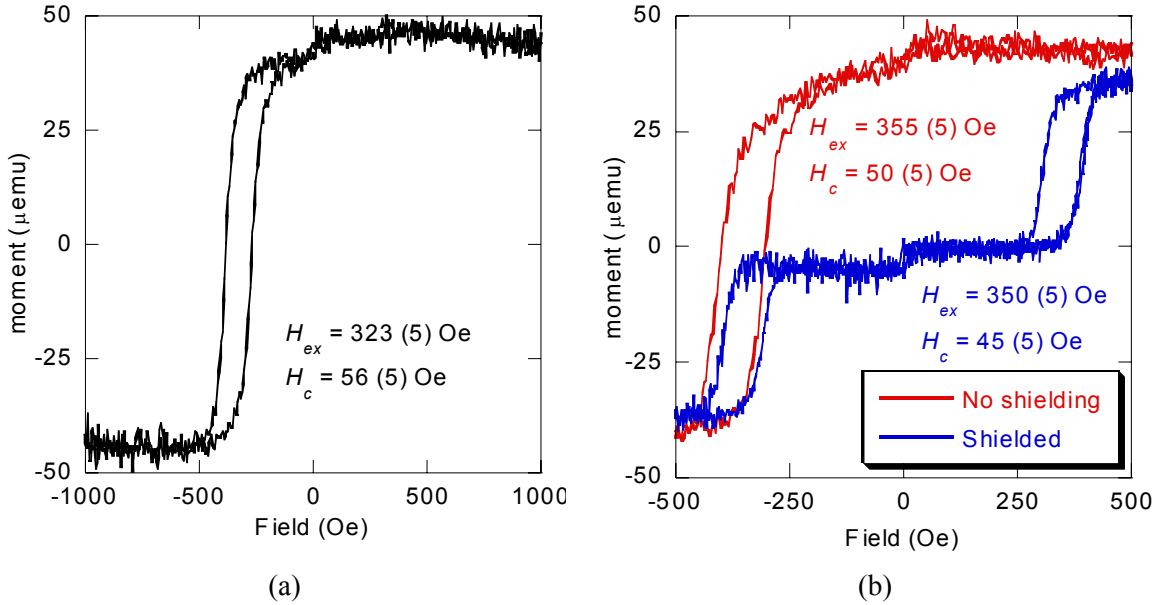


Figure 5.4 $M(H)$ loops of (a) NiFe (4 nm)/FeMn (10 nm) deposited with shielding and (b) Co (2 nm)/FeMn (10 nm) deposited with and without shielding (b). All measurements were made along the direction of the sample rod ($\theta = 0^\circ$).

5.3.3 FeMn/FM bilayers

Apart from FM/FeMn bilayers shown in Figure 5.4, FeMn/FM bilayers were also deposited. The results were rather different from the FM/FeMn results (Figure 5.5). While it is easy to induce exchange anisotropy by depositing bilayers in the sequence of FM/FeMn, it is in general more difficult to induce bias in FeMn/FM structures by simply depositing them in an *in situ* field. For example, thick Cu buffer layer (100 nm) was used to induce H_{ex} in FeMn/NiFe bilayers [8]. In this study the thin Cu buffer (4 nm) mainly served the purpose of replacing the bottom NiFe layers in the otherwise trilayer structure.

As seen from the $M(H)$ loops of FeMn/Co and FeMn/NiFe samples shown in Figure 5.5, no H_{ex} could be observed, at least at RT. Some evidence could be found from the $M(H)$ loops of the FeMn/NiFe sample (Figure 5.5(b)), which shows the $M(H)$ loops of the sample together with the

initial magnetization curve at various θ values. The loop of $\theta = 0^\circ$ was the virgin loop of the sample, which started at ~ 0 emu with $H = 0$ Oe. Magnetization would have started at some non-zero value at $H = 0$ Oe were the structure biased at the beginning of the experiment.

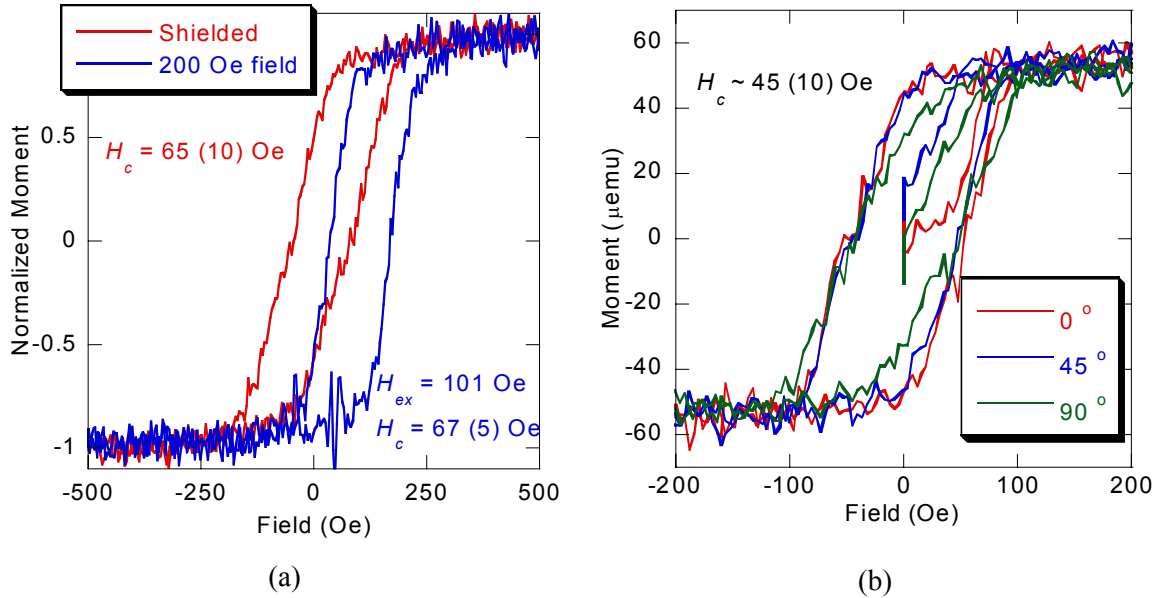


Figure 5.5 (a) $M(H)$ loops of Cu (4 nm)/FeMn (10 nm)/Co (2 nm) deposited at different field conditions. (b) Angular hysteresis loops of Cu (4 nm)/FeMn (10 nm)/NiFe (4 nm), deposited with field shielding. Legends indicate the θ values. All measurements were made at RT. Note that the loops in (b) are not recorded after training (In particular, the loop of $\theta = 0^\circ$ is a virgin loop). H_c values dropped after training, but were within the errors of the first loops.

Similar to the FM/FeMn bilayers deposited with field shielding, H_c of the FM layers in the FeMn/FM samples deposited with field-shielding were much enhanced from that of the corresponding single FM layer samples (Figure 5.3). The FeMn layer must have taken part in the enhancement, although it does not necessarily give rise to the H_{ex} .

There are some differences between the H_c values of the shielded FeMn/FM samples and that of shielded FM/FeMn bilayers (Co H_c increased from about 50 to 65 Oe, while that of NiFe dropped from 56 to 45 Oe) (Figure 5.4). A number of explanations are possible for the scenario. As seen from the single Co layer deposited on different buffer layers, thick buffer layers seem to increase the coercivity of the FM layers. On the other hand, the FM layers can be *locally* exchange coupled to the FeMn layer along any random direction. It is known that in EB structures, H_c drops

with the angle away from the biasing direction [9]. The hysteresis loop of the FeMn/FM bilayers, which is the resultant of all these local (but interacting) EB systems, should have an H_c smaller than that of a properly biased system (NiFe/FeMn in Figure 5.4(a), for example) measured along the biasing direction. Competition between such mechanisms could lead to the final H_c difference between the FM/AF and AF/FM structure.

5.3.4 NiFe/FeMn/Co trilayer

A study has been performed on a sample of structure NiFe (4 nm)/FeMn (8 nm)/Co (2 nm). Figure 5.6(a) shows the RT magnetization curve of the sample. Two loops can be seen from the curve. The upper, biased loop corresponds to the signal from the NiFe/FeMn structure, and the lower loop represents the FeMn/Co part. While the NiFe layer was shifted from the zero field axis, this did not seem to be the case for the Co layer. No signs of H_{ex-Co} could be observed down to 20 K. Angular measurements of samples were performed to check if the sample was biased at angles other than $\theta = 0^\circ$. Figure 5.6(b) shows the results for angular measurements at 100 K. While it was difficult to separate the NiFe and Co layers in some cases, no clear sign of loop shifting could be seen for the Co layer.

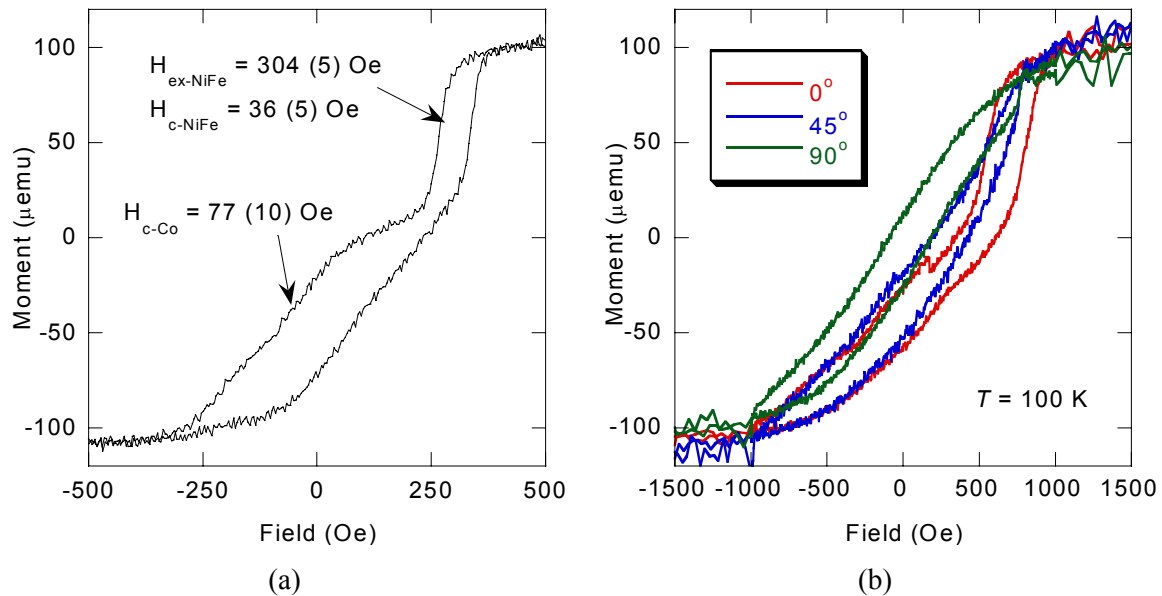


Figure 5.6 Hysteresis loops of NiFe (4 nm)/FeMn (8 nm)/Co (2 nm) sample, measured at RT with $\theta = 0^\circ$ (a) and at 100 K with different orientations (b).

The $M(H)$ loops of the trilayer sample recorded at various temperatures along $\theta = 0^\circ$ are shown in Figure 5.7. Similar to the measurements at RT, the NiFe layer exhibited a finite value of H_{ex} , while no shifting of the Co loop was detected. As T increased $H_{ex-NiFe}$ and H_c of both layers dropped accordingly. An interesting feature of the $M(H)$ loops was that there seems to be some kind of ‘synchronized’ switching of the two FM layers, at least at low temperatures (below 250 K). Starting from a positive saturation field, the Co layer starts switching as the NiFe layer finishes the reversal process. When the field is increasing from negative saturation field the Co switches first, and NiFe starts to switch as soon as the Co layer is reversed. Certainly it could not be ruled out it is just an artifact of measurement, but if it were real it could have some implications on the mechanism behind the EB effect. This will be further elaborated in the discussion.

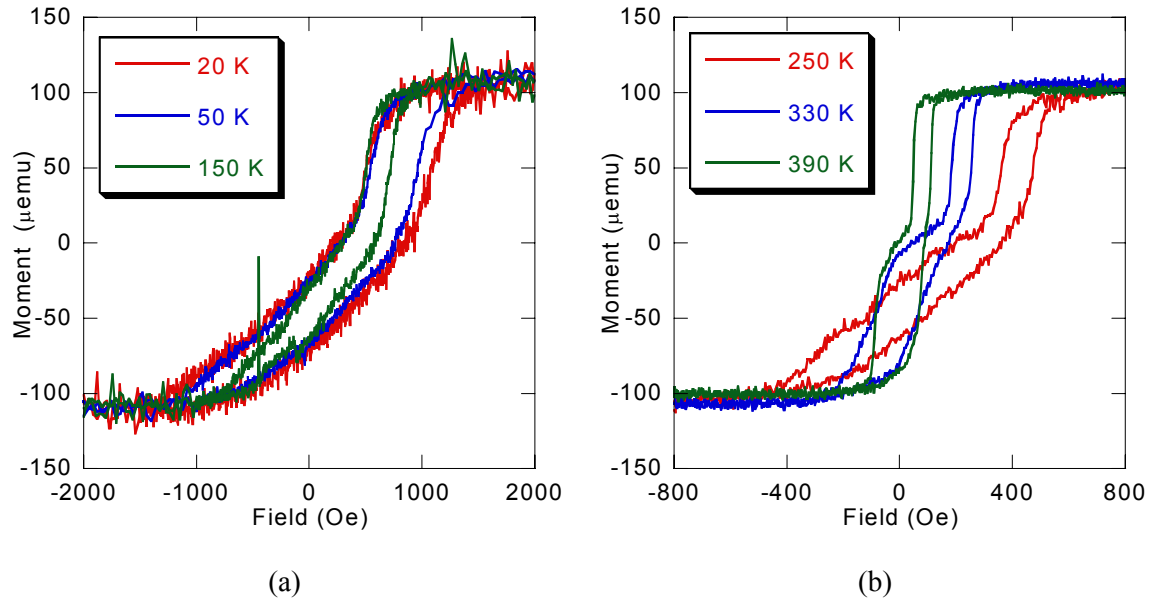


Figure 5.7 $M(H)$ loops of trilayer structure NiFe (4 nm)/FeMn (8 nm)/Co (2 nm) measured along $\theta = 0^\circ$ at low (a) and high (b) ranges of T .

The temperature dependence of H_{ex} and H_c of the trilayer sample, under ZFC condition, are shown in Figure 5.8. As seen from Figure 5.7, H_{ex} was observed in the NiFe layer up to the blocking temperature (~ 420 K). This value was consistent with the literature value for similar FeMn thickness [6]. On the other hand, there was no observable H_{ex} for the FeMn/Co structure at the range of temperature where measurements took place. If the results were to follow that of

Yang and Chien [6], an AF spiral should have been induced during the deposition of the FeMn layer on the NiFe, leading to observable H_{ex-Co} . It was not observed in this experiment.

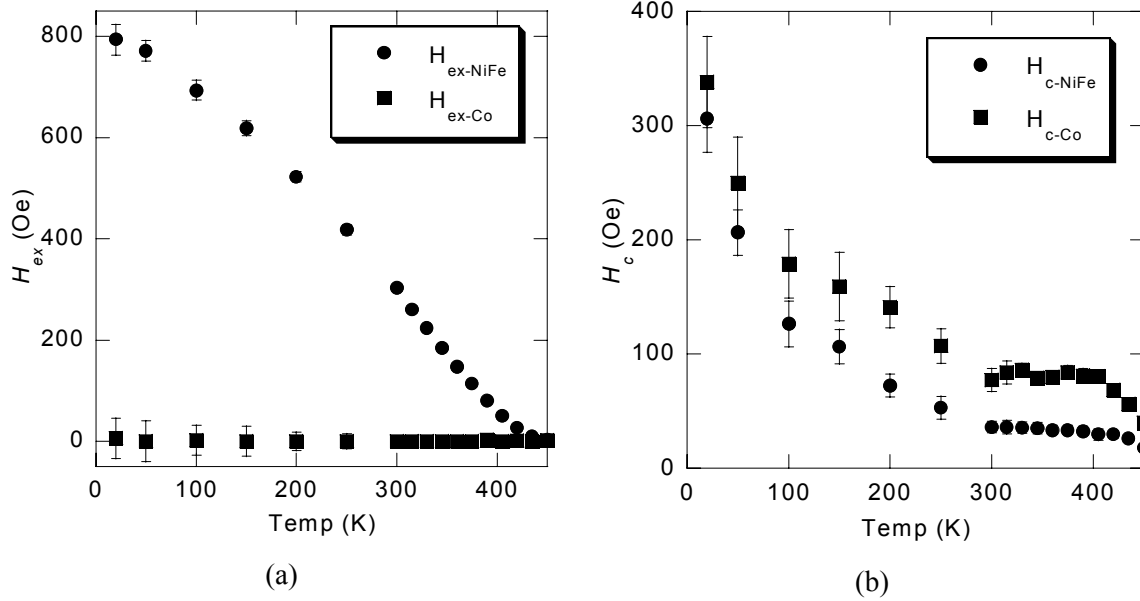


Figure 5.8 Temperature dependence of (a) H_{ex} and (b) H_c of NiFe and Co layers in the trilayer sample NiFe (4 nm)/FeMn (8 nm)/Co (2 nm), under ZFC condition. All measurements were made at $\theta = 0^\circ$.

The temperature dependence of ZFC H_{c-NiFe} and H_{c-Co} of the trilayer sample is shown in Figure 5.8(b). In both layers the H_c dropped rapidly at low T (< 300 K). At temperatures close to T_B , however, the rate of decreased of H_c slowed down or even peaked slight before it further dropped. In epitaxial Fe/MnF₂ samples, Leighton *et. al.* observed a peaking behaviour of H_c around T_N at low t_{AF} and high t_{FM} values [10], while at high t_{AF} (low t_{FM}) the H_c vs. T trace changed to a monotonic decreasing behaviour. They attributed this behaviour to the relative contribution of the AF and FM layers to the losses in the reversal process, as suggested by Stiles and McMichael [11-13]. At low t_{AF} (high t_{FM}) there is a significant reversal loss in the AF layer, which is strongest around T_N . At high t_{AF} (low t_{FM}) losses occur primarily at the FM layer, which occurs at all temperature. It can be the case that the t_{FeMn} values used in this work is in the intermediate range that both types of behaviour appeared.

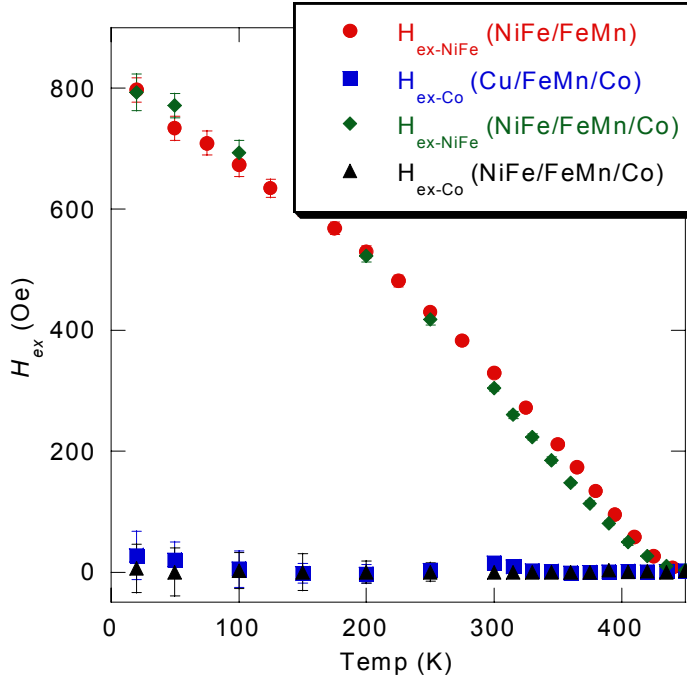


Figure 5.9 Temperature dependence of H_{ex} of various FM layers in bilayer and trilayer samples (structure as indicated in legend). Note that in bilayers (NiFe/FeMn and FeMn/Co), $t_{FeMn} = 10$ nm, whereas in the trilayer sample $t_{FeMn} = 8$ nm. In all cases, $t_{NiFe} = t_{Cu} = 4$ nm, $t_{Co} = 2$ nm.

Comparison of H_{ex} in all bilayer and trilayer samples is shown in Figure 5.9. Note that all the results shown in the figure are extracted from ZFC measurements *except* for the NiFe/FeMn bilayer, which was measured after FC treatment (section 5.2.2). This should not make much difference for the results, given that the NiFe/FeMn structure was properly biased even in the as-deposited state (Figure 5.4(a)). Another thing to note is that the t_{FeMn} values used in bilayer and trilayer samples were slightly different (10 nm in bilayers and 8 nm in trilayers).

The virtually overlapping $H_{ex-NiFe}$ of the bilayer and trilayer samples over the whole temperature range is apparent from Figure 5.9(a). In the bilayer and trilayer samples, there should not be any difference in terms of the structure of the NiFe/FeMn bilayers, at least up to $t_{FeMn} = 8$ nm. According to the random field model, this should give rise to an equal $H_{ex-NiFe}$, as the interfacial states should be equal in bilayer and trilayer samples. This was exactly what was seen in Figure 5.9. On the other hand, no clear signs of H_{ex-Co} could be observed in both bilayer and trilayer samples.

The temperature dependence of H_{c-NiFe} in different samples (single layer, NiFe/FeMn bilayer and NiFe/FeMn/Co trilayer) is shown in Figure 5.10(a). As mentioned before, the enhanced H_{c-NiFe} in the presence of FeMn indicates that the increase originated from the presence of FeMn. H_{c-NiFe} of the bilayer was higher than that of the trilayer sample at all temperature ranges. According to the

literature [14], however, one would expect a smaller H_c for thicker FeMn layers. Since the NiFe/FeMn systems are identical in the bilayer and trilayer samples (up to $t_{\text{FeMn}} = 8$ nm), such result could be related to the presence of the Co layer in the trilayer sample.

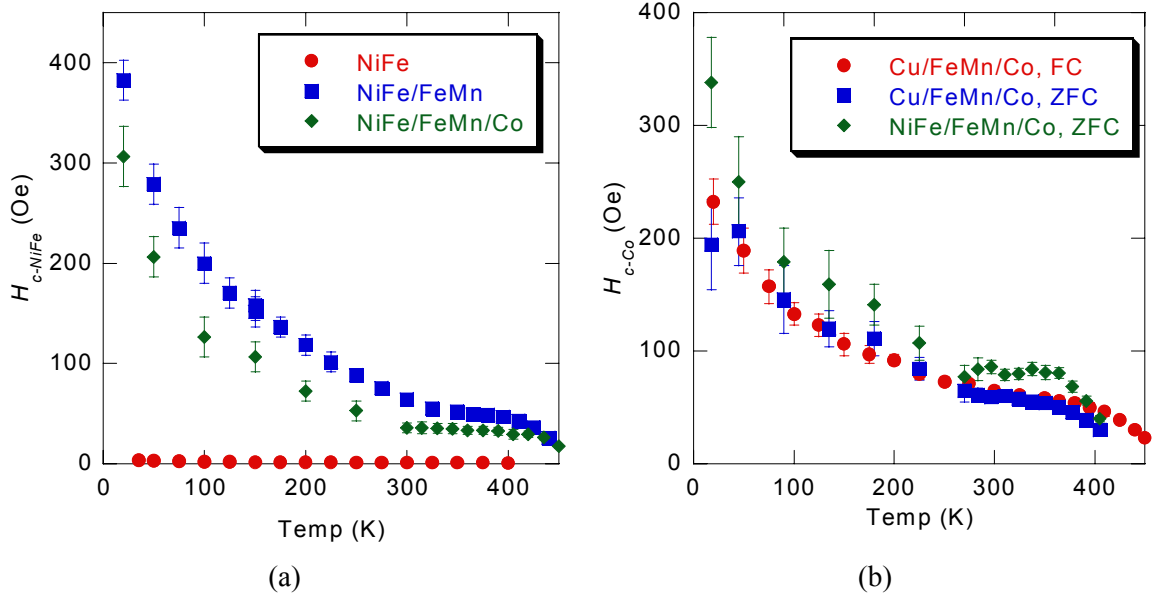


Figure 5.10 Temperature dependence of H_{c-NiFe} (a) and H_{c-Co} (b) in different structures and field cooling conditions (as shown in the legends). In all bilayers $t_{\text{FeMn}} = 8$ nm, and $t_{\text{FeMn}} = 10$ nm in the NiFe/FeMn/Co trilayer sample. $t_{\text{Co}} = 2$ nm and $t_{\text{NiFe}} = t_{\text{Cu}} = 4$ nm in all samples except in the single NiFe layer (5 nm).

A comparison of H_{c-Co} between bilayer (Cu/FeMn/Co) and trilayer (NiFe/FeMn/Co) samples is shown (Figure 5.10(b)). H_{c-Co} data under FC and ZFC conditions are shown for the bilayer sample, which showed essentially the same behaviour. In the temperature range measured up to about 400 K, H_{c-Co} of the trilayer sample was higher than that of the bilayer sample, which was opposite to the case of H_{c-NiFe} but was consistent with the literature findings.

It is possible that the Co layers of the bilayer and trilayer samples have intrinsically different anisotropies which caused the observation in Figure 5.10(b), similar to the case of the single Co layers deposited on different buffers (~ 20 Oe at RT, 50 Oe at 50 K) (Figure 5.3). This can arise from the different density of pinning sites in the FM layer. X-ray diffraction of the two samples (Figure 5.11), however, showed that the two samples have similar crystallinity. Nevertheless, the NiFe/FeMn system seems to be a more well-controlled system in this work, permitting a fair comparison among different samples.

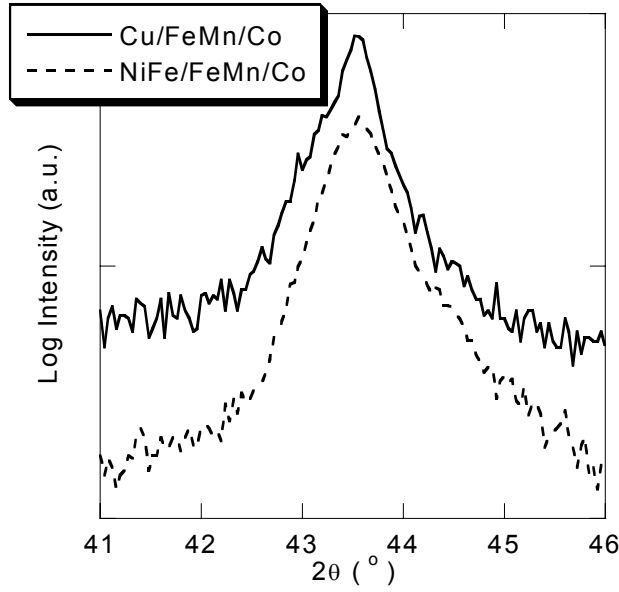


Figure 5.11 High angle $\theta/2\theta$ scans of Cu/FeMn/Co (solid line) and NiFe/FeMn/Co (dashed line) samples (thickness of the layers are indicated in the caption of Figure 5.10)

FC was also performed on the trilayer structure. The $M(H)$ loops of the sample at two temperatures (250 and 375 K) are shown in Figure 5.12. The upper loops in each set of data correspond to the signals from the NiFe layer (this was back deduced from the data at 450 K, at which the exchange bias effect vanished and showed essentially a ‘pseudo spin-valve’ behaviour¹, due to the differences of H_c in NiFe and Co layers). H_{c-NiFe} of the FC measurement was larger than the ZFC data at both temperatures. Besides, $H_{ex-NiFe}$ of FC data seems to be lower than that measured under ZFC condition at 250 K.

Data were extracted from the loops of the FC trilayer sample and the results are shown in Figure 5.13, alongside with the corresponding data of bilayers and ZFC measurement of the trilayer sample. In terms of the loop shifting, $H_{ex-NiFe}$ of FC trilayer sample fell compared with that in the bilayer and ZFC trilayer sample at all T , while H_{ex-Co} of FC trilayer rose compared with the data obtained from FC NiFe/FeMn bilayer sample. In terms of the coercivity, H_{c-NiFe} of the trilayer sample, after FC, was very similar to that of the NiFe/FeMn bilayer over the whole range of T measured. The H_{c-Co} , on the other hand, was consistently higher in the trilayer sample, regardless of FC or ZFC measurements.

¹ Spin valves will be introduced in Chapter 6 of this thesis.

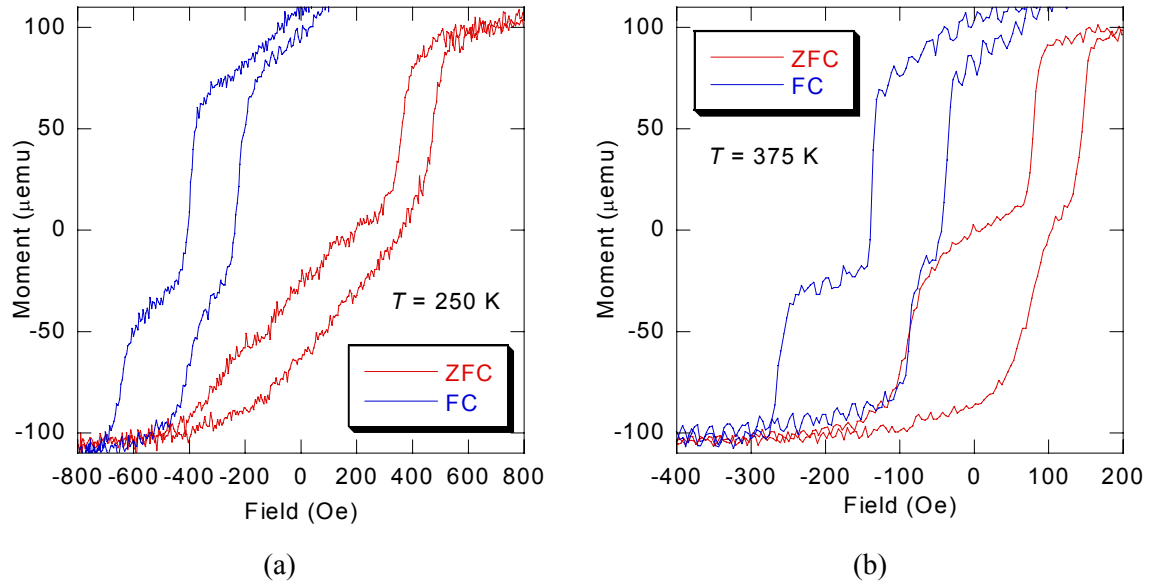
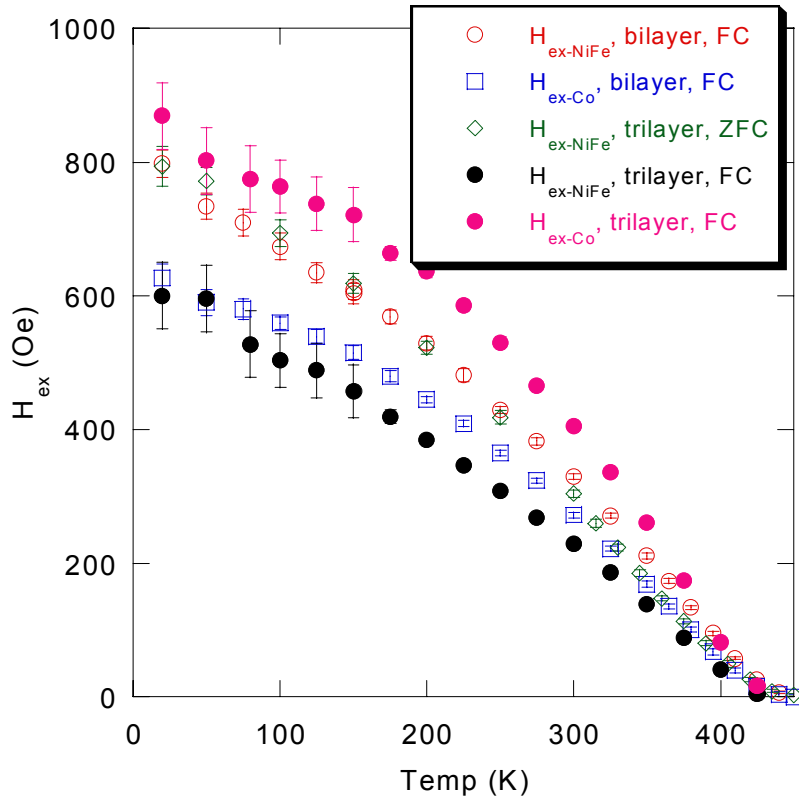


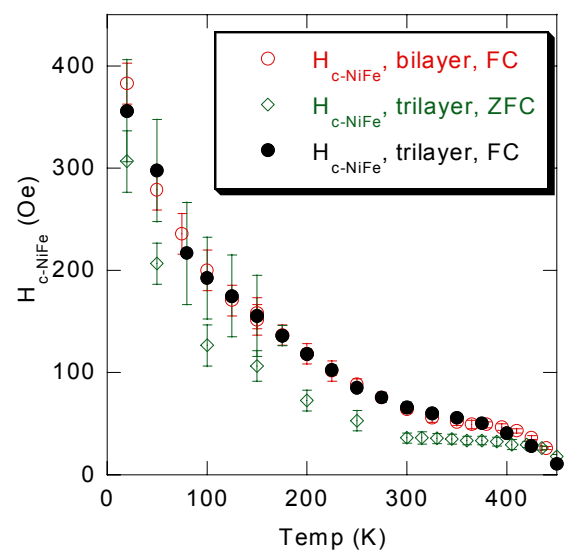
Figure 5.12 Comparison of $M(H)$ loops for the trilayer sample NiFe (4 nm)/FeMn (8 nm)/Co (2 nm) at (a) 250 K and (b) 375 K, under different field cooling conditions.

The results shown in Figure 5.13 are quite confusing, and there did not seem to be any correlation among those results. FC treatment appeared to be an answer at the first sight. H_{c-NiFe} matched well in the FC bilayer and trilayer samples, but it was certainly not the case of $H_{ex-NiFe}$: in terms of the Stiles and McMichael model, irreversible hysteretic losses in the AF are strongly suppressed at low temperature and contributions from reversible AF grains should dominate the H_c behaviour. Given that at such interfaces random fields are also responsible for H_{ex} , one would expect that the temperature dependence of H_{ex} and H_c (at least at low temperature) in the bilayer and trilayer systems should be identical. This conclusion contradicted the results in Figure 5.13(a) and (b). The presence of the other FM layer seemed to be an explanation (for example the H_c behaviour shown in Figure 5.10). Unfortunately, only partial success could be obtained, as illustrated clearly from Figure 5.13(b).

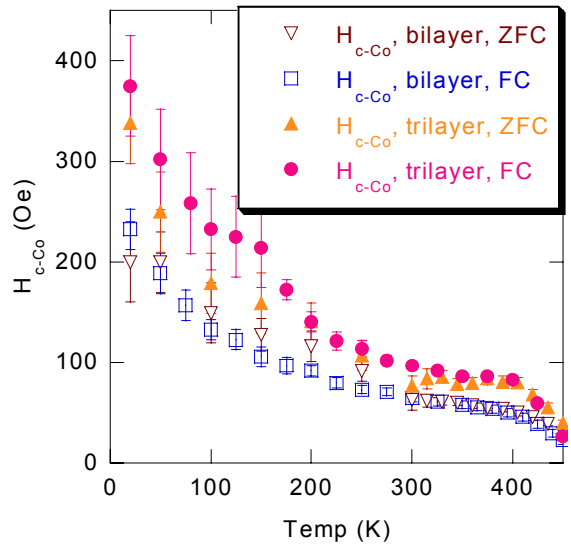
An important aspect that has been neglected so far is the magnetic states of the layers and interfaces during the measurement. In Figure 5.13, data illustrated in open symbols represent layers without an established EB system on the other side of the FeMn, whereas solid symbols refer to those layers that have an established EB on the other side of FeMn. This point will be further elaborated in the discussion.



(a)



(b)



(c)

Figure 5.13 Temperature dependence of H_{ex} (a), H_{c-NiFe} (b) and H_{c-Co} (c) of bilayer and trilayer samples, under different field cooling conditions. The 'bilayer sample' for the NiFe measurements was the sample NiFe (4 nm)/FeMn (10 nm), and for Co measurements the sample was Cu (4 nm)/FeMn (10 nm)/Co (2 nm). The trilayer sample was NiFe (4 nm)/FeMn (8 nm)/Co (2 nm).

Some concern did arise from the data extracted from the FC trilayer sample. In particular, attention was drawn to the H_{ex} values of the trilayer at low temperature (~ 600 Oe for $H_{ex-NiFe}$ and ~ 870 Oe for H_{ex-Co} at 20 K). These values happened to be very close to H_{ex} of the *other* FM material in the bilayer samples (for example, $H_{ex-Co} \sim 630$ Oe and $H_{ex-NiFe} \sim 800$ Oe in the corresponding FC bilayer samples). It was difficult to extract the data of the NiFe and Co layers at low temperature for the FC trilayer sample, especially the signals from the two layers were of comparable magnitude in the current case. However, the data should be reliable for two reasons:

- Although measurements were made from 20 K with increasing temperature, data were extracted from the trilayer $M(H)$ loops at 450 K down to 20K. The loop at 450 K (Figure 5.14), as mentioned before, showed clearly the ‘double coercivity’ behaviour. The moments of individual layers in the trilayer sample matched well with that of the corresponding single FM layers. This minimized the chance that the layers were ‘misidentified’ from the very first place.
- The temperature behaviour of the trilayer at the high temperature regime (> 250 K) was quite easy for NiFe and Co layers to be recognized (see Figure 5.12(b)). At this temperature range, the H_{ex} behaviour of NiFe and Co in the FC trilayer sample is very clear, and can be seen to be different compared with the H_{ex} behaviour of other samples (Figure 5.13(a)).

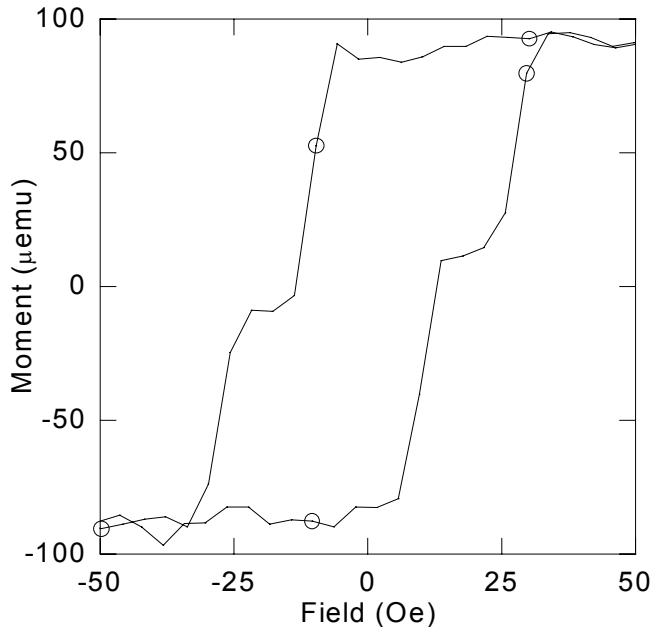


Figure 5.14 $M(H)$ loop of the trilayer sample at 450 K, showing a double coercivity behaviour.

5.4 Discussion

5.4.1 AF spiral?

As mentioned in the introduction, the trilayer work on NiFe/FeMn/Co shown in this chapter is a modified version of the work in [6]. While a relative orientation between $H_{ex-NiFe}$ and H_{ex-Co} orientation was observed in the work of Yang and Chien, no H_{ex-Co} was detected in the ZFC trilayer sample in this work in the measured temperature range (20 – 450 K). Initial magnetization measurement of the virgin loop of ZFC trilayer showed that the Co layer had zero magnetization state before the measurement, similar to the results shown in Figure 5.5(b)). This showed that the Co layer was also locally biased in random directions.

The difference between the work of [6] and this work was the magnetic treatment employed to the sample. While both of the layers were saturated in [6] and cooled from above T_{N-FeMn} to RT, the Co layers in this work were intentionally deposited in a low field condition. In the former case, the FeMn spin ordering took place when the trilayers were cooled below T_N . The NiFe and Co layers should have dominated the spin structure at the two FM/FeMn interfaces. On the other hand, the FeMn spin structure was established before the Co layer was deposited in the trilayer structure. If the spiral was present the Co layer should also be biased in this work, and it was not the case. It is possible to say that the AF spiral, as appeared in [6], was *induced* as a consequence of the specific magnetic treatment employed, and is not an explanation of the EB effect on its own (at least in the current system).

There are some possible arguments about the discussion above. It was mentioned in section 3.1.2.2.3 that A_{ex} of magnetic materials (FM or AF) scales roughly with their transition temperatures. The exchange stiffness of FeMn ($T_N = 490$ K, Table 4.1) is expected to be lower than that of the Co layer ($T_C = 1403$ K [15]). It therefore becomes questionable if the Co layer would follow the spins at the FeMn surface, especially when the Co layer gets thicker. One can study this effect by varying the t_{Co} in the trilayers. Another possibility to avoid the problem is by choosing a FM that has a T_C below T_{N-FeMn} . Some of the alloys of 3d transition metals, such as Cu_xNi_{1-x} , have a wide range of T_C depending on the relative concentration of Cu and Ni [16]. The EB behaviour in the bilayer structure with $T_C \ll T_N$ was rarely studied, as mentioned in section 4.3.2, and virtually no work has been done on the trilayer structures.²

² Some exploratory work on Co/FeMn/CuNi system was performed by Blamire *et. al.* recently.

5.4.2 Effect of magnetic states of FM and FeMn on temperature dependence of H_{ex} and H_c

As seen in the H_c vs. T behaviour of the NiFe and Co layers in bilayer and trilayer samples, FM layers deposited adjacent to the FeMn layer always show an enhanced H_c compared with the corresponding single layer FM samples (Figure 5.10). These signs clearly indicated that the presence of FeMn layer was responsible for the observations. The results of Figure 5.13, however, showed that the specific magnetic treatment also has to be taken into account. As suggested in the results section, the magnetic states of the FeMn and the other FM layer (in the case of trilayer structure) seems to play an important role in deciding the H_{ex} and H_c behaviour of the resultant structure. In the following an attempt is made to explain the results obtained so far along this line of thinking, with the aid of existing EB theories (random field model and Stiles and McMichael model in particular).

In the case of FM/FeMn (or FeMn/FM) bilayers, the random field model suggests that a net spin structure is necessary to induce a unidirectional anisotropy. As mentioned in section 4.1, this can be achieved either by FC the structure under an applied field from above T_N (as in FC measurements), or by depositing the structure when the FM is in a saturated state (either globally as in NiFe/FeMn, or locally as in Co/FeMn, see Figure 5.4). In the case of the FeMn/FM system deposited with field shielding, no mechanism was available for the FeMn to induce a random field *along a particular direction*. Subsequent deposition of the FM layer would yield a bias locally along a random direction in the film plane, leading to the vanishing H_{ex} . Coercivity enhancement, on the other hand, can still take place, because the layers are still coupled *locally* and so the corresponding H_c -enhancement mechanism (Stiles and McMichael model) are still present.

In the shielded trilayer sample, EB is established at the NiFe/FeMn system but not in the FeMn/Co. Nevertheless, coupling between Co and FeMn layers is present. Any of the AF switching events can trigger the reversal of the Co layer. AF reversal is more difficult in a single FeMn layer or at the uncoupled surfaces, due to the very small net moments available in these systems for the external field to couple with (through the Zeeman energy term). The AF reversal is much easier when a FM layer is present, due to the strong exchange interaction between the FM and AF spins and the more pronounced Zeeman energy associated with the FM layer.

The above argument appears plausible to explain a number of observations in this work. H_{ex} is determined by the size of the random field. Since in ZFC trilayer the NiFe/FeMn was established, the random field and hence $H_{ex-NiFe}$ was the same as that of the corresponding bilayer results (Figure 5.9). This could also explain the vanishing H_{ex-Co} in the ZFC bilayer and trilayer samples. H_{c-NiFe} of the bilayer, on the other hand, was higher than that of the ZFC trilayer (Figure 5.10(a)). This could be explained by the assisted AF reversal in the bulk of the FeMn by the Co layer in the trilayer sample, as presented in the last paragraph.

Besides, the above argument can be used to explain the ‘synchronized switching’ of the NiFe and Co layers in the ZFC trilayer sample. The switching of the NiFe layer is accompanied by the irreversible switching events in the AF (which was reflected through the enhanced H_{c-NiFe}). These events are transmitted through the AF layer to the Co, triggering the switching in the Co layer and initiated its reversal process. The effectiveness of the transmission should depend on how strong the coupling at the top FeMn/Co interface. This is in turn controlled by factors such as grain sizes [17] or roughness [18], which can be varied with the thickness and the nature of the buffer layers. On the other hand, reversal of the FeMn layer was harder in the NiFe/FeMn sample without the assistance of Co, leading to a larger value of H_{c-NiFe} even the FeMn layer was thicker.

The situation faced by the NiFe layer in FC trilayer sample was very different from ZFC trilayer case. When the trilayer was FC from above the T_N , long-range spin rearrangement occurs in the FeMn, which was the equilibrium between two EB systems (NiFe/FeMn and FeMn/Co). This could possibly affect the size of anisotropic random interactions at the FM/FeMn interfaces, leading to the observed change in H_{ex} compared with other samples. For the reversal of the NiFe layer, irreversible switching also takes place in the bulk of FeMn. The switching of these AF magnetic structures, however, has to overcome the interaction with other AF domains that do *not* switch irreversibly (which are responsible for the H_{ex-Co}). This explains the increased H_{c-NiFe} in FC sample compared with ZFC ones (Figure 5.13(b)). This could also be an explanation for the temperature dependence of H_{c-Co} in bilayer and trilayer samples (Figure 5.13(c)), although such difference could also be due to the interfacial and microstructural properties of the FeMn/Co systems in bilayer and trilayer samples, as explained in section 5.3.3.

5.5 Summary

In this chapter FM/FeMn and FeMn/FM bilayer samples (FM = NiFe, Co) were compared with the NiFe/FeMn/Co trilayer sample. Samples were deposited in a field condition such that it was enough to saturate the NiFe layer *in situ* but not the Co layer. A summary of results is shown in Table 5.1. Zero-field cooled temperature dependence measurement of the trilayer sample showed no signs of H_{ex-Co} down to 20 K. This showed that the ‘AF spiral’ obtained by Yang and Chien [6] was *induced* by the specific field cooling method, and was not the mechanism of EB by its own in such system. Besides, FC and ZFC measurements on these samples showed the importance of the magnetic states of the FM and the AF layers during the measurement on the H_{ex} and H_c of the layers, which could be explained by some recent models of exchange bias.

Table 5.1 Summary of magnetic measurement results of bilayer and trilayer samples. ‘Bilayers’ refer to NiFe (4 nm)/FeMn (10 nm) sample for NiFe values and Cu (4 nm)/FeMn (10 nm)/Co (2 nm) sample for Co values. Trilayer sample is NiFe (4 nm)/FeMn (8 nm)/Co (2 nm). Upper (lower) values represent data collected at 20 K (RT), and the corresponding errors are put in brackets.

		Bilayers		Trilayers	
		ZFC	FC	ZFC	FC
H_{ex} (Oe)	NiFe	N/A	798 (20)	793 (30)	600 (50)
		0 (10)	330 (4)	304 (5)	229 (5)
	Co	28 (40)	627 (20)	6 (40)	869 (50)
		15 (10)	272 (4)	0 (10)	405 (3)
H_c (Oe)	NiFe	N/A	383 (20)	306 (30)	356 (50)
		45 (10)	65 (4)	36 (5)	66 (5)
	Co	200 (40)	232 (20)	338 (40)	375 (50)
		65 (10)	65 (4)	77 (10)	97 (3)

References for Chapter 5

1. P. Miltényi, M. Gierlings, J. Keller, B. Beschoten, G. Guntherodt, U. Nowak and K.D. Usadel, *Phys. Rev. Lett.* **84**, 4224-4227 (2000).
2. P.A.A. van der Heijden, C.H.W. Swuste, W.J.M. de Jonge, J.M. Gaines, J. van Eemeren and K.M. Schep, *Phys. Rev. Lett.* **82**, 1020-1023 (1999).
3. A.S. Edelstein, R.H. Kodama, M. Miller, V. Browning, P. Lubitz, S.F. Cheng and H. Sieber, *Appl. Phys. Lett.* **74**, 3872-3874 (1999).
4. M.E. Filipkowski, J.J. Krebs, G.A. Prinz and C.J. Gutierrez, *Phys. Rev. Lett.* **75**, 1847-1850 (1995).
5. M.H. Pan, J. Chen, J.G. Long, L.N. Tong, M. Lu, J. Du, A. Hu and H.R. Zhai, *J. Magn. Magn. Mater.* **226**, 1817-1819 (2001).
6. F.Y. Yang and C.L. Chien, *Phys. Rev. Lett.* **85**, 2597-2600 (2000).
7. P. Gaunt, *Philos. Mag. B* **48**, 261-276 (1983).
8. C. Tsang, N. Heiman and K. Lee, *J. Appl. Phys.* **52**, 2471-2473 (1981).
9. H.W. Xi and R.M. White, *Phys. Rev. B* **61**, 1318-1323 (2000).
10. C. Leighton, M.R. Fitzsimmons, A. Hoffmann, J. Dura, C.F. Majkrzak, M.S. Lund and I.K. Schuller, *Phys. Rev. B* **65**, art. no.-064403 (2002).
11. M.D. Stiles and R.D. McMichael, *Phys. Rev. B* **59**, 3722-3733 (1999).
12. M.D. Stiles and R.D. McMichael, *Phys. Rev. B* **60**, 12950-12956 (1999).
13. M.D. Stiles and R.D. McMichael, *Phys. Rev. B* **63**, 4405-+ (2001).
14. J. Wang, W.N. Wang, X. Chen, H.W. Zhao, J.G. Zhao and W.S. Zhan, *J. Appl. Phys.* **89**, 3897-3899 (2001).
15. D. Jiles, *Introduction to magnetism and magnetic materials*, p 96, Chapman & Hall (1997).
16. T.B. Massalski, H. Okamoto, P.R. Subramanian, L. Kacprzak and ASM International., *Binary alloy phase diagrams*. 2nd ed. ASM International (1990).
17. K. Nishioka, C.H. Hou, H. Fujiwara and R.D. Metzger, *J. Appl. Phys.* **80**, 4528-4533 (1996).
18. C. Liu, C. Yu, H. Jiang, L. Shen, C. Alexander and G.J. Mankey, *J. Appl. Phys.* **87**, 6644-6646 (2000).

Chapter 6 Spin Valves

In this chapter the ‘spin valve (SV)’ magnetic multilayer structure is discussed, which combines the two phenomena mentioned in the previous chapters (giant magnetoresistance and exchange biasing effect) to achieve technically desirable properties. Several types of SV structures will be introduced, and some of the important parameters affecting the performances of these structures will be discussed. General review on SV can be found in [1, 2].

6.1 Introduction

6.1.1 Problems with GMR repeated bilayers

As mentioned in chapter 3, the magnitude of the GMR effect (80% at RT in [Co/Cu] [3]) have surpassed the AMR effect. Such property is desirable in the fabrication of devices such as hard disk read heads or magnetic sensors. However, these magnitudes can only be achieved with an applied field in the range of kOe (Figure 3.5), implying a sensitivity of less than 0.1 % Oe⁻¹.

However, it was seen in equation [3.9] that the GMR effect in multilayered systems can take place whenever there is a relative orientation between the magnetization of two FM layers. Interlayer exchange coupling (AF coupling) through the spacer layer is one means of achieving such a state of relative orientations. A combination of both high GMR and low saturation field, however, is relatively difficult to be obtained in such systems.

6.1.2 Spin valve structures

A solution to this dilemma was provided by Dieny *et. al.* [4]. A schematic of their proposed structure is shown in Figure 6.1. Instead of relying on interlayer exchange coupling to achieve the parallel/antiparallel magnetization configuration, Dieny *et. al.* used a structure which had two FM layers *uncoupled* from each other. This was achieved by using a relatively thick spacer layer (2.6-nm of Cu in the case of [4]). In this way, the saturation field could effectively be reduced to that of the individual FM layers. To achieve the state of relative orientation of magnetizations between the FM layers Dieny *et. al.* employed the exchange bias effect (Chapter 4). One of the FM layers (pinned layer) was deposited adjacent to an AF layer (pinning layer). Therefore the remaining FM layer (free layer) could switch easily while the pinned layer magnetization remains

fixed in a particular direction until a larger field was applied. Dieny *et. al.* observed a maximum RT MR of 5% within 10 Oe ($0.2 \% \text{ Oe}^{-1}$) in their SV structure, and much higher sensitivity ($2 \% \text{ Oe}^{-1}$) has also been reported with careful optimization of parameters [5].

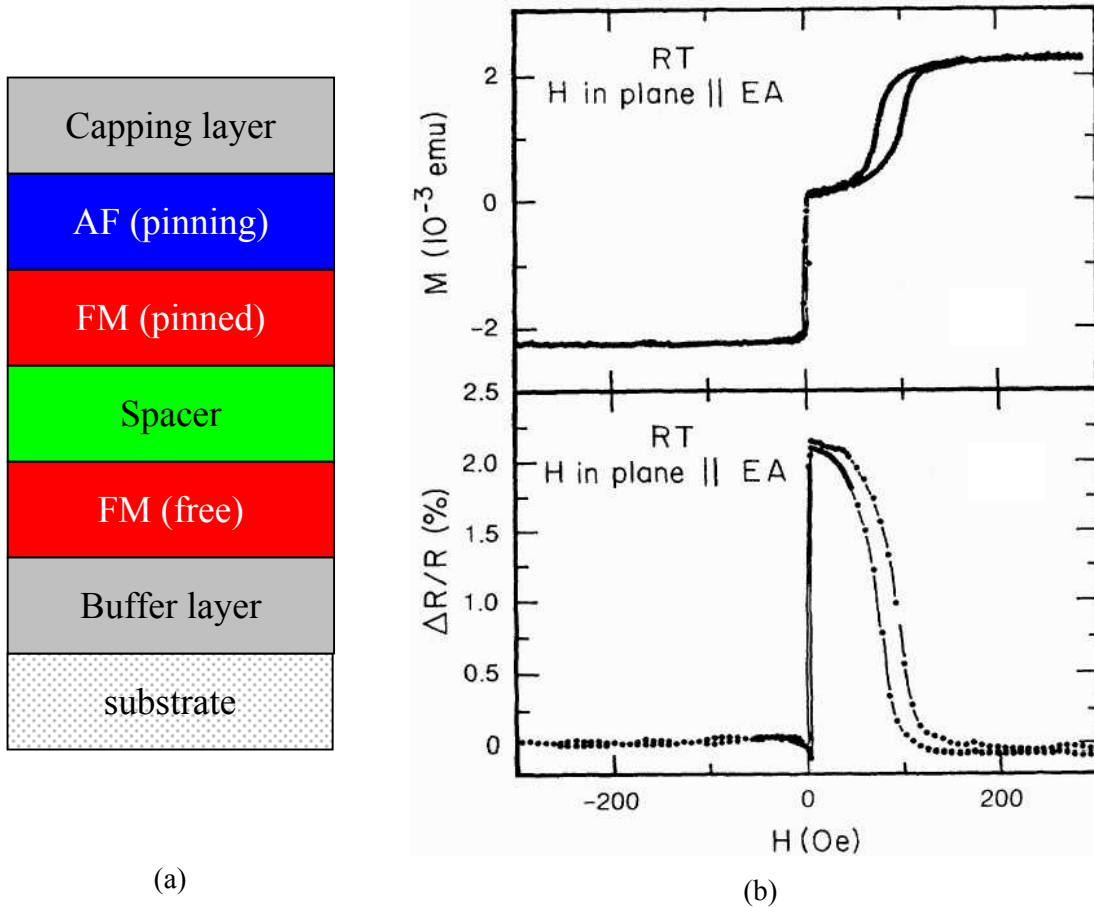


Figure 6.1 (a) Schematic of a conventional spin valve structure, which relies on the exchange bias effect to achieve the relative orientation of magnetizations. Buffer and capping layers are optional. (b) Magnetic and transport measurements of NiFe (15 nm)/Cu (2.6 nm)/NiFe (15 nm)/FeMn (10 nm)/Ag (2 nm), performed by Dieny *et. al.* [4].

6.1.3 Variations of spin valve structures

It was stressed that a necessary condition for the occurrence of the GMR effect is the ability of FM layers in the multilayer system to exhibit a change in the relative magnetization orientation. AF interlayer exchange coupling (section 2.1) and exchange biasing in conventional spin valves are just two of the examples in which such a change can be obtained. There are some other ideas that have been employed in achieving such a change in relative orientations.

- Synthetic SV

In close analogy with the conventional SV structure is the synthetic SV structure (e.g. [6, 7]). The only difference between this type of SV and that in Figure 6.1(a) is the pinning layer. Instead of employing common AF materials (FeMn or IrMn for example) for the pinning layer, a GMR stack with strong AF interlayer exchange coupling is used. It is therefore much harder to bring the pinned layer to saturation than the free layer, allowing a change of magnetization directions (Figure 6.2 (a) and (b)). The main advantage of such configuration is the large pinning field and high thermal stability compared with the common AF materials [7].

- Pseudo SV

Another very simple SV structure is what generally known as the ‘pseudo SV’ (Figure 6.2 (c) and (d)). As contrasted with the conventional SV, this type of SV does not rely on the exchange anisotropy between the FM and the AF layer to facilitate the occurrence of relative orientation of the FM layers. It works simply by the differences between the anisotropies (be it induced [8], shape [9] or magnetocrystalline [10] in nature) of the two FM layers. When the two layers are uncoupled, the softer layer switches its magnetization before the hard layer does, achieving an antiparallel state of magnetization between the two layers and thus a rise in the stack resistance due to the GMR effect.

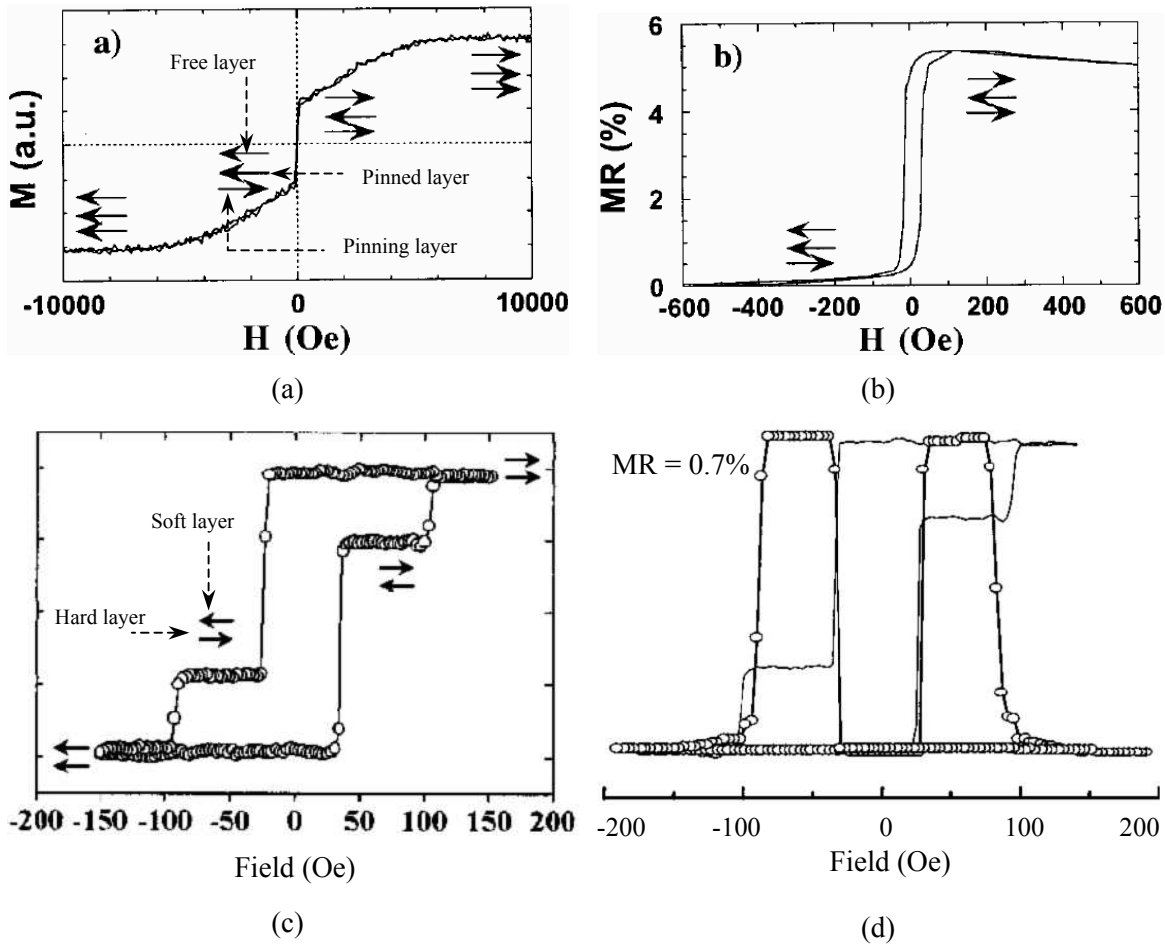


Figure 6.2 Magnetic and transport behaviour of typical synthetic spin valve ((a) and (b)) [6] and pseudo spin valve ((c) and (d)) [10] structures. The synthetic SV shown here has a structure: substrate/Cr (2.1 nm)/Co (3 nm)/Ru (0.7 nm)/Co (3 nm)/Cu (2.5 nm)/Co (3 nm)/(NiFe 2.8 nm)/Ru (2.1 nm); and the pseudo SV has the structure: GaAs/Co (2 nm)/Cu (6 nm)/NiFe (6 nm). Arrows in (a) and (c) indicate the orientation of corresponding layers at particular fields. Note also that only a minor loop is shown in (b).

6.2 Control of magnetoresistive performance in spin valves

It would be a daunting task to review all the works that have been done on the pursuit of improving MR properties in SV structures. The intensive research in this area has been strongly boosted by the prospects of employing these structures in magnetic storage technology and miniaturized devices. In the following a short summary is made on the effect of some selected parameters on the MR performance of the spin valve structures.

6.2.1 Layer thickness

Figure 6.3 shows the dependence of the MR ratio on the thickness of the free layer and NM. For t_{NM} dependence (Figure 6.3 (a)) there is a monotonic decrease of MR with increasing spacer thickness. Such a trend is a consequence of the increased scattering within the spacer, together with the shunting effect by the spacer layer. These behaviours can be modelled as [11, 12]

$$MR(t_{NM}) \propto \frac{\exp(-t_{NM}/t_1)}{(1+t_{NM}/t_2)} \quad [6.1]$$

The constant term t_1 is related to δ_{NM} , while t_2 is the normalization constant depending on the structure of the SV. It should be noted that the MR ratio discussed here refers to the *maximum* MR possible from the structures, as a consequence of the change of the state from total parallel to total antiparallel alignment of the FM layers. It is to be differentiated from the MR behaviour of the GMR repeated bilayer structures (Figure 3.5), which shows oscillating MR with t_{NM} . In this case the formation of antiparallel alignment of the FM layers can be impeded by the strong ferromagnetic coupling, leading to a suppression of the GMR effect.

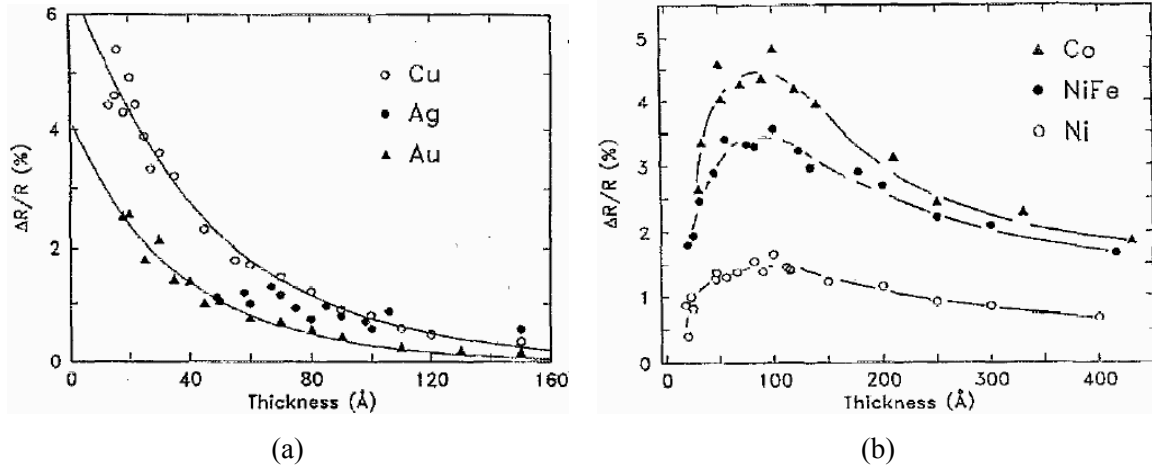


Figure 6.3 Thickness dependence of MR in (a) Co (70 Å)/NM (t_{NM} Å)/NiFe (47 Å)/FeMn (78 Å)/NM (15 Å) and in (b) FM (t_{FM} Å)/Cu (22 Å)/NiFe (47 Å)/FeMn (78 Å)/Cu (15 Å). After Dieny *et. al.* [13].

The free layer thickness (t_{FM}) dependence of MR is more complicated. The MR ratio shows a sharp rise with increasing t_{FM} , reaches a peak before it falls asymptotically. Similar expression as derived by Dieny *et. al.* [14] showed that

$$MR(t_{FM}) \propto \frac{1 - \exp(-t_{FM}/t_3)}{(1 + t_{FM}/t_4)} \quad [6.2]$$

The numerator represents the angular averaged probability that an electron is not being scattered in the free layer, and the denominator arises from the shunting effect of the layer. The peak position of the maximum GMR is dependent on t_3 and t_4 and so should be dependent on relative importance of scattering events (t_3) and the structure of the rest of the SV (t_4). This is actually the case, as the calculated peaks are dependent on number of repeats of the GMR-active elements and the probability of specular scattering at the surfaces [12].

6.2.2 Roughness and intermixing at interfaces

Very different results have been reported in literature concerning the effect of roughness on the MR ratio of spin valves or GMR repeated bilayers. In the case of Fe/Cr system a rise of the GMR effect has been reported. For example, Schad *et. al.* [15] characterized high quality MBE-grown [Fe (2.8 nm)/Cr (1.1 nm)]₁₀ superlattices. They varied the roughness by annealing the samples at different temperatures. They found that ΔR of the samples increased with a drop in $\xi_{//}$. Further annealing of the samples led to a rise in σ and hence a further rise in the MR ratio with roughness. Their analysis showed negligible bulk defects within the sample and sharp interfaces in all samples. This was in contrast with the [Co/Cu] system, in which no enhanced GMR effect was observed in all types of samples, when the sample roughness was increased [16]. Some of the suggestions of the observed differences include the relative contribution of interface and bulk spin-dependent scattering [16], greater stability of Fe ions with respect to interface mixing compared with Co [11]. One should, however, note that increased surface roughness would lead to increased FM-type coupling strength between the ferromagnetic layers, leading to a reduced ability to achieve the AF alignment and hence a drop in the observed MR. Coupling effect of this type will be further discussed in section 6.3.

Generally rough samples are accompanied by the presence of interfacial mixing. This is particularly the case of the sputtered films, where the grain boundaries acting as channels for diffusion across different layers. This may provide some clue on the difference of the observed results in the same system prepared by different methods (see the discussion of [15]). In fact the trend is quite general in the case of intermixed interfaces: spin-independent scattering tends to dominate, either as a consequence of reduced spin-dependent scattering or the formation of magnetically dead layers [17].

6.2.3 Capping and buffer layers

There are some studies dedicated on the issue of buffer layers on the MR performance of SV structures [18-21], most of them used complicated structures in the hope of optimizing the MR, leading to a difficulty in generalizing the behaviour. Ta by far is the most commonly employed buffer layer for its high resistivity and the ability to produce smooth interfaces. However, there were reports of potential interfacial interactions between NiFe and Ta that yields magnetically dead layers [22].

On the other hand, some attempts have been made to use specific materials such as noble metals as capping layers [23-25]. In usual case one would expect the capping layers to behave as shunting layers and lead to a drop of the MR effect. When these layers are of optimum thickness, however, an enhancement of the MR ratio has actually been observed. This has been attributed to the specular reflection of electrons at the boundaries of these layers [26], which effectively increased the distance in which electrons travelled before being scattered (outer boundaries of films tend to scatter electrons diffusely) and lead to an enhanced MR ratio.

6.3 *Coupling effect in spin valve structures*

Ideal spin valve structures have FM layers that are uncoupled from each other. In practice, this is never achieved due to imperfection of FM layers and interfaces. A number of possible causes of such coupling will be discussed in this section.

6.3.1 Magnetic bridges

At the beginning of Chapter 3, it was mentioned that the magnetic bridges (pinholes) within the spacer could lead to ferromagnetic coupling between the two FM layers. The origin of this type of coupling is the interaction between two FM layers. Magnetic bridges are occasionally invoked as the source of coupling in GMR multilayers [27] and magnetic tunnel junctions [28]. Imaging of such bridges in GMR multilayers is particularly difficult [27, 29], given their small dimensions (in the range of nanometres) and the problems in distinguishing different species of *3d* transition metals. Other methods, such as X-ray fluorescence technique [30], could be helpful in providing the relative amount of different element species in a particular depth, providing an estimation

about the degree of coupling through the NM layers by magnetic impurities. In general such kind of coupling could be neglected in sputtered multilayers when the spacer thickness is more than 2 nm [2], provided that care has been exercised in ensuring the uniformity of the deposited films during the growth procedure.

Theoretical calculations of the coupling strength through pinholes are surprisingly rare, given its widespread influence in magnetic multilayered structures. A theory developed in the 1960s [31] assumed a conical structure of the pinholes (Figure 6.4). Magnetization rotation was assumed to take place only in the region of the neck, as it was less favourable to spread the rotation into the wider parts of the bridges. The coupling energy associated with the rotation could be written as:

$$U = 2\pi A_{ex} d \left(\frac{R}{d} \right)^2 \left[(1 - \cos \alpha_1) + (1 - \cos \alpha_2) + (1 + k)^2 (1 - \cos \alpha_3)^2 \right] \quad [6.3]$$

where k is a geometrical factor $\frac{d \tan \phi}{R}$, and α_i refers to the spin orientation of i -th layer relative to the $(i-1)$ -th layer. This was certainly a simplified model. For example, one would expect pinholes to exist not only in conical shapes but also in other forms, such as diffused atoms along grain boundaries or even as impurities in the spacers.

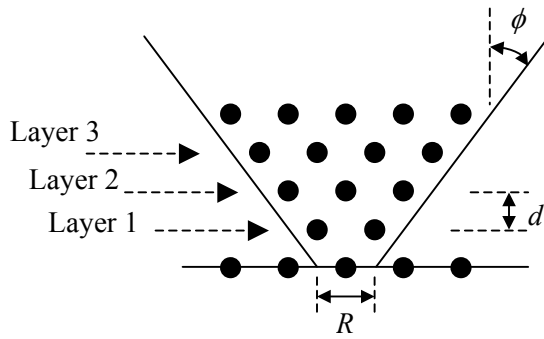


Figure 6.4 Model of magnetic pinhole across NM spacer [31].

6.3.2 Interlayer exchange coupling

In theory, the bilinear coupling strength drops off approximately with $\frac{1}{t_{NM}^2}$ as mentioned in section 3.1. A sample calculation with the [Co/Cu] repeated bilayer system ($J_1 \sim 0.25$ erg/cm² at $t_{NM} = 0.9$ nm [32]) implies a *maximum* coupling strength of magnitude 0.02 erg/cm² at $t_{Cu} \sim 3$ nm. This is usually smaller and can take both positive and negative signs, given the oscillatory nature of the J_1 with t_{NM} .

Another factor leading to the reduction of J_I is the roughness of surfaces. This effect, however, has to be treated with care. As pointed out by Bruno and Chappert [33], it has to be considered for correlated and uncorrelated surfaces. In case the surfaces are uncorrelated, the effective coupling strength can be considered as the average of the coupling strength across the surface, assuming that the lateral fluctuation of J_I is not so rapid that it is stable locally (this usually requires $t_{NM} \ll \xi_{//}$) (section 3.1). The effect is that the averaged J_I value would be substantially suppressed. A simple calculation of such a situation is presented in Figure 6.5. In the case of correlated roughness, the suppression effect would be much smaller due to the less severe local t_{NM} variations. However, the small fluctuation would lead to suppression of oscillations which have much smaller periods, for example, in Fe/Cr system [34].

On the other hand, interfacial roughness can also induce J_2 coupling, as discussed in section 3.1. The J_2 coupling strength is extremely sensitive to the variation of roughness: an increase of σ by 0.2 nm could lead to an increase of the coupling strength by an order of magnitude, as shown in Figure 6.6 (a). It is also very sensitive to the values of L used. Two effects on J_2 could be seen from Figure 6.6 (b) by varying L : the initial coupling strength increases with a larger L , and that the rate in which J_2 falls with t_{NM} decreases dramatically with the increase of L .

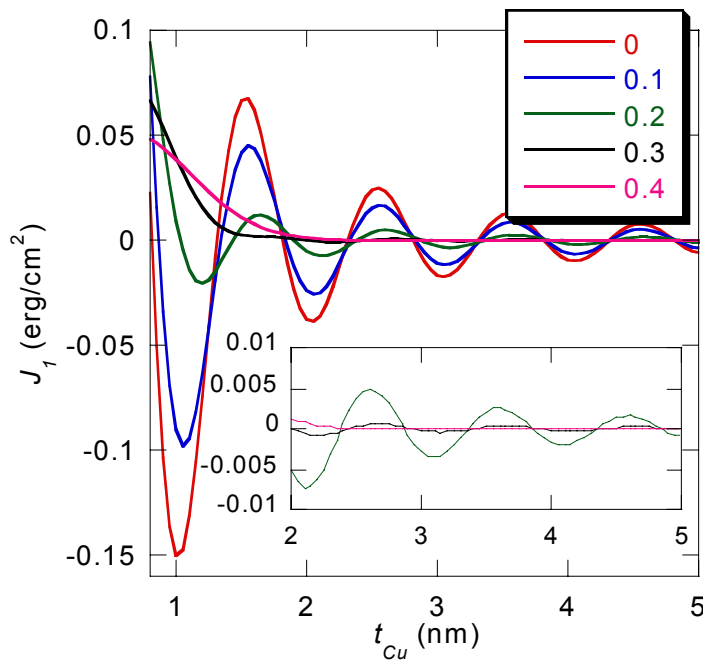


Figure 6.5 Suppression of J_1 interlayer exchange coupling due to uncorrelated roughness. Legends indicate rms roughness σ in nm. Inset is an enlarged view of the section $t_{Cu} = 2-5$ nm for $\sigma = 0.2$ to 0.4 nm. The magnitude is scaled according to literature value of J_1 coupling in [Co/Cu] system (0.15 erg/cm $_2$ with $t_{Cu} = 0.93$ nm) [35].

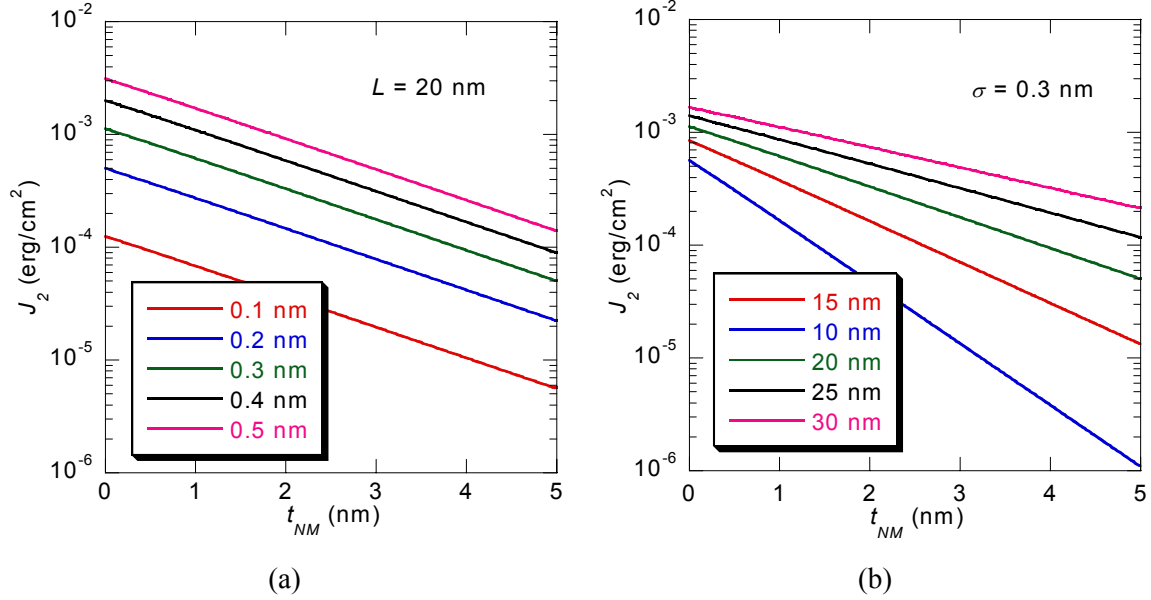


Figure 6.6 Variation of J_2 coupling strength as function of t_{NM} for different interface roughness values σ (a) and peak-to-peak distance L (b), as calculated from equation [3.5]. Co layers ($M_{FM} = 1420 \text{ emu/cm}^3$) of thicknesses 5 nm were assumed.

6.3.3 Magnetostatic ('orange peel') coupling

Roughness at FM surfaces can also generate magnetic dipoles, leading to magnetostatic coupling between FM layers commonly known as the 'orange peel' coupling. The energy associated with such type of coupling, as first formulated by Néel [36, 37], can be written as:

$$E = \frac{\pi^2 h^2}{\sqrt{2}L} M_f M_p \exp\left(-\frac{2\sqrt{2}\pi t_{NM}}{L}\right) \quad [6.4]$$

where h is the peak-to-valley interface width, M_f and M_p are the magnetizations of the free and the pinned layers respectively, and L ($\gg h$) is the repeating distance of the wavy interface. The formulation of Néel was confined to the cases where the interfaces had identical widths σ . Modifications have been made by Kools *et. al.* to take into the account of the unequal interface widths [38]. In any cases, however, the formulations were based on the assumption that the interfaces were correlated. Uncorrelated interfaces would disrupt the formation of suitable dipoles and reduce the coupling strength.

The orange peel coupling was invoked by Kools *et. al.* to explain the shifting of the free layer hysteresis loop from the zero field position in SV structures (refer to Figure 8.1 for example). The

value of the H_o can then be calculated from equation [6.4]. High-resolution electron microscopy analysis on interfacial roughness has been employed by Portier *et. al.* to examine the validity of such a suggestion [39]. Together with the magnetic measurements, they have shown a good agreement between the suggestion by Kools *et. al.* and experimental results.

6.3.4 Domain wall coupling

Stray field from domain walls of a FM layer can act as local barriers to the wall motions in the adjacent FM layers, resulting in coupling between FM layers across spacers. The strength of the coupling has been calculated by Fuller and Sullivan [40], who considered the interaction between two straight parallel 180° Néel wall (Figure 6.7). Assuming one of the walls (say FM2) is fixed, the coupling energy arises from the magnetostatic interaction due to stray field from the domain walls, together with the energy associated with the displacement of the wall in FM1. The field needed for the wall in FM1 to escape from the influence of FM2's wall is

$$\frac{aH_{esc}}{t_{FM2}M_{FM2}} = \frac{u+B}{v^2+(u+B)^2} + \frac{u-B}{v^2+(u-B)^2} - \frac{u+A}{v^2+(u+A)^2} - \frac{u-A}{v^2+(u-A)^2} \quad [6.5]$$

where $u = x/a$ and $v = s/a$, $s = (t_{NM} + 0.5 \times (t_{FM1} + t_{FM2}))$, $A = (1 + b/a)$, $B = (1 - b/a)$ (the original formula of [40] could be obtained by putting $a = b$). Equation [6.5] assumed that the effect of fringe fields on the wall profiles was negligible. The equation has been applied in deducing the relative strength of the domain wall coupling in magnetic heterostructures [41, 42].

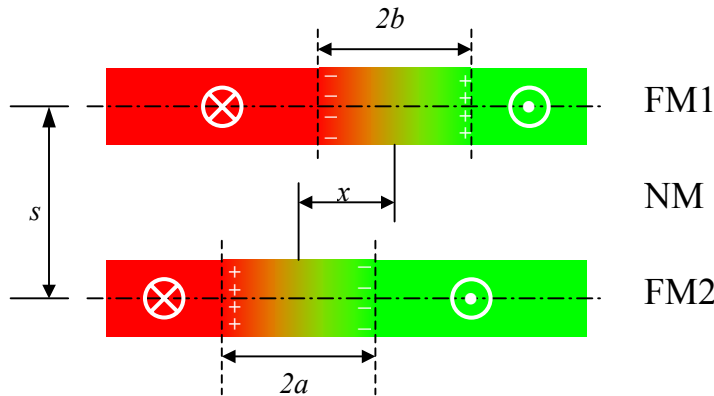


Figure 6.7 Model of domain wall coupling, after [40]. Wall widths and their lateral separation are $2a, 2b$ and x , respectively

References for Chapter 6

1. R. Coehoorn, J.C.S. Kools, T.G.S.M. Rijks and K.M.H. Lenssen, *Philips J. Res.* **51**, 93-124 (1998).
2. B. Dieny, *J. Magn. Magn. Mater.* **136**, 335-359 (1994).
3. K. Kagawa, H. Kano, A. Okabe, A. Suzuki and K. Hayashi, *J. Appl. Phys.* **75**, 6540-6542 (1994).
4. B. Dieny, V.S. Speriosu, S.S.P. Parkin, B.A. Gurney, D.R. Wilhoit and D. Mauri, *Phys. Rev. B* **43**, 1297-1300 (1991).
5. B. Dieny, in *Magnetism and structure in systems of reduced dimension*, edited by R.F.C. Farrow. Vol. 309, Plenum Press (1993).
6. J.L. Leal and M.H. Kryder, *J. Appl. Phys.* **83**, 3720-3723 (1998).
7. J.L. Leal and M.H. Kryder, *IEEE. Trans. Magn.* **35**, 800-805 (1999).
8. R.D. McMichael, C.G. Lee, J.E. Bonevich, P.J. Chen, W. Miller and W.F. Egelhoff, *J. Appl. Phys.* **88**, 5296-5299 (2000).
9. D. Morecroft, C.W. Leung, N.A. Stelmashenko, J.L. Prieto, D.B. Jardine and M.G. Blamire, *IEEE Trans. Magn.* **37**, 2079-2081 (2001).
10. W.S. Lew, A. Samad, S.P. Li, L. Lopez-Diaz, G.X. Cheng and J.A.C. Bland, *J. Appl. Phys.* **87**, 5947-5949 (2000).
11. E.Y. Tsymbal and D.G. Pettifor, *Perspectives of giant magnetoresistance*, in *Solid State Physics*. Vol. 56, pp. 113-237, Academic Press Inc. (2001).
12. B. Dieny, *J. Phys.: Condes. Matter* **4**, 8009-8020 (1992).
13. B. Dieny, V.S. Speriosu, S. Metin, S.S.P. Parkin, B.A. Gurney, P. Baumgart and D.R. Wilhoit, *J. Appl. Phys.* **69**, 4774-4779 (1991).
14. B. Dieny, P. Humbert, V.S. Speriosu, S. Metin, B.A. Gurney, P. Baumgart and H. Lefakis, *Phys. Rev. B* **45**, 806-813 (1992).
15. R. Schad, P. Belien, G. Verbanck, V.V. Moshchalkov, Y. Bruynseraede, H.E. Fischer, S. Lefebvre and M. Bessiere, *Phys. Rev. B* **59**, 1242-1248 (1999).
16. M.J. Hall, B.J. Hickey, M.A. Howson, C. Hammond, M.J. Walker, D.G. Wright, D. Greig and N. Wiser, *J. Phys.: Condes. Matter* **4**, L495-L502 (1992).
17. V.S. Speriosu, J.P. Nozieres, B.A. Gurney, B. Dieny, T.C. Huang and H. Lefakis, *Phys. Rev. B* **47**, 11579-11582 (1993).
18. A. Dinia, N. Persat, S. Colis, C. Ulhaq-Bouillet and H.A.M. van den Berg, *Eur. Phys. J. B* **18**, 413-419 (2000).
19. T. Li, H.L. Shen, Q.W. Shen, S.C. Zou, K. Tsukamoto and M. Okutomi, *J. Magn. Magn. Mater.* **224**, 55-60 (2001).
20. S. Colis, A. Dinia, D. Deck, G. Schmerber and V. Da Costa, *J. Appl. Phys.* **88**, 1552-1558 (2000).
21. Z.T. Diao, S. Goto, K. Meguro, S. Tsunashima and M. Jimbo, *J. Appl. Phys.* **81**, 2327-2335 (1997).
22. G.H. Yu, C.L. Chai, H.C. Zhao, F.W. Zhu and J.M. Xiao, *J. Magn. Magn. Mater.* **224**, 61-64 (2001).
23. H. Sakakima, E. Hirota and Y. Kawawake, *J. Magn. Magn. Mater.* **184**, 49-54 (1998).
24. D.J. Keavney, S.K. Park, C.M. Falco and J.M. Slaughter, *J. Appl. Phys.* **86**, 476-479 (1999).
25. W.F. Egelhoff, P.J. Chen, C.J. Powell, M.D. Stiles, R.D. McMichael, J.H. Judy, K. Takano, A.E. Berkowitz and J.M. Daughton, *IEEE Trans. Magn.* **33**, 3580-3582 (1997).
26. W.F. Egelhoff, P.J. Chen, C.J. Powell, D. Parks, G. Serpa, R.D. McMichael, D. Martien and A.E. Berkowitz, *J. Vac. Sci. Technol. B* **17**, 1702-1707 (1999).

27. W. Zou, H.N.G. Wadley, X.W. Zhou, R.A. Johnson and D. Brownell, *Phys. Rev. B* **64**, art. no.-174418 (2001).
28. R. Schad, D. Allen, G. Zangari, I. Zana, D. Yang, M. Tondra and D.X. Wang, *Appl. Phys. Lett.* **76**, 607-609 (2000).
29. D.X. Yang, H.D. Chopra, B. Shashishekar, P.J. Chen and W.F. Egelhoff, *Appl. Phys. Lett.* **80**, 2493-2495 (2002).
30. T.P.A. Hase, *Ph. D. Thesis*, University of Durham (1998).
31. O. Massenet, F. Biragnet, H. Juretschke, R. Montmory and A. Yelon, *IEEE Trans. Magn.* **2**, 553-556 (1966).
32. C.H. Marrows, N. Wiser, B.J. Hickey and T.P.A. Hase, *J. Phys: Cond. Mater.* **11**, 81-88 (1999).
33. P. Bruno and C. Chappert, *Phys. Rev. B* **46**, 261-270 (1992).
34. J. Unguris, R.J. Celotta and D.T. Pierce, *Phys. Rev. Lett.* **67**, 140-143 (1991).
35. S.S.P. Parkin, R. Bhadra and K.P. Roche, *Phys. Rev. Lett.* **66**, 2152-2155 (1991).
36. L. Néel, *On a magnetostatic problem relating to thin ferromagnetic layers*, in *Selected works of Louis Néel*, edited by N. Kurti, Gordon and Breach (1988).
37. L. Néel, *On a new mode of coupling between the magnetization of two thin ferromagnetic layers*, in *Selected works of Louis Néel*, edited by N. Kurti, pp. 463-466, Gordon and Breach (1988).
38. J.C.S. Kools, W. Kula, D. Mauri and T. Lin, *J. Appl. Phys.* **85**, 4466-4468 (1999).
39. X. Portier, A.K. PetfordLong, P. BayleGuillemaud, T.C. Anthony and J.A. Brug, *J. Magn. Magn. Mater.* **199**, 110-112 (1999).
40. H.W. Fuller and D.L. Sullivan, *J. Appl. Phys.* **33**, 1063-1064 (1962).
41. H.D. Chopra, D.X. Yang, P.J. Chen, D.C. Parks and W.F. Egelhoff, *Phys. Rev. B* **61**, 9642-9652 (2000).
42. B. Altuncevahir and A.R. Koymen, *J. Appl. Phys.* **89**, 6822-6824 (2001).

Chapter 7 Evolution of the Structural Properties in NiFe-Co Based Top Spin Valves

In the following two chapters, results are presented on the studies of a conventional top spin valve structure (with an AF pinning layer on top of the pinned FM layer, as shown in Figure 6.1(a)) by means of a ‘built-up samples’ strategy. Samples were prepared with a progressive increase in the number of constituent layers of the target structure Nb (5 nm)/NiFe (4 nm)/Cu (3 nm)/Co (5 nm)/FeMn (10 nm)/Nb (5 nm), using sputtering deposition. Thorough characterization of these samples was performed, using the techniques introduced in Chapter 2. Evolution and correlation of structural, magnetic and electric properties in the structure was investigated, as the layers were subsequently added. In this chapter structural properties are investigated, while electrical and magnetic properties are dealt with in Chapter 8.

7.1 Introduction

As shown in the previous chapter, numerous studies have been done in order to characterize the various properties of different types of SV. Some typical characterization examples include: structural characterization by x-ray techniques [1-3] and transmission electron microscopy [4], magnetic and electrical studies using different conditions, such as varying annealing temperature [5]. Different constituent materials for various layers (for example the pinning layer [6]) has also been studied, as well as the dependence on layer thicknesses [7], among many others.

However, the issue of how the various properties of SV evolve with successive deposition of the layers has been rarely studied [1-3]. These properties can vary with the addition of materials, either of the same or different chemical species, and would impose effects on the final performance of the SV structure. For example, the roughness of thin metallic films tend to increase with the total film thickness [8], which can give rise to coupling between FM layers across the spacer (section 6.2). It would therefore be desirable to study the evolution of such characteristics, and how they correlate to each other.

In this project an attempt was made to characterize these properties and their evolution in conventional top SV structure by means of ‘built-up’ samples. The built-up samples refer to a batch of multilayered films deposited with different number of layers, in which the layers are stacked up according to the sequence of the target SV structure. The schematic explanation is

shown in Figure 7.1. Through studying the built-up samples it was hoped that information could be obtained on how the properties of the SV are developed upon the deposition of each layer.

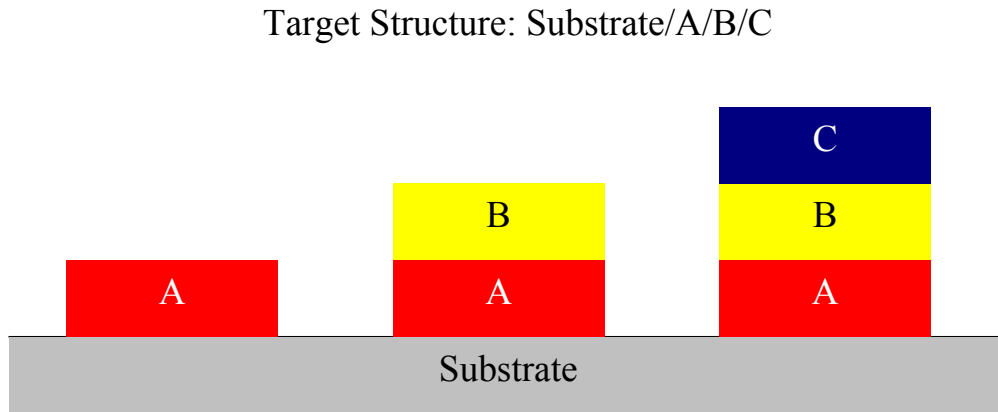


Figure 7.1 Schematic showing a batch of 'built-up' samples of a particular target structure.

7.2 Experimental

7.2.1 Sample fabrication

All the samples investigated were sputter deposited in the planetary deposition chamber (UFO 1) described in section 1.3. In this work a nominal structure of Nb (5 nm)/NiFe (4 nm)/Cu (3 nm)/Co (5 nm)/FeMn (10 nm)/Nb (5 nm), deposited on Si (100) substrates covered with ~ 250 nm thick oxides, was used. The thicknesses of the layers were not optimized for any particular performance, but they are typical values used for SV structures [9]. The Cu spacer (3 nm) was thick enough to decouple the two FM layers [7]. A relatively thick FeMn AF layer (compared with the critical thickness of ~ 6 nm at RT [10]) was chosen for testing the properties of the SV, since it is less prone to variations in exchange bias due to potential thickness changes (e.g. oxidation). The use of a Nb buffer layers is not common for spin valve structures (usually Ta is used), except in cases where current has to be driven perpendicular to the heterostructures [11]. However, since both Nb and Ta have high melting points and identical lattice structure (body-centred-cubic (bcc) structure and very close lattice constants [12]), and that all the layers were deposited at low temperatures (< -100 °C), it was expected that Nb could also provide a relatively smooth substrate for subsequent growth of the SV.

It was discussed in Chapter 4 that *in situ* field deposition was sometimes necessary in order to induce the unidirectional anisotropy of FM/AF bilayer structures (in this case Co/FeMn). This was achieved by attaching a pair of permanent magnets to the stainless steel sample holder, which provided an in-plane field (~ 200 Oe) across the substrate. The field (*in situ* field) was larger than the stray field from the chamber (Chapter 5) and so the exchange anisotropy was established along the *in situ* field direction. To standardize the deposition procedure, each sample was deposited in the presence of such an *in situ* field. During the batch of runs, the order in which the built-up samples were deposited was randomized (see Table 7.1 for details). This would prevent any systematic error (such as the deposition rate variation with the number of runs) to be incorporated into the samples. Complete target structures (full SV) were deposited in the first and the last samples of the series of built-up samples to ensure repeatability of results.

7.2.2 Structural characterization

Structural characterization was carried out on the built-up samples, using AFM and x-ray reflectivity described in section 2.1. Comparisons were then made between the samples to determine and examine any changes induced due to the addition of successive layers.

7.2.2.1 X-ray reflectivity (XRR) measurements

The basic concepts of XRR were introduced in section 2.1. In this work both specular and off-specular reflectivity scans were obtained. Alignment to the specular condition was obtained by performing transverse scans (which are basically low-angle ω -scans) at a number of detector angles ($1 - 3^\circ 2\theta$). Differences in the determined specular sample angles were always within 0.005° (the minimum step size for the sample angle), which was too small to affect the specular reflectivity measurement results. Specular (off-specular) scans were then carried out with the sample angle set at (-0.1° away from) the specular condition.

First of all the reproducibility of these results by depositing built-up samples in separate runs has to be addressed. Specular reflectivity scans for the two control full SV samples are shown in Figure 7.2. Excellent matching of the modulations can be observed, implying the minimal thickness deviation of individual layers. This addresses the concern over the potential drift in the deposition rates with the number of runs. Even so, it has been mentioned that the amplitude of the Kiessig fringes did not match perfectly in the two scans, which may imply a run-to-run variation

in terms of the interface width. Further investigation on the reproducibility of the full SV structure is shown by electrical and magnetic characterization, which is the subject of the next chapter.

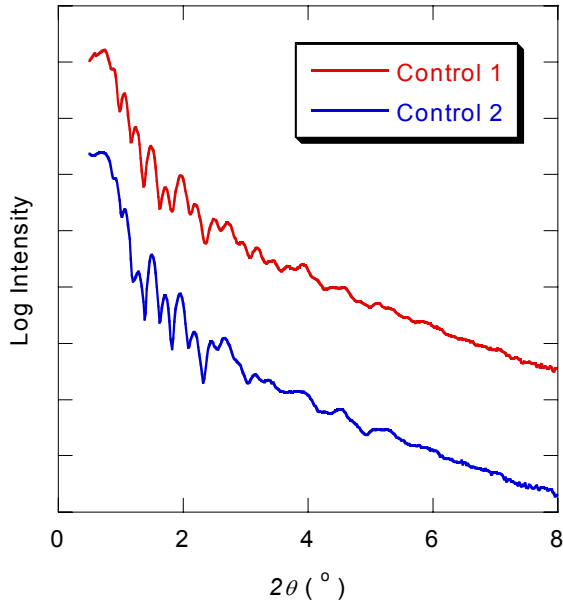


Figure 7.2 Specular reflectivity scans of two control full SV samples, deposited before ('Control 1') and after ('Control 2') the batch of built-up samples were fabricated.

Specular reflectivity scan results are shown in Figure 7.3, superimposed with the corresponding fitted results (see Table 7.1 for the parameters). The fitting process is summarized in the flowchart in Figure 7.4. The built-up sample with the smallest number of layers (in this case Nb (5 nm)) was fitted first. As the XRR measurements were performed *ex situ*, an oxide layer was included above the Nb layer. During the fitting process initial estimates on the parameters (such as layer thickness, roughness and density) were provided, based on which the REFSIM program attempted to find the optimum solution to fit the reflectivity data. As an additional layer (NiFe) was added, the metallic oxide (niobium oxide) layer was converted back to its parent metal by means of the fitted densities. The original metal (Nb) layer thickness was then found by adding the thicknesses of the unoxidized metal layer and the part reduced back from the oxide layer. During the fitting of the new (SiO_x/Nb/NiFe) sample, all parameters obtained from the preceding (Nb) sample was assumed constant, with the exception of the roughness of newly formed interface (Nb/NiFe). The refinement process was repeated until the last sample (the full SV with the Nb cap) of the series.

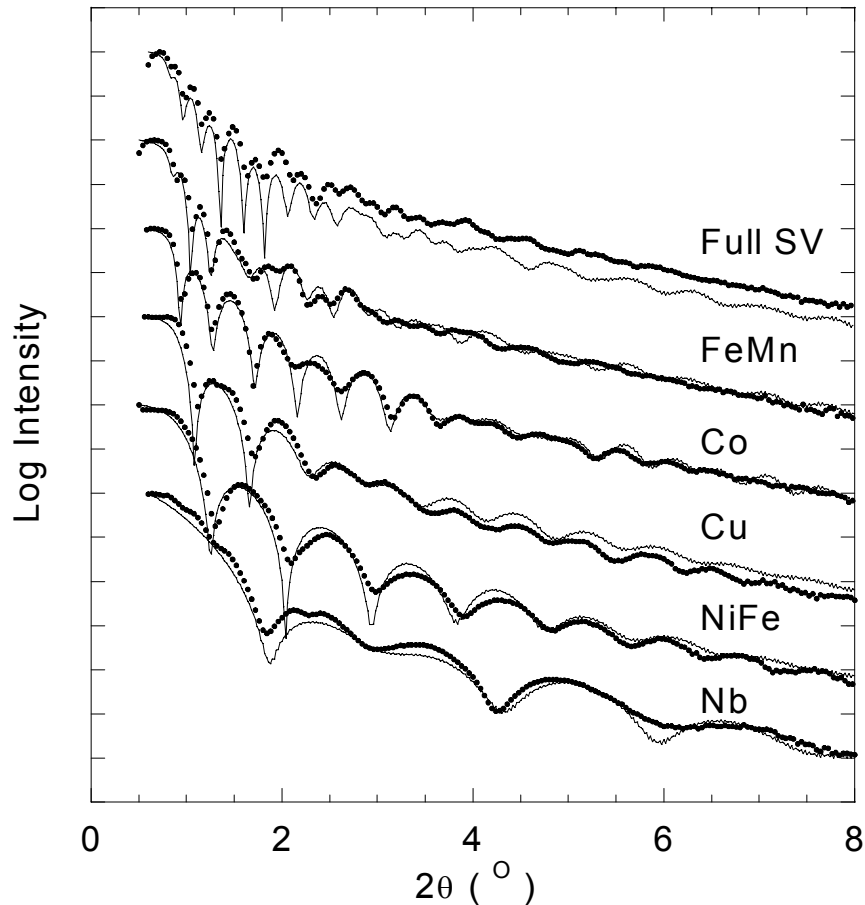


Figure 7.3 Specular reflectivity scans for the built-up samples (symbols) and the corresponding refinement fits (solid lines). Labels next to the scans refer to the composition of the top layer of the built-up samples (except the full SV). Scans were offset for clarity.

One should observe the general difficulty in obtaining information of buried layers and interfaces in common SV structures, which are usually composed of $3d$ transition metals (Ni, Fe, Co or their alloys as pinned and free layers, Cu as the spacer layer, Mn-based alloys as the pinning layer). Since the degree of x-ray scattering is dependent on the electron density of the layers (which is closely related to the atomic numbers), it is particularly difficult to distinguish between the different layers in the SV structures by XRR. As shown in the error estimates of the corresponding parameters (last two columns of Table 7.1), the error could be so large as to produce meaningless results in attempting to fit the whole SV structure. This conclusion led to serious doubts to the results from the previous experiments [1, 2]. The same conclusion has also been drawn by Hase [13], who showed that it is possible to refine the reflectivity scan of a full SV with only a single material (Cu), illustrating the inability of Cu K_{α} radiation in discriminating

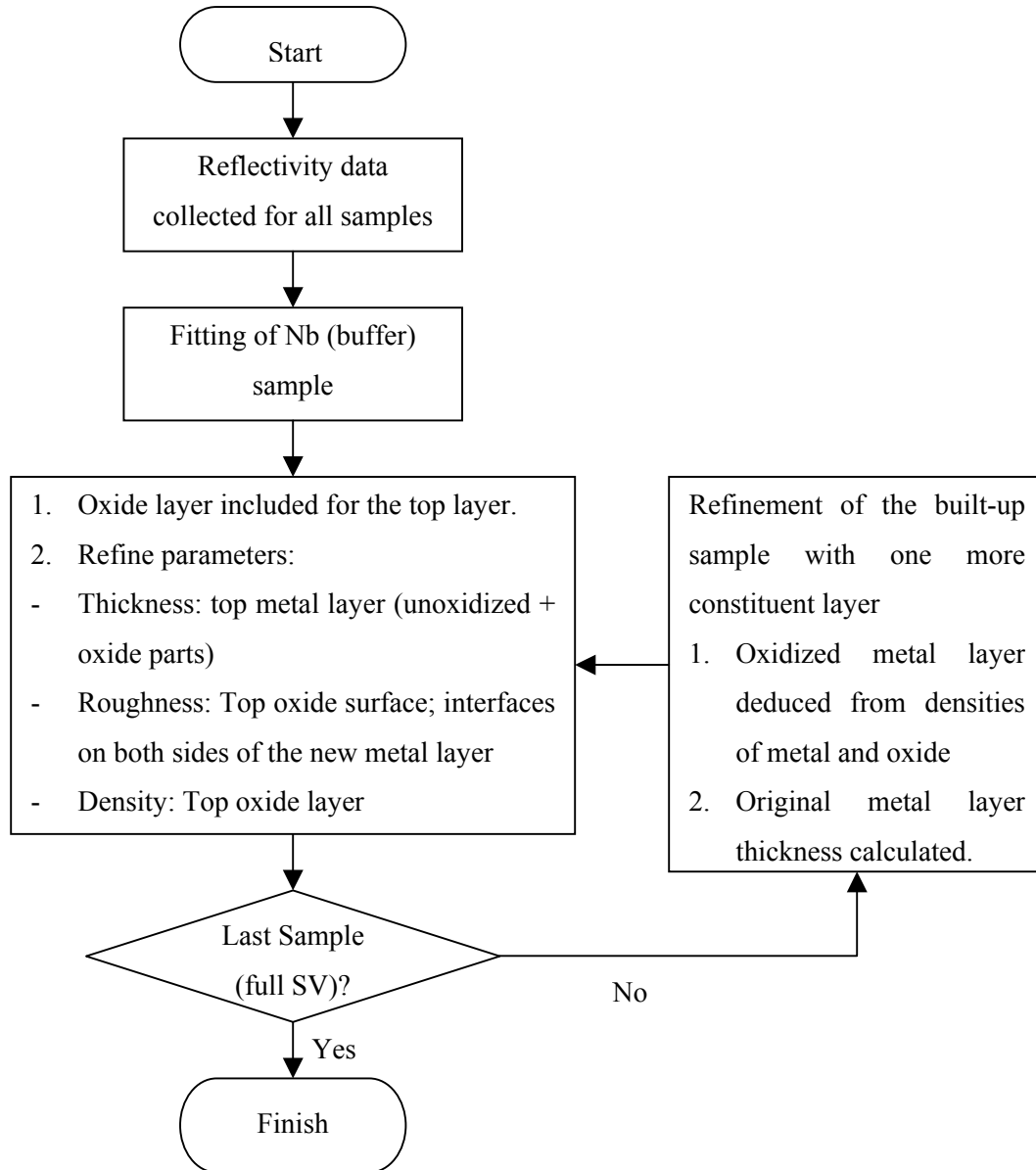


Figure 7.4 Refinement process of specular reflectivity scans of built-up samples.

between the different $3d$ transition metals. The problem can be overcome by choosing a radiation with λ close to the absorption edge of particular elements within the multilayers, which can be easily achieved in synchrotron radiation sources. By far the most commonly used laboratory radiation is $\text{Cu } K_{\alpha}$, which lacks this power. The above discussion reflects the importance of studying the SV structure in the built-up manner in order to eliminate the potential errors.

Table 7.1 Simulated thickness (left column) and interface width (right column) for SV built-up samples (in nm). Parameters in parentheses at the top of each column represent the oxide layers of a particular built-up sample. Values in square brackets are uncertainties. The order in which the built-up samples were deposited is listed at the bottom of the table. The last two data columns (full SV) show the refinement result of the full SV reflectivity scan, using the results obtained from the 'built-up samples' analysis as an initial guess. Direct refinement without using these initial guesses failed to yield any satisfactory fits.

Constituent Layers	Topmost Layer												Full SV		
	Nb (buffer)		NiFe		Cu		Co		FeMn		Nb (cap)				
(Niobium Oxide)											(1.46)	(0.79)	(1.46)	(0.79)	
											[0.12]	[0.06]	[0.22]	[0.1]	
Nb (cap)										(3.5)	(1.2)	4.50	0.99	4.50	0.99
										[0.1]	[0.10]	[0.32]	[0.24]	[0.32]	[0.24]
FeMn							(1.08)	(0.50)	7.6	0.82	9.66	0.6	9.66	0.6	
							[0.06]	[0.03]	[0.25]	[0.2]	[0.1]	[2]	[0.2]	[0.3]	
Co					(1.42)	(0.68)	4.69	0.42	5.31	0.45	5.31	0.45	5.31	0.45	
					[0.12]	[0.04]	[0.11]	[0.06]	[0.4]	[0.15]			[0.4]	[2]	
Cu			(0.9)	(0.48)	1.98	0.48	2.92	0.35	2.92	0.35	2.92	0.35	2.92	0.32	
			[0.03]	[0.04]	[0.03]	[0.04]	[0.14]	[0.10]					[0.2]	[0.2]	
NiFe	(1.49)	(0.43)	3.48	0.48	4.07	0.4	4.07	0.4	4.07	0.4	4.07	0.4	4.07	0.4	
	[0.03]	[0.02]	[0.03]	[0.05]	[0.05]	[3]							[0.2]	[5]	
Nb (buffer)	4.46	0.41	5.22	0.6	5.22	0.6	5.22	0.6	5.22	0.6	5.22	0.6	5.22	0.6	
	[0.02]	[0.02]	[0.03]	[0.3]									[0.2]	[5]	
SiO _x		0.22	0.22		0.22		0.22		0.22		0.22			0.22	
		[0.02]												[0.02]	
Deposition Order	6		4		2		5		3		1,7				

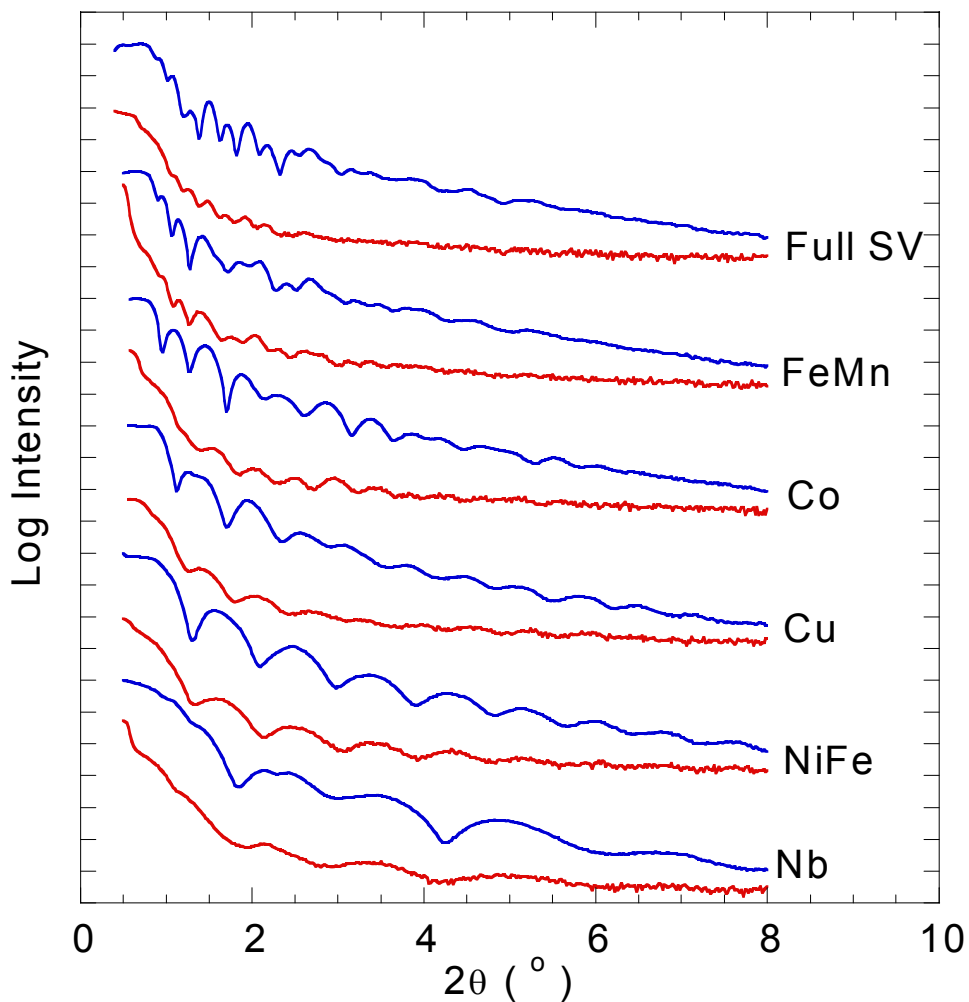


Figure 7.5 Specular (blue line) and off-specular (red line) reflectivity scans of the built-up samples. Labels next to each pair of scans refer to the composition of the top layer of the particular built-up sample. Scans were offset for clarity.

Specular reflectivity scans do not provide information concerning the roughness correlation between two interfaces (i.e. how good the morphological features were copied from one layer to another). An insight into the extent of the vertical correlation could be gained through the comparison between specular and off-specular XRR scans, as shown in Figure 7.5. Kiessig fringes could be seen clearly in the off-specular reflectivity scans, whose periods matched fairly well with that of the corresponding specular scans. This shows a good out-of-plane roughness correlation between layers.

Interface width values provided in specular reflectivity scans are actually a combination of the geometrical fluctuation (roughness) and chemical intermixing. In order to separate the two effects transverse scans have to be performed. Such measurements (and subsequent fitting) are also needed for the quantitative analysis of the correlation lengths (both lateral and out-of-plane) of the multilayers. These experiments are generally performed with synchrotron radiation due to the need of high intensity x-ray sources. A more in-depth discussion can be found in [14].

7.2.2.2 AFM surface imaging

A collection of the AFM images of six built-up samples is presented in Figure 7.6. Qualitatively the granular structures of the films could be observed from the pictures. In general the films were very smooth, with σ in the range of 0.16 to 0.55 nm. It should be noted that the roughness shown here, as measured across the whole image, shows a general increase with an increase in scanning dimension. This could be understood under the self-affine model of film surface mentioned in chapter 2: short distance height variation tend to dominate in the roughness measurement at small scanning distance, and the small height variation has led to a drop in the measured σ . A very major exception is the Nb (5 nm) sample surface, which was unexpectedly rough. Similar results can actually be observed from reflectivity scans in Table 7.1. By ‘cross-sectioning’ the images a peak-to-peak periodicity L in the range of 16 – 40 nm was obtained.

In order to obtain quantitative information on the scans, numerical data were extracted from AFM images of sizes $(500 \times 500) \text{ nm}^2$ to $(2 \times 2) \mu\text{m}^2$, and the height-height correlation function $H(r)$ (equations [2.3] and [2.4]) was used to analyse these data. Typical $H(r)$ vs. r plots for a number of $1 \mu\text{m}^2$ scans of the built-up samples are shown in Figure 7.7, and the analysed results for all the scans are summarized in Table 7.2. Roughness values obtained from the height-height correlation functions were close to the values shown in Figure 7.6, and were comparable to those shown in Table 7.1. Differences did arise though, most notably on the Co and FeMn layers. It is, however, difficult to determine which method is more accurate: AFM imaging, being a local technique, is prone to problem of the finite area of scans and that only a few spots on samples can be examined practically. On the other hand, XRR scans of SV suffers from the contrast issues for different layers that have close atomic numbers.

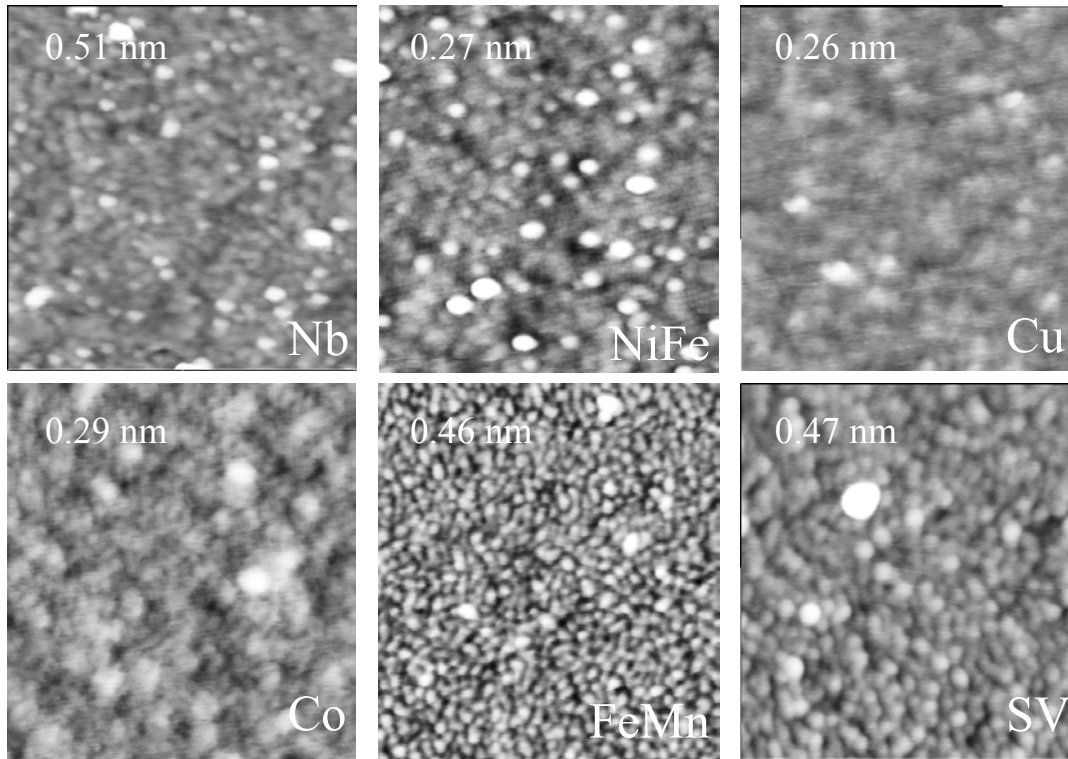


Figure 7.6 AFM images of the surfaces of NiFe/Co SV built-up samples. Scanning area were $(500 \text{ nm})^2$, and the height range were identical (5 nm) in all cases. The values at the left hand corners of the images represent the rms roughness of the corresponding surfaces, whose top layer (except full SV) were shown at the bottom right hand corner of the images.

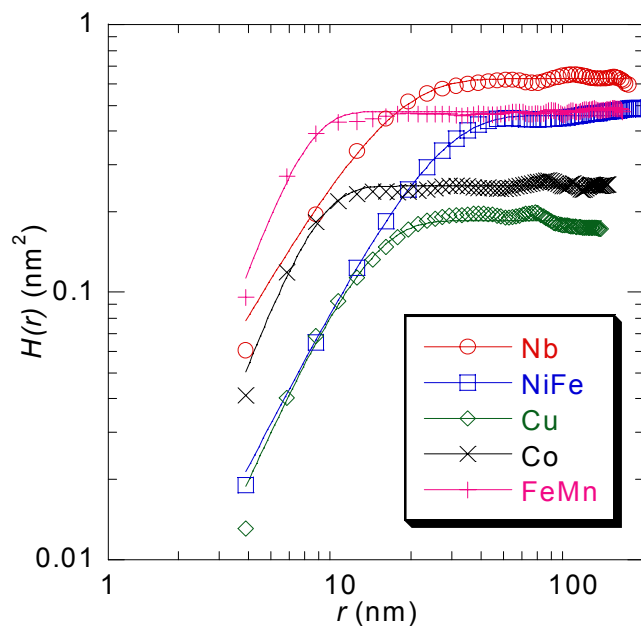


Figure 7.7 Height-height correlation functions for the built-up samples. Height data were extracted from $1 \mu\text{m}^2$ AFM scans. Solid lines are fits using equations [2.3] and [2.4] (see text for explanations). Legends indicate the topmost layers in the corresponding samples (Nb in the legend refers to the sample with only a Nb buffer layer).

Table 7.2 Compiled values of σ , $\xi_{//}$ and h . These values were extracted and averaged from the height-height correlation functions $H(r)$ of 3 – 5 AFM images of the built-up samples, scanning range between 500 nm to 2 μm . Results up to the uncapped full SV are shown.

Top Layer	σ (nm)	$\xi_{//}$ (nm)	h
Nb (buffer)	0.53 ± 0.03	12 ± 3	0.88 ± 0.13
NiFe	0.41 ± 0.07	18 ± 10	0.90 ± 0.13
Cu	0.32 ± 0.09	14 ± 7	0.92 ± 0.17
Co	0.30 ± 0.05	17 ± 10	0.88 ± 0.14
FeMn	0.44 ± 0.06	9 ± 4	0.87 ± 0.12

In terms of the lateral correlation length $\xi_{//}$, the values obtained (~ 10 to 20 nm) were close to the values reported in literature [15, 16]. Strictly speaking, $\xi_{//}$ has a different meaning from L (average peak-to-peak distance on rough interfaces), but they should have similar values. The roughness exponent h , as observed from Table 7.2, is about 0.9. It implies a smooth local roughness structure, and is characteristic among compact films with relatively few voids and overhangs. Such film structures are common among metal thin film growth [17].

7.2.2.3 High-angle XRD

A high angle $\theta/2\theta$ scan is presented in Figure 7.8. Fitting the peaks with the PROFIT program described in Chapter 3 was carried out to quantitatively analyse the scans. From the position of the peaks can be the out-of-plane d -spacing of a particular layer, and hence the texture of the films, can be deduced (using equation [2.6]), by checking against the compiled literature data. It can be seen from Figure 7.8 that most of the peaks concerned are lying in a small region of 2θ (40 – 48 $^\circ$). The sharp peak around 33 $^\circ$ corresponds to the Si (200) peak and the very broad peak around 38 $^\circ$ is the Nb (110) reflection from the Nb buffer. A comparison between the two control full SV samples is shown in Figure 7.9. Qualitatively they are of very similar behaviour, with the peaks lying close to one another. This implies a similar texture between two samples.

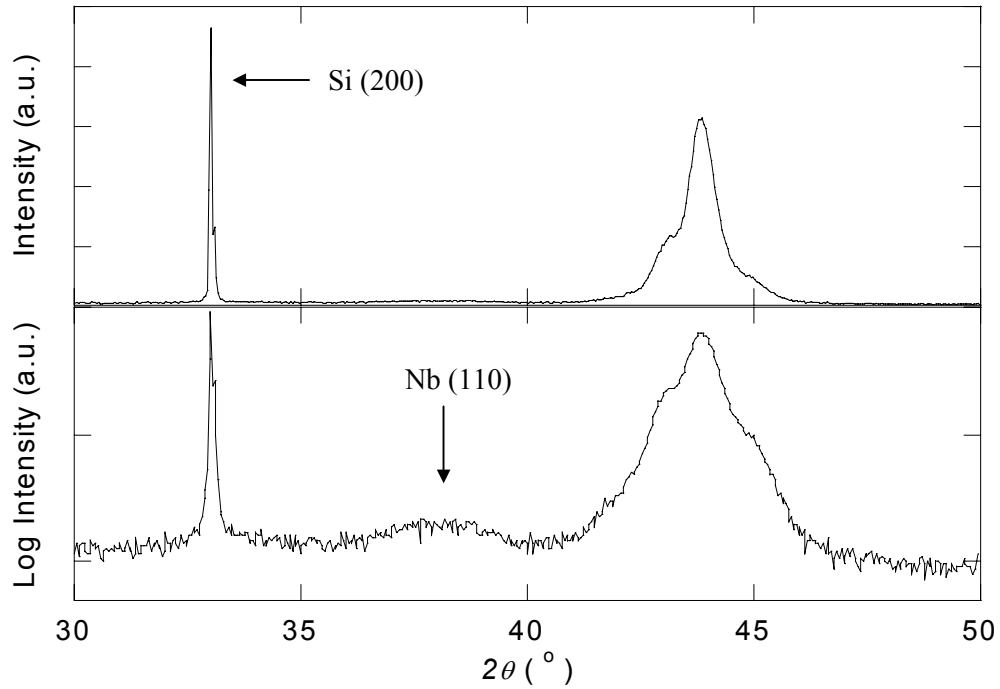


Figure 7.8 $\theta/2\theta$ scans of the built-up sample Nb/NiFe/Cu/Co/FeMn in the 2θ range of $30 - 50^\circ$. The same scan is shown in linear (upper graph) and log (lower graph) scales to reveal the peaks. The peaks at $2\theta = 33^\circ$ and $\sim 38^\circ$ are the Si substrate and Nb buffer layer peaks. Peaks of the other layers (in the range of $40 - 48^\circ$) are discussed in further details in Figure 7.10.

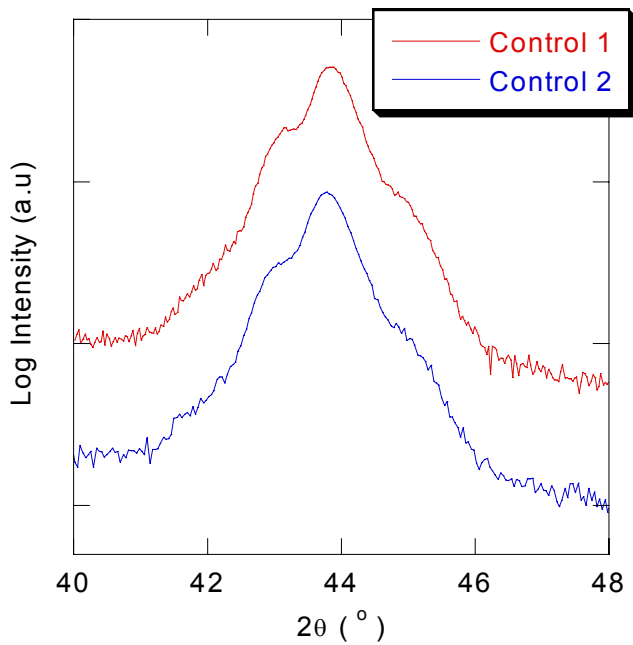


Figure 7.9 High angle $\theta/2\theta$ scans of the control full SV samples.

High angle $\theta/2\theta$ scans of the built-up samples are illustrated in Figure 7.10, showing how consecutive diffraction peaks from different layers are added to the scans. The evolution of the microstructures could be seen with the subsequent deposition of various layers. With a small number of layers, broad peaks with low intensities were detected. With the increasing number of layers, the peaks became sharper, sometimes accompanied by a change in the peak positions (see the NiFe/Cu peak for example). The layers in the samples, except Nb, were found to be fcc (111) textured. While the Nb capping layer was bcc (110) textured, a very weak and broad peak was observed for the buffer layer.

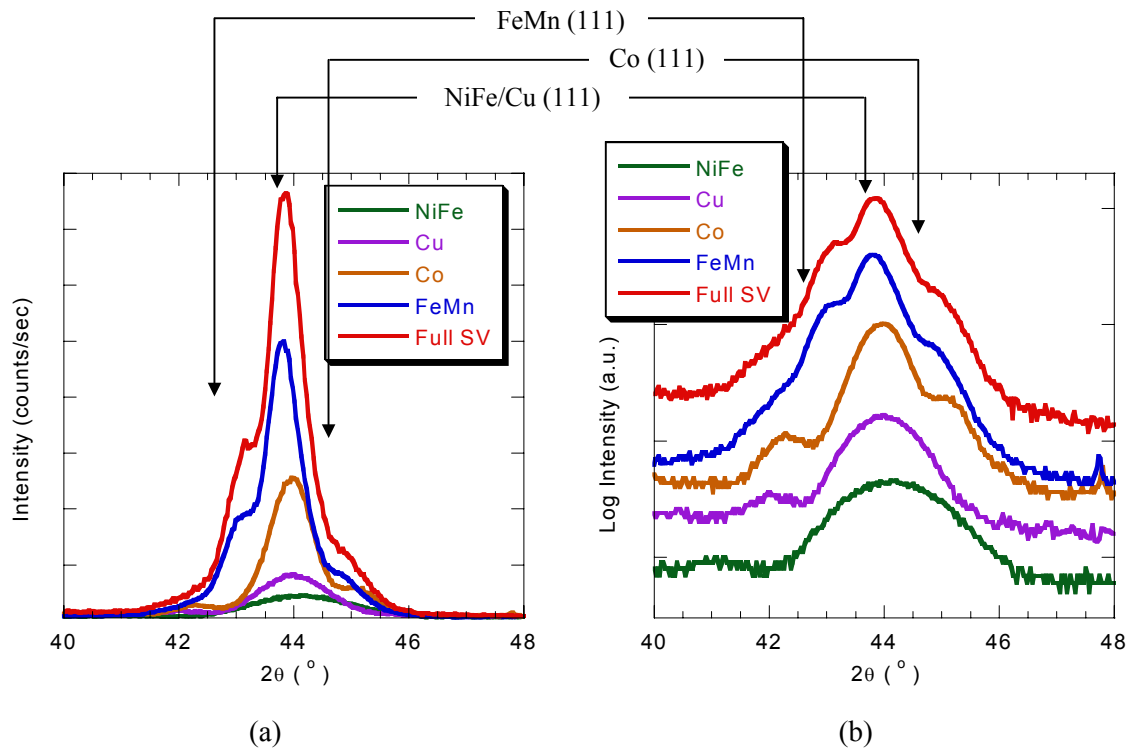


Figure 7.10 High angle $\theta/2\theta$ scans of the built-up samples. The intensities are shown in linear (a) and log scales (b) to reveal the details of the peaks. The Nb layers were omitted from the scans. Labels above the scans indicate the 2θ values for (111) reflections of NiFe, Cu, Co and FeMn.

Figure 7.11 shows the variation of the d -spacings of the NiFe/Cu, Co and FeMn layers with the subsequent addition of constituent layers. From the $\theta/2\theta$ scans of Nb/NiFe/Cu samples in Figure 7.10(b), a bump was observed at the left hand side of the main peak at around 44° 2θ . Given the small intensity of the peak it was thought to arise from the intermixing of the NiFe and Cu at the interface instead of contribution from the Cu layer alone (compare with Figure 7.10(a)). The proximity of the NiFe and Cu peaks prevented the extraction of the exact peak positions.

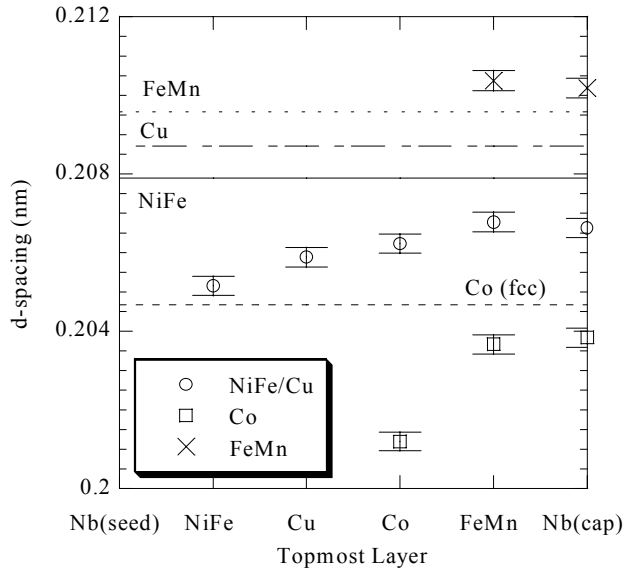


Figure 7.11 The *d*-spacing values extracted from the $\theta/2\theta$ scans, by means of the PROFIT profile fitting program. Horizontal labels show the *d*-spacing of the (111) reflections of corresponding layers.

From Figure 7.11 one could obtain some insight on the evolution of stress states in various layers. In the $\theta/2\theta$ scans it is the out-of-plane *d*-spacing that is being probed. Assuming elastic distortions of the lattices, a drop in the *d*-spacing in the out-of-plane direction from the bulk value implies a corresponding rise in the *in-plane* lattice spacing and hence a tensile stress in the film plane. From this a number of observations can be drawn from Figure 7.11. The NiFe, Cu and Co layers have shown an *in-plane* tensile stress in all the samples, while the FeMn layer showed a compressive stress. It was also interesting to observe how the stress changed with the addition of various layers. All the layers have shown a tendency of returning to the equilibrium *d*-spacing with the addition of layers, implying a decrease in the stress magnitude with the addition of layers.

It has to be clarified that it was the *global* stress that was discussed, since local stress states would not affect the lattice structure of the whole film. Besides, the method could not distinguish the possible uniaxial stress states from biaxial stresses. These two different types of stresses can combine together and give rise to a change in the lattice spacing in the vertical direction. Ideally other simple x-ray methods (such as ω -scans in two different *in-plane* axes) could be employed to detect the presence of *in-plane* uniaxial stresses, but they did not seem to work well in the present structure. Problems arise when the microstructural properties of different layers (lattice constant and lattice structures) are very close together and the peaks are wide (due to their polycrystalline nature). In fact, most of the studies on film stresses have assumed biaxial stress states, given that the films were deposited in an otherwise homogenous environment.

Figure 7.12(a) illustrates the evolution of the 2θ -peak widths in relations to the subsequent deposition of various layers. Grain sizes calculated by Scherrer equation (equation [2.8]) are shown in Figure 7.12(b). The use of $\beta_{2\theta}$ instead of FWHM- 2θ was due to the fact that only $\beta_{2\theta}$ could be corrected for instrumental broadening using equation [2.7]. The general trend of variation of FWHM- 2θ and $\beta_{2\theta}$ with regard to the addition of layers was essentially identical, so the choice of parameters did not have significant influence on any conclusions.

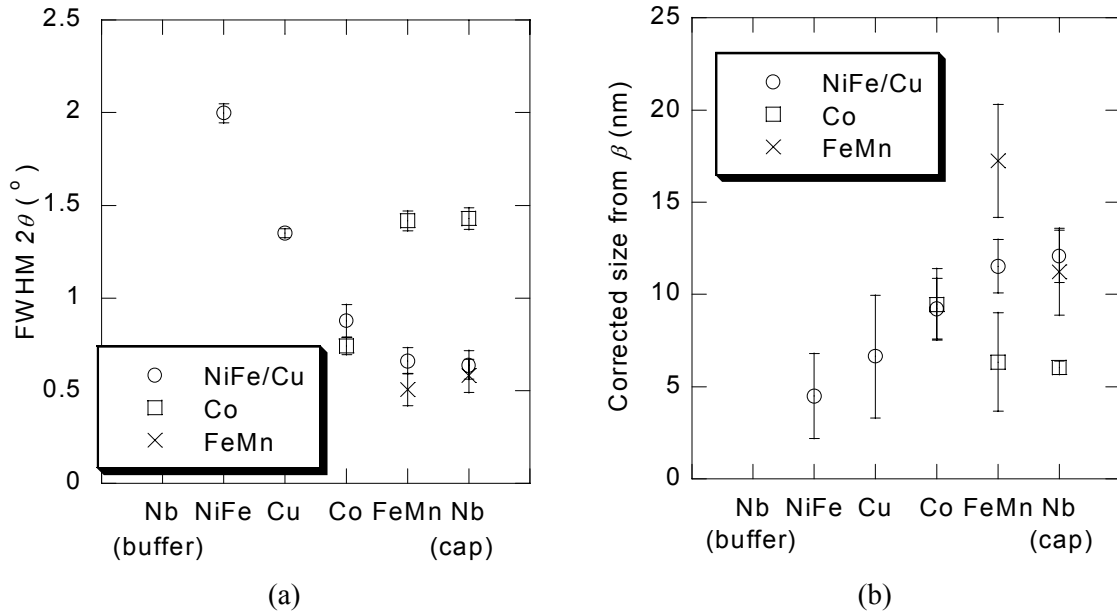


Figure 7.12 As-extracted FWHM- 2θ values (a) and grain sizes calculated from $\beta_{2\theta}$ by the Scherrer equation after corrections for instrumental broadening (section 2.1.2.2.) (b).

An attempt has been made to obtain the microstrain and grain size by means of the Williamson-Hall plots (section 2.1.2). The idea was to obtain higher order reflection ((222) reflections in this case) from the built-up samples. The contribution of peak broadening due to grain sizes and microstrain could then be separated, once the constant terms and the slopes of the two-point fitted lines were extracted (equation [2.9]). Unfortunately, the results obtained were far from satisfactory. Unrealistically large or negative grain sizes have been obtained, revealing the large degree of uncertainty in determined parameters. This was thought to be caused by the poor counting statistics obtained during the experiments. Low peak intensity, especially at the higher order of reflections, meant large errors (which scaled as $\frac{1}{\sqrt{N}}$, where N is the number of counts

obtained in the x-ray measurements). Besides, the high degree of out-of-plane texture of the layers meant that only (111) and (222) reflections of the layers were available for analysis.

It is also interesting to investigate the mosaicity of the layers. This has been done by means of performing ω -scans at the corresponding peaks. As-measured FWHM- ω values are shown in Figure 7.13. The large values (5.4 – 7.8°) clearly show the polycrystalline nature of the films. The Nb buffer layer, which is not shown in the data, has a FWHM more than 10° (the background was not reached for a 30°-range ω -scan about the specular condition). This, together with the very low intensity of the $\theta/2\theta$ peak, suggests a highly disordered Nb buffer layer.

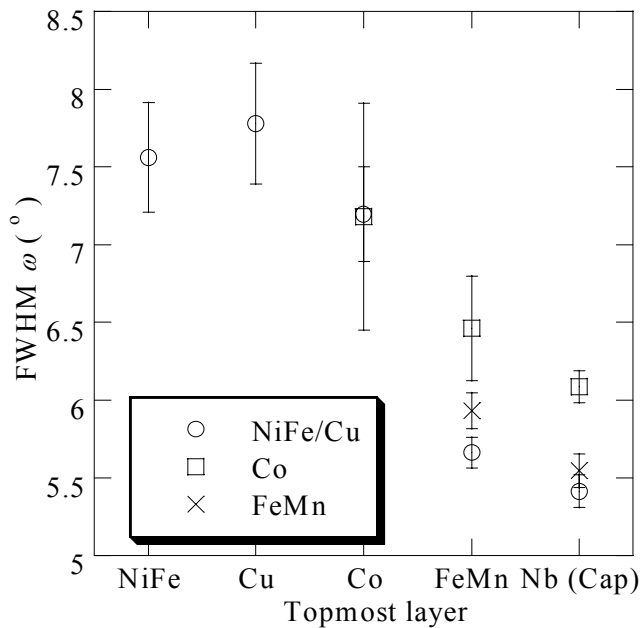


Figure 7.13 As-measured FWHM- ω values of the corresponding peaks along the line of built-up samples. X-axis refers to the topmost layer of the corresponding samples.

What was puzzling though was the continuous drop in the peak width of the ω -scan peaks with the addition of subsequent layers. This happened to all the constituent layers, as evident from Figure 7.13. The results are quite puzzling, as one would expect that the addition of materials on top would not greatly affect the microstructures of the layers underneath. A possibility is the temporary heating effect during the deposition of the layers. Energetic adatoms and reflected neutrals have to lose energy before they are settled in their equilibrium positions. This provided the heat for local annealing the films underneath, leading to an improvement in the crystallinity. However, the chance of such a scenario is questionable, given that the low substrate temperature during deposition.

7.3 Discussion

The results shown above have clearly indicated the importance and usefulness of using the strategy of ‘built-up’ samples in the investigation of structural properties of the SV structures. This can be argued as follows:

1. The low angle reflectivity measurements, as probed through the built-up samples, have yielded more reliable results than simply examining the complete SV structures. As seen in Table 7.1, the uncertainties in determining the morphological parameters (thickness and, in particular, roughness) could be much reduced by studying the built-up samples. This is particularly important with Cu K_α radiation, which lacks discriminating power for different 3d-transition metals. The use of the AFM in quantitative extraction of the structural information, unless performed *in situ*, could only be applied by means of the ‘built-up samples’ technique as well.
2. Evolution of microstructures and in-plane stress states with the deposition of subsequent layers can certainly be studied only through the high angle XRD of the built-up samples.

Uncovered surfaces are prone to oxidation. As illustrated in Figure 7.4, oxide layers have to be introduced during the fitting of reflectivity scans of the built-up samples. Problems may arise in determining the phase(s) of the possible oxide(s) present on a built-up sample. Nb, for example, have a very complex oxides family [18], and the oxidation of thin films can be very different from bulk states [19]. This has led to uncertainties in determining the real thickness of a particular layer. A compromise can be made by capping the samples with thin layers of chemically inert material. Ideally the material should have a minimum intermixing effect with the built-up sample, resistant towards oxidation and readily identifiable from the x-ray studies. To this end Au seems to be a good choice, due to its chemically inert nature, low intermixing with metals, and the large atomic number (= 79) compared with the 3d-transition metals and Nb (= 41).

7.4 Summary

In this chapter experimental results on the structural characterization of SV built-up samples were presented. Through this study detailed information concerning the structural properties of the SV structure was obtained, which is more reliable than simply studying the complete SV structure. Such information proved to be useful in the investigation of the electrical and magnetic properties of the SV, as shown in the following chapter.

References for Chapter 7

1. T.C. Huang, J.P. Nozieres, V.S. Speriosu, B.A. Gurney and H. Lefakis, *Appl. Phys. Lett.* **62**, 1478-1480 (1993).
2. T.C. Huang, J.P. Nozieres, V.S. Speriosu, H. Lefakis and B.A. Gurney, *Appl. Phys. Lett.* **60**, 1573-1575 (1992).
3. E. Brown and M. Wormington. *An investigation of giant magnetoresistance (GMR) spin-valve structure using x-ray diffraction and reflectivity.* in *49th Annual (2000) Denver X-ray Conference*. 2000. Denver, Colorado.
4. X. Portier and A.K. Petford-Long, *J. Phys. D: Appl. Phys.* **32**, R89-R108 (1999).
5. F. Bensmina, A. Dinia, C. Meny, P. Panissod and D. Muller, *Eur. Phys. J.: Appl. Phys* **11**, 97-101 (2000).
6. A.J. Devasahayam and M.H. Kryder, *IEEE Trans. Magn.* **35**, 649-654 (1999).
7. B. Dieny, *J. Magn. Magn. Mater.* **136**, 335-359 (1994).
8. C. Eisenmenger-Sittner, *J. Appl. Phys.* **89**, 6085-6091 (2001).
9. B. Dieny, V.S. Speriosu, S.S.P. Parkin, B.A. Gurney, D.R. Wilhoit and D. Mauri, *Phys. Rev. B* **43**, 1297-1300 (1991).
10. W.J. Antel, F. Perjeru and G.R. Harp, *Phys. Rev. Lett.* **83**, 1439-1442 (1999).
11. R.D. Slater, J.A. Caballero, R. Loloee and W.P. Pratt, *J. Appl. Phys.* **90**, 5242-5246 (2001).
12. N.W. Ashcroft and N.D. Mermin, *Solid State Physics*. Saunders College (1976).
13. T.P.A. Hase, B.K. Tanner, P. Ryan, C.H. Marrows and B.J. Hickey, *IEEE Trans. Magn.* **34**, 831-833 (1998).
14. T.P.A. Hase, *Ph. D. Thesis*, University of Durham (1998).
15. S.O. Demokritov, *J. Phys. D: Appl. Phys.* **31**, 925-941 (1998).
16. J.C.S. Kools, W. Kula, D. Mauri and T. Lin, *J. Appl. Phys.* **85**, 4466-4468 (1999).
17. H.N. Yang, G.C. Wang and T.M. Lu, *Diffraction from rough surfaces and dynamic growth fronts*, pp. 136-168, World Scientific Pub. (1993).
18. J. Halbritter, *Appl. Phys. A-Mater. Sci. Process.* **43**, 1-28 (1987).
19. O. Hellwig and H. Zabel, *Physica B* **283**, 228-231 (2000).

Chapter 8 Electrical and Magnetic Characterization of NiFe/Co Spin Valve Built-up Samples

As a continuation of Chapter 7, this chapter summarizes the electrical and magnetic measurements on the SV built-up samples. A number of unexpected results have been obtained in these measurements. Investigations on the possible causes of these results are detailed.

8.1 Control full SV results

In this section comparison of magnetic and electrical measurement results of the two samples are illustrated. The $R(H)$ measurements of the samples in Figure 8.1(a) indicate that the samples have similar MR ratios ($\sim 4.5\%$), although the H_{ex} (-200 and -170 Oe) and H_c (20 and 13 Oe) of the pinned layers of the samples do not match very well. The free layers of the samples, on the other hand, have similar H_o (-13 and -17 Oe for control samples 1 and 2 respectively) and H_c (~ 1 Oe). Similar values have been observed in the $M(H)$ measurements shown in Figure 8.1(b). The results suggest that while the bottom layers (NiFe/Cu/Co) had excellent reproducibility, at least the Co/FeMn structure did not reproduce well. This fact has to be remembered during the analysis of the built-up sample results.

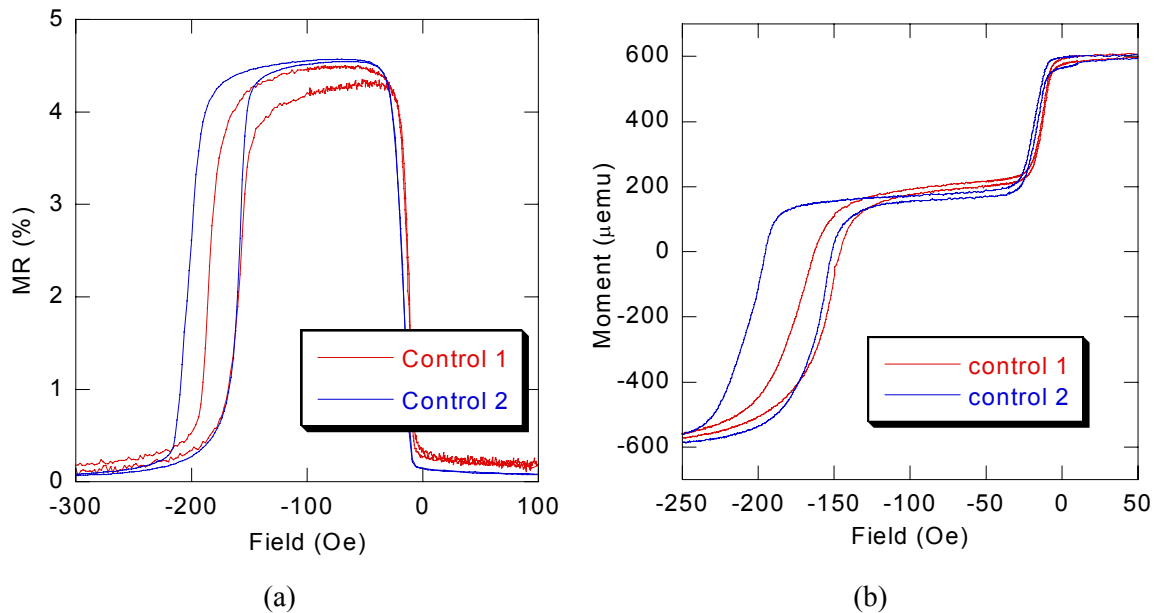


Figure 8.1 Comparison of the two control full SV samples in (a) $R(H)$ measurements and (b) $M(H)$ measurements. All measurements were made along the in-situ field direction.

8.2 Electrical measurements

8.2.1 Van der Pauw resistivity measurements

Electrical properties of the built-up samples as measured by the van der Pauw geometry are shown in Table 8.1. The sheet resistances of the built-up samples were calculated by equation [2.12] (shown as the ‘stack resistance’ in the table). Then by assuming a parallel circuit model, resistances of the layers were extracted from the sheet resistance of the corresponding and the previous built-up samples. The resistivity of the layer was then obtained by multiplying the layer’s sheet resistance with the layer thickness.

In general the resistivities of the layers were about 4 to 10 times that of the literature bulk resistivity values. This is an expected result for thin films. Defects in metallic films can scatter electrons, leading to an increased resistivity. In sputtered film these defects exist in vast quantity compared with the bulk materials (in the form of grain boundaries, impurities, dislocations, etc.). This can be clearly seen in the Nb cap and buffer layers, for example. The high resistivity of Nb buffer compared with the cap again shows its highly disordered nature.

Table 8.1 Resistivity measurement results as obtained by van der Pauw method for build-up samples (assuming parallel circuits for individual layers and neglecting oxidation effects). Figures in brackets are errors of the corresponding results. Literature values of resistivities are also listed in the table. The FeMn value next to literature value was obtained by resistivity measurement on a (183 ± 10)-nm sputter deposited film sample.

Constituent layers	RT stack resistance (Ω/sq)	RT layer resistance (Ω/sq)	RT layer resistivity ($10^{-8} \Omega \text{ m}$)	RT Bulk resistivity ($10^{-8} \Omega \text{ m}$)
Nb (seed)	300.3 (1.4)	300.3 (1.4)	157 (16)	14.5 [1]
NiFe	52.87 (0.25)	64.17 (0.44)	23.6 (2.5)	~15 [2]
Cu	29.67 (0.14)	67.6 (1.1)	22.3 (2.6)	1.70 [1]
Co	17.29 (0.12)	41.43 (0.94)	22.0 (2.7)	5.8 [1]
FeMn	10.73 (0.090)	28.29 (0.93)	27.3 (3.6)	88.12 [3]; 140
Nb (cap)	9.844 (0.082)	119 (23)	62 (18)	14.5 [1]

There are a number of observations that appeared puzzling at the first sight. The first one is the high resistivity of the Cu layer ($(22.3 \pm 2.6) \times 10^{-8} \Omega \text{ m}$), which is of similar value to that of the neighbouring Co ($(22.0 \pm 2.7) \times 10^{-8} \Omega \text{ m}$) or even NiFe ($(23.6 \pm 2.5) \times 10^{-8} \Omega \text{ m}$) layers. The second one is the abnormally low FeMn resistivity ($(27.3 \pm 3.6) \times 10^{-8} \Omega \text{ m}$). The resistivity of a thick calibration FeMn sample has been measured, which was found to be higher than that of the literature value and about 5 times higher than that in the built-up sample.

A number of reasons could have led to these results:

- Oxidation of the top layers has not been taken into account of the resistivity calculations. Such calculations are difficult, as the oxide layers may comprise of several different phases as mentioned in last chapter. Nevertheless, even conductive oxides should have much higher resistivity compared with the metal films and should have led to a rise in the calculated resistivity. While this may be the case of the Cu film, it could not explain the low resistivity of the FeMn film. Measurements have been repeated on fresh Nb/NiFe/Cu built-up samples taken out of the deposition chamber, which gave virtually the same results.
- Surface effects: As mentioned in Chapter 2, thin film/air can interfaces give rise to scattering of electrons. In the case of very thin films, the increased probability of surface scattering effectively lowered the electrons' mean free path of travel in the film, leading to a rise in the resistivity. Again this explanation is applicable only in the observed Cu layer resistivity. Specular reflection (section 6.2.3), on the other hand, can cause a drop in the resistivity of the stack underneath and hence lead to an apparent decrease of the resistivity, which may explain the case of ρ_{FeMn} . This effect, however, are usually observed with noble metal caps, and they are often short-range effects [4].
- Presence of interfacial states is yet another possibility that has led to resistance change. The effect of such states is not so simple. In general, alloying of two metals at interfaces could lead to a rise in resistivity. On the other hand, segregation of atoms have been reported in literature [5, 6]. In particular, if the segregated atoms form large clusters they may become 'easy paths' for electronic conduction, effectively leading to a reduced resistivity.

Additional experiments were performed to investigate the potential causes of the abnormal results, as described below.

8.2.1.1 Cu layer resistivity investigation

A batch of samples of structure Nb (5 nm)/NiFe (4 nm)/Cu (t_{Cu} nm) were deposited under conditions identical to those used for preparing the built-up samples. The idea of this experiment was to investigate whether surface effect was responsible for the rise of the Cu layer resistivity in the built-up samples. Figure 8.2 shows the results of the measurements, with the copper layer conductivity σ_{Cu} plotted against t_{Cu} . The use of σ_{Cu} enabled numerical fitting of the Fuchs-Sondheimer model (equation [2.11]). σ_{Cu} increases from 3 to 14×10^6 ($\Omega \text{ m}$)⁻¹ (which was equivalent to a drop of resistivity from 30 to $7 \times 10^8 \Omega \text{ m}$) as t_{Cu} increases from 2 to 11 nm. By fitting with equation [2.11], with $\sigma_{Cu}(\infty)$ set to 5.88×10^7 ($\Omega \text{ m}$)⁻¹ (Table 8.1), one gets $\delta_{Cu} = 102 \pm 20$ nm, which is larger than the literature value (42 nm) [7]. Attempts have also been made to fit the data with specular reflection included at the surfaces, but the δ_{Cu} value so obtained was always larger than 102 nm.

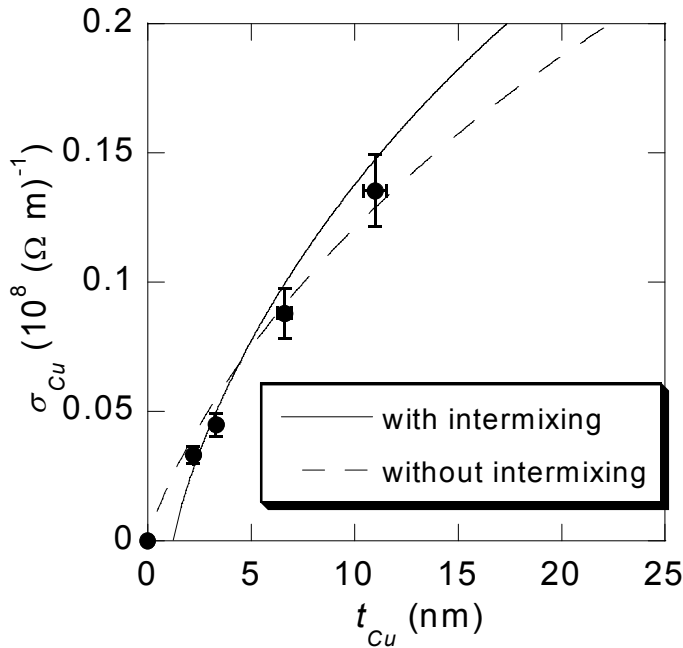


Figure 8.2 Copper layer conductivity σ_{Cu} against copper layer thickness t_{Cu} as measured from Nb (5 nm)/NiFe (4 nm)/Cu (t_{Cu} nm) samples. Dashed line is a fit of σ_{Cu} by direct application of equation [2.11], without taking into account of the possible NiFe/Cu intermixing. Solid line is a modified fit with the introduction of an intermixed NiFe/Cu interface.

On the other hand, it is well known that Cu intermixes strongly with Ni in permalloy, which introduces a paramagnetic ‘dead layer’ at the interface and lowers the MR ratio [8]. The effect of interface mixing was considered by adding a second layer in parallel with the NiFe layer for analysis. Numerical fitting with such a model (solid line in Figure 8.2) gave a dead layer thickness of 1.2 ± 0.4 nm and $\delta_{Cu} = 74 \pm 6$ nm, which is a closer estimate to the literature values.

8.2.1.2 FeMn layer resistivity investigation

Samples of structure Nb (5 nm)/NiFe (4 nm)/Cu (3 nm)/Co (5 nm)/FeMn (t_{FeMn} nm) were also deposited to investigate the t_{FeMn} dependence of ρ_{FeMn} . Figure 8.3 shows the corresponding results. In marked contrast with the results of the Nb/NiFe/Cu samples, the resistivity of the FeMn layer *increases slowly* with the addition of the FeMn thickness. These results clearly cannot be explained in the framework of the Fuchs-Sondheimer resistivity model. It is noted that the ρ_{FeMn} value of the data shown in Figure 8.3(b) is nearly 3 times higher than that shown in Table 8.1 for about 10 nm of FeMn. Even so the low value of ρ_{FeMn} was evident from Figure 8.3 in the range of t_{FeMn} investigated, and a mechanism other than surface scattering has to be sought after to deal with the issue.

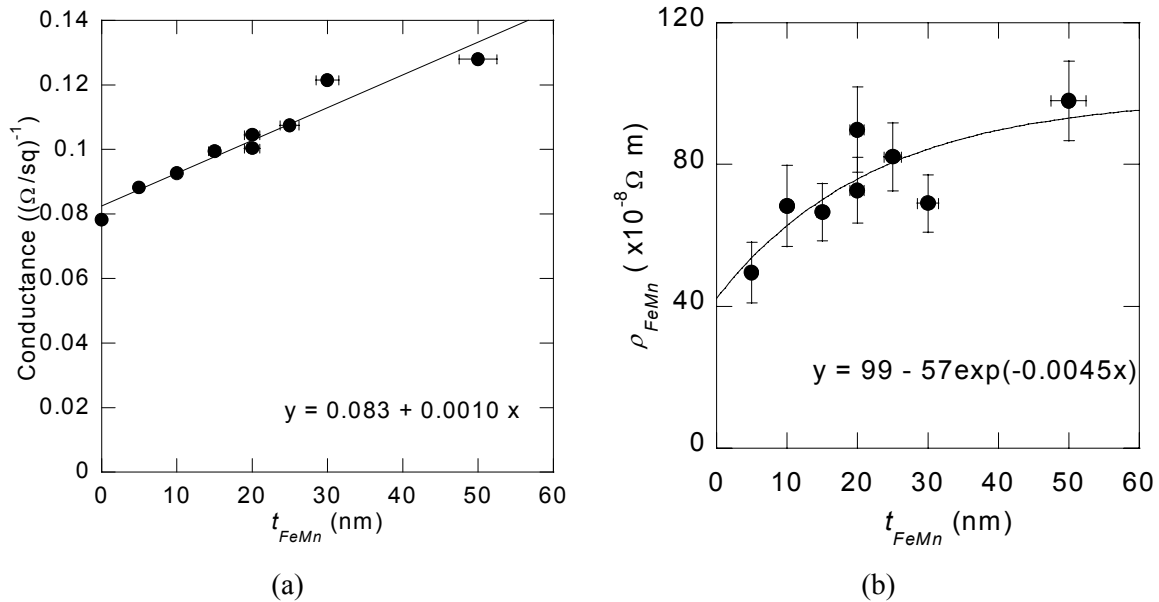


Figure 8.3 Sheet conductance of samples Nb (5 nm)/NiFe (4 nm)/Cu (3 nm)/Co (5 nm)/FeMn (t_{FeMn} nm) (a) and the corresponding FeMn layer resistivity extracted from the samples, assuming a parallel circuit model (b). Solid line in (a) is a fit to the data using a parallel circuit model, and (b) is an exponential fit. Note that the asymptotic limit of the fit in (b) ($146 \times 10^{-8} \Omega \cdot \text{m}$) matched well with the FeMn resistivity measured from the bulk calibration sample (Table 8.1).

As mentioned before, two different mechanisms were suggested for the possible drop of ρ_{FeMn} . If specular reflection was the case, one would expect a rise in the stack (Nb/NiFe/Cu/Co/FeMn) conductance at very small t_{FeMn} , which then approach asymptotically to a straight line with slope equal to the FeMn bulk conductivity. No clear evidence of such trend could be observed from the

data in Figure 8.3(a). A straight line was used to fit the data, assuming a parallel circuit model without specular scattering. The parameters as obtained from the fit correspond to a stack resistance of 12 ± 0.4 (Ω/sq) at $t_{\text{FeMn}} = 0$ and $\rho_{\text{FeMn}} = 99 \pm 10 \times 10^{-8} \Omega \text{ m}$.

To investigate the effect of possible intermixing and segregation at interfaces, a number of samples with 10-nm of FeMn deposited on top of different buffer layers were prepared. Table 8.2 shows the corresponding results. While FeMn films deposited on Nb and Co have more sensible resistivity values, the corresponding result for FeMn layer deposited on Cu/Co buffer does have value close to those shown in Figure 8.3. This suggested the existence of interfacial states when FeMn were deposited on Cu/Co (or even on Co) films. It would be hard to investigate what was the exact cause of the phenomenon, at least with the characterization techniques used in this project, but the results in Table 8.2 have shed some light on the possible direction of investigations.

Table 8.2 Resistivity measurement of 10-nm thick FeMn films deposited on different types of buffer layers, as measured by the van der Pauw geometry. Figures in brackets are errors of measurements.

Buffer layer	Buffer layer resistance (Ω/sq)	Total stack resistance (Ω/sq)	FeMn layer resistivity ($\times 10^{-8} \Omega \text{ m}$)
Nb (5 nm)	146 (8)	72.5 (6)	142
Co (5 nm)	106 (8)	51 (5)	98
Cu (3 nm)/Co (5 nm)	39.5 (2)	23.5 (2)	60

8.2.2 Field dependent resistivity ($R(H)$) measurements

The RT angular $R(H)$ measurements of the built-up samples are shown in Figure 8.4, with ϕ being the angle between the *in situ* deposition field and the measurement field directions. In all the measurements current was applied along the *in situ* field direction, implying that ϕ was also the angle between the measurement field and the applied current in these measurements. The field dependence of the Nb/NiFe and Nb/NiFe/Cu samples shown in (a) and (b) of Figure 8.4 are attributed to the AMR response of the NiFe layer. The MR of the two samples were qualitatively similar, except that the magnitude the former one (0.55%) was larger than the later one (0.47%). This could be attributed, at least partly, to the current shunting of the Cu layer. This was not adequate though, given that the *absolute* resistance change in the Nb/NiFe/Cu (0.15 Ω/sq) is less

than half ($0.36 \Omega/\text{sq}$) of the Nb/NiFe sample. Intermixing of the NiFe and Cu may have to be taken into account to explain this. It is known that intermixed layers between NiFe and Cu are magnetically dead [8]. Besides, the AMR response of FM films are highly sensitive to the thickness of the FM layer, as mentioned in Chapter 3. Such effects have to be taken into account to fully explain the MR drop.

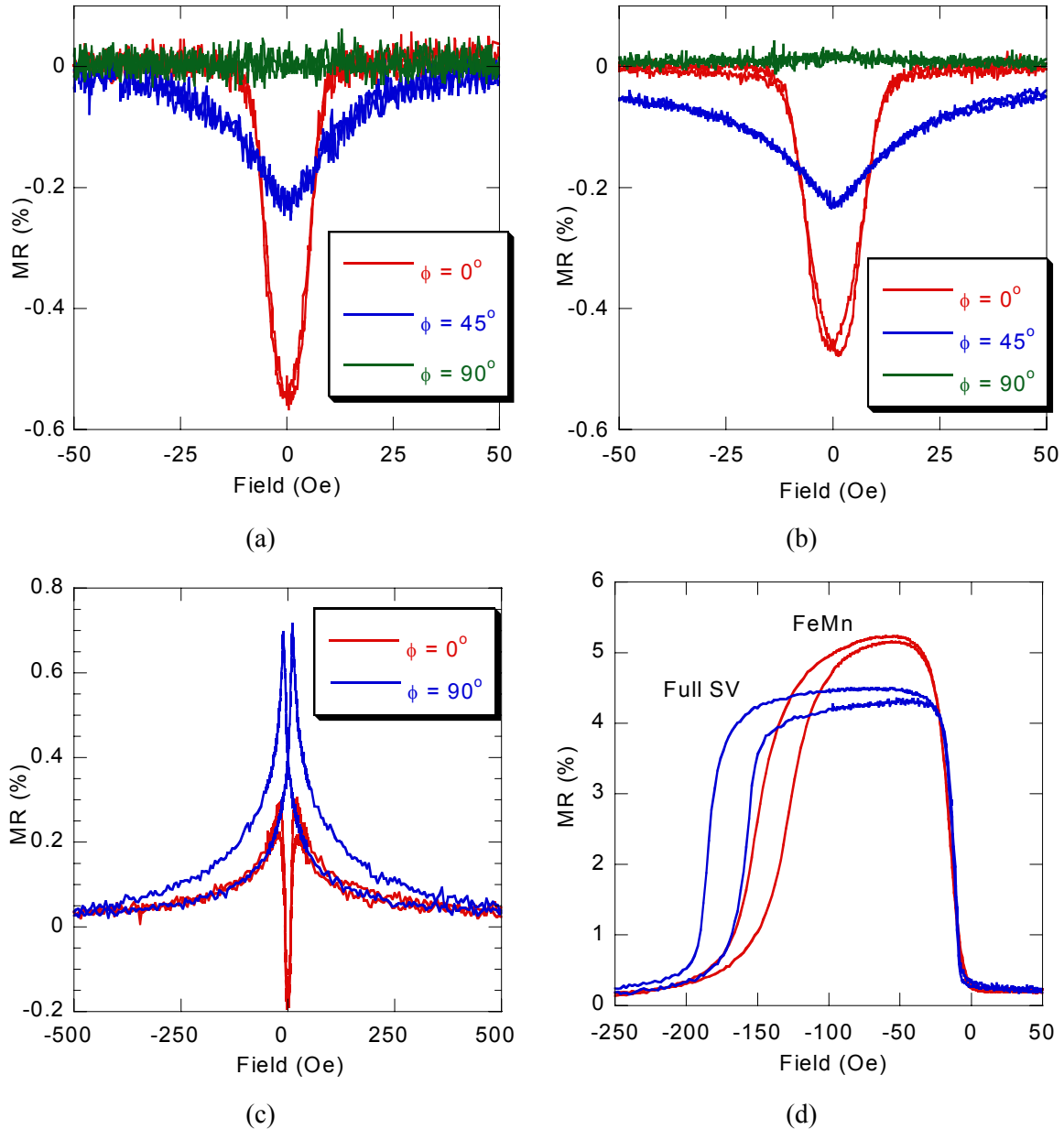


Figure 8.4 RT $R(H)$ responses of the built-up samples with different orientations ϕ (angle between measurement field and in-situ deposition field): (a) Nb/NiFe; (b) Nb/NiFe/Cu; (c) Nb/NiFe/Cu/Co; and (d) SV samples measured at $\phi = 0^\circ$.

The absence of the AMR effect at $\phi = 90^\circ$, however, worth some discussions. As mentioned in Chapter 2 that the AMR effect arises whenever there is a relative orientation between the magnetization and current directions, which has a $\cos^2\eta$ dependence (equation [3.8]). Therefore, AMR occurs if the FM orientation changes. This can be done by applying an external field. At high magnetic fields, the sample is saturated along the field direction (for NiFe this can happen within a few Oe, as seen in Figure 5.3). The absence of the AMR effect implies that the system fails to distinguish between the high and low-field magnetization states of the FM. This could be possible if the magnetization reversal took place by domain wall motion. In such a case individual domains align either parallel or antiparallel to the current direction (neglecting the influence of domains walls and domains aligned in other orientations), giving no contribution to MR.

However, domain wall motions are expected to be more dominant when the applied field axis is close to the anisotropy axis, which is $\phi = 90^\circ$ according to Figure 8.4(a) and (b). Thus puzzle arises, as this direction was *perpendicular* to the *in situ* deposition field direction. It was expected that a hard-axis behaviour would be observed along this direction due to induced anisotropy (section 1.2), which is clearly not the present case. To obtain more direct evidence, however, one has to resort to magnetic measurements (such as M(H) loops), which is presented in the next section.

Figure 8.4(c) shows the $R(H)$ behaviour of the ‘pseudo SV’ (Nb/NiFe/Cu/Co) built-up sample. Compared with that of the top SV samples (Figure 8.4(d)), the MR ratio of the pseudo SV was much lower (maximum 0.7%). This could imply that the MR can be solely contributed from the AMR responses of the NiFe and Co layers. However, it is known that Co and NiFe have AMR response that they show a resistance drop when the magnetization vector points perpendicular to the applied current compared with the case when they are running parallel to each other [9]. If there were only AMR response from the layers then one should expect that at $\phi = 0^\circ$ the resistance of the stack should be the highest at H_s , leaving behind a negative (or at most zero) MR signal, which is not the case in Figure 8.4(c). Therefore there must be contribution of GMR effect from the samples, amid its small magnitude. Apparently, the NiFe and Co layers were strongly coupled with one another. The origin of the coupling between the NiFe and Co layers can arise from any of those mechanisms discussed in section 6.3. It will be shown in the discussions section that the interlayer exchange coupling and the ‘orange peel’ type couplings appear to be the dominant coupling mechanisms the pseudo SV sample.

The MR ratio of $\sim 5\%$ in the SV samples (capped and uncapped) is close to the literature value of conventional SV [10, 11]. Two differences are evident between the MR response of the two samples. The full SV sample shows a decrease of the MR ratio (4.5%) compared with the uncapped sample (5.2%), and the exchange bias field of the pinned layer of the full SV is higher (170 and 141 Oe). These results show the effect of the Nb cap on the final performance of the SV structures. The Nb cap sacrificially protects the FeMn layer from oxidation, as seen from Table 7.1. Since the effective FeMn thickness was about 7.6 nm in the uncapped sample, it was close to the critical thickness of FeMn systems (~ 6 nm [12]) and could have possibly led to the drop H_{ex} compared with the full SV. It has to be stressed that this is not absolutely certain, given the uncertainty in the H_{ex} obtained from the control samples (Figure 8.1). On the other hand, the MR drop in the full SV can be attributed to the Nb capping, since the resistance drops are similar (0.53 - 0.56 Ω/sq) in both samples. The offset field of the free layers H_o , on the other hand, shows similar results in the two samples (-13 and -15 Oe in capped and uncapped samples, respectively).

8.3 Magnetic measurements

8.3.1 Nb/NiFe and Nb/NiFe/Cu samples

Figure 8.5 shows the angular hysteresis loops for the samples Nb/NiFe and Nb/NiFe/Cu. The hysteresis loops change from a hard-axis like behaviour (skewed loop) at $\phi = 0^\circ$ to a typical easy-axis behaviour at $\phi = 90^\circ$. These results are in echo with the analysis of the $R(H)$ measurement results presented in Figure 8.4(a) and (b). As stressed before, an anisotropy axis is expected to develop along the $\phi = 0^\circ$ axis in the two samples with the presence of the *in situ* deposition field. It has to be mentioned that a thick NiFe calibration sample (~ 325 nm) was deposited under identical condition, and it showed an easy axis close to the *in situ* field direction (Figure 8.9).

To investigate the effect, H_c and remanence (M_r/M_s , where M_r is the remanent magnetization) of the hysteresis loops were extracted and are shown in Figure 8.6. Clearly the remanence data implies an easy axis behaviour around $\phi = 90^\circ$ direction. The coercivity behaviour (Figure 8.6(b)), on the other hand, is quite different from that deduced from the SW model (Figure 1.11). An attempt is made to investigate the observed results by considering the competition between anisotropy contribution from the Nb/NiFe interface and the NiFe layer, as to be shown in the discussion section.

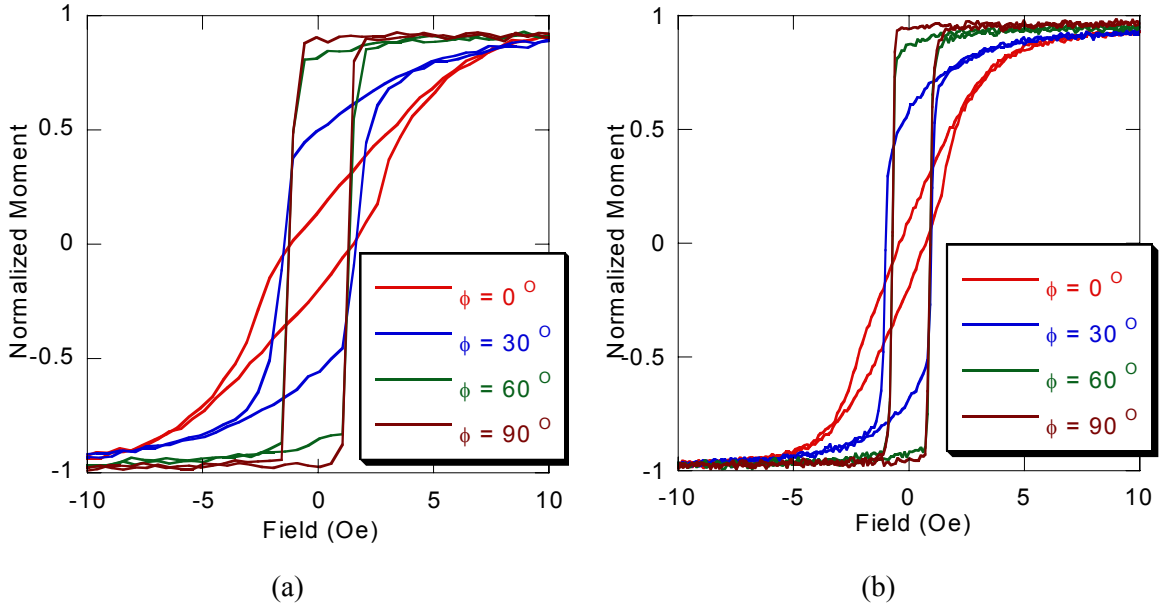


Figure 8.5 RT normalized magnetic hysteresis loops for Nb/NiFe (a) and Nb/NiFe/Cu samples.

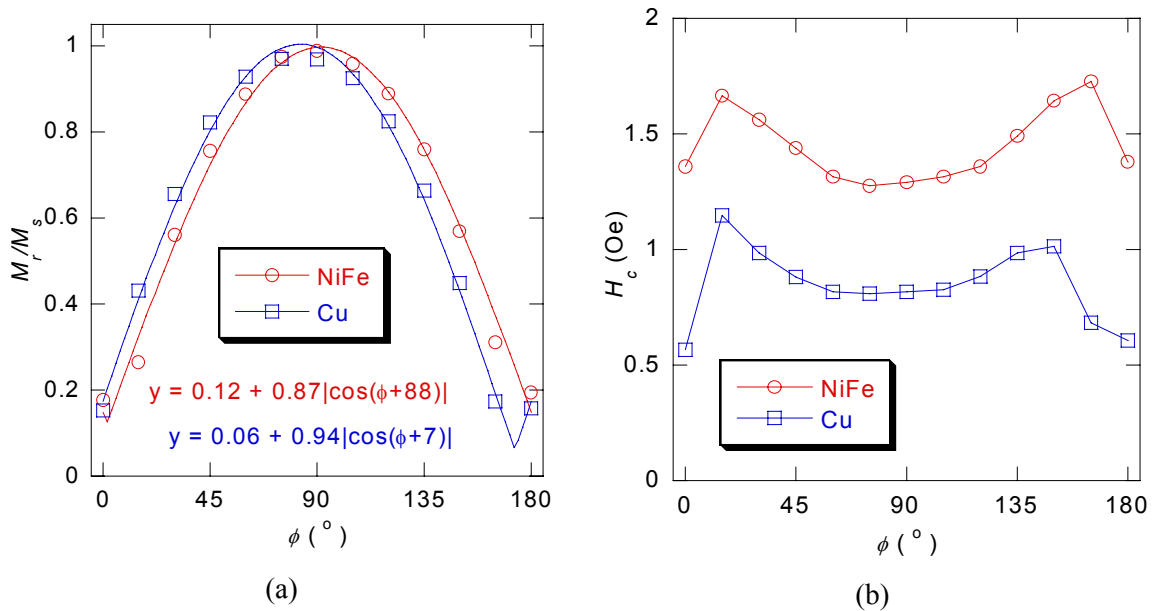


Figure 8.6 ϕ -dependence of remanence (a) and H_c (b) of Nb/NiFe and Nb/NiFe/Cu samples. Legends indicate the uppermost layers of the built-up samples. Equations shown in (a) are fits to the data, while fits in (b) are guides to the eyes only.

8.3.2 Pseudo SV sample

$M(H)$ loops of the pseudo SV sample (Nb/NiFe/Cu/Co) are presented in Figure 8.7. Only single loops could be seen in these measurements instead of the ‘double coercivity’ behaviour expected in the usual pseudo SV samples. The loss of the double loop indicated a significant FM coupling effect between the NiFe and Co layers. This conclusion is consistent with the $R(H)$ measurements results in Figure 8.4(c), in which only a tiny GMR effect was observed.

8.3.3 SV samples

Figure 8.8 compares the $M(H)$ loops of capped and uncapped SV built-up samples. Similar to the $R(H)$ measurements shown in Figure 8.4(d), H_{ex} of the capped SV was higher than that of the uncapped sample (-163 and -153 Oe respectively). In case of the free layer loop, both samples have shown an offset field H_o of -13 Oe, comparable with the $R(H)$ measurement results.

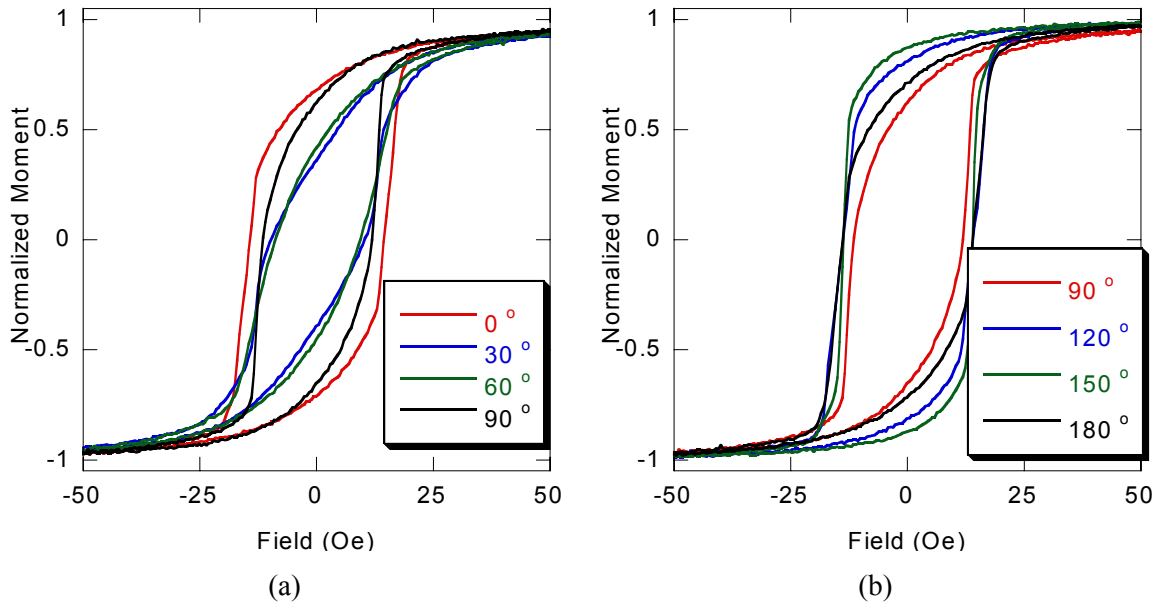


Figure 8.7 RT normalized magnetic hysteresis loops for Nb/NiFe/Cu/Co sample. Legends indicate the ϕ values at which the loops were recorded.

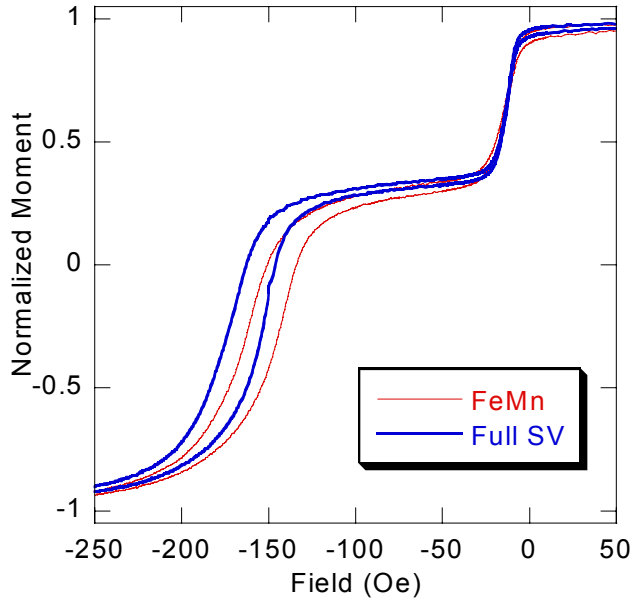


Figure 8.8 RT hysteresis loops for uncapped and Nb capped SV, measured along the *in situ* field direction ($\phi = 0^\circ$).

8.4 Discussions

As seen from the previous section, experimental results of the NiFe layer and the pseudo SV were not consistent with the findings in the literature. In the following more detailed discussions are presented on the investigations of the corresponding effects.

8.4.1 Shifted anisotropy in NiFe films

Further experiments were performed in order to investigate the origin of the switched anisotropy axis from the *in situ* field direction. Since the shifted anisotropy was observed in samples with small t_{NiFe} but not in the thick calibration sample, surface effect was suspected to be the cause. To this end two sets of samples were prepared: one batch of these samples had fixed Nb buffer thickness but varying t_{NiFe} , and the other set had the same thickness of NiFe grown on Nb buffers with different thickness.

Angular (ϕ) dependence of remanence of the batch of Nb (5 nm)/NiFe (t_{NiFe} nm) samples are shown in Figure 8.9(a), clearly indicating a trend of switching anisotropy with t_{NiFe} . The corresponding change in the phase angle (as fitted by a $|\cos\phi|$ model, see Figure 1.11(c)) is shown in Figure 8.9(b). On the other hand, the effect of t_{Nb} on remanence can be seen in Figure 8.10. It appears that the Nb buffer was also responsible for the switching of the anisotropy axis process.

Interestingly, the magnitude of remanence oscillation of the Nb (2 nm)/NiFe (5 nm) sample showed a drop in the magnitude compared with the samples with $t_{Nb} = 0$ nm and 5 nm.

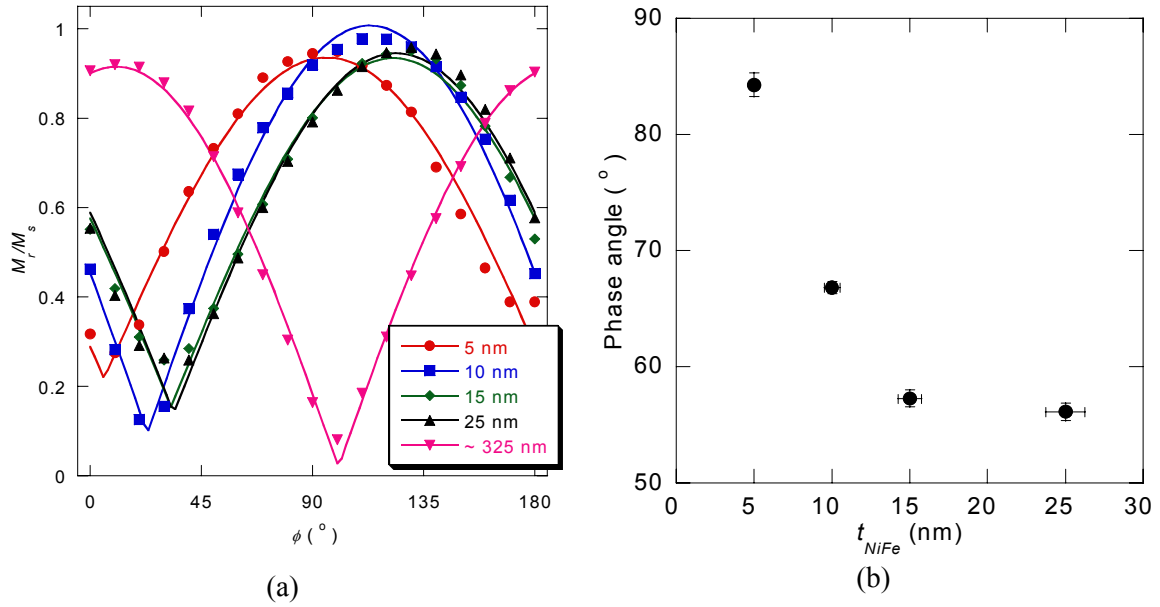


Figure 8.9 Angular dependence of remanence of Nb (5 nm)/NiFe (t_{NiFe} nm) samples (a). Data of a thick calibration NiFe sample (~ 325 nm) was shown in the same figure. The corresponding phase angle is shown in (b).

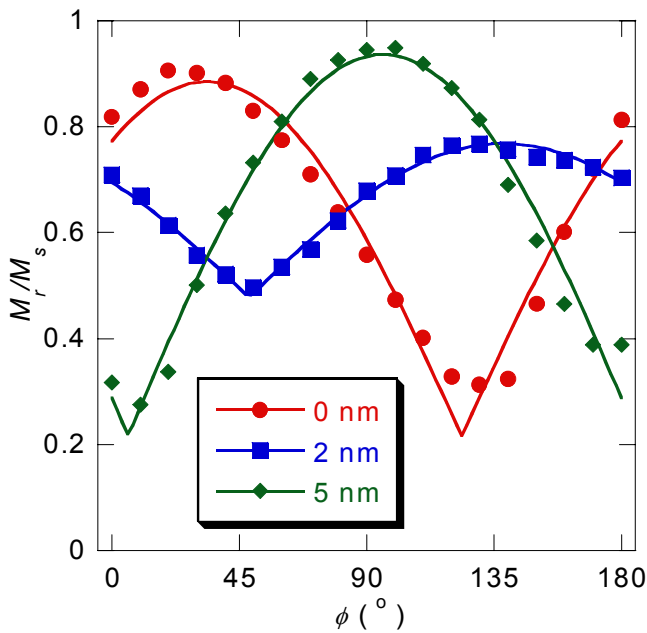


Figure 8.10 Angular dependence of remanence of Nb (t_{Nb} nm)/NiFe (5 nm) samples.

The systematic variation of the anisotropy direction with t_{NiFe} indicates the surface nature of the effect. It is useful to construct a model to describe the effect based on this idea. The energy equation can be written as:

$$E = -t_{NiFe}HM_{FM} \cos(\theta - \alpha) - t_{NiFe}K_{FM} \cos^2 \alpha - K_s \cos^2(\alpha - \psi) \quad [8.1]$$

with K_s being the surface contribution of anisotropy energy (which is independent of t_{NiFe}), K_{FM} being the uniaxial anisotropy of NiFe layer, and ψ being the angular deviation of K_s from K_{FM} . In fact the equation can be simplified into the form

$$E = -t_{NiFe}HM_{FM} \cos(\theta - \alpha) - A \cos^2(\alpha - B) + C \quad [8.2]$$

where

$$A = \sqrt{(t_{NiFe}K_{FM})^2 + K_s^2 + 2t_{NiFe}K_{FM}K_s \cos 2\psi} \quad [8.3(a)]$$

$$B = \frac{1}{2} \tan^{-1} \left(\frac{K_s \sin 2\psi}{t_{NiFe}K_{FM} + K_s \cos 2\psi} \right) \quad [8.3(b)]$$

$$C = \frac{1}{2} (A - t_{NiFe}K_{FM} - K_s) \quad [8.3(c)]$$

The model above indicates that the whole magnetic structure can have a single anisotropy with the presence of two anisotropy components, in which the magnitudes and directions are given by equations [8.3 (a)] and [8.3(b)]. The interesting point is that the magnitude of A (and hence the effective anisotropy) of the system can vary with t_{NiFe} . This may give some hint for the drop of remanence amplitude of the Nb (2 nm)/NiFe (5 nm) sample, in which A may be small enough that the film is sensing a ‘loss’ of anisotropy. The constant B , which is the ‘phase angle’ measured from K_{FM} , determines the final anisotropy direction. C is a constant and is negligible for energy calculations. A plot of the phase angle dependence is shown in Figure 8.11.

The origin of the surface anisotropy is a hard question to be answered. Some possibilities are suggested below.

a. Stress-induced anisotropy

The effect of external stress on the magnetization behaviour of magnetic films was discussed in section 1.2.1.3, and the possibility of magnetostrictive effect in NiFe films below 10 nm thick have been shown. To achieve a particular anisotropy axis, the presence of a *uniaxial* stress in the

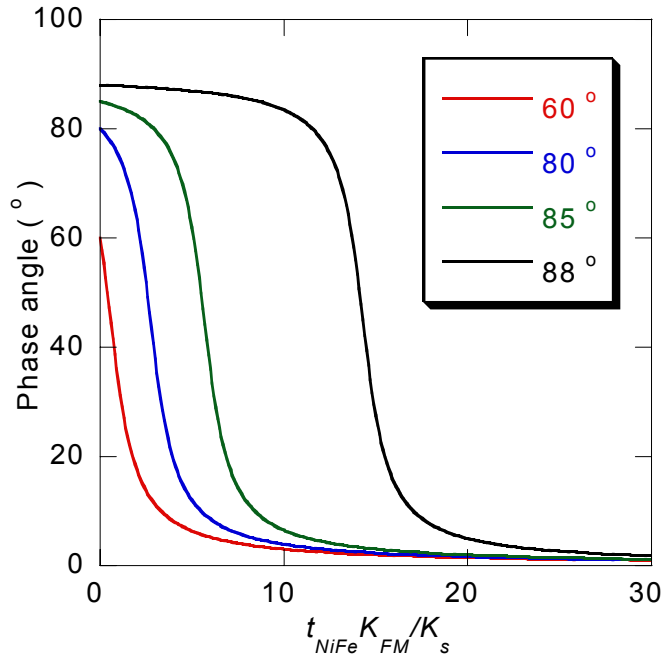


Figure 8.11 Phase angles between K_{FM} and the final uniaxial anisotropy direction as a function of the normalized parameter $(t_{NiFe}K_{FM}/K_s)$ for various values of ψ .

film plane is needed. The condition inside the deposition chamber should have provided a homogenous environment for the film deposition, except the presence of the *in situ* deposition field. However, this conclusion contradicts with most literature finding (as well as the thick calibration sample) that the *in situ* field induces an anisotropy *along* the field direction.

b. Morphology-induced anisotropy

The *in situ* field can also influence the plasma in another way. In the case of charged plasma, Lorentz force would give rise to a bent trajectory to the otherwise normal incidence of the incoming adatoms. This effectively leads to an oblique-incidence like deposition environment and gives rise to a uniaxial anisotropy (section 1.2.1.3).

If they were the real mechanisms then a more interesting question that has to be answered will be why the *in situ* field interacts differently on Nb and NiFe layer, as the degree of anisotropy switching was different for NiFe samples deposited with and without Nb buffers (Figure 8.10).

8.4.2 Coupling in pseudo SV samples

As mentioned in Chapter 6, most of the literatures have attributed the coupling between two FM layers separated by a (metallic or insulating) spacer to either one or more of the following mechanisms:

- a. Direct exchange coupling through pin-holes in spacers.
- b. Indirect interlayer exchange coupling, either bilinear or biquadratic (section 2.1).
- c. Magnetostatic ('orange peel') coupling due to roughness of interfaces.
- d. Coupling of domain walls across the spacer.

It has to be stressed that it is common to have a coupling strength of magnitude ~ 10 Oe between the FM layers in the conventional SV structures [13]. Such a coupling can be measured from the offset field H_o in the full spin valve structure. The double coercivity effect could not be observed in the pseudo SV built-up sample simply because the structure was not optimized for this purpose. Magnetically harder materials, such as CoFe, can be employed to ensure that the anisotropy of the hard layer is high enough such that the two FM layers can be switched independently.

There are some studies devoted to investigate the origin of such coupling effects. In some cases, thickness of the spacers were varied and the contributions from different sources were separated [14, 15], based on the assumption that the layer parameters (such as roughness and the crystallinity) did not vary strongly with the thickness of individual layers. Temperature dependence evaluation of the coupling strength [16], on the other hand, eliminates the potential problems of parameter variations among samples. However, assumptions have to be made on the mechanism of temperature dependence of each type of coupling, which is a matter of controversy [17, 18].

By means of the structural information obtained from the built-up samples (Chapter 7), some idea could be obtained on the relative importance of each type of coupling effect. For example, One can estimate the possibility of the direct exchange coupling effect due to geometric crossover of the NiFe/Cu and Cu/Co, with the aid of the roughness values obtained in Table 7.1. Assuming that the two surfaces were continuous and perfectly *uncorrelated*, and that the interface height variation at the interfaces were normally distributed, namely

$$P_{\text{NiFe/Cu}} \sim N(0,0.4) \quad [8.4(a)]$$

$$P_{\text{Cu/Co}} \sim N(2.93,0.35) \quad [8.4(b)]$$

the probability of the two surfaces touching each other is then given by

$$P(z_{\text{NiFe/Cu}} < z_{\text{Cu/Co}}) = \int_{-\infty}^{\infty} p_{\text{NiFe/Cu}}(z = x) p_{\text{Cu/Co}}(z < x) dx \quad [8.5]$$

which yields a value of 2×10^{-8} . If the pinholes were of sizes of a single Cu atom, this would imply a pinhole formed per every $(2.5 \text{ } \mu\text{m})^2$. The above calculations should only be treated as a rough estimate, and was based on a number of assumptions. For example, real interfaces possess vertical roughness correlation (refer to the results of Figure 7.5), and this is expected to reduce the chance of interface crossovers. On the other hand, the calculations neglected the effect of grain boundary diffusion and diffusion effect at the NiFe/Cu and Cu/Co interfaces. These sites provide paths for the formation of magnetic bridges between two FM layers.

A more direct evidence of the negligible pinhole coupling effect comes from the low temperature $R(H)$ responses of the built-up samples. If pinholes were present they should have a distribution of sizes. Small bridges become superparamagnetic at high temperature, failing to couple the NiFe and Co layers [19]. Therefore, pinhole coupling should be accompanied by a strong temperature dependence, and is expected to be much stronger at low temperature. From the MR behaviour of the pseudo SV and top SV samples in Figure 8.12 this did not appear to be the case. H_o of the free layer in the full SV sample at 77 K was 27 Oe, compared with 13 to 17 Oe as measured at RT. Unless the pinholes have a very narrow distribution of sizes, the reduced thermal activation should permit smaller pinholes to take part in the coupling.

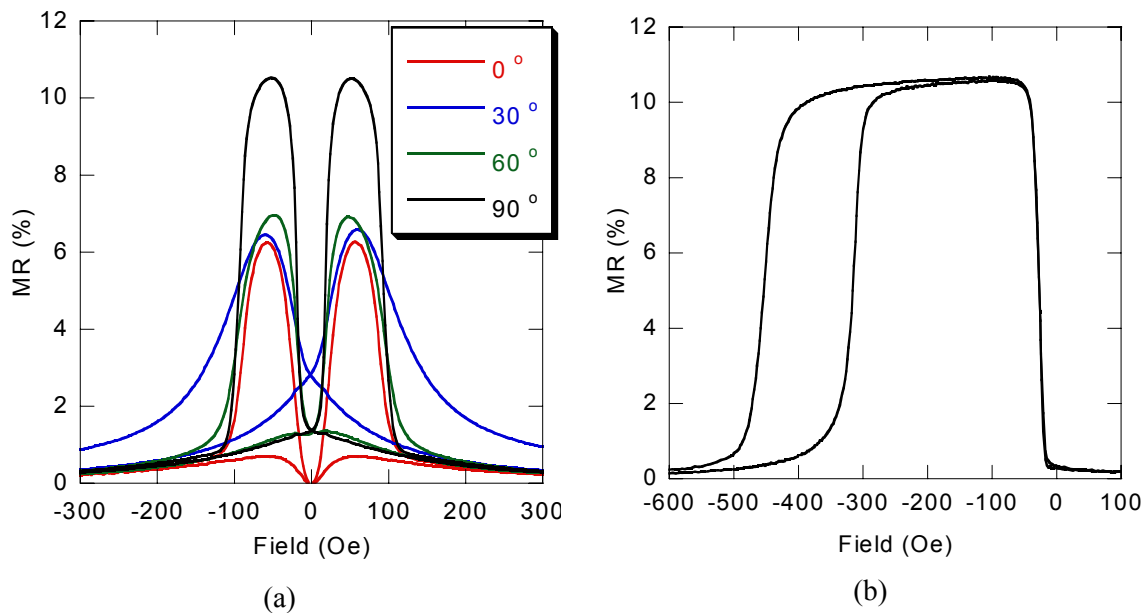


Figure 8.12 77K $R(H)$ measurements of pseudo SV built-up samples at various ϕ directions (a), and the corresponding measurement of the full SV sample at $\phi = 0^\circ$.

By means of equation [6.3], an estimate of the coupling field due to domain wall coupling was made. By fitting FM1 as NiFe and FM2 as Co, wall widths of the order 10 nm [20], the coupling field strength was calculated to be in the range of 600 – 1000 Oe. The high coupling field strength could not explain simultaneously the presence of the double coercivity behaviour at 77 K but its absence at RT. One can, however, still argue for the presence of such coupling (with the strength about 10 Oe at all temperatures so it coupled the FM layers only at RT).

By far the most commonly recognized sources of coupling in SV are the interlayer exchange coupling and ‘orange peel’-type magnetostatic coupling. An absolute determination of the significance of two effects can be done by measuring the temperature (or spacer thickness) dependence of the coupling strength, as mentioned before. Again the built-up samples strategy permit more accurate determination of the structural parameters, which is essential for the calculation of the interlayer exchange coupling and magnetostatic coupling effects.

8.5 Summary

In this chapter electric and magnetic responses of the built-up SV samples were presented. A number of unexpected results were found in these samples, and experimental attempts were made to provide some insight on these results. Structural characterization data have been employed to explain some of the observations.

The analysis in this chapter has again shown the importance of the study of built-up samples. With accurate estimate of the structural parameters, contribution of various possible sources of coupling can be identified. Besides, such technique provides a systematic optimization process for designing various magnetic structures for particular purposes. Instead of tuning various properties of different layers at the whole parameter space, the process permit one to identify and adjust these properties in a layer-by-layer approach. This should permit a more efficient design of various magnetic systems.

Reference for Chapter 8

1. C. Kittel, *Introduction to solid state physics*, p 160, Wiley (1996).
2. *CRC handbook of chemistry and physics*. 74th edition ed. CRC Press (1994).
3. M. Shiga and M. Nakamura, *J. Phys. Soc. Jpn.* **19**, 1743 (1964).
4. D.J. Keavney, S.K. Park, C.M. Falco and J.M. Slaughter, *J. Appl. Phys.* **86**, 476-479 (1999).
5. M.H. Li, G.H. Yu, H.W. Jiang, J.W. Cai, W.Y. Lai and F.W. Zhu, *J. Appl. Phys.* **92**, 2620-2623 (2002).
6. G.H. Yu, H.C. Zhao, M.H. Li, F.W. Zhu and W.Y. Lai, *Appl. Phys. Lett.* **80**, 455-457 (2002).
7. N.W. Ashcroft and N.D. Mermin, *Solid State Physics*, pp. 10,38, Saunders College (1976).
8. V.S. Speriosu, J.P. Nozieres, B.A. Gurney, B. Dieny, T.C. Huang and H. Lefakis, *Phys. Rev. B* **47**, 11579-11582 (1993).
9. T.R. McGurie and R.I. Potter, *IEEE Trans. Magn.* **11**, 1018-1038 (1975).
10. Z.Q. Lu, W.D. Wang, C.L. Chai, W.Y. Lai and Y.K. Zheng, *IEEE Trans. Magn.* **36**, 2869-2871 (2000).
11. B. Dieny, V.S. Speriosu, S.S.P. Parkin, B.A. Gurney, D.R. Wilhoit and D. Mauri, *Phys. Rev. B* **43**, 1297-1300 (1991).
12. W.J. Antel, F. Perjeru and G.R. Harp, *Phys. Rev. Lett.* **83**, 1439-1442 (1999).
13. J.C.S. Kools, W. Kula, D. Mauri and T. Lin, *J. Appl. Phys.* **85**, 4466-4468 (1999).
14. C.H. Marrows, N. Wiser, B.J. Hickey and T.P.A. Hase, *J. Phys: Cond. Mater.* **11**, 81-88 (1999).
15. J.L. Leal and M.H. Kryder, *IEEE Trans. Magn.* **32**, 4642-4644 (1996).
16. C.L. Lee, J.A. Bain, S. Chu and M.E. McHenry, *J. Appl. Phys.* **91**, 7113-7115 (2002).
17. N. Persat and A. Dinia, *Phys. Rev. B* **56**, 2676-2679 (1997).
18. J. Lindner, C. Rüdte, E. Kosubek, P. Pouloupoulos, K. Baberschke, P. Blomquist, R. Wappling and D.L. Mills, *Phys. Rev. Lett.* **88**, article no. 167206 (2002).
19. B.D. Cullity, *Introduction to magnetic materials*, in *Addison-Wesley series in metallurgy and materials*, pp. 410-418, Addison-Wesley Pub. Co (1972).
20. U. Ebels, A. Radulescu, Y. Henry, L. Piraux and K. Ounadjela, *Phys. Rev. Lett.* **84**, 983-986 (2000).

Chapter 9 Conclusions and Outlook

This chapter summarizes the work carried out during this project and discussed in this thesis. The potential applications and significance of the experiments will be mentioned. As a concluding chapter some potential directions in which research of SV and associated structures can proceed are highlighted.

9.1 Conclusions

9.1.1 Exchange bias study

In this work preliminary studies on the trilayer structure NiFe (4 nm)/FeMn (8 nm)/Co (2 nm) was carried out and compared with the corresponding single ferromagnetic layers and exchange biased bilayers (NiFe/FeMn and FeMn/Co). The samples were deposited in a specific field condition such that only the NiFe layer was saturated *in situ*. By depositing under such conditions, exchange biased structures were obtained in NiFe but not in Co in the trilayer sample. This suggested that the ‘spiral’ in the FeMn layer obtained by Yang and Chien [1] in the similar structure was *induced* by the specific field treatment they used instead of an exchange bias mechanism of its own.

Exchange bias field and coercivity of NiFe and Co layers at different temperatures for bilayers and trilayers were compared. Results obtained in this work suggested that the magnetic states of the FM and AF layers were important in determining the magnetization reversal behaviour of the systems. Besides, results of the trilayer sample showed that exchange bias in a trilayer FM/AF/FM system has to be treated as a system of its own, and change in the magnetic states of any layers can influence the exchange bias and coercivity behaviour of the whole system.

9.1.2 Spin valve built-up sample investigations

Another part of the project was concerned with the in-depth characterization of the conventional top-SV structure Nb (5 nm)/NiFe (4 nm)/Cu (3 nm)/Co (5 nm)/FeMn (10 nm)/Nb (5 nm), using a ‘built-up samples’ approach. Such samples, which represent different stages of growth of the spin valve structure, were prepared under identical deposition conditions. Structural, magnetic and

electrical measurements were performed on these samples. Correlation was drawn between these properties to investigate how they are developed during the deposition process.

A number of unusual properties were found in the built-up samples. These included the switched in-plane anisotropy of the NiFe layer from the *in situ* field direction, the coupling of the NiFe and Co layers across the Cu spacer, and the abnormal resistivity of the Cu and FeMn layers. By means of some complementary experiments deeper understanding was made on the phenomena observed.

The main point stressed by this work is the usefulness of the ‘built-up samples’ technique in studying SV or multilayers in general. Interesting properties could have been shadowed if completed samples alone were deposited and studied. Such kind of negligence occurs frequently in the literature, and these subtle or hidden effects often provide vital clues on solving particular problems [2, 3]. While *in situ* environment is ideal for such studies, thorough examination of the built-up samples *ex situ* can be sufficient to provide many useful information, and can be easily implemented in all laboratories.

9.2 Outlook

9.2.1 Spin valves

The ‘built-up samples’ technique, as seen from this project, can be employed as a protocol for detailed analysis of SV or different types of magnetic multilayer structures. For example, the study can be modified to investigate the effect of working gas pressure for depositing FeMn layer on the MR performance of the SV structure [4]. While many of the studies have been targeted at the effect of a particular parameter (for example buffer layer [5], use of surfactants [6-8] and stability of AF layers [9, 10]) on the MR performance, the effect can actually be a consequence of complicated evolution of many intermediate processes. An understanding of such processes permits more efficient optimization of various magnetic heterostructures.

9.2.2 Exchange bias

Despite the intensive efforts made in the study of exchange bias effect, a *generalized* microscopic picture of the phenomenon is elusive [11]. In terms of experimental studies, some recent tests

have been put through to challenge the existing ideas about the EB effect [12-16]. Recent theories [17-19] seem to provide a clue on these observations, but still more experimental work has to be carried out for verifications.

Trilayer structure of FM/AF/FM turns out to be a good system for investigation the exchange bias effect. Interactions between two FM layers through an AF spacer have been studied in some systems [1, 20-22]. However, surprisingly few of these works have reported exchange bias effects [23], and many of the experimental work have suggested biquadratic coupling between the FM layers. The ‘low field deposition’ strategy employed in this work, combined with specific field annealing measurements, could provide some further insight on the problem.

The results presented in this thesis are preliminary. For example, t_{FeMn} variation on the NiFe/FeMn/Co trilayer structure could be employed to study the interaction between NiFe and Co layer through the FeMn layer. On the other hand, there is a large room for physical studies of the exchange bias systems in the regime of $T_C \ll T_N$. Experimental implementation so far is lacking [12, 24]. Compared with the EB systems in which $T_C \gg T_N$, such system do not suffer from the drawback of $A_{FM} > A_{AF}$. This means that the FM is more likely to probe the magnetic state of the AF interface without disturbing the AF spin structure, possibly permitting a better studies on the reversal process of the AF. By replacing one or even both of the FM layers in the NiFe/FeMn/Co structure, more complete understanding of the exchange bias effect, extended to the regime of $T_C \ll T_N$, could be made.

9.2.3 Nanomagnetism

A very important motive for all the studies of the GMR and related phenomena explored in this project is their potential in applications. The empirical Moore’s Law for computer-related technologies (processor speed, storage density) have been closely followed for nearly 40 years [25]. To cope with such a trend, thorough studies of miniaturized magnetic structures have to be made. At the moment a lot of basic investigations are carried out, most of them concentrating on single FM layers with different geometries. Some initial attempts have been made on studying nanopatterned heterostructures [26]. Many issues have to be overcome in such processes, such as size and geometry dependence of properties [27, 28], the effect of fabrication procedures

[26, 29-31], interaction between different structures [32]. Extension of these studies in different magnetic structures is certainly a major area of studies, and can hopefully compliment the much-heated research of 'spintronics' [33, 34].

References for Chapter 9

1. F.Y. Yang and C.L. Chien, *Phys. Rev. Lett.* **85**, 2597-2600 (2000).
2. W.E. Bailey, S.X. Wang and E.Y. Tsybal, *Phys. Rev. B* **61**, 1330-1335 (2000).
3. W.E. Bailey, S.X. Wang and E.Y. Tsybal, *J. Appl. Phys.* **87**, 5185-5187 (2000).
4. Z.Q. Lu, W.D. Wang, C.L. Chai, W.Y. Lai and Y.K. Zheng, *IEEE Trans. Magn.* **36**, 2869-2871 (2000).
5. S. Colis, A. Dinia, D. Deck, G. Schmerber and V. Da Costa, *J. Appl. Phys.* **88**, 1552-1558 (2000).
6. W.F. Egelhoff, P.J. Chen, C.J. Powell, M.D. Stiles, R.D. McMichael, C.L. Lin, J.M. Sivertsen, J.H. Judy, K. Takano, A.E. Berkowitz, T.C. Anthony and J.A. Brug, *J. Appl. Phys.* **79**, 5277-5281 (1996).
7. W.F. Egelhoff, P.J. Chen, C.J. Powell, M.D. Stiles and R.D. McMichael, *J. Appl. Phys.* **79**, 2491-2496 (1996).
8. W.F. Egelhoff, P.J. Chen, C.J. Powell, M.D. Stiles, R.D. McMichael, J.H. Judy, K. Takano and A.E. Berkowitz, *J. Appl. Phys.* **82**, 6142-6151 (1997).
9. J.P. Nozieres, S. Jaren, Y.B. Zhang, A. Zeltser, K. Pentek and V.S. Speriosu, *J. Appl. Phys.* **87**, 3920-3925 (2000).
10. A.J. Devasahayam and M.H. Kryder, *IEEE Trans. Magn.* **35**, 649-654 (1999).
11. M. Kiwi, *J. Magn. Magn. Mater.* **234**, 584-595 (2001).
12. X.W. Wu and C.L. Chien, *Phys. Rev. Lett.* **81**, 2795-2798 (1998).
13. P. Miltényi, M. Gierlings, J. Keller, B. Beschoten, G. Guntherodt, U. Nowak and K.D. Usadel, *Phys. Rev. Lett.* **84**, 4224-4227 (2000).
14. P.J. van der Zaag, Y. Ijiri, J.A. Borchers, L.F. Feiner, R.M. Wolf, J.M. Gaines, R.W. Erwin and M.A. Verheijen, *Phys. Rev. Lett.* **84**, 6102-6105 (2000).
15. H. Ohldag, T.J. Regan, J. Stohr, A. Scholl, F. Nolting, J. Luning, C. Stamm, S. Anders and R.L. White, *Phys. Rev. Lett.* **87**, 7201-+ (2001).
16. S.M. Zhou and C.L. Chien, *Phys. Rev. B* **63**, 4406-+ (2001).
17. M.D. Stiles and R.D. McMichael, *Phys. Rev. B* **59**, 3722-3733 (1999).
18. M.D. Stiles and R.D. McMichael, *Phys. Rev. B* **60**, 12950-12956 (1999).
19. M.D. Stiles and R.D. McMichael, *Phys. Rev. B* **63**, 4405-+ (2001).
20. M.E. Filipkowski, J.J. Krebs, G.A. Prinz and C.J. Gutierrez, *Phys. Rev. Lett.* **75**, 1847-1850 (1995).
21. P.A.A. van der Heijden, C.H.W. Swuste, W.J.M. de Jonge, J.M. Gaines, J. van Eemeren and K.M. Schep, *Phys. Rev. Lett.* **82**, 1020-1023 (1999).
22. H.W. Xi and R.M. White, *Phys. Rev. B* **62**, 3933-3940 (2000).
23. M.H. Pan, J. Chen, J.G. Long, L.N. Tong, M. Lu, J. Du, A. Hu and H.R. Zhai, *J. Magn. Magn. Mater.* **226**, 1817-1819 (2001).
24. J.W. Cai, K. Liu and C.L. Chien, *Phys. Rev. B* **60**, 72-75 (1999).
25. G.E. Moore, *Electronics* **38** (1965).
26. J.A. Katine, A. Palanisami and R.A. Buhrman, *Appl. Phys. Lett.* **74**, 1883-1885 (1999).
27. A. Lebib, S.P. Li, M. Natali and Y. Chen, *J. Appl. Phys.* **89**, 3892-3896 (2001).
28. T.H. Wu, J.C. Wu, C.S. Wu, B.M. Chen and H.P.D. Shieh, *J. Magn. Magn. Mater.* **209**, 220-223 (2000).
29. G. Xiong, D.A. Allwood, M.D. Cooke and R.P. Cowburn, *Appl. Phys. Lett.* **79**, 3461-3463 (2001).
30. T. Mewes, R. Lopusnik, J. Fassbender, B. Hillebrands, M. Jung, D. Engel, A. Ehresmann and H. Schmoranzer, *Appl. Phys. Lett.* **76**, 1057-1059 (2000).
31. A. Mougín, T. Mewes, M. Jung, D. Engel, A. Ehresmann, H. Schmoranzer, J. Fassbender and B. Hillebrands, *Phys. Rev. B* **63**, 0409-+ (2001).

32. A.O. Adeyeye, R.P. Cowburn and M.E. Welland, *J. Magn. Magn. Mater.* **213**, L1-L6 (2000).
33. S.A. Wolf, D.D. Awschalom, R.A. Buhrman, J.M. Daughton, S. von Molnar, M.L. Roukes, A.Y. Chtchelkanova and D.M. Treger, *Science* **294**, 1488-1495 (2001).
34. G.A. Prinz, *Science* 282, 1660-1663 (1998).